Model-Based Experimental Investigation of Hydrogenase-Like Electrocatalytic Inactivation and Activation Mechanisms

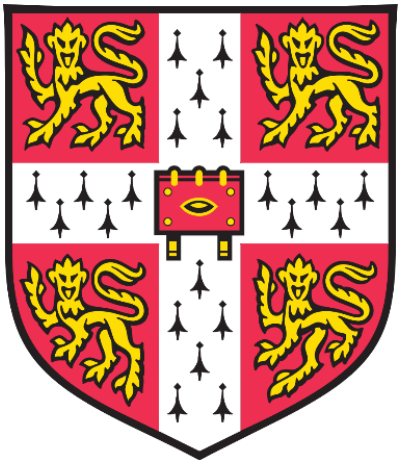

Yian Wang

Fitzwilliam College

Department of Chemical Engineering and Biotechnology

University of Cambridge

September 2018

This dissertation is submitted for the degree of

Doctor of Philosophy

Declaration

I hereby declare that this thesis is carried out in the Department of Chemical Engineering and Biotechnology, University of Cambridge from October 2014 to September 2018, and has not been submitted in whole or in part for consideration for any other degree or qualification in this, or any other University. The result in this dissertation is of my own work and includes nothing which is the outcome of work done in collaboration except where specifically indicated in the text. This work contains fewer than 65,000 words including appendices, references, tables and equations and has less than 150 figures.

Yian Wang

September 2018

Abstract

Model-Based Experimental Investigation of Hydrogenase-Like Electrocatalytic Inactivation and Activation Mechanisms

Yian Wang

This thesis describes an experimental design framework study which is focused on the investigation of highly complex electrocatalytic mechanisms. Fully model-based approaches combined with the Butler-Volmer model is employed from a pure theoretical model to a validation of practical chemical reactions.

The initial chapters introduce the fundamentals and applications of the electrochemistry. Chapter 1 provides an overview of the electrode processes and the governing physical factors which may limit an electrolysis reaction. In Chapter 2, detailed simulation techniques are introduced to interpret an abstractive system into a mathematic problem then to find an accurate, efficient and stable path to the solution.

The results begin in Chapter 3, in which a novel high-order operator-splitting (OS) scheme, with fully implicit finite difference (FIFD) method is first time proposed to numerically solve the stiff nonlinear problems in electrochemistry, particularly in electrocatalysis. The developed algorithm is tested through a series of validations for different electrochemical reactions on large planar electrodes. The model predictions employing this method were verified against a classic two-point time evolution implicit finite difference method for typical electrochemical systems.

In Chapter 4, the numerical methods are applied to explore a complex redox system, a recently observed hydrogenase-like reaction. Subtle kinetic and mechanistic information is extracted from the voltammetric behaviour and quantitative mechanistic insights obtained.

In Chapter 5, an alternative chronoamperometric voltammetry is introduced to explore the same electrocatalytic system described in Chapter 4 in order to explore some unusual current features observed in the redox chemistry.

These stepwise studies support a mechanism for glucose oxidation that proceeds most likely through a complex electrocatalytic (EC'CE) scheme with catalytic steps similar to the ones

reported for [NiFe] hydrogenases. The overall mechanism of the molecular inactivation and activation process (IAP) was detailed on the basis of our experimentally validated models and compared to [NiFe] hydrogenase IAP. Our findings offer novel perspectives to design finely optimised catalysts by eliminating the inactivation phenomena.

Acknowledgments

First and foremost, I would like to express my deepest gratitude to my supervisor Dr Adrian Fisher, who offered me the opportunity to undertake my PhD project and continue my research in his group after transferring from another research group. I sincerely appreciate that his long-time guidance and support, both technically and logistically, helped shape this work. I am also extremely grateful to Dr Kamal Elouarzaki for the experimental data, the profound knowledge of chemistry, the discussion of the work and all the generous supports during my PhD life in Cambridge CARES in Singapore.

I also would like to thank Dr Viet Nguyen for the kind guidance on numerical modelling when I started simulation and programming. Many thanks to Dr Alexander Vikhansky for his ideas and contributions of operator splitting method presented in Chapter 3. I thank Vishvak Kannan for his great encouragement not only on my study, but also on my life in Singapore.

My sincere thanks also extend to my dear colleagues, Dr Peng Song, Dr Chencheng Dai, Dr Hongkai Ma, Dr Xiangming Gao, Luwen Meng, Feng Zheng and other members of CREST group in Cambridge, and Dr Ashoke Raman, Shengliang Zhang and other members of Cambridge CARES in Singapore. Particularly, a very special thanks to my friends who accompany me during time in Cambridge and in Singapore. Thank you for all the patient conversation with me when I am under great pressure.

I acknowledge Amanda Taylor in the Department of Chemical Engineering and Biotechnology, Xiangning Leong in Cambridge CARES in Singapore and all other assistant staff for their kindness and friendliness.

Finally, and above all to my dearest parents, my father Shimin Wang and mother Zhifang Dong, for their selfless financial support and constant encouragement in my whole PhD experience. Their material and spiritual support let my overseas life feel joyful. I love you.

Publications

Song, P., Ma, H., Meng, L., Wang, Y., Nguyen, H. V., Lawrence, N. S., & Fisher, A. C. Fourier transform large amplitude alternating current voltammetry investigations of the split wave phenomenon in electrocatalytic mechanisms. *Physical Chemistry Chemical Physics*, **19**, 24304-24315 (2017).

Elouarzaki, K., Wang, Y., Kannan, V., Xu, H., Cheng, D., Lee, J., & Fisher, A. C. Hydrogenase-like electrocatalytic activation and inactivation mechanism by three-dimensional binderless molecular catalyst. *ACS Applied Energy Materials*, **2**, 3352-3362 (2019).

Wang, Y., Elouarzaki, K., Kannan, V., Lee, J., & Fisher, A. C. Surface electrochemistry of rhodium porphyrin functionalised multi-walled carbon nanotube electrodes species and oxygen reduction electrocatalysis: formation of a dimeric species. Under review.

Vikhansky, A., Wang, Y., Nguyen, H. V., & Fisher, A. C. High order, fully implicit, operator-splitting finite difference scheme for cyclic voltammetry. In preparation.

Nomenclature

Standard Subscripts

a	anodic	b	backward
c	cathodic	dl	double layer
eq	equilibrium	f	forward
O	species O in $O + ne \rightleftharpoons R$	p	peak
r	reversal	R	species R in $O + ne \rightleftharpoons R$
sw	switch	S	substrate

Roman Symbols

Symbol	Meaning	Unit
A	electroactive surface area	cm^2
C_{dl}	double layer capacitance	F
C_j	concentration of species *j*	M, mol cm^{-3}
C_j^*	bulk concentration of species *j*	M, mol cm^{-3}
$C_j(x,t)/C^t_{[j],x}$	concentration of species *j* at distance x at time t	M, mol cm^{-3}
D_j	diffusion coefficient of species *j*	$cm^2\ s^{-1}$
d_c	width of the cell	cm
E	electrode potential	V
E^0	standard potential of an electrode	V
E_{ac}	ac component of potential	V
E_{dc}	dc component of potential	V
E_{eq}	equilibrium potential of an electrode	V
E_i	initial potential	V
E_p	peak potential	V
$E_{p/2}$	half-peak potential where $i = i_p/2$ in LSV	V
E_{pa}	anodic peak current	V
E_{pc}	cathodic peak current	V

E_v	vertex potential	V
$E_{1/2}$	half-wave potential in voltammetry	V
ΔE	amplitude of ac excitation in AC voltammetry	mV
ΔE_p	pulse height in SWV	mV
ΔE_s	staircase height in SWV	mV
F	Faraday constant	$\mathrm{C \cdot mol^{-1}}$
f	F/RT	$\mathrm{V^{-1}}$
	SWV frequency	$\mathrm{s^{-1}}$
h	half-height of the channel	cm
i	current	A
i_c	capacitive current	A
i_f	faradic current	A
i_p	peak current	A
i_ss	steady-state current	A
i_0	exchange current	A
$J_\mathrm{j}(x,t)$	flux of species *j* at distance x at time t	$\mathrm{mol\ cm^{-2}\ s^{-1}}$
j	current density	$\mathrm{A\ cm^{-2}}$
j_0	exchange current density	$\mathrm{A\ cm^{-2}}$
K_eq	equilibrium constant	$-$
k	first order rate constant for a homogeneous reaction	$\mathrm{s^{-1}}$
	second order rate constant for a homogeneous reaction	$\mathrm{cm^3\ s^{-1}\ mol^{-1}}$
k_0	standard rate constant for a heterogeneous reaction	$\mathrm{cm\ s^{-1}}$
k_b	backward rate constant for a homogeneous reaction	$\mathrm{s^{-1}}$
k_f	forward rate constant for a homogeneous reaction	$\mathrm{s^{-1}}$
l	thickness of solution in a thin-layer cell	cm
n	Stoichiometric number of electrons involved in an electrode reaction	$-$
R	universal gas constant	$\mathrm{J\ mol^{-1}\ K^{-1}}$
R_u	uncompensated resistance	Ω
r	radius of an electrode	cm

T	absolute temperature	K
t	time	s
Δt	timestep	s
t_{p}	pulse width in SWV	s
t_{s}	staircase width in SWV	s
u^n	independent variable at timestep n in operator-splitting scheme	–
v	scan rate	$\mathrm{V\ s^{-1}}$
v_{j}	component velocity in the *j* direction	$\mathrm{cm\ s^{-1}}$
w_{e}	width of a band electrode	cm
x	distance from a planar electrode	cm
x_{e}	length of a band electrode	cm
Δx	space step	cm
y	distance from an RDE	cm
z_{j}	charge on species *j* in signed units of electronic charge	–

Greek Symbols

Symbol	Meaning	Unit
α	charge transfer coefficient	–
Γ_{j}	surface excess of species *j*	$\mathrm{mol\ cm^{-2}}$
Γ^*	total surface excess	$\mathrm{mol\ cm^{-2}}$
δ_{j}	diffusion layer thickness for species *j* at an electrode fed by convection	cm
$\delta_{0/i}$	Kronecker's delta	–
η	overpotential, $E - E_{\mathrm{eq}}$	V
θ	$\exp[(nF/RT)(E - E^0)]$	–
$\mathcal{L}$	operator function in splitting method	–
τ	pseudo timestep	s
Φ	the ratio/fraction of two parts	–

ϕ^n	the increment of the independent variable at timestep n in operator-splitting scheme	$-$
ϕ_j	electrostatic potential of species j	V
ψ	normalised current in voltammetry	$-$
ψ^n	the increment of the independent variable at timestep n in operator-splitting scheme	$-$
ω	angular frequency of a sinusoidal oscillation	s^{-1}

Abbreviations

Abbreviation	Meaning
AC	alternating current
CV	cyclic voltammetry
DC	direct current
DPDE	deuteron-porphyrin dimethyl-ester
EC	heterogeneous electron transfer coupled with homogenous chemical reaction
EC’	electrocatalytic reaction
FDM	finite difference method
FEM	finite element method
FVM	finite volume method
FIFD	fully implicit finite difference method
FIRM	fully implicit Richtmyer modification
IAP	inactivation and activation process
LSV	linear sweep voltammetry
MBED	model based experimental design
OS	operator splitting scheme
PDE	partial differential equation
RDE	rotating disc electrode
RDS	rate-determining step
SWV	square wave voltammetry

Contents

Chapter 1

1. Electrochemical Fundamentals

The advent of rapid digital technologies and computational strategies has led to the development of model based experimental design (MBED) across a broad and diverse research community. The growing computing power has allowed more accurate prediction of experimental measurements and under some circumstances, the number of experimental measurements required can be reduced due to high-fidelity multi-physics systems which can be more easily tested and understood qualitatively and/or quantitatively via using digital simulations rather than real data. A schematic diagram of an MBED is summarised in Figure 1.1[1]. The methodologies can be separated into two elemental stages: the evaluation of experiments for model discrimination before estimating the parameters, and the validation of pre-designed experimental models by simulating the system. The first step decides the appropriate models that can be used to depict the physics and chemistry observed in the experiments. This stage of work can be affected by academic background and experience. Once a reasonable hypothesis is raised, it is essential to validate the precision of the model with selected modules and controlled variables in the subsequent stage. The pre-designed model is satisfied after repeating the second stage and detailing the system. An accurate, efficient and powerful simulation tool then can be finally applied for the realistic system after fully validation. Following these two procedures of MBED, scientists are offered deep insights into scientific fields. The model based experimental design is widely used in applied physics[2,3], chemistry[4-6], chemical engineering[7,8], or related field[9,10].

In an electrochemical context, MBED is important for the understanding of chemical reactions and optimisation of experimental processes. This approach has led to rapid developments in clean energy conversion systems[11-14], environment-friendly technologies[15-17], molecular synthetic engineering[18-20]and the biochemical industry[21-23] in the past two decades. These applications have recently started driving the demand for mechanistic analysis especially in more realistic and complicated circumstances. One of these applications is the kinetic investigation of electrocatalytic systems, which play a vital role in exploring extremely efficient electrocatalysts.

The goal of this thesis is to unravel a variety of complex electrocatalytic phenomena by setting up fully model-based experimental techniques. Different numerical models are employed to study from non-catalytic electrochemical systems to electrocatalytic systems, from simple electrochemical mechanisms to very complex electrocatalytic cases.

In this chapter an introduction to the key fundamentals of the electrochemistry used for mechanistic analysis is reviewed associated with the relevant literature. This is then followed in Chapter 2 with further details of digital simulation methodologies applied to electrochemical analysis covered in the result chapters.

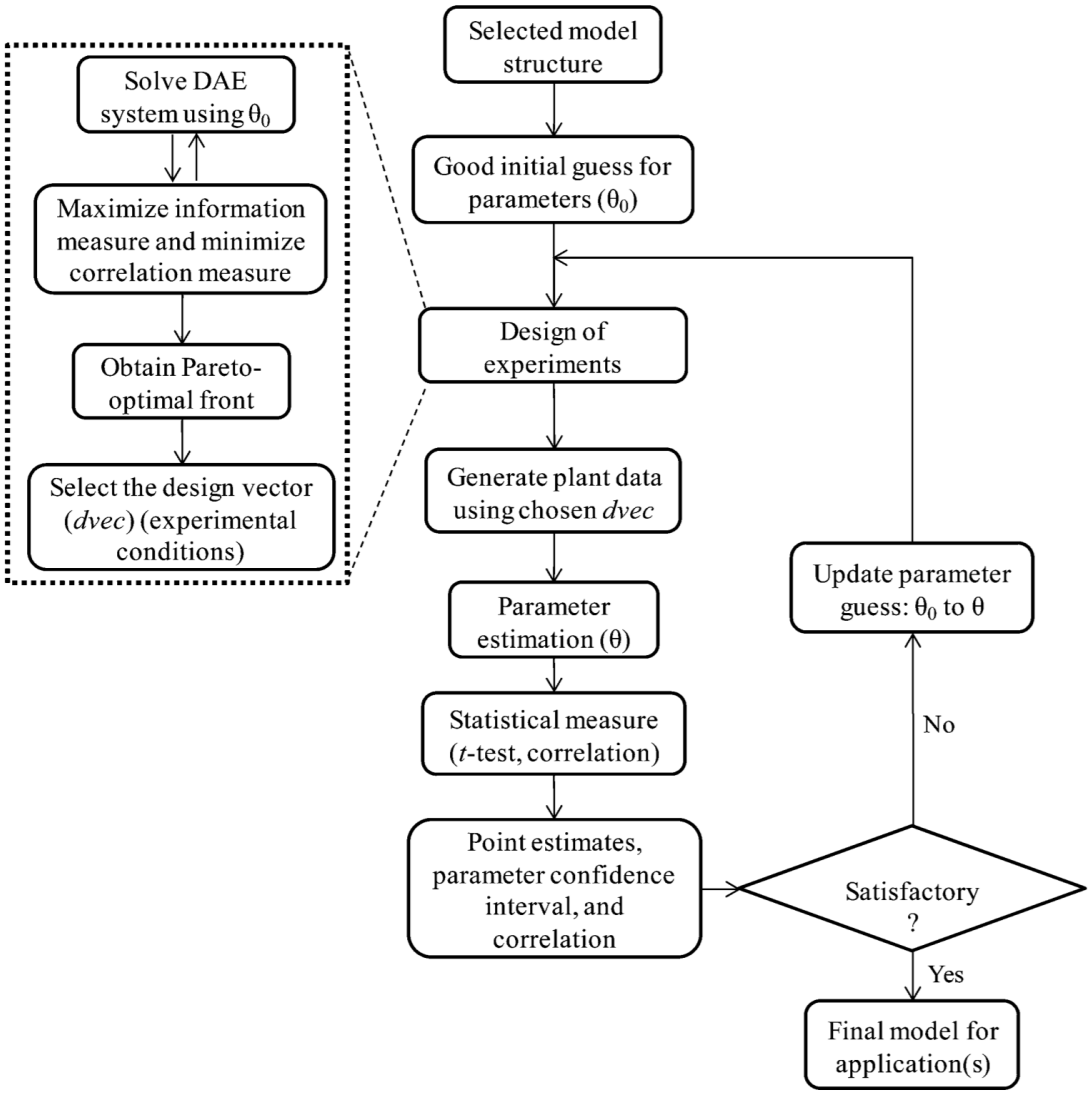

Figure 1.1: A schematic framework of model based experimental design (MBED) adapted from Samavedham *et al.*'s work[1].

1.1. Kinetics of Electrochemical Reactions

Dynamic electrochemistry is a branch of physical chemistry that deals with electron transfer reactions between reactant molecules and electrodes[24]. The field encompasses a wide range of scientific research and industrial applications. Examples include the synthesis of fine chemicals[25-27], electroplating[28,29], and the production of aluminium[30], copper[31] and other corrosion-protection materials[31]. Other well-known examples involve but are not limited to electrochemical-based sensors (e.g., glucose sensors[32,33], gas detectors[34] and pH meters[35]) and chlor-alkali industries[36].

Electrochemists study the chemical reactions which involve electron exchange processes, in which the reactions can exchange the electrons in the same phase (homogeneous kinetics), or at an interface (heterogeneous kinetics). In the first case, the transfer process can exist everywhere within the medium at a uniform rate[37]. In contrast, the heterogeneous electron transfer reaction occurs only between an electrode and an electrolyte or liquid-liquid interfaces.

The latter case is of great scientific interest, as it allows direct probing of electronic energy levels contained within an electrode through an external power source. In this way, the kinetic and thermodynamic information can be obtained. The rate of this charge transfer process is affected by:

- Material transport between the electrode and bulk solution
- Controlled-potential methods applied on electrode surface
- Electrode reaction with coupled homogeneous chemical reactions

The aim of this section is to quantify the potential dependence of heterogeneous electrochemical reactions for electron transfer. A fundamental redox process involving single electron transfer at a common electrode-electrolyte interface:

$$\mathrm{O} + \mathrm{e}^- \underset{k_\mathrm{b}}{\overset{k_\mathrm{f}}{\rightleftharpoons}} \mathrm{R} \tag{1.1}$$

where O and R represent the oxidised and reduced forms of electroactive species, respectively.

This reductive/oxidative pair is treated as a conductive surface corresponding to a three-electrode system in a practical system for example shown in Figure 1.2. The electric circuit is composed of a working electrode, counter electrode and the electrolyte solution, with a reference electrode

employed to measure the potential difference. Once an external driving force such as a potential is applied to the working electrode, an output current flow can be measured between the working electrode and counter electrode.

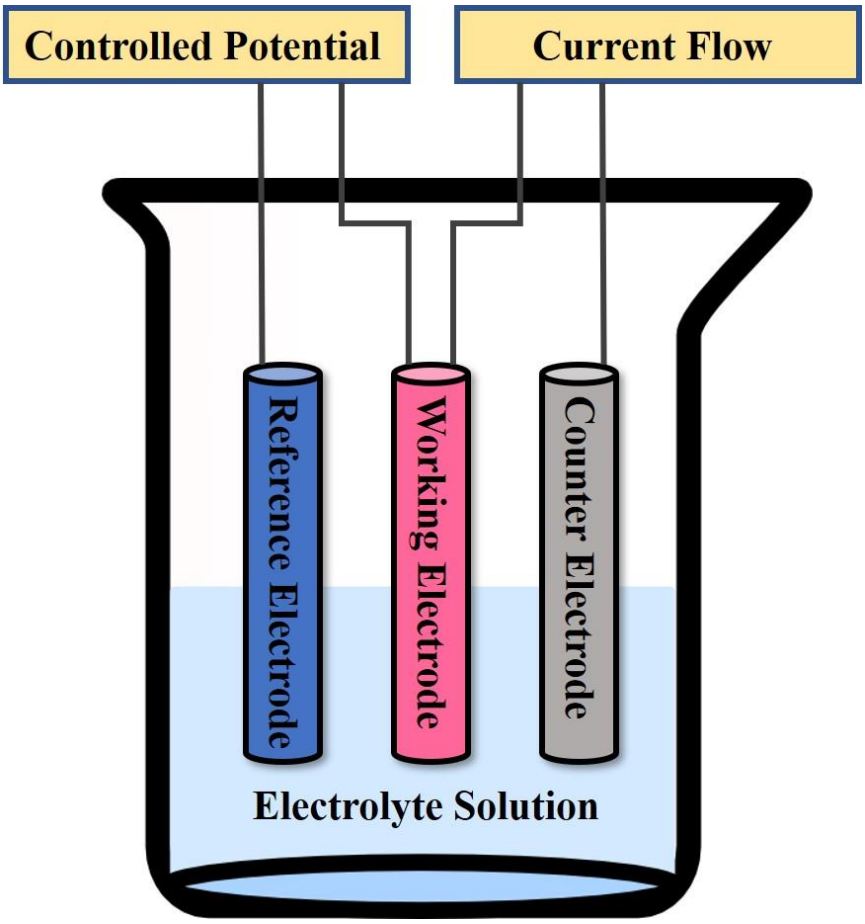

Figure 1.2: Typical three-electrode cell used for electrochemical measurements.

The current generated by electron transfer can be quantified as

$$i = nFAJ_j(0,t) \tag{1.2}$$

where n is the stoichiometric number of electrons involved in an electrode reaction. F is the Faraday constant ($\mathrm{C\ mol^{-1}}$), A is given as the electroactive surface area ($\mathrm{cm^2}$) and $J_j(0,t)$ presents the flux of species *j* at the electrode ($\mathrm{mol\ cm^{-2}\ s^{-1}}$). The flux is an important parameter since it is directly related to the current, and it also reflects the rate of the forward and backward process for the electrochemical reactions.

For a fully reversible case given in Equation 1.1, the flux for forward and backward processes could be predicted respectively as,

$$J_{\mathrm{f}}(0,t) = k_{\mathrm{f}} C_{\mathrm{O}}(0,t) \tag{1.3}$$

$$J_{\mathrm{b}}(0,t) = k_{\mathrm{b}} C_{\mathrm{R}}(0,t) \tag{1.4}$$

where k_{f} and k_{b} are the respective heterogeneous rate constants for reductive and oxidative electron transfer reaction, $C_{\mathrm{O}}(0,t)$ and $C_{\mathrm{R}}(0,t)$ are concentrations of O and R at electrode surface. Therefore, the new current flowing in Equation 1.2 is written by substitution of Equations 1.3 and 1.4,

$$i = i_{\mathrm{a}} + i_{\mathrm{c}} = nFA[k_{\mathrm{b}} C_{\mathrm{R}}(0,t) - k_{\mathrm{f}} C_{\mathrm{O}}(0,t)] \tag{1.5}$$

where i_{c} is the cathodic (forward) current and i_{a} is the anodic (backward) current.

The pioneers[38,39] of physicists derived k_{b} and k_{f} from the Arrhenius equation[40] and transition state theory[41] to obtain the relationship between rate constants and applied potential. Detailed derivation can be found in the relative references[24,42,43] and the results are concluded to show the dependency of rate constant and operating potential,

$$k_{\mathrm{f}} = k_0 e^{-\alpha \frac{F}{RT}(E - E^0)} \tag{1.6}$$

$$k_{\mathrm{b}} = k_0 e^{(1-\alpha) \frac{F}{RT}(E - E^0)} \tag{1.7}$$

where R is the universal gas constant (J mol^{-1} K^{-1}) and T is absolute temperature (K). α is the charge transfer coefficient having a value range from zero to unity, which reflects the symmetry of the free-energy curve. A value of 0.5 is used for most cases in this dissertation, which suggests the transition state stands midway between reactants and products. E^0 is the standard potential of an electrode in which k_{f} has the same value as k_{b} at equilibrium and k^0 is standard rate constant for a heterogeneous reaction. Thus, the formulation of electrode kinetics establishes the important *current-potential characteristic*:

$$i = nFAk_0 \left[C_{\mathrm{R}}(0,t) e^{(1-\alpha) \frac{F}{RT}(E - E^0)} - C_{\mathrm{O}}(0,t) e^{-\alpha \frac{F}{RT}(E - E^0)} \right] \tag{1.8}$$

At equilibrium, the net current equals zero, and the concentrations of O and R can be summarised as

$$\frac{C_{\mathrm{O}}(0,t)}{C_{\mathrm{R}}(0,t)} = e^{\frac{F}{RT}\left(E_{\mathrm{eq}} - E^{0}\right)} \tag{1.9}$$

where E_{eq} is equilibrium potential of an electrode. When $t = 0$, this value presents an exponential form of the Nernst equation,

$$E_{\mathrm{eq}} = E^{0} + \frac{RT}{F}\ln\frac{C_{\mathrm{O}}^{*}}{C_{\mathrm{R}}^{*}} \tag{1.10}$$

Faradaic current here can be presented in terms of exchange current, i_0, which has the same absolute value to either component current, i_{a} and i_{c}. That is

$$i_0 = nFAk_0 C_{\mathrm{O}}^{*\,(1-\alpha)} C_{\mathrm{R}}^{*\,\alpha} \tag{1.11}$$

The advantages of using i_0 instead of k^0 is that the current response could be presented in terms of overpotential $\eta = E - E^0$. From Equations 1.8 and 1.11, the *current-overpotential* equation can be obtained as

$$i = i_0\left[\frac{C_{\mathrm{R}}(0,t)}{C_{\mathrm{R}}^{*}} e^{(1-\alpha)\frac{F}{RT}\eta} - \frac{C_{\mathrm{O}}(0,t)}{C_{\mathrm{R}}^{*}} e^{-\alpha\frac{F}{RT}\eta}\right] \tag{1.12}$$

Equation 1.12 describes the current behaviour shown in Figure 1.3 where the solid curve is the Faradic current summed by i_{a} and i_{c} illustrated as dashed curves. Leaving either direction from E_{eq}, the magnitude of current grows dramatically because an exponential factor dominates the current responses. At extremely positive/negative overpotentials, the cathodic/anodic component can be negligible, and the total current flow approximately equals $i_{\mathrm{a}}/i_{\mathrm{c}}$. When the current levels off on either side, it is limited by mass transport instead of electron transfer reaction. This will be discussed in detail in the next section.

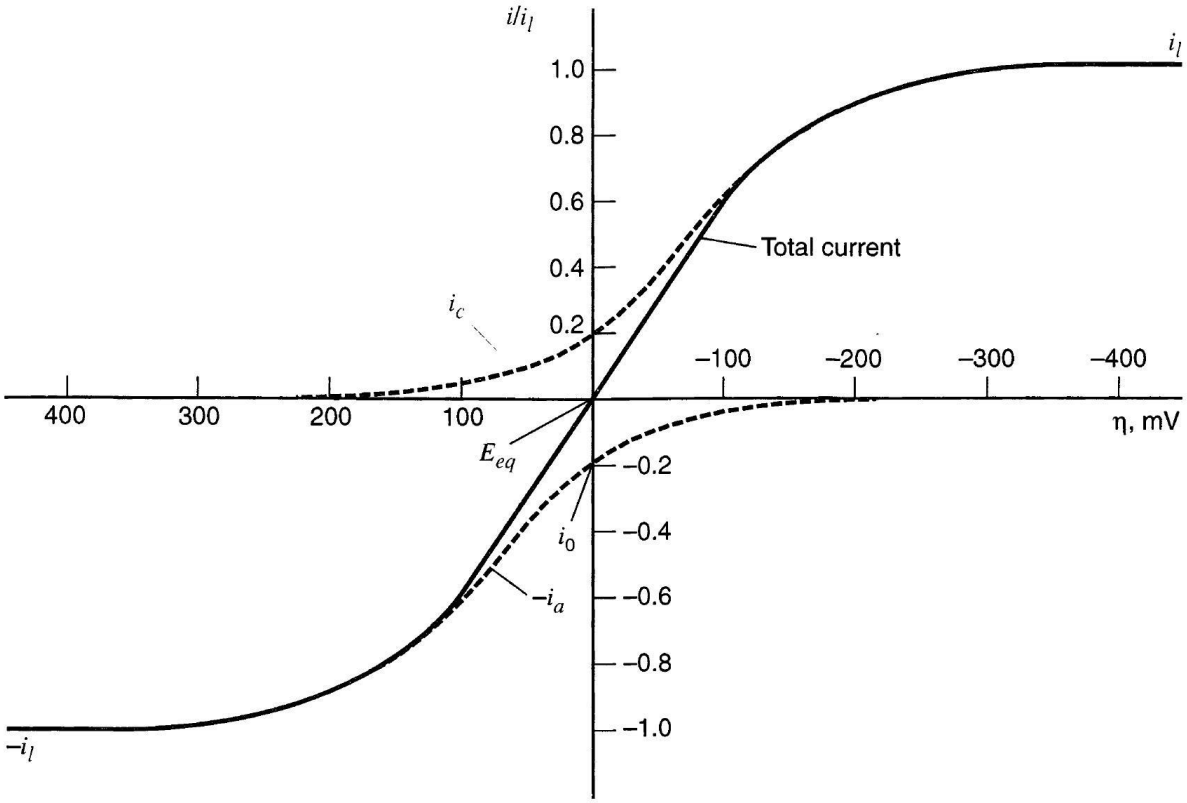

Figure 1.3: Current-overpotential traces for a reversible electron transfer system $O + e^- \rightleftharpoons R$. The solid line shows the total current and dashed curves represent anodic/cathodic current. Reprinted from Bard and Faulkner's work[24].

One specific ramification of current-overpotential equation needs to be identified here, which is useful for the resulting chapters. If the solution is fully stirred to prevent a large difference between surface concentration and bulk concentration, Equation 1.12 can be written as

$$i = i_0 \left[e^{(1-\alpha)\frac{F}{RT}\eta} - e^{-\alpha\frac{F}{RT}\eta} \right] \tag{1.13}$$

which is broadly known as the *Butler-Volmer* equation to approximate current with no mass-transfer effects.

1.2. Mass Transport

There are two primary scenarios where electrolytes in solution interact with conductors. Let us consider the generic case of a single-electron transfer reaction with a pair of electroactive species O and R. In the first situation, O and R are confined on the electrode surface, where the electron transfer can only take place in surface bound. Such an adsorption process at the electrode can either be physisorption or chemisorption. Alternatively, both electroactive species O and R can move freely in solution as shown in Figure 1.4. When the potential is applied on the electrode interface, chemical gradients of O and R occur in the solution because of the consumption or production of both electroactive species. The responses of the system will balance this concentration gradients by mass transport. In practice, the generated R might have a series of sequential electroinactive chemical steps in the solution to yield an aimed product (P).

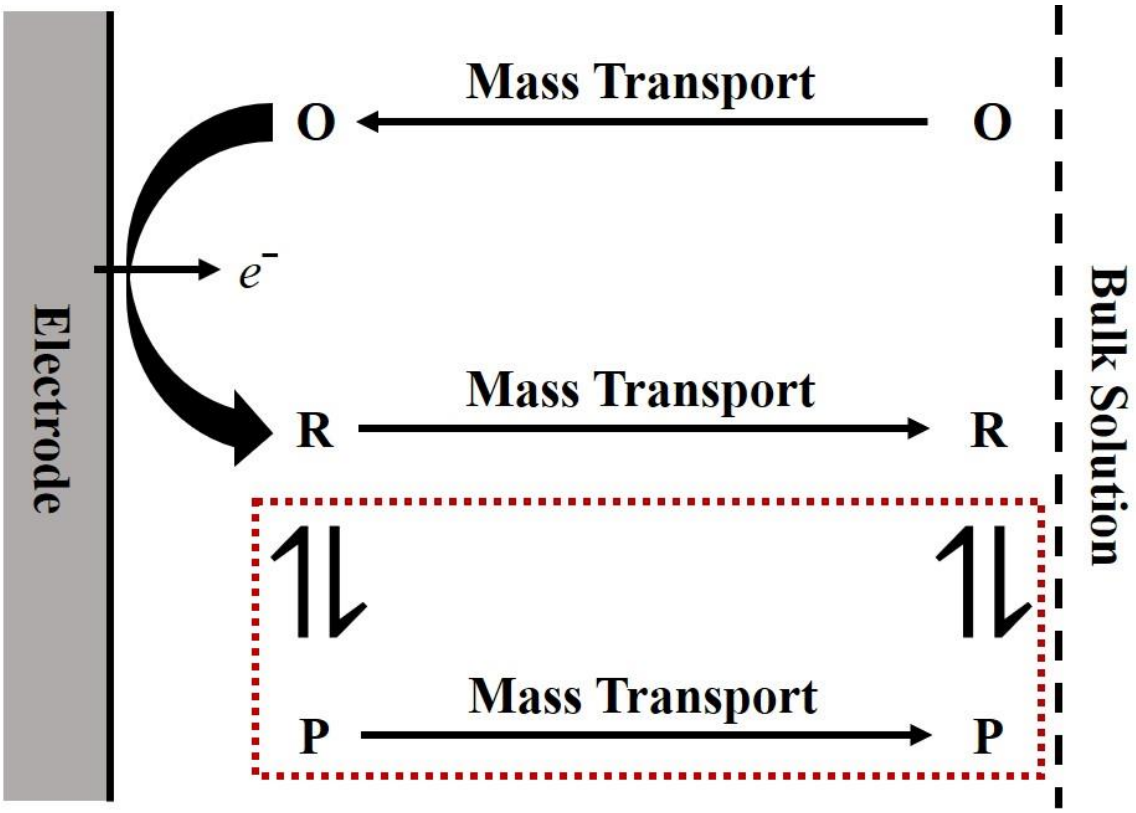

Figure 1.4: A schematic diagram for an electrochemical system where the electroactive species O is reduced to R. Electron tunnelling under a favourable thermodynamic potential, leads to the occurrence of the concentration gradient. Extra chemical or electrochemical steps follow to yield the electro-inactive product (P).

Before detailing the mass transport, it is essential to consider the electrode geometry, which greatly influences the way electrolyte transports to and from the electrode surface. However, it is a complicated matter to determine the optimum electrode size. On one hand, smaller size electrodes have higher pacing impedance, resulting in a lower current drain and longer pacemaker longevity. On the other hand, smaller size electrodes lead to higher electrode polarisation, which greatly affects its cardiac sensing functions and pacing efficiency[44].

A typical electrochemical measurement may use electrodes consisting of a conducting metal or glassy carbon embedded in an insulating wall. When the surface is a rectangle or disc of diameter $\geq \sim 100\ \mu m$, it can be classified as macroelectrode and can generally be treated as a planar electrode in both experiment and experimental design model.

In comparison to the macroelectrodes, microelectrodes are often circular discs with a radius of $\leq 10\ \mu m$ [45-47]. Microdisc electrodes and microband electrodes are one of the simpler but more widely used tools in experiments. The former is generally fabricated by sealing a conducting wire made of gold, platinum or graphite into an insulator like plastic or glass[46], and the latter can be designed in an analogous way via sealing a thin film of foil between two blocks[46].

The electrode size results in the different edge effects as demonstrated in Figure 1.5, which decides the different behaviour of mass transport. If not specifically mentioned, all the electrodes used in this dissertation are treated as macroelectrodes or planar electrodes. The features and applications of microelectrodes can be found in literature[48-50]. In this section, the effects caused by diffusion, convection and migration of reactant molecule transport are discussed in depth.

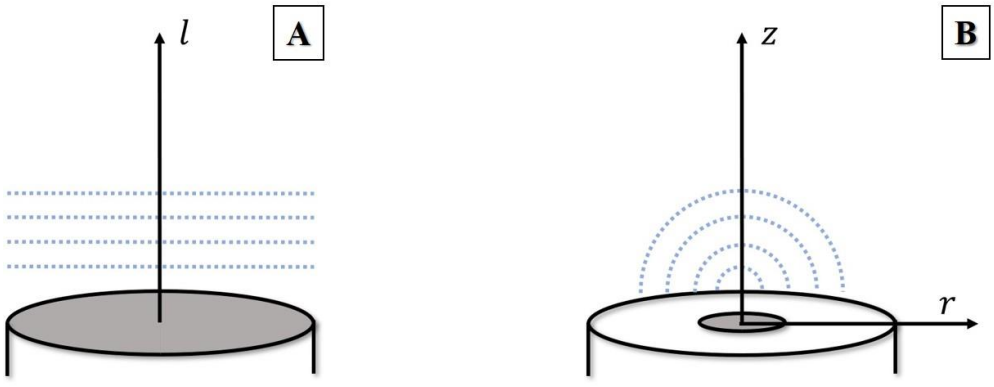

Figure 1.5: Mass transport between macroelectrodes (A) and microelectrodes (B). For microelectrodes, the edge effects become smaller from edges of the electrode towards the centre.

1.2.1. Diffusion

Diffusion arises from uneven spatial concentration distribution in the solution, and it acts to maximise entropy via smoothing out inhomogeneities of various ingredients[51]. The rate of diffusion is the net movement of atoms, molecules and other particles randomly blend together as a result of their kinetic energy. In our case, this leads to a phenomenon where they move from an area of high concentration to an area of low concentration. Diffusion is driven by the concentration gradient in the system, which can be mathematically given by *Fick's first law*[52] as:

$$J_{\mathrm{j}}(x) = -D_{\mathrm{j}} \frac{\partial C_{\mathrm{j}}(x)}{\partial x} \tag{1.14}$$

where J_{j} is the diffusional flux for species j (in one-dimension planar surface), D_{j} is species j's diffusion coefficient ($\mathrm{cm^2\ s^{-1}}$) that is the inherent characteristics of material, C_{j} is the concentration of species j ($\mathrm{mol\ cm^{-3}}$) and x is a one-dimension Cartesian coordinate (cm). In most electrochemical systems, researchers are quite often concerned with species' concentration at a certain point as a function of space and time. This demands a more general treatment of the time-dependent diffusional process, which is known as *Fick's second law*[52]. This differential equation derived from Fick's first law can be expressed as:

$$\frac{\partial C_{\mathrm{j}}(x)}{\partial t} = D_{\mathrm{j}} \frac{\partial^2 C_{\mathrm{j}}(x)}{\partial x^2} \tag{1.15}$$

In a three-dimensional Cartesian system, the diffusional equation can be expanded to depict higher dimensions:

$$\frac{\partial C_{\mathrm{j}}(x,y,z)}{\partial t} = D_{\mathrm{j}} \frac{\partial^2 C_{\mathrm{j}}(x,y,z)}{\partial x^2} + D_{\mathrm{j}} \frac{\partial^2 C_{\mathrm{j}}(x,y,z)}{\partial y^2} + D_{\mathrm{j}} \frac{\partial^2 C_{\mathrm{j}}(x,y,z)}{\partial z^2} \tag{1.16}$$

When given adequate initial and boundary conditions, Equation 1.16 can be fully solved for concentration evolution as a function of space and time. This relationship also holds well for lower concentrations of solute because the medium can be treated as stagnant compared to the movement of solute molecule. However, for higher concentrations of solute, the Stefan-Maxwell equation is used to explain the relative motion between solute and solvent molecules[53].

For traditional electrochemical experiments, where a huge number of molecules are involved, the tridimensional problems are reduced into one or two dimensions because of the symmetry of the

diffusion field. The first and simplest case corresponds to linear, (hemi)spherical and cylindrical diffusion associated with the use of planar, (hemi)spherical and cylindrical electrodes.

In linear diffusion systems, a planar electrode such as a platinum disk[54] and an unstirred solution are presumed. Diffusion is effectively planar as shown in Figure 1.6(A). Fick's second law for planar electrode is the same as Equation 1.15 in one dimension.

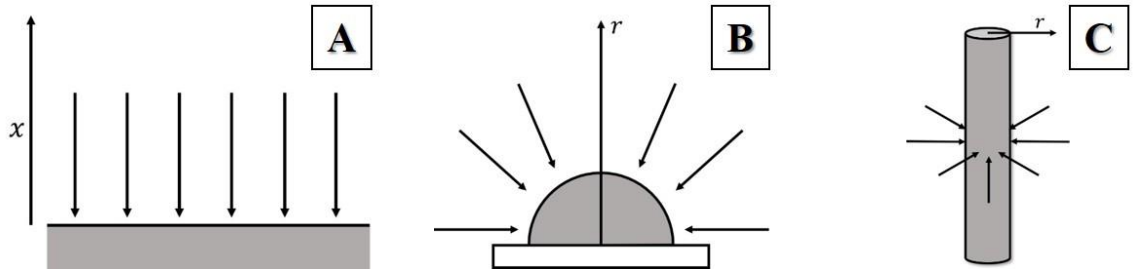

Figure 1.6: Geometrical illustration of the diffusion region at macroelectrodes involving planar, hemispherical and cylindrical electrode.

If the electrode in the experiment is hemispherical rather than planar (e.g., a hanging drop of mercury placed on a conducting disc[55,56]) shown in Figure 1.6(B), one must consider a hemispherical diffusion field and this law becomes

$$\frac{\partial C_{\mathrm{j}}(r)}{\partial t} = D_{\mathrm{j}}\left[\frac{\partial^2 C_{\mathrm{j}}(r)}{\partial r^2} + \frac{2}{r}\frac{\partial C_{\mathrm{j}}(r)}{\partial r}\right] \tag{1.17}$$

For cylindrical electrodes that are fabricated by an insulator embedded through a wire[57] shown in Figure 1.6(C), this law is written by

$$\frac{\partial C_{\mathrm{j}}(r)}{\partial t} = D_{\mathrm{j}}\left[\frac{\partial^2 C_{\mathrm{j}}(r)}{\partial r^2} + \frac{1}{r}\frac{\partial C_{\mathrm{j}}(r)}{\partial r}\right] \tag{1.18}$$

These electrode geometries might not be fabricated precisely in practice, however, they are useful for theoretical investigations since the low dimensionality of mass-transport equation allows it to be resolved analytically under diffusion-only conditions[58]. For example, the steady-state currents for a spherical electrode due to the convergent diffusion is

$$i_{\mathrm{ss}} = 4\pi n F D_{\mathrm{j}} C_{\mathrm{j}}^{*} r \tag{1.19}$$

Obviously, a hemispherical electrode bounded by a planar cover with the same r has half of the current of the corresponding Equation 1.19.

1.2.2. Convection

Convection refers to bulk movement of the material arising from a mechanical force acting on a solution. There are two types of convection: natural convection and forced convection. Natural convection can be present in any solution. It occurs from thermal gradients and/or density differences of the bulk solution. This sort of convection generally leads to an evident perturbation in electrolysis conducted with macroelectrodes on the time-scale of around 10-20 seconds or longer[51]. However, such effects are uncontrolled and difficult to analyse.

Forced convection is generally larger and is designed to be controllable in comparison to natural convection. This effect can be introduced by external forces like pumping, stirring or gas bubbling[51]. This hydrodynamic-based convection has evolved to become a popular electrochemical technique to enhance the rate of mass transport in the vicinity of the electrode. This method can be generally classified according to the electrodes that move in respect to the electrolytic solution, for example rotating disc[59] in Figure 1.7(A) or electrolyte that moves with respect to the electrode for example channel flow cell[60,61] in Figure 1.7(B), and other cases[62-65].

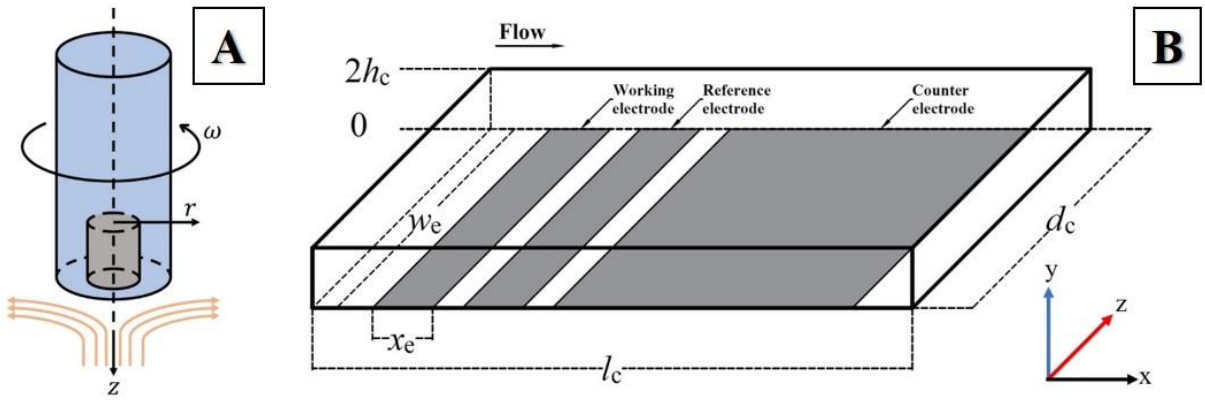

Figure 1.7: A schematic diagram showing rotating disc with forced convection marked in orange (A), and co-ordinate system for a three-electrode channel flow cell with forced convection driven by the flow (B).

Although hydrodynamic systems increase the difficulties and complexities in both fabrication and simulation rather than diffusion-only systems, they offer a more convenient path of varying the rate of mass transport in order to optimise the conditions for electroanalytic and mechanistic investigations. The efficient mass transport has an additional benefit of achieving greater

sensitivities and steady-state responses which are not influenced by the double-layer charging[37]. Mathematically, the *convective* equation for the flux of species *j* is given as:

$$J_{\mathrm{j}}(x) = v_{\mathrm{j}} C_{\mathrm{j}}(x) \tag{1.20}$$

where v_{j} is the velocity of the solution (cm s^{-1}) driven by external force which is commonly seen in a well-defined hydrodynamic electrochemical system. Concentration changes as a result of movement of the solution can be derived from Equation 1.20 and described as:

$$\frac{\partial C_{\mathrm{j}}(x)}{\partial t} = -v_{\mathrm{j}} \frac{\partial C_{\mathrm{j}}(x)}{\partial x} \tag{1.21}$$

This expression is the convection analogue of Equation 1.15.

1.2.3. Migration

Migration acts as an electrostatic force that leads to the movement of ions in the bulk solution from or to the electrode interface. This is caused by the potential gradient ($\mathrm{d}\phi_j(x)/\mathrm{d}x$), which exists between electrode and bulk solution interface as a result of the drop in electrical potential[51]. The general flux equation for species *j* can be written as,

$$J_j(x) = -z_j f D_j C_j(x) \frac{\partial \phi_j(x)}{\partial x} \tag{1.22}$$

where z_j is charge on species *j* in signed units of electronic charge. The pre-factor $z_j f D_j$ represents the ionic mobility for species *j*, which is known as the *Einstein-Smoluchowski* equation[66] and generally relied on the ionic charge and magnitude, or the viscosity of the solution.

The interaction of migration effects and electrolysis in the system arises the complexity of mass transport process which is difficult to handle. In many electrochemical measurements, a large amount of inert supporting electrolyte is added to experimentally eliminate the migration effects. An additional benefit of having a supporting electrolyte reduces the potential gradient, which also helps to reduce the flux. Under several circumstances like in biological systems, however, it is not desirable to introduce such a large excess of supporting electrolyte. The migration effects here should be considered mathematically. As a consequence, a charged species *j* in solution will be constrained to transport via diffusion, convection and migration, which can be described by the well-known *Nernst-Planck* equation[67,68]:

$$J_j(x) = -D_j \frac{\partial C_j(x)}{\partial x} + v_j C_j(x) - z_j f D_j C_j(x) \frac{\partial \phi_j(x)}{\partial x} \tag{1.23}$$

1.3. Electroanalytical Techniques

Recalling the controlled-potential experiment for the electrode reaction in Section 1.1,

$$\mathrm{O} + \mathrm{e}^- \underset{k_\mathrm{b}}{\overset{k_\mathrm{f}}{\rightleftharpoons}} \mathrm{R} \tag{1.24}$$

which holds a *current-overpotential characteristic* derived as

$$i = FAk_0 \left[C_\mathrm{R}(0,t) e^{(1-\alpha)\frac{F}{RT}(E-E^0)} - C_\mathrm{O}(0,t) e^{-\alpha\frac{F}{RT}(E-E^0)} \right] \tag{1.25}$$

Equation 1.25 implies that the current responses could be predicted by electrode potential quantitatively. Experimentally, this process of measuring current as a function of the applied potential is called voltammetric techniques. This applied potential can be swept across a range to obtain a current-potential plot or can be a constant value to record the current-time plot. However, quantitative research requires theoretical support that can predict the response functions in terms of the experimental parameters of time, potential, concentration, mass transfer coefficients and rate constants.

This section is concerned with specific voltammetric techniques in which the electrode potential is applied using a predetermined program. The potential can be set constant or be varied with time in a designed manner because the current is measured as a function of applied voltage. This family of techniques is a large single group that contains some of the more powerful analytical methods available to electrochemistry. To simplify the problem, single electron transfer mechanism (Equation 1.24) is considered and only diffusion occurs as the mass transport of electroactive species in conjunction with current-potential property, which will lead to the time-dependent surface concentration $C_\mathrm{R}(0,t)$ and $C_\mathrm{O}(0,t)$.

1.3.1. Step Potential & Chronoamperometry

The most basic and simplest class of voltammetric techniques is the potential step where the value of potential, is switched from a value E_1 (generally below the standard potential of the electrode E^0 where no current flows) to a value E_2 (well above E^0 where the reaction yields current responses) in Figure 1.8(A). The resulting current flow as a function of time is given in Figure 1.8(B).

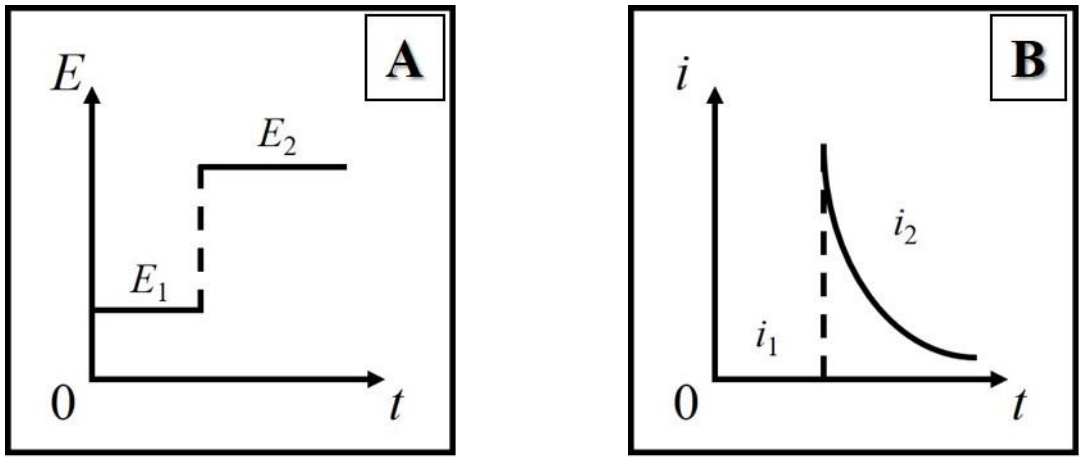

Figure 1.8: Waveform for a potential step experiment (A), and the current behaviour with time (B).

Under only-diffusion conditions, the flux at the electrode surface is proportional to the current, and the relationship between current and concentration is expressed as,

$$-J_{\mathrm{O}}(0,t) = \frac{i(t)}{nFA} = D_{\mathrm{O}}\left[\frac{\partial C_{\mathrm{O}}(x,t)}{\partial x}\right]_{x=0} \tag{1.26}$$

Equation 1.26 gives the current-time response when given the initial and boundary conditions in Equation 1.27.

$$\text{Initial conditions: } C_{\mathrm{O}}(x,0) = C_{\mathrm{O}}^{*}$$
$$\text{Boundary conditions: } \begin{cases} \lim\limits_{x\to\infty} C_{\mathrm{O}}(x,t) = C_{\mathrm{O}}^{*} \\ C_{\mathrm{O}}(0,t) = 0 \text{ (for } t > 0) \end{cases} \tag{1.27}$$

This current behaviour is known as the *Cottrell* equation[69]

$$i(t) = nFAC_{\mathrm{O}}^{*}\sqrt{\frac{D_{\mathrm{O}}}{\pi t}} \tag{1.28}$$

The concentration profile can be obtained as a time-dependent function,

$$C_{\mathrm{O}}(x,t) = \mathrm{erf}\left[\frac{x}{2(D_{\mathrm{O}}t)^{1/2}}\right] \tag{1.29}$$

It is notable that the speed of depleting the electroactive species near the electrode brings out a reciprocal $t^{1/2}$ function according to Equation 1.29.

After the introduction of the potential step, a complex sequence of steps for analysis may be considered. The most general arrangement is the double-step technique, which is known as the chronoamperometric reversal technique or often referred to double-step chronoamperometry. The first step shows the same effect as that of the step potential method, but the second step is used to regenerate the initial species to examine the first action when applying a total reversal potential. An example is given in Figure 1.9(A). Assuming that an electrode is immersed in a solution of species O that is reversibly reduced at E^0, if the initial potential E_1 is at the potential out of the working range, no electrolysis occurs until the potential is abruptly switched to E_2. Species R is then generated electrolytically for a period, then the second shift comes which generally satisfies $E_2 - E^0 = E^0 - E_3$. The reduced form R then can no longer coexist with the electrode, and it is re-oxidised to O. Chronoamperometry, like other reversal techniques, is designed to provide a direct observation of species R after its electrogeneration. This feature is useful for evaluating the participation of species R in chemical reactions on a time scale in comparison to the time between first and second potential jumps.

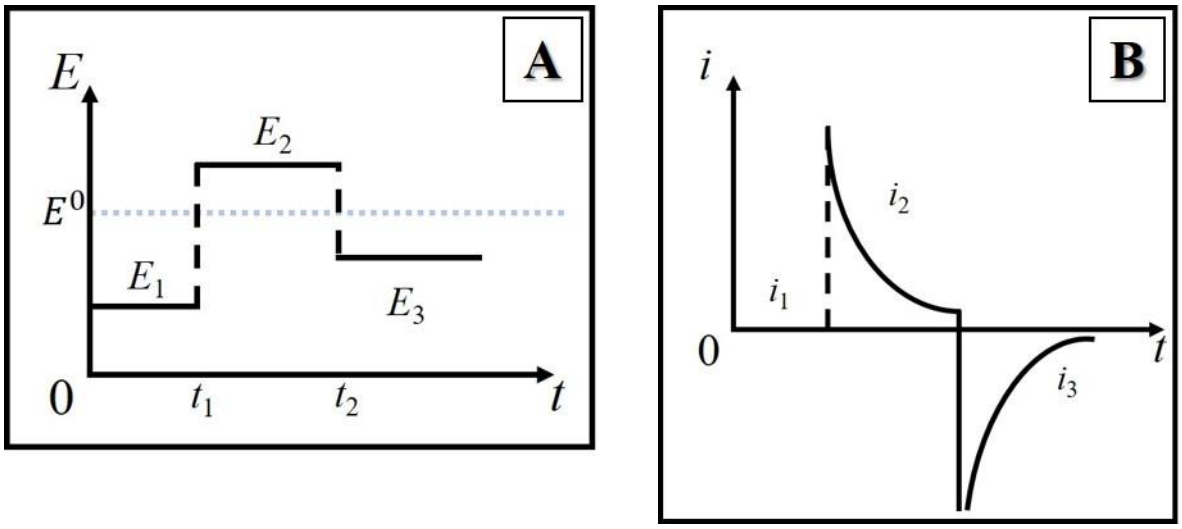

Figure 1.9: Waveform for chronoamperometric reversal techniques (A), and the current response with time (B).

To obtain a quantitative description of chronoamperometry, one might consider first the result of the forward step, then use the concentration profiles obtained before the second switch as initial conditions for the diffusion equation describing events in the reversal step. In the case outlined in step potential, the effects of the forward step are the same as above. The forward current is given by Equation 1.28, which is restated in the present context as

$$i_{\mathrm{f}}(t) = nFAC_{\mathrm{O}}^{*}\sqrt{\frac{D_{\mathrm{O}}}{\pi t}} \tag{1.30}$$

For the current during the reversal step, Kambara obtained a simplified result[70],

$$i_{\mathrm{b}}(t) = -nFAC_{\mathrm{O}}^{*}\sqrt{\frac{D_{\mathrm{O}}}{\pi}}\left[\frac{1}{\sqrt{t-t_2}} - \frac{1}{\sqrt{t}}\right] \tag{1.31}$$

where the special case of interest satisfies

$$\begin{aligned} E_2 &\approx E^0 \text{ in the forward step} \\ E_3 &\to \infty \text{ in the backward step} \end{aligned} \tag{1.32}$$

The current responses can be observed in Figure 1.9(B).

1.3.2. Potential Sweep Methods

The overall electrochemical behaviour of the system can be studied through a sequence of steps to different applied potentials with recording of the current-time curves, which yields a three-dimensional i-t-E surface shown in Figure 1.10(A). However, the accumulation and analysis of these data might be very slow especially when a stationary electrode is used. In addition, it is quite difficult to recognize the presence of different species by only observing the waves from the recorded i-t curves alone, and it also needs small enough potential steps (≤ 1 mV) to ensure the derivation of well-resolved i-E curves. To obtain more information through a single experiment, the potential can be swept with respect to time and the i-E curve can be recorded directly. This amounts to traversing the three-dimensional i-t-E realm Figure 1.10(B).

In this subsection, the current recorded as a function of potential, which is obviously equivalent to recording current versus time, is discussed in detail. The formal name for this approach is linear potential sweep chronoamperometry, but most literature refer to this as linear sweep voltammetry (LSV). This is then followed by cyclic voltammetry (CV), a very popular electroanalytical technique for initial electrochemical studies of new systems. Square wave voltammetry (SWV) and alternating current (AC) voltammetry will be extended as branches of pulse voltammetry, which is a family of more complex schemes devised for applying potential steps and sampling currents.

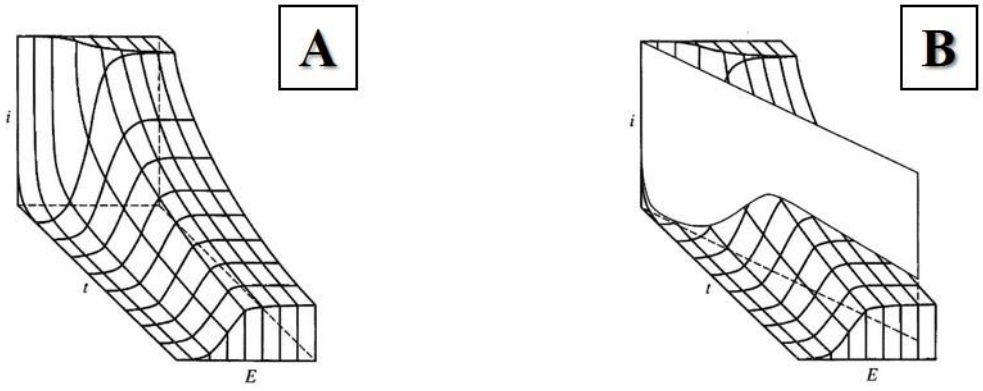

Figure 1.10: A portion of the i-t-E surface for a Nernstian reaction with the potential axis in units of $60/n$ mV (A). Linear potential sweep across this surface (B). Reprinted from Reinmuth's work[71].

1.3.2.1. Linear Sweep Voltammetry (LSV) & Cyclic Voltammetry (CV)

In the second class of voltammetry, which is the most widely used approaches, the applied potential varies linearly as a function of time from the initial value E_i to its vertex value E_v shown in Figure 1.11(A).

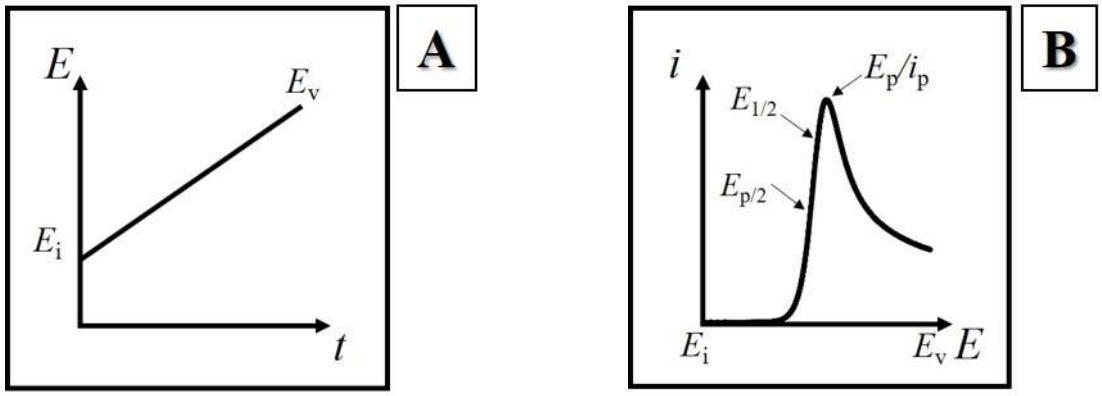

Figure 1.11: Waveform for a linear sweep voltammetry (A), and the current response versus applied potential (B)[24].

When given a certain scan rate v (V s^{-1}), the "potential ramp" gives

$$E(t) = E_\mathrm{i} + vt \tag{1.33}$$

In the case of the rate of electron transfer being swift on the electrode, the species O and R instantly approach to the ratio dominated by the Nernst equation. Figure 1.11(A) shows the current response that the electrode reaction between O and R, in which some parameters are also notable to provide analytical information. In Nernstian reversible system the *peak current*[72], i_p, is

$$i_\mathrm{p} = (2.69 \times 10^5) n^{3/2} A D_\mathrm{j}^{1/2} C_\mathrm{j}^{*} v^{1/2} \tag{1.34}$$

The corresponding *peak potential* at 25°C, E_p, can be read from Table 6.2.1[24],

$$E_\mathrm{P} = E_{1/2} - 1.109 \frac{RT}{nF} = \frac{28.5}{n}\,\mathrm{mV} \tag{1.35}$$

where $E_{1/2}$ is called *half-wave potential* in voltammetry.

Another parameter of interest is the *half-peak potential* $E_{\mathrm{p}/2}$, which is

$$E_{\mathrm{p}/2} = E_{1/2} + 1.09\frac{RT}{nF} = E_{1/2} + \frac{28.0}{n}\,\mathrm{mV} \tag{1.36}$$

It is notable that a general diagnosis for a Nernstian wave is given in Equation 1.37 when $E_{1/2}$ stands around midway between E_{p} and $E_{\mathrm{p}/2}$,

$$\left|E_{\mathrm{p}} - E_{\mathrm{p}/2}\right| = 2.20\frac{RT}{nF} = \frac{56.5}{n}\,\mathrm{mV} \tag{1.37}$$

Equation 1.37 implies that E_{p} is independent of scan rate for a Nernstian system and i_{p} is proportional to the square root of scan rate. For quasi-reversible systems or totally irreversible systems, the values of i_{p}, E_{p} and $E_{\mathrm{p}/2}$ can be found in literature[24].

Cyclic voltammetry is recorded as the reversal linear sweep experiment in LSV shown in Figure 1.12. The forward and backward potentials are carried out by switching the scanning direction after reaching the vertex potential E_{v}, then swept back to its initial value, E_{i}. Thus, the potential is given as a function of time,

$$\begin{gathered} E(t) = E_{\mathrm{i}} + vt \;(dE/dt = v) \\ E(t) = E_{\mathrm{v}} - v(t - t_{\mathrm{R}}) \;(dE/dt = -v) \end{gathered} \tag{1.38}$$

The resulting current given in Figure 1.12 (B)

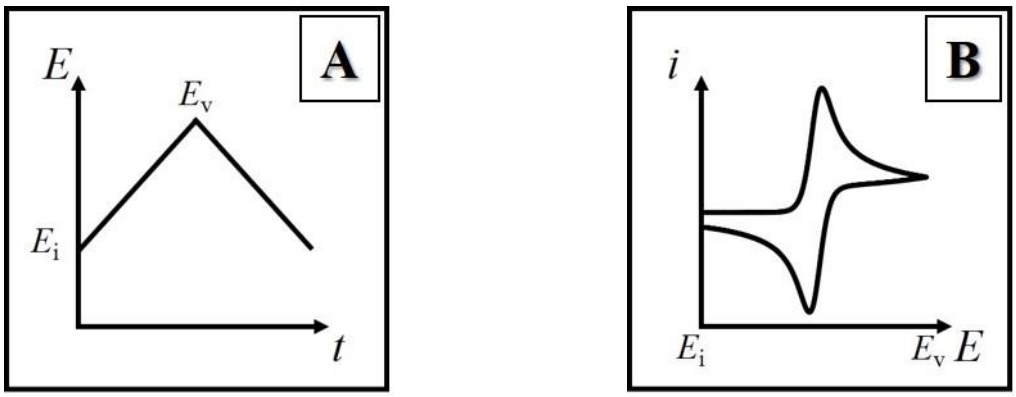

Figure 1.12: Waveform for a cyclic voltammetry (A), and the current response against applied potential (B).

1.3.2.2. Square Wave Voltammetry (SWV)

Square Wave Voltammetry (SWV) is a large-amplitude differential technique which was first reported in the literature in 1952[73]. This approach became popular over time and is now widely used to eliminate capacitive current components for electroanalytical applications. Using the various dependence of a linear sweep voltammetric current component such as diffusion, double-layer charging or kinetics, on scan rate, the elimination procedure (EP) is capable of conserving or eliminating some current components[74]. The variable parameter for the designed elimination in SWV is square-wave frequency. Even though SWV is a pulse voltammetric method which suppresses the influence of the charging current, the EP still increases the sensitivity of SWV by one magnitude order[75]. For a completely adsorbed electroactive species, eliminating simultaneously the charging currents also provides a specific signal in the form of peak/counter-peak and from the electroanalytical point of view this type of signal does not require a baseline correction.

The SWV combines almost all merits of other pulse voltammetric methods, which includes the background inhibition and sensitivity of differential pulse voltammetry, the diagnostic capability of normal pulse voltammetry and the power to directly analyse products in a manner similar to reverse pulse voltammetry. It also achieves larger ranges of time scales than any other pulse voltammetric techniques[24].

Figure 1.13 demonstrates the waveform and measurement scheme for square wave potential superimposed on a staircase waveform. The SWV is identified by the pulse height, ΔE_{p} and the pulse width, t_{p}, which can be also expressed in terms of square wave frequency, $f = 0.5t_{\mathrm{p}}$. The staircase height, ΔE_{s} defines the potential step in elemental cycle and the staircase width t_{s} decides the experimental time scale, where scan rate can be described as $v = \Delta E_{\mathrm{s}}/2t_{\mathrm{p}} = f\Delta E_{\mathrm{s}}$.

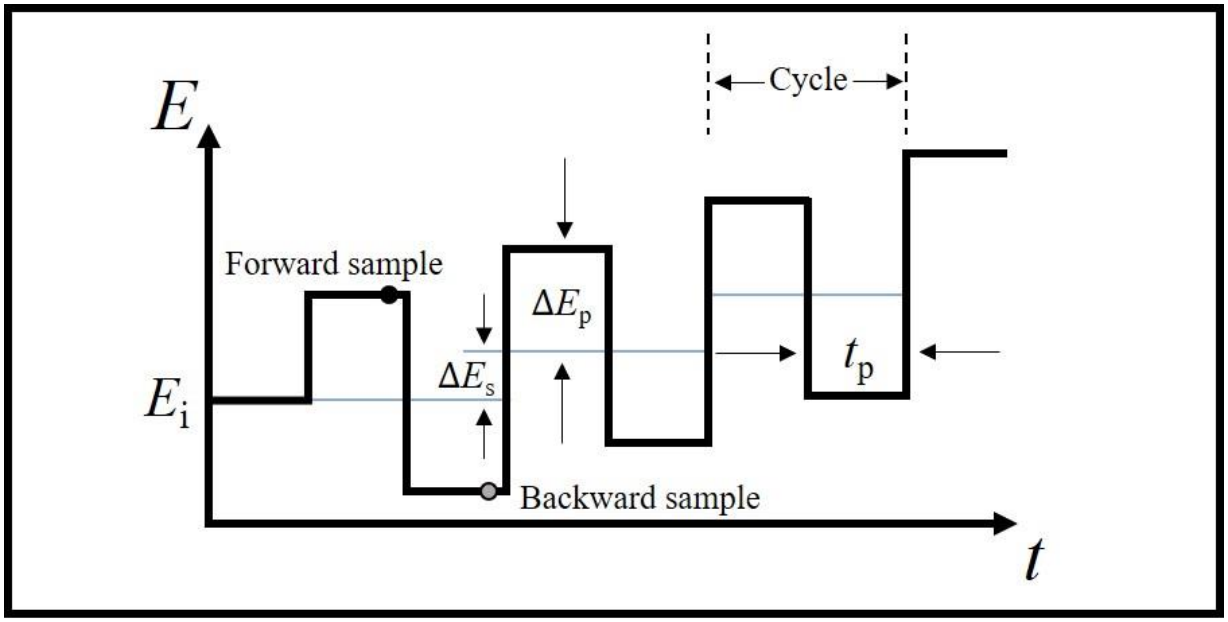

Figure 1.13: Waveform and measurement scheme for square wave voltammetry.

For the resulting current, two samples in normalised form are recorded per cycle as the forward current, ψ_{f}, at the end of forward pulse (black dot in Figure 1.13) and as the reversal current, ψ_{r}, at the end of backward pulse (grey dot in Figure 1.13), respectively. The dimensionless difference current is calculated as $\Delta\psi = \psi_{\mathrm{f}} - \psi_{\mathrm{r}}$. Figure 1.14 illustrates three forms of normalised current responses including forward current, reversal/backward current and difference current versus the applied potential.

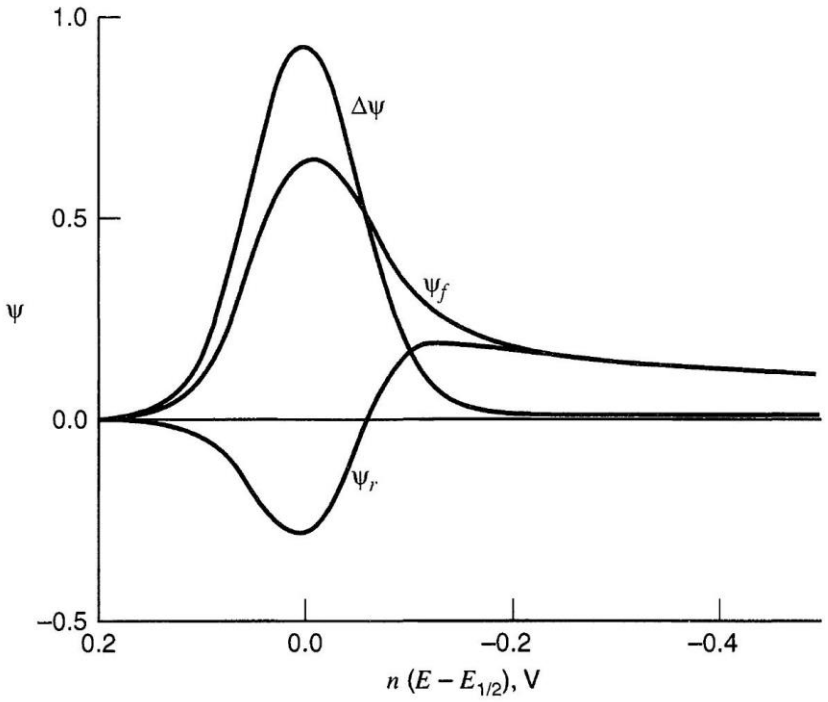

Figure 1.14: Dimensionless square wave voltammograms for the reversible O/R case with $C_{\mathrm{R}}^{*} = 0$. $n\Delta E_{\mathrm{p}} = 50$ mV and $n\Delta E_{\mathrm{s}} = 10$ mV. Forward currents (ψ_{f}), reverse currents (ψ_{r}), and difference currents ($\Delta\psi$) versus potential. Reprinted from Osteryoung and O'Dea's work[76].

The *half-wave potential* in SWV gives

$$E_{1/2} = E^{0} + \frac{RT}{nF}\ln\left(\frac{C_{\mathrm{O}}}{C_{\mathrm{R}}}\right)^{1/2} \tag{1.39}$$

and the dimensional current can be written as

$$i_{\mathrm{p}} = \frac{nFAD_{\mathrm{j}}^{1/2}C_{\mathrm{j}}^{*}}{\pi^{1/2}t_{\mathrm{p}}^{1/2}}\psi_{\mathrm{p}} \tag{1.40}$$

Equation 1.40 shows that the actual current has a linear dependence on the bulk concentration and the square root of frequency. A more comprehensive relationship between peak current with ΔE_{p} and ΔE_{s} can be found in Ramaley and Krause's work[77].

1.3.2.3. Alternating Current (AC) Voltammetry

Another powerful and popular voltammetric technique, in which a periodic waveform is superimposed onto the applied potential is called alternating current (AC) voltammetry. In the linear/cyclic sweep form introduced in Section 1.3.2.1, the potential is varied a over defined range with a known scan rate and the current is determined as a function of applied potential or time. The employed potential is known as direct current (DC) voltage, E_{dc}, shown in Figure 1.15(A). In this AC voltammetry, Figure 1.15(B) present a sinusoidal perturbation of angular frequency, ω, playing as ac voltage, E_{ac}, which is superimposed onto the DC waveform. Consequently, the overall applied potential can be described in Equation 1.41 and be given in Figure 1.15(C)

$$E(t) = E_{\mathrm{dc}} + E_{\mathrm{ac}} = E_{\mathrm{dc}} + \Delta E \sin(\omega t) \tag{1.41}$$

where ΔE is the amplitude of AC excitation in AC voltammetry. The current response is measured as a function of both applied DC potential and angular frequency to extract additional kinetic and thermodynamic information in comparison to current responses from only using DC voltage[78].

As a more fundamental tool compared to other pulse waveform, AC voltammetry particularly with large amplitude is reported to obtain a pure faradic current with less capacitive current and fewer background effects in higher harmonics[78]. This approach also offers the capability to estimate some important parameters like equilibrium kinetics and uncompensated resistance in the electron transfer reactions[78]. Recently, some other important applications of AC voltammetry are to evaluate the kinetics in coupled homogeneous reactions and electrocatalytic reactions[78-80]. However, the complicated analysis procedures still restrict its application in contrast to the classical techniques.

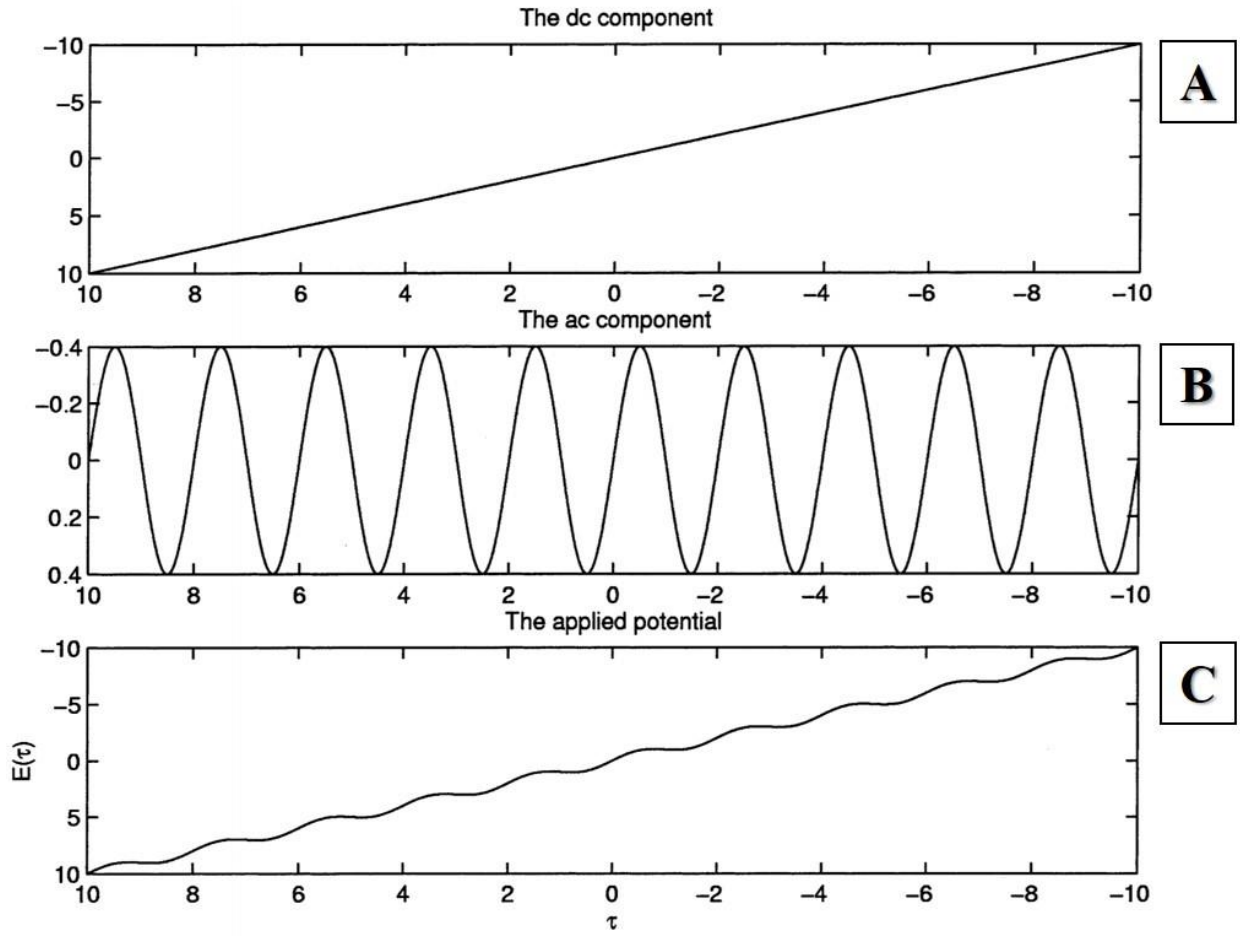

Figure 1.15: The dc component of the applied potential (A), the ac component with of the applied potential (B), and the combined potential (C). Reprinted from Gavaghan and Bond's work[78].

1.4. Electrochemical Mechanisms

The previous sections have described a few popular electrochemical techniques and the responses obtained when an electroactive species (O) is converted by a heterogeneous electron-transfer reaction to the product (R). However, the sampled electrode reaction is subjected to a simple one-electron transfer, where an outer-sphere reaction breaks no chemical bonds, or does not establish new bonds with species O and R. The restricted view helps us to qualitatively and quantitatively understand major characteristics of electrode kinetics, however, the actual electrode processes commonly involve more than one electron transfer. In many cases, the electrode reaction is coupled to homogeneous reactions that happen in the electrolyte and involve electroactive O or R. For example, electrolysis of water is a fundamental reaction but involves several elementary reactions at both anode and cathode.

$$\begin{aligned} &\text{Overall reaction: } 2\mathrm{H_2O}(l) \rightarrow 2\mathrm{H_2}(g) + \mathrm{O_2}(g) \\ &\text{Cathode: } 2\mathrm{H_2O}(l) + 2\mathrm{e^-} \rightarrow \mathrm{H_2}(g) + 2\mathrm{OH^-}(aq) \\ &\text{Anode: } 4\mathrm{OH^-}(aq) \rightarrow \mathrm{O_2}(g) + 2\mathrm{H_2O}(l) + 4\mathrm{e^-} \end{aligned} \tag{1.42}$$

To reveal a complex system of such chemical reactions, the distinct theoretical relationship between current and potential for each mechanistic sequence is required, in addition to the linkage of primary reactants and products. Several researches in literature discuss the mechanisms of complex electrode reactions involving organic[81-83] and inorganic species[84-86], because they can be used to obtain both thermodynamic and kinetic information and are applicable in many solvents. Moreover, reactions can be examined over a wide time window by electrochemical techniques. The species of interest can be synthesised near the electrode by the electron-transfer reaction and then be immediately detected and analysed electrochemically.

Understanding the basic mechanistic scheme greatly helps to obtain the embedded information corresponding to the kinetics and thermodynamics of inorganic and organic species. In this section, mechanistic studies of important electrochemical reactions are derived from the basic mechanistic studies to show the features of different reactions, of which the cyclic voltammogram can be extended to investigate huge amounts of more complex electrochemical systems.

1.4.1. Multi-Electron Transfer Mechanism

Electrochemical reactions can occur with more than one electron in successive transfer steps and this is frequently observed in the electrochemistry of organic molecules[87-90] and biological compounds[91-93]. Consider an overall two-electron process in which electroactive species O and R are the initial reactant and final product respectively, for $\mathrm{O} + 2\mathrm{e}^- \rightleftharpoons \mathrm{R}$,

$$\begin{gathered} \overset{k_0^1}{\mathrm{O} + \mathrm{e}^- \rightleftharpoons \mathrm{O}'} \\ E_1^0 \\ \overset{k_0^2}{\mathrm{O}' + \mathrm{e}^- \rightleftharpoons \mathrm{R}} \\ E_2^0 \end{gathered} \tag{1.43}$$

where O' is the intermediate in the reaction. Assuming the second step is slower than the first ($k_0^2 \ll k_0^1$), thence k_0^2 controls the rate of overall reaction. If the difference of standard potentials from both reactions is a small value, $\Delta E = |E_2^0 - E_1^0| < 75\ \mathrm{mV}$, the second process is then recognised as the rate-determining step (RDS), and the current-potential relationship under CV derived from Equation 1.8 can be given as

$$i = nFAk_0^{\mathrm{RDS}}\left[C_{\mathrm{R}'}(0,t)e^{(1-\alpha)\frac{F}{RT}(E-E_{\mathrm{RDS}}^0)} - C_{\mathrm{O}'}(0,t)e^{-\alpha\frac{F}{RT}(E-E_{\mathrm{RDS}}^0)}\right] \tag{1.44}$$

where $n = 2$, k_0^{RDS} approximately equals to k_0^2 and E^0 gives value to E_{RDS}^0. The current response assumes a similar shape with the single electron transfer mechanism, but the peak current is twice as the magnitude of single electron transfer mechanism. The comparison can be observed in Figure 1.16.

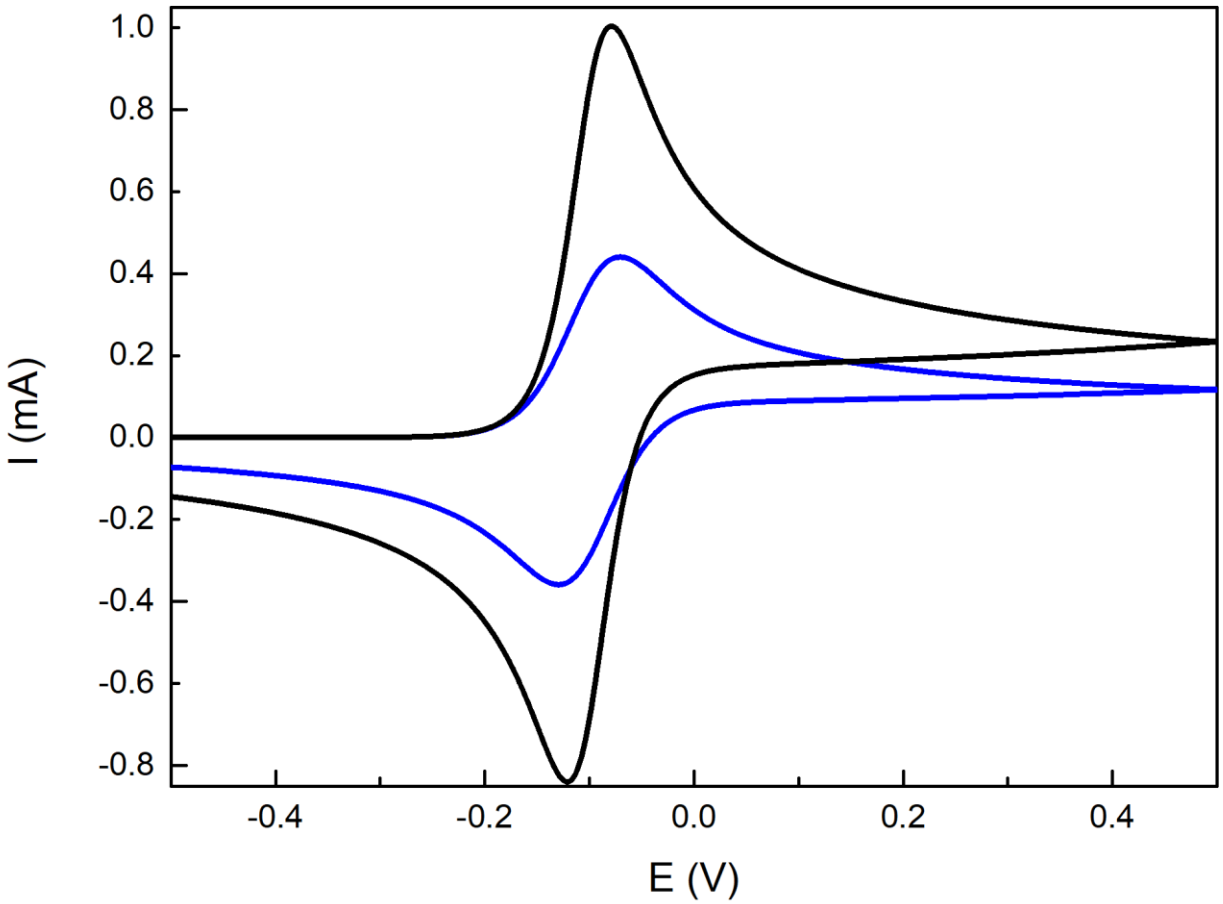

Figure 1.16: The comparison of shapes and peak current between the simulations of single electron transfer mechanism (Blue) for $\alpha = 0.5$, $k_0 = 1$ cm s^{-1} and $E^0 = -0.1$ V and two-electron transfer mechanism (Black) for $\alpha = 0.5$, $k_0^1 = 1$ cm s^{-1}, $k_0^2 = 10$ cm s^{-1} and $E_1^0 = E_2^0 = -0.1$ V.

When the difference, $\Delta E = E_2^0 - E_1^0$, is greater than ~75 mV, the special characteristic of two-electron transfer mechanisms shows split peaks that can be observed in Figure 1.17 under cyclic voltammetry. For this case corresponding to two successive electron transfer processes, the resulting current leads to

$$\frac{i}{FA} = k_0^1\left[C_{\mathrm{O}'}(0,t)e^{(1-\alpha)\frac{F}{RT}(E-E_1^0)} - C_{\mathrm{O}}(0,t)e^{-\alpha\frac{F}{RT}(E-E_1^0)}\right] + k_0^2\left[C_{\mathrm{R}}(0,t)e^{(1-\alpha)\frac{F}{RT}(E-E_2^0)} - C_{\mathrm{O}'}(0,t)e^{-\alpha\frac{F}{RT}(E-E_2^0)}\right] \quad (1.45)$$

The concentrations of the intermediates O′ are not only limited by the interplay between mass transport and electron transfer kinetics, but also decided by the properties of the preceding and following reaction. For such complicated cases, the analysis will be carried out on a case-by-case basis which will be discussed in the subsequent chapters.

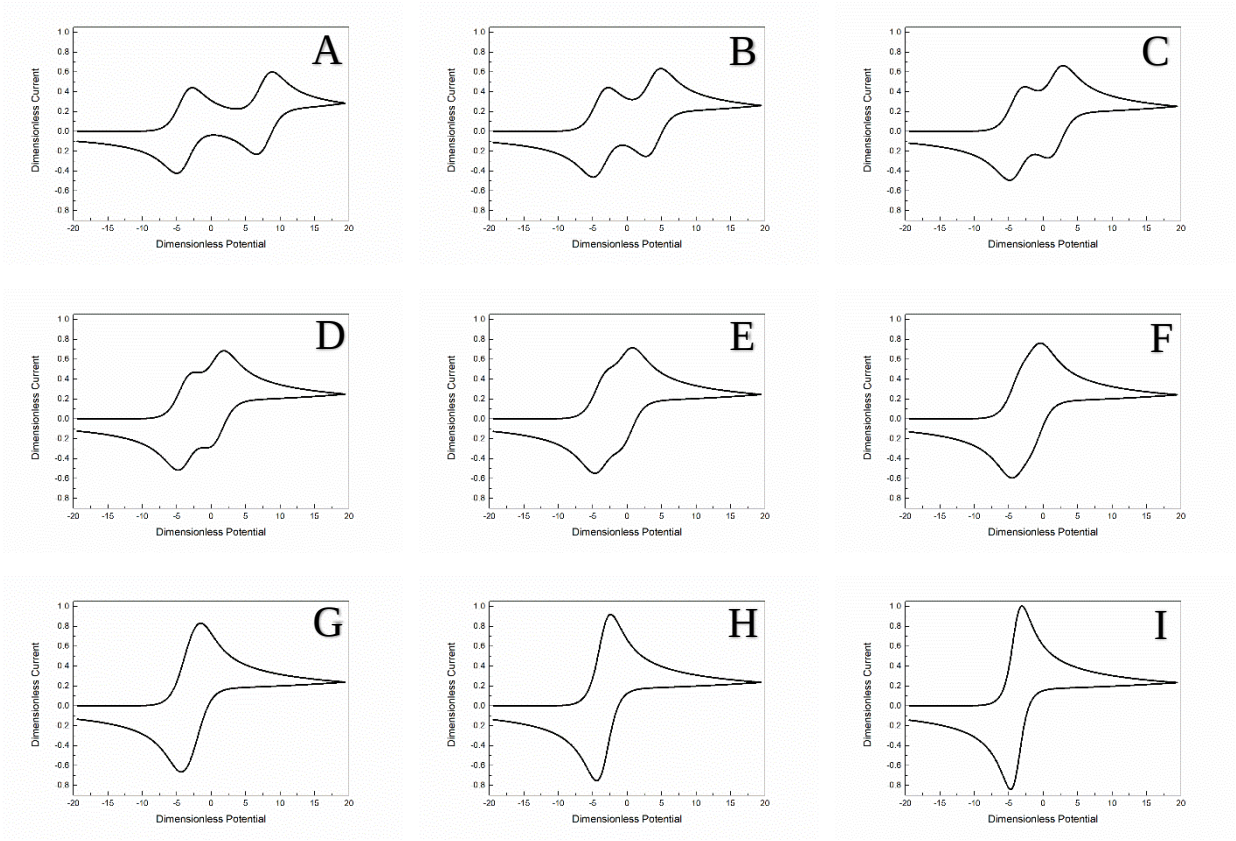

Figure 1.17: Comparison of dimensionless current behaviours of two-electron transfer mechanism for different $\Delta E^0 = E_2^0 - E_1^0$ obtained by numerical simulations with $\alpha = 0.5$, $k_0^1 = k_0^2 = 1\ \mathrm{cm\ s^{-1}}$ and E_1^0 is fixed as -100 mV. $\Delta E^0 = 300$ mV (A), $\Delta E^0 = 200$ mV (B), $\Delta E^0 = 150$ mV (C), $\Delta E^0 = 125$ mV (D), $\Delta E^0 = 100$ mV (E), $\Delta E^0 = 75$ mV (F), $\Delta E^0 = 50$ mV (G), $\Delta E^0 = 25$ mV (H), $\Delta E^0 = 0$ mV (I).

1.4.2. EC Mechanism

Another case is where the electrochemical system undergoes not only an electron transfer process, but also a coupled homogeneous chemical reaction. The preceding electron transfer step is denoted as “E” and the following chemical reaction is denoted as “C” according to electrochemical terminology. Thus, the EC_{irre} mechanism has a governing equation

$$\begin{gathered} O + e^- \rightleftharpoons R \\ R \xrightarrow{k_1} Y \end{gathered} \tag{1.46}$$

where k_1 is a first-order homogeneous rate constant for reductant producing an electroinactive species Y in the solution. The influence of the chemical reaction on the cyclic voltammogram of the EC_{irre} reaction at a planar electrode is demonstrated in Figure 1.18. When the chemical reaction is relatively slow in comparison to the electron transfer rate (k_1 is small), the forward peak is seldom influenced but there is a distinguishable effect on the backward peak. This resulted from the conversion of R into the electroinactive species Y, which decreases the anodic peak under a reverse scan. With k_1 increasing corresponding to a faster chemical step, the backward peak current is no longer be observed and the cathodic peak increases slightly and shifts to more negative potentials. This difference provides the ratio of forward and backward peaks and helps to validate the rate of coupled chemical reaction in the analysis of a cyclic voltammogram of an EC_{irre} mechanism.

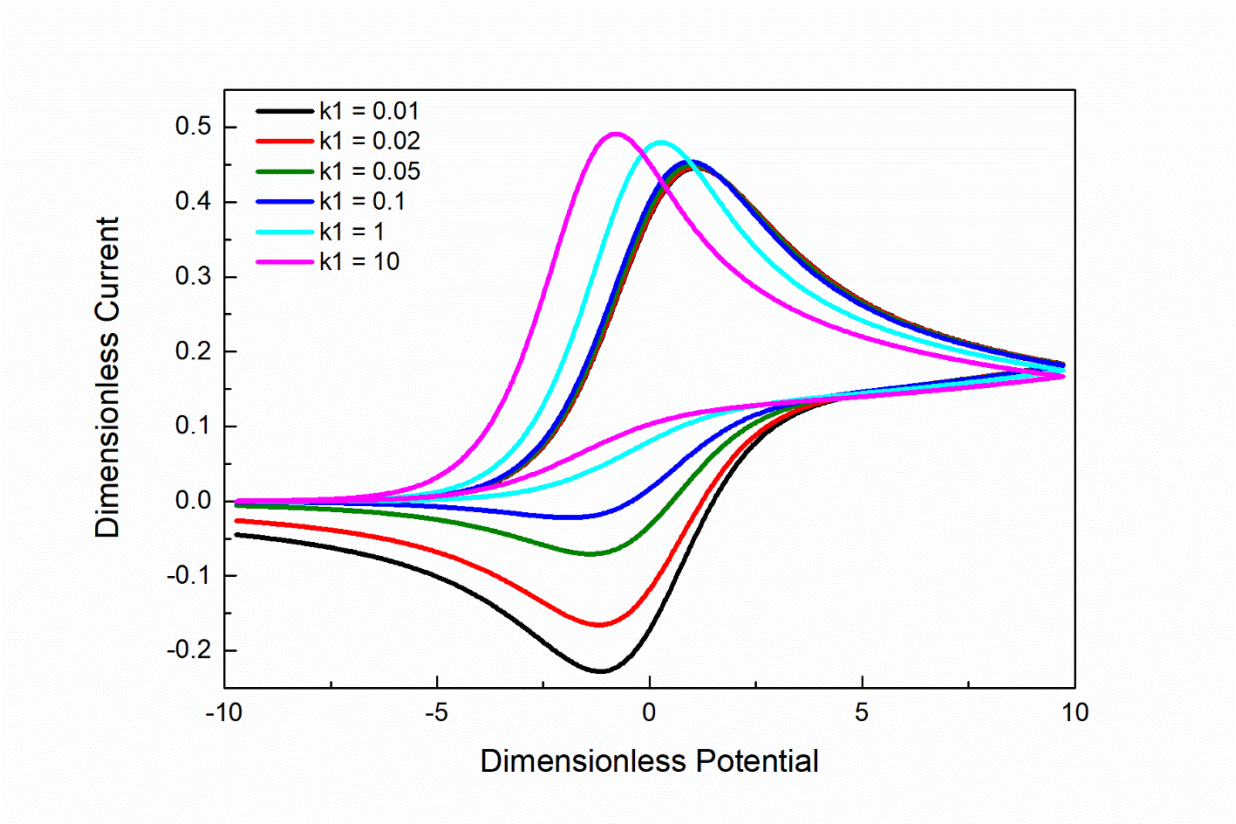

Figure 1.18: Comparison of dimensionless current behaviours of EC_{irre} mechanism for different chemical kinetics, $k_1 = 0.01\ s^{-1}$ (black), $k_1 = 0.02\ s^{-1}$ (red), $k_1 = 0.05\ s^{-1}$ (olive), $k_1 = 0.10\ s^{-1}$ (blue), $k_1 = 1.0\ s^{-1}$ (cyan), $k_1 = 10.0\ s^{-1}$ (magenta). The result is obtained by numerical simulations with $\alpha = 0.5$, $k_0 = 1\ cm\ s^{-1}$ and $E^0 = 0\ mV$.

1.4.3. Electrocatalytic Mechanism

In chemistry, a catalyst is a substance that speeds up a chemical reaction but is not consumed by the reaction. It can be recovered chemically unchanged at the end of the reaction after being used to speed up. Catalysts lower the energy barrier, in which an alternative route allows the chemical bond rearrangements converting the reactants into products more easily. In any given time intervals, the presence of a catalyst allows a greater proportion of the reactant species to pick up sufficient energy to pass through the transition state and become products. This definition can be directly extrapolated for electrocatalysis. The electrocatalytic mechanism is more complex than EC mechanism, which is denoted as EC' scheme (or EC prime). The initial reactant O is regenerated via a chemical reaction from the consumption of R, so that the catalytic process is given as

$$\begin{gathered} \mathrm{O} + \mathrm{e}^- \rightleftharpoons \mathrm{R} \\ \mathrm{R} + \mathrm{X} \underset{k_{-1}}{\overset{k_1}{\rightleftharpoons}} \mathrm{O} + \mathrm{Y} \end{gathered} \tag{1.47}$$

When the electroinactive species C_{X}^* and C_{Y}^* are in excess compared to O and R, the catalytic reaction can be treated as pseudo-first-order with the rate constant $k_1' = k_1 C_{\mathrm{X}}^*$, and $k_{-1}' = k_{-1} C_{\mathrm{Y}}^*$. On the other hand, if the concentrations of X and Y are not large , k_1 and k_{-1} are treated as second-order rate constants with the unit, $\mathrm{cm}^3\ \mathrm{s}^{-1}\ \mathrm{mol}^{-1}$.

Figure 1.19 shows the cyclic voltammograms of a second-order catalytic scheme with different equilibrium catalytic rate constants, $K_{\mathrm{eq}} = k_1/k_{-1}$. For small K_{eq} of the catalytic reaction, the resulting current is analogous to that demonstrated for E mechanism. With the increase of K_{eq}, the cathodic current of the forward scan is increasing and the anodic wave of the backward scan is reducing because of the chemical transformation from species R to O. When the equilibrium kinetics reaches 10^5, a prewave can be observed in the forward direction sweep, and it becomes more pronounced when $K_{\mathrm{eq}} = 10^6$. The prewave occurs at a negative overpotential place because of the catalytic step given that species R is consumed as soon as produced. There is a concentration drop of the electroinactive species X near the electrode surface, so that the current of prewave falls. By keeping scanning to the vertex potential, the overpotential trends to zero and the remaining unreacted species O is electroreduced to arise the second current peak.

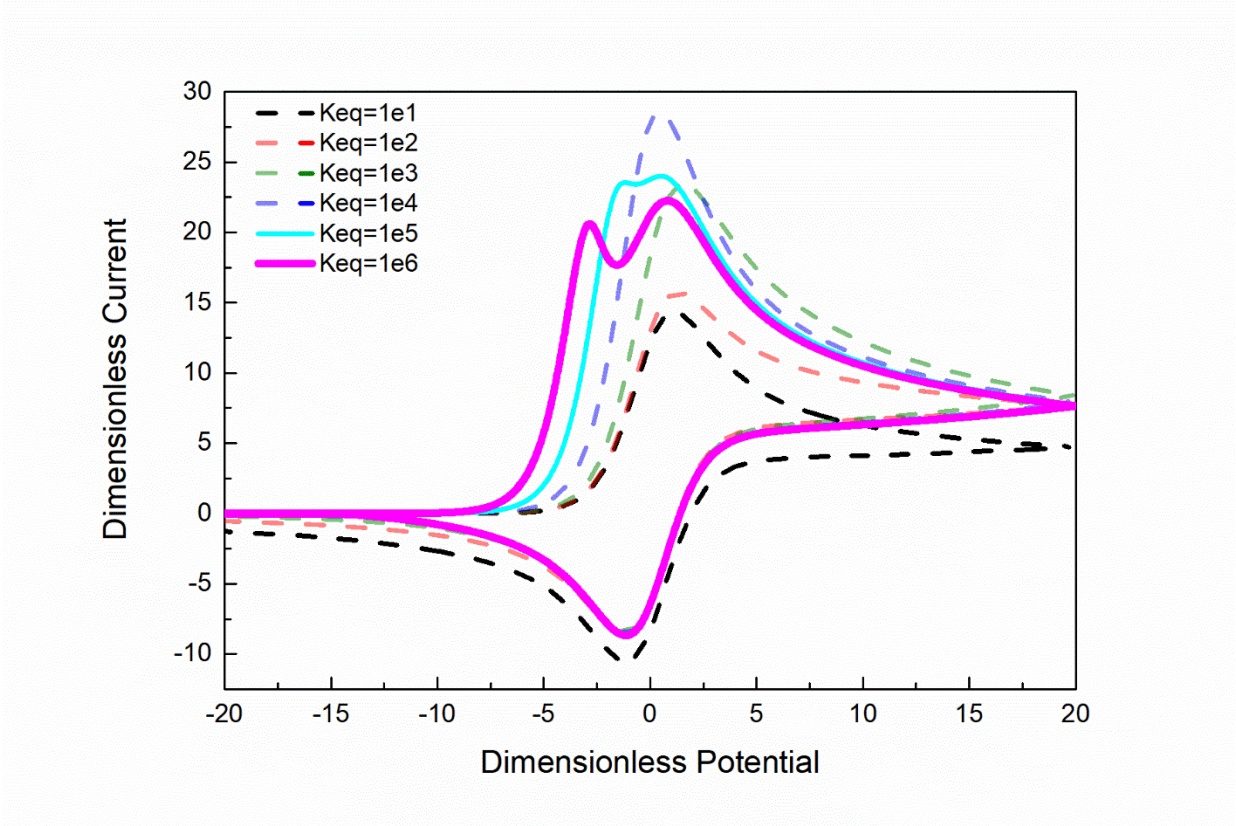

Figure 1.19: Cyclic voltammetry of second-order EC' mechanism for different chemical kinetics with $C_{\mathrm{O}}^{*} = C_{\mathrm{X}}^{*} = C_{\mathrm{Bulk}}^{*}$ and $C_{\mathrm{R}}^{*} = C_{\mathrm{Y}}^{*} = 0$. The prewave can be observed when $K_{\mathrm{eq}} \geq 10^{5}$.

1.5. Electrocatalysis

The EC' electrocatalysis mechanism that was discussed in the last section is found in inter-disciplinary problems and attracts the interest of chemists, physicists, physical-chemists, biochemists, surface and materials scientists, and engineers. This subject has been successfully explored in the past few decades to probe the impact of electrode materials[94-96], dynamic electrochemistry[97-99], redox mediator[100-103] and mass transfer phenomenon[104-107] with promising advances. In addition, renewable energy conversion and generation also drives the demands of highly active and robust electrocatalysts[108-111] for practical applications instead of our dependence on fossil fuels. Other applications in subject areas include but not limited to

- electrochemical generation of gases
- electrosynthesis, organic electrochemistry, and electrocatalytic hydrogenation
- electrochemical reactions taking place at matrix-supported electrocatalysts
- electrode reactions occurring in electrochemical sensors
- electrochemical degradation of pollutants

In this section, we discuss recent progress in promoting electrocatalysis involving hydrogenases and glucose sensors, whose catalytic mechanisms are discussed in Chapter 3, 4 and 5. Hydrogenases are extremely active and efficient microbial enzymes that catalyse interconversions between H_2 and water. As the substrate used for the electrocatalytic systems discussed in this document employ glucose as a substrate, a review the development of glucose sensors is also presented.

1.5.1. Hydrogenases

In recent years research on hydrogenases has grown significantly due to the scientific and technological interest in hydrogen as a clean energy carrier, potential transportation fuel, and important basic chemical reagent[112,113]. A future "hydrogen economy" requires processes for producing H_2 from renewable sources (like water) by clean, low-carbon and low-cost techniques. In this respect electrocatalysis plays a key role as it is used in biological processes. The study of hydrogenases and the detailed understanding of their enzymatic reactions can provide a structural and functional basis for the chemical and electrochemical development, the future employment of tailor-made modified biological systems for hydrogen production, and the use of molecular hydrogen, e.g., in fuel cells, aiming at the replacement of noble metals like platinum.

Hydrogenases are a diverse group of metalloenzymes[114-116] that catalyse one of the simplest molecular reactions, the conversion of dihydrogen into protons and electrons and the reverse reaction, the generation of dihydrogen: $H_2 \rightleftharpoons H^+ + H^- \rightleftharpoons 2H^+ + 2e^-$. The reaction takes place at a specialised metal centre that dramatically increases the acidity of H_2 and leads to a heterolytic splitting of the molecule which is strongly accelerated by the occurrence of a nearby base. The reverse reaction, the hetero-genesis of H_2, involves the respective coupling of H^+ and H^-.

Hydrogenases are widespread in nature and they occur in bacteria, archaea, and some eukarya[114,115,117-119]. Hydrogenases can be classified according to the metal ion composition of their active sites in [NiFe], [FeFe], and [Fe] hydrogenases[114,115,120,121].

A characteristic feature of the [NiFe] and [FeFe] hydrogenases is that the iron atoms are ligated by small inorganic ligands (CO and CN−), which were first detected by Fourier-transform infrared (FTIR) spectroscopy[122,123]. These enzymes contain sulphur bridged bimetallic centres, typically with an open coordination site on one metal (Figure 1.20). A subgroup of [NiFe] is formed by the [NiFeSe] hydrogenase, in which one of the cysteine ligands of the nickel is replaced by a seleno cysteine[124-126]. The third class of enzymes was shown to harbour a single iron atom[127,128] with an unusual coordination sphere; they also contain CO ligands at the iron. These enzymes are called [Fe] hydrogenases or iron−sulphur-cluster-free hydrogenases. They can activate H_2 only in the presence of a second substrate (methenyltetrahy-dromethanopterin)[129].

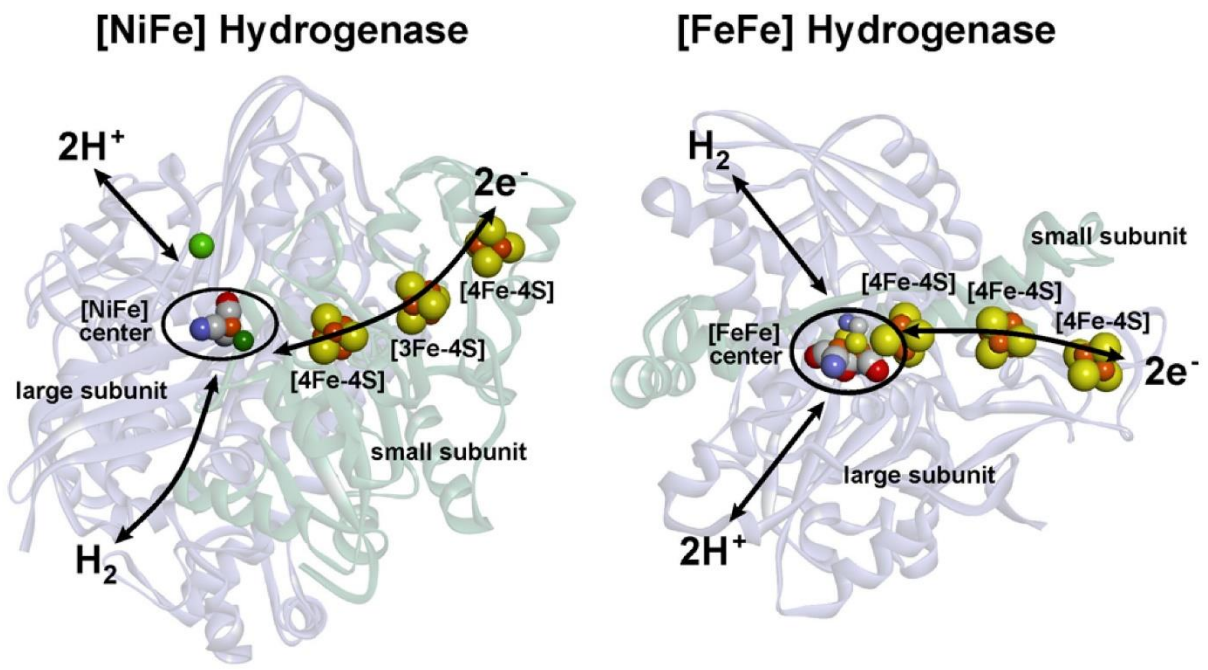

Figure 1.20: Structures of the [NiFe] hydrogenase from *Desulfovibrio vulgaris Miyazaki F* (*Dv*MF)[130] and of the [FeFe] hydrogenase from *Desulfovibrio desulfuricans* (*Dd*)[131]. Schematically indicated are the electron-transfer chain as well as pathways for the dihydrogen and the H^+ transfer. Reprinted from Lubitz *et al.*'s work[132].

Hydrogenases are found in the periplasm or cytoplasm, either in soluble form or membrane-bound; in eukaryotic cells they are often located in specialized compartments. The primary functions of hydrogenases are to provide energy for the organisms by oxidation of molecular hydrogen and to balance the redox potential of the cell. They can remove reducing equivalents by production of molecular hydrogen or provide electrons by splitting H_2. Depending on the location in the cell, hydrogenases may either be tuned for hydrogen evolution or hydrogen uptake. They may also be involved in building transmembrane proton gradients. The same principle to bind hydrogen at the active site (e.g. at the [NiFe] centre) during the catalytic process has also been used to sense the presence of hydrogen and regulate the expression of genes required for the biosynthesis of hydrogenases.

The [NiFe] hydrogenases are often more active in H_2 oxidation and the [FeFe] hydrogenases in the production of molecular hydrogen. The activity can be measured by several assays described in the literature[114,133]. Some [FeFe] hydrogenases are, for example, extremely active in H_2

generation[134]: each molecule of enzyme can produce up to ~10000 molecules of H_2 per second at room temperature[135]. The catalytic activities reported for [NiFe] hydrogenases are usually lower.

The active site is bound in a highly optimised functional protein matrix that provides not only ligands for the metals but also a pocket for the catalytic reaction and pathways for reactants and products to the protein surface. This is depicted for the catalytic [NiFe] and [FeFe] hydrogenases schematically in Figure 1.20, showing H^+ transfer, e^- transfer, and the gas channels for H_2 that are all ending close to the active site.

1.5.2. Glucose Sensors

Various kinds of sensors have been developed by employing electrocatalysts to detect organic and inorganic substances. Carbon materials, such as fullerene, carbon nanotubes and graphene and their derivatives have been widely studied and accepted as efficient materials for electrocatalytic sensors, both in the chemical and medical fields[136,137]. For example, electrons are transferred from the mono-anion fullerene to organic acid, which results in the deprotonation of the C−H bond of an organic acid[137]. The variation of current signal can be recorded for characterisation. The kinetic rate of the electron transfer among molecules can be obtained by controlling the concentration of electroinactive substances.

One important application is enzymatic glucose sensors that have been widely commercialised and applied in the blood monitoring systems[138]. Electrochemical redox couples are applied as mediators to contact the enzyme. By characterising the electron transfer characteristics of a reversible redox reaction and enzyme, the concentration of glucose can be detected in an indirect path. Alloy electrodes and graphene-based electrodes are predominantly used for enzymatic glucose sensors[137,139]. The development of enzymatic glucose sensors is presented in Figure 1.21.

The first generation of enzymatic glucose sensors was first commercialised in 1975 after Clark and Lyon came up with the initial definition of a glucose enzymatic electrode[140]. Electrons are carried from flavin adenine dinucleotide (FAD) to glucose. The reduced FAD−H_2 is oxidised by O_2, and then produces FAD and H_2O_2. The detection of hydrogen peroxide based on the EC' mechanism is the core part for first-generation glucose sensors. However, the effect of other electroactive species in the blood introducing a noise signal and the dependence on the free oxygen led to the imprecision as the concentration of oxygen varies[138]. Different from the first-generation, the second-generation sensors avoid the dependence on oxygen by introducing a redox mediator, such as ferrocene derivatives[141] and ferricyanide[142]. However, these artificial mediators or nanomaterials used to transport the electrons to the electrode are partially toxic. The development of the electrode materials promotes the evolution of third-generation glucose sensor[143-145], which employs direct electron transfer to the electrode, thus eliminating toxic artificial electron mediators and avoiding errors due to variations in the concentration of oxygen in the blood samples.

In addition to biological sensing, electrocatalytic methods have been used to investigate the detection of sulphide species. The high toxicity of liberated hydrogen sulphide leads to physiological distress in low concentration and causes fatal sickness in high concentration[146]. Even though the high reactivity of sulphide species in aquatic systems has decreased the accumulated levels in the environment and risk level[147], quantification and monitoring technologies of sulphide are significant for those who are exposed in sulphide circumstances, such as drilling and refining of crude oil. In comparison with the conventional detection routes, such as spectroscopic technology and chromatography, electrochemical detection devices stand out with low price, simplicity of design and high sensitivity[148]. Development of electrodes [146,149] and redox mediators for electrocatalysts[147,148] has been widely discussed.

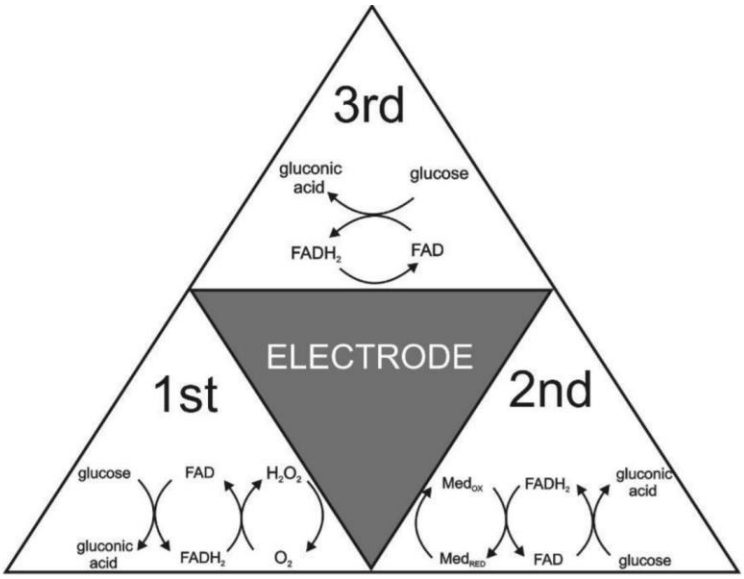

Figure 1.21: Mechanistic schemes of enzymatic glucose oxidation involving first-, second- and third-generation sensors.

1.6. Thesis Outlines

The rest of the thesis chapter is structured as follows. In Chapter 2, general procedures for the implementation of numerical modelling techniques are fully expanded to detail the approaches that we used for electrochemical investigations in the work. Wherein, the finite difference method (FDM) is employed rather than other existing simulation approaches corresponding to the definition of the system (including mass transport, coupled chemical reactions and boundary conditions).

Chapter 3 proposes a novel high-order operator-splitting (OS) scheme, with fully implicit finite difference (FIFD) method as its base which is employed in the solutions of the governing nonlinear PDEs describing the electrochemical system. This algorithm for the first time is employed in electrochemistry for the analysis of electrode reactions at a planar electrode. The framework offers an efficient and more accurate way for the numerical modelling of mass transfer, electron transfer and coupled homogeneous chemical reactions. This model will then be verified by comparing it to the results obtained through conventional numerical models that are established by discretising the time by two-point derivate.

In order to further develop the operator-splitting scheme, it is necessary to test the approach in a well-defined practical electrochemical system. Therefore, Chapter 4 describes the investigation of a unique current behaviour generated from a chosen electrochemical system, in which a totally inverted backward peak occurs on the reversal scan by cyclic voltammetry. This specific example has recently been reported in the open literature based on a non-enzymatic catalyst by preparing a rhodium-porphyrin catalyst on a multi-walled carbon nanotube matrix. Such a phenomenon has been observed in literature for only surface confined hydrogenase, which exhibits an electrocatalytic inactivation and activation processes (IAPs). A very detailed mechanistic analysis is carried out to understand the thermodynamics and kinetics of IAPs and the stepwise investigations offer a mechanism for glucose oxidation which proceeds an EC'CE scheme with catalytic steps like the ones presented for hydrogenase. This mechanism was tested using the developed OS scheme and comparisons were done using a conventional FDM to evaluate the applicability of the developed numerical scheme.

Chapter 5 presents a deeper investigation of the same electrocatalytic inactivation and activation processes (IAPs) by chronoamperometric voltammetry. The important kinetic parameters are obtained through an alternative technique. The approach surprisingly leads to an unexpected difference between the anodic and cathodic peak current at a far more negative potential. Cyclic voltammetry is used again with increased sweeping range; as a result, an additional reduction peak is observed at -1.15 ± 0.05 V under low scan rate (< 50 mV/s). This observation implies extra electrochemical (coupled with chemical) steps in the system, which is resulted from the formation of dimeric rhodium intermediates. The implementation of computational-based model is utilised to quantitatively analyse the dimer formation scheme, which is upgraded from pre-designed mathematical models from Chapter 4.

Chapter 2

2. Numerical Modelling Techniques

Chapter 1 describes the background theory and application of different electrochemical systems and provides an established experimental framework to explore the kinetic and mechanistic processes linked to electrolytic reactions. The link between the current/voltage inputs and outputs offers critical information including: mass transfer behaviour, the electrode properties, interfacial reaction rate constants and the reaction mechanisms. To investigate cyclic voltammetry properties of an electrochemical reaction at a planar electrode, the electrode kinetic behaviour can be predicted by $i(E)$ functions, such as a single electron-transfer, by recalling Equation 1.8 from the first chapter,

$$i = FAk_0\left[C_{\mathrm{R}}(0,t)e^{(1-\alpha)\frac{F}{RT}(E-E^0)} - C_{\mathrm{O}}(0,t)e^{-\alpha\frac{F}{RT}(E-E^0)}\right] \qquad (2.1)$$

Equation 2.1 provides an analytical solution when the electron transfer process is fully reversible (k^0 is large, and the problem will be reduced to Nernstian equation). However, when the complexity of the electrochemical system increases, for example an ECE mechanism, EC' mechanism or hydrogenase, the resolutions of these mathematical problems involving partial differential equations (PDEs) cannot be performed analytically anymore.

In such circumstances, numerical approximations of these governing partial differential equations, also referred to as numerical methods give an alternative approach to obtain solutions of these problems by employing efficient numerical algorithms at a reduced computational cost. In electrochemistry, numerical methods have been used for a variety of purposes[150-153] to study the kinetics and thermodynamics. The modelling of voltammetry necessitates fully understanding the systems in terms of mass transport, electrode reactions and processes with coupled homogeneous chemical reactions. In the following sections the general procedures for the basic implementation of numerical simulations are introduced in order to build the electrochemical models and solve the appropriate mathematical problems.

2.1. Different Numerical Techniques

Numerical techniques rely on the approximation of a continuous quantity (usually a derivative) of partial differential equations into a set of algebraic equations, each of which is computed at discrete points, known as nodes, inside the computational domain. These set of linear equations are then solved through various direct and iterative techniques. These methods for solving the partial differential equations (PDEs) include, but do not limit to, the finite-element method (FEM), the finite-volume method (FVM) and the finite-difference method (FDM).

2.1.1. Finite-Difference Method (FDM)

The FDM is the simplest and most popular technique to discretise the space and/or time dependent terms of the PDE into algebraic form over a set mesh of points (often referred to as "nodes") spanning across the computational domain. At each point, the derivatives in the mass transfer equation are approximated as differences of the concentrations at the given and surrounding points. Consider a spatial co-ordinate, x, and a temporal co-ordinate, t, divided into N_x and N_t points at a distance Δx and a timestep Δt, respectively. i and k are used to index a particular spatial point ranged from 1 to n, and a particular temporal point ranged from 1 to m, respectively. Figure 2.1 demonstrate the scheme of FDM with the concentration gradient at point (i, k) and the expression of its adjunction concentrations.

These methods are well-suited to simulations performed on structured-Cartesian grids, which is often compatible with an electrochemical cell by accurate and effective procedures. These are by far the most popular methods for electrochemical simulations and abundant literature comprehensively depict the mathematical foundations and applications of FDM[154-157] is available. This technique is used throughout this thesis.

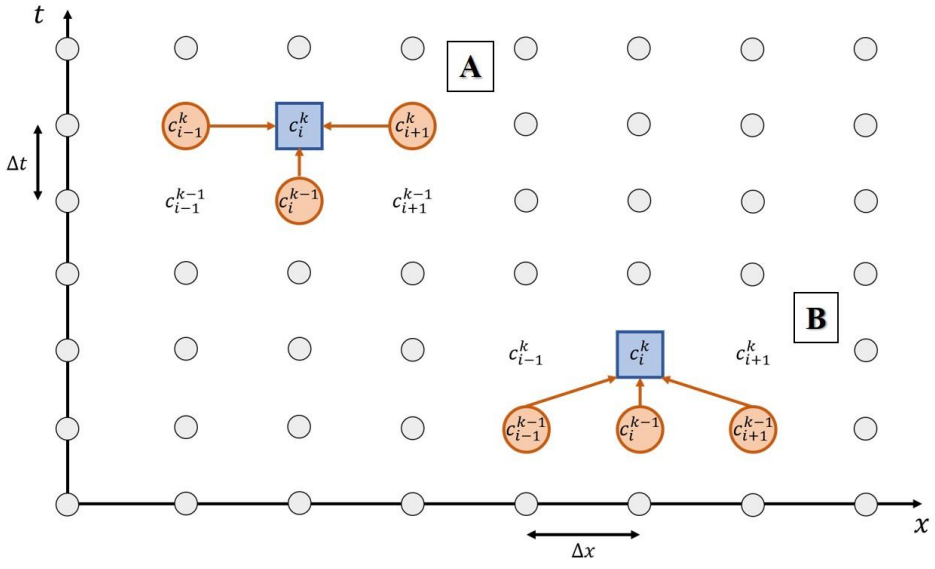

Figure 2.1: Discrete simulation involving in concentration terms on the finite difference space-time grid. The unknown C_i^k is given by implicit (A) and explicit (B) formulations. The blue squares depict the term to be solved for and orange circles show the terms that need in the equation.

2.1.2. Finite-Element Method (FEM)

The FEM is a general computational technique to solve PDEs in which the space domain of the continuum can be subdivide into tiny but finite-sized elements of geometrically simple of arbitrary sizes and shapes. Since any polygonal structure with rectilinear or curved sides can be finally be reduced to triangular and quadrilateral figures, the latter are the basis for the space division. In this method, the governing equations are solved in their integral form in which the integral equation breaks up into a sum of integrals over each element. In an element, the concentration distribution is approximated by the weighted sum of a set of interpolating functions of the nodal values. These functions are chosen to have a value of unity at only one node and zero at all others, and then are substituted into the variational form of the discretised equation which leads to a set of linear equations for each element. Summing over all elements leads to a set of linear equations which is generally symmetric for the unknown nodal values.

One major advantage of FEMs rather than FDMs is the way in which the former guarantees a very accurate approximation when given finer mesh involving locally high-order polynomials for a multi-physics analysis. They can therefore be applied to problems with a complex geometry, for example elevated and recessed electrodes[158] and simulation of rough electrodes[149]. However, finite element methods are more complex to program, especially when simulating chemical steps, and result in a linear system of equations which is not neatly banded. The precision of the method requires advanced mathematical expertise for its implementation. Another disadvantage is that it is relatively difficult for FEM to use explicit solvers in comparison to FDM and FVM, although, the finite-element technique has been proven commercialised successfully in some industrial cases.

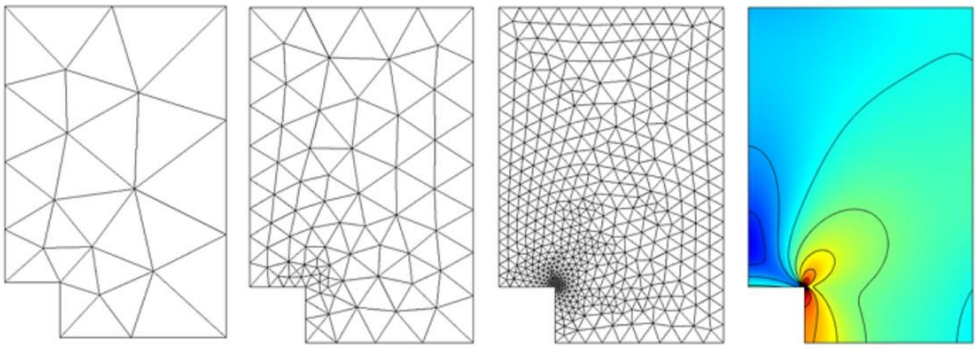

Figure 2.2: Adaptive mesh refinement generated from COMSOL (a commercial FEM based software) to display the elements into regions.

2.1.3. Finite-Volume Method (FVM)

The FVM is a very similar approach to the FEM as the flow field or *domain* is subdivided into a set of non-overlapping cells that cover the whole domain. Apart from the first step, the finite-volume methods are referred to the concept of cells or volumes rather than the idea of elements from finite-element method[159]. This method preserves conservation laws as the cell-based approach in solving the integral form of the governing equations ensures that the input flux strictly identical to the output flux leaving into the adjacent volume, which ends up with a relationship consisting of flux conservation equations defined in an averaged sense on the cells. This method is very successfully in solving computational fluid dynamic problems. However, the use of high-order mesh to improve the efficiency and accuracy is still a significant bottleneck in industrial applications for FVM[160].

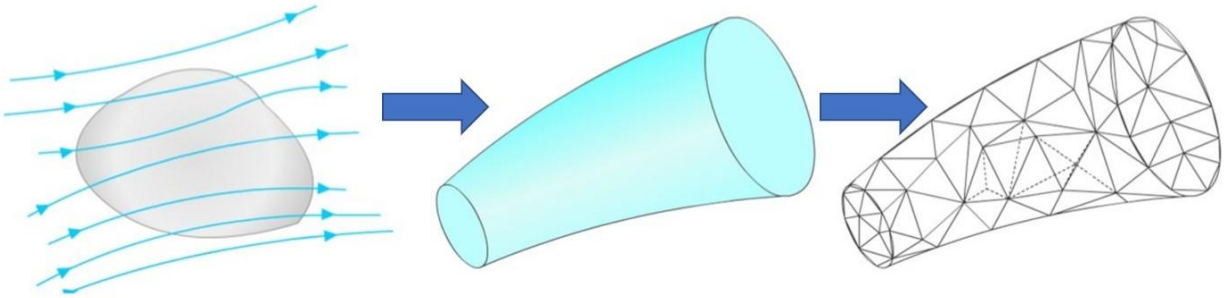

Figure 2.3: Schematic diagram of finite-volume method spatial discretisation.

2.2. Finite-Difference Methods

The basic principles of finite difference methods were introduced in Subsection 2.1.1. In this section, it is shown how electrochemical mass transfer equations can be approximated by different finite difference discretisation schemes. Each scheme offers varying amounts of “implicitness” as the relative advantages. The result of discretisation is a set of linear and nonlinear simultaneous equations, to which boundary conditions (defining the edge effects of the cell, and the characteristics of the electrode) must be applied. The following sections of this chapter address the solution of these system of equations, and conclude by providing details on how the problems with increasing complexity might be solved by nonlinear solvers.

2.2.1. Boundary Conditions

Recalling the single electron transfer mechanism, $O + e^- \rightleftharpoons R$, with a diffusion-only mass transport at a planar electrode introduced in Chapter 1, the problem is modelled with *Fick's second law*,

$$\frac{\partial C_j(x)}{\partial t} = D_j \frac{\partial^2 C_j(x)}{\partial x^2} \tag{2.2}$$

Equation 2.2 describes a single property, concentration, which evolves in space and time. In order to solve an equation of this type numerically, it is essential to know the initial condition of the system. At starting time, $t = 0$, we start the experiment in which the concentration of species O has a fixed value and is uniform everywhere. This concentration is called the bulk concentration of species O, and we have the initial condition,

$$C_O(x, 0) = C_O^* \tag{2.3}$$

A similar condition applies to the species R which is assumed to be absent initially. Thus, $C_R(x, 0) = 0$. At times $t > 0$, we strictly constrain the system concentration at a finite region from electrode to the bulk concentration,

$$\lim_{x \to \infty} C_O(x, t) = C_O^* \tag{2.4}$$

and the concentrations at the electrode surface vary as a function of predesigned potential in absence of material balances. Thus, the interface can be written as,

$$C_O(0, t) = 0 \text{ (for } t > 0) \tag{2.5}$$

The problem, now, is fully described for E mechanism.

2.2.2. Spatial Discretisation

Under a finite difference scheme, a continuous function is represented in its discretised form. In our case, the function we need to focus on is the concentration as it changes in space, $C_j(x)$, and its first and second derivatives. To approximate the function $C_j(x)$, the one-dimensional space under consideration is divided into n points with a uniform spacing Δx between the nodes. Figure 2.1 is recalled here to illustrate the space grid.

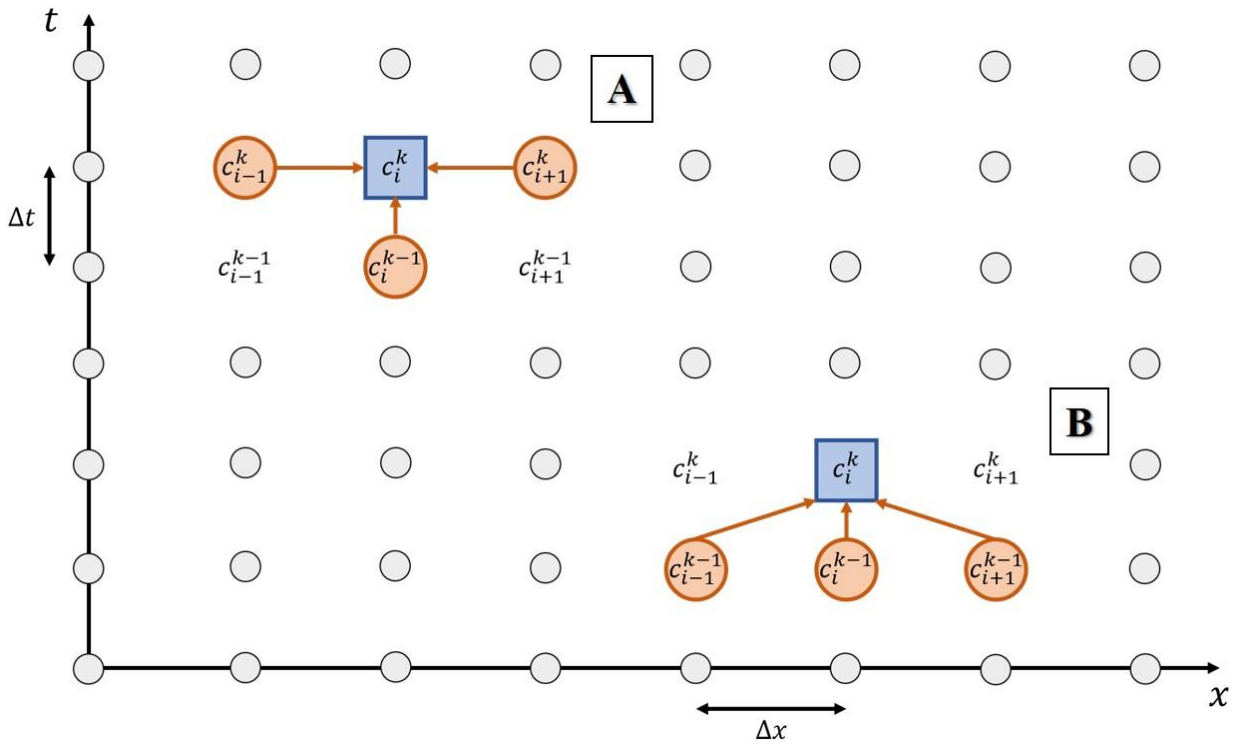

Figure 2.4: Discrete simulation involving in concentration terms on the finite difference space-time grid. The unknown C_i^k is given by implicit (A) and explicit (B) formulations. The blue squares depict the term to be solved for and orange circles show the terms that need in the equation.

According to the definition, space grid holds,

$$x_{i+1} - x_i = x_i - x_{i-1} = \Delta x$$
$$n = \frac{x_{\text{bulk}} - x_{\text{electrode}}}{\Delta x} \tag{2.6}$$

Now let us consider the first derivative of which the mathematical definition is the ratio of the change in concentration to the change of distance

$$\frac{\partial C_{\mathrm{j}}(x_i)}{\partial x} = \lim_{\Delta x \to 0} \frac{C_{\mathrm{j}}(x_{i+1}) - C_{\mathrm{j}}(x_i)}{\Delta x} \tag{2.7}$$

From this definition, we can approximate the first derivative as

$$\frac{\partial C_{\mathrm{j}}(x_i)}{\partial x} \approx \frac{C_{\mathrm{j}}(x_{i+1}) - C_{\mathrm{j}}(x_i)}{\Delta x} \tag{2.8}$$

This is called the forward difference approximation of the first derivative. Alternatively, the backward difference approximates the derivative as

$$\frac{\partial C_{\mathrm{j}}(x_i)}{\partial x} \approx \frac{C_{\mathrm{j}}(x_i) - C_{\mathrm{j}}(x_{i-1})}{\Delta x} \tag{2.9}$$

Another first-order differencing scheme may be obtained by considering the average derivative given by the forward and backward schemes, and this is called the central difference approximation,

$$\frac{\partial C_{\mathrm{j}}(x_i)}{\partial x} \approx \frac{1}{2}\left[\frac{C_{\mathrm{j}}(x_{i+1}) - C_{\mathrm{j}}(x_i)}{\Delta x} + \frac{C_{\mathrm{j}}(x_i) - C_{\mathrm{j}}(x_{i-1})}{\Delta x}\right] \tag{2.10}$$

For this approach, the error by considering the Taylor series expansion of the concentration is second-order, which provides higher accuracy than the first-order error given by either the forward or backward schemes[37]. Thus, the central scheme provides a more accurate approximation of the first derivative, and Equation 2.10 could be re-written as

$$\frac{\partial C_{\mathrm{j}}(x_i)}{\partial x} \approx \frac{C_{\mathrm{j}}(x_{i+1}) - C_{\mathrm{j}}(x_{i-1})}{2\Delta x} \tag{2.11}$$

The second derivative of the concentration can be also obtained by Taylor series expansion[161] with a second-order error,

$$\frac{\partial^2 C_{\mathrm{j}}(x_i)}{\partial x^2} \approx \frac{C_{\mathrm{j}}(x_{i+1}) - 2C_{\mathrm{j}}(x) + C_{\mathrm{j}}(x_{i-1})}{(\Delta x)^2} \tag{2.12}$$

Throughout this thesis I shall use the approximation of Equations 2.11 and 2.12 as the primary numerical techniques.

The distribution of nodes of the equal spatial grid leads to a higher number of points in the entire regions of the concentration profile, which greatly decrease the efficiency of the simulation. Here a more advanced discretisation for the spatial grids is introduced by adding expanding spatial grids. Figure 2.5 shows the expanding grid scheme for the variation of the reactant concentration with the distance from the electrode. A large overpotential is applied to the working electrode such that the reactant species is consumed quite rapidly on the electrode surface. This creates a concentration gradient near the electrode and consequently the diffusion of species towards the electrode surface occurs such that the depletion layer extends towards the bulk solution as time proceeds. Therefore, the spacing between grid points in this region must be small enough to minimise the error of the finite difference approximation. On the other hand, the concentration profiles of the electroactive species are only slightly affected in the regions of the solution farther away from the electrode surface.

Considering the above aspects, it is beneficial to establish a grid that mimics the concentration profile and provides a high number of points near the electrode surface but minimises the total number, which makes the simulation process more efficient. With this aim, unequally spaced grids or transformation of the spatial coordinates can be employed.

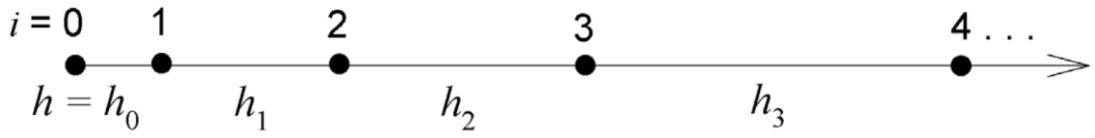

Figure 2.5: An expanding grid scheme for a concentration profile of species O.

It is efficient to use patching schemes that combine both uniform and unequally compressing grids. For example, assuming that the main changes in concentration take place next to the electrode surface, a dense and uniform grid in that region ($x \leq x_{\mathrm{sw}}$) leads the distribution of the points in the vicinity of electrode with equal spacing. When the distance to the electrode is far away but still constrained to the entire diffusion layer ($x_{\mathrm{sw}} \leq x \leq x_{\mathrm{diff}}$), an expanding grid is then implemented towards the bulk solution. This stepwise strategy can be present,

$$\begin{gathered} \Delta x = h_i = h_0 \text{ (for } x \leq x_{\mathrm{sw}}) \\ \Delta x = h_i = h_0 \omega_x^{i-(x_{\mathrm{sw}}/h_0)+1} \text{ (for } x_{\mathrm{sw}} \leq x \leq x_{\mathrm{diff}}) \end{gathered} \tag{2.13}$$

where h_0 is the initial point representing the electrode surface, ω_x is a weighted parameter that can adjust the growth of expanding grids. x_{sw} can be defined to balance the computational cost and the number of nodes.

2.2.3. Temporal Discretisation

So far, we discussed how the concentration changes in dependence on the spatial variable, the position x in the RHS of Equation 2.2. However, modelling of an electrochemical system requires the solution of Fick's second law and a partial differential equation in which concentrations also varies as a function of time, t, given in the LHS. We must now consider how the system evolves in time. Before discretising the time derivative, some basic input parameters are needed to be defined under cyclic voltammetry (CV) technique. The popularity of CV has led to its extensive study and numerous simple criteria are available for immediate analysis of electrochemical systems from the shape, position and time-behaviour of the experimental voltammograms. Recall the definition of CV from Equation 1.38,

$$\begin{aligned} E(t) &= E_{\mathrm{i}} + vt \ (dE/dt = v) \\ E(t) &= E_{\mathrm{v}} - v(t - t_{\mathrm{R}}) \ (dE/dt = -v) \end{aligned} \tag{2.14}$$

where the starting point and vertex point of the potential are generally defined to cover the standard potential E^0 of the electrode reaction. The scan rate, v, is the constant rate at which the voltage sweeps from E_{i} to E_{v} and back again. Thus, the reversal switch point t_{R} and the total running time $t_{\max}$ can be easily calculated,

$$\begin{aligned} t_{\mathrm{R}} &= \frac{|E_{\mathrm{v}} - E_{\mathrm{i}}|}{v} \\ t_{\max} &= 2t_{\mathrm{R}} = 2\frac{|E_{\mathrm{v}} - E_{\mathrm{i}}|}{v} \end{aligned} \tag{2.15}$$

Then, the thickness of the diffusion layer, δ, (also referred to $x_{\mathrm{diff}} = x_{\mathrm{bulk}} - x_{\mathrm{electrode}}$, or $x_{\max}$ in this thesis) is generally suggested to give

$$\delta = \sqrt{6D_{\max}t_{\max}} \tag{2.16}$$

where $D_{\max}$ is the greatest diffusion coefficient of the species involved in the problem.

For the one-dimensional system under consideration, the state of the system (which is represented in a discretised form by the set of concentrations from $C_{\mathrm{j}}(x_0), \cdots, C_{\mathrm{j}}(x_{n-1})$) at any moment in time depends on two things: the spatial boundary conditions (the electrode surface and bulk solution boundaries), and the state of the system at the previous moment in time. Discretising time follows a similar manner as space discretisation, with a constant interval between adjacent time steps, Δt .

When modelling, the state of the system is set from the starting time of the experiment, t_0, to its finishing time, $t_{\max}$, so the total number of timesteps, *m*, is given by

$$m = \frac{t_{\max} - t_0}{\Delta t} \tag{2.17}$$

As previously discussed, at the beginning of the experiment, the system is homogeneous. The concentration of the starting species O is uniform across the whole space as given by the initial conditions $C_{\mathrm{O}}(x, 0) = C_{\mathrm{O}}^{*}$. Therefore, the values of the set of concentrations are all equal to those of bulk solution for the first timestep. The concentrations at timestep t^k are then a function of those at t^{k-1}. For the derivative of Fick's second law to obtain the concentration versus time, it is obvious to use a backward finite difference scheme as we have no information about the state of the system at any timesteps beyond the current one. Then, the LHS of Fick's second law is given by

$$\frac{\partial C_{\mathrm{j}}(t^k)}{\partial t} \approx \frac{C_{\mathrm{j}}(t^k) - C_{\mathrm{j}}(t^{k-1})}{\Delta t} \tag{2.18}$$

Combining both, spatial and temporal discretised components of Fick's second law, the overall equation is then

$$\frac{C_{\mathrm{j}}(\, t^k) - C_{\mathrm{j}}(t^{k-1})}{\Delta t} = D_{\mathrm{j}} \frac{C_{\mathrm{j}}(x_{i+1}) - 2C_{\mathrm{j}}(x) + C_{\mathrm{j}}(x_{i-1})}{(\Delta x)^2} \tag{2.19}$$

For a single species, Equation 2.19 rewrites

$$\frac{C_i^k - C_i^{k-1}}{\Delta t} = D_{\mathrm{j}} \frac{C_{\mathrm{i}-1} - 2C_{\mathrm{i}} + C_{\mathrm{i}+1}}{(\Delta x)^2} \tag{2.20}$$

Only equal temporal discretisation is employed in the following parts, thus, there is no details on the unequally temporal grids.

From Equation 2.20, there is now an important choice as to whether the concentrations on the RHS are chosen to be at C_i^k and C_i^{k-1}. Recalling the Figure 2.4 again, we will briefly consider the former case, generally known as the explicit method, illustrated in Figure 2.6(Right), before moving on to the latter, the implicit method, illustrated in Figure 2.6(Left), which will be used throughout the rest of the thesis.

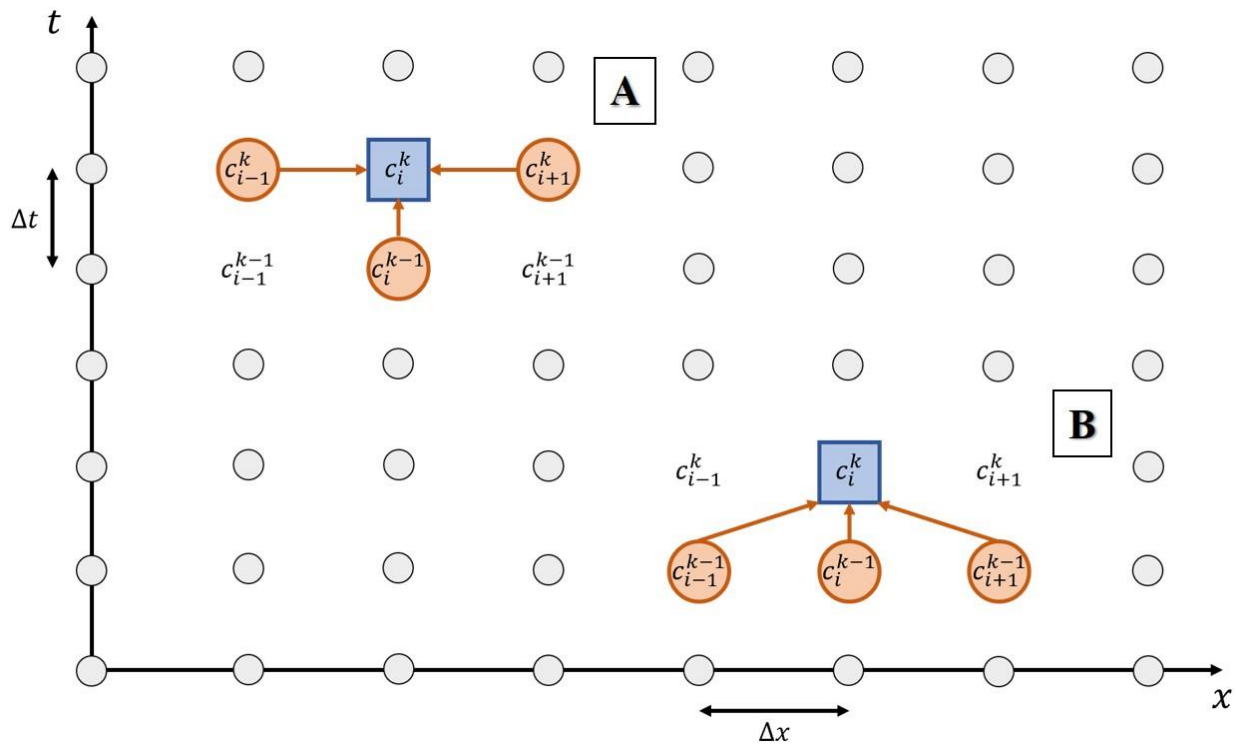

Figure 2.6: Discrete simulation involving in concentration terms on the finite difference space-time grid. The unknown C_i^k is given by implicit (A) and explicit (B) formulations. The blue squares depict the term to be solved for and the orange circles show the terms that need in the equation.

The explicit method consists of solving the equation

$$\frac{C_i^k - C_i^{k-1}}{\Delta t} = D_{\mathrm{j}} \frac{C_{i-1}^{k-1} - 2C_i^{k-1} + C_{i+1}^{k-1}}{(\Delta x)^2} \tag{2.21}$$

which for convenience may be rearranged to

$$C_i^k = C_i^{k-1} + \frac{D_{\mathrm{j}} \Delta t}{(\Delta x)^2} \left(C_{i-1}^{k-1} - 2C_i^{k-1} + C_{i+1}^{k-1} \right) \tag{2.22}$$

This is a simple equation to solve, and each value of C_i^k can be solved for independently at every timestep because all the terms appearing on the RHS of the equation are fully known in contrast with the implicit method.

The backward implicit method consists of second derivative on the time evolution solving the Equation 2.20

$$\frac{C_i^k - C_i^{k-1}}{\Delta t} = D_\mathrm{j} \frac{C_{i-1}^k - 2C_i^k + C_{i+1}^k}{(\Delta x)^2} \tag{2.23}$$

The only difference from Equation 2.22 is the timestep at which the concentrations on RHS are taken. Rearranged to a more useful form, it becomes

$$-\frac{D_\mathrm{j}\Delta t}{(\Delta x)^2} C_{i-1}^k + \left[1 + \frac{2D_\mathrm{j}\Delta t}{(\Delta x)^2}\right] C_i^k - \frac{D_\mathrm{j}\Delta t}{(\Delta x)^2} C_{i+1}^k = C_i^{k-1} \tag{2.24}$$

This equation contains a single known value, C_i^{k-1} , and three unknowns, C_{i-1}^k, C_i^k and C_{i+1}^k. Unlike the explicit method, the implicit method cannot be solved in isolation for any given point, *i*. At each timestep, *k*, the complete set of equations for the concentration at every point must be solved simultaneously. The solution methods of the implicit method shall come to shortly in next section.

The third option is to mix the explicit and implicit methods. We can then write the equation as

$$\begin{aligned} &C_i^k - \frac{\alpha D_\mathrm{j}\Delta t}{2(\Delta x)^2}\left(C_{i-1}^k - 2C_i^k + C_{i+1}^k\right) \\ &= C_i^{k-1} + \frac{(1-\alpha) D_\mathrm{j}\Delta t}{2(\Delta x)^2}\left(C_{i-1}^{k-1} - 2C_i^{k-1} + C_{i+1}^{k-1}\right) \end{aligned} \tag{2.25}$$

where α is an adjustable parameter which varies between zero (fully explicit) and unity (fully implicit). When $\alpha = 0.5$, this is known as the Crank-Nicolson method. The Crank-Nicolson method is less stable but more accurate than the fully implicit scheme[162].

Taking the Crank-Nicolson idea one step further, Feldberg and co-workers[163] have developed an improved version of this method by employing a more accurate higher order backward difference method for one-dimensional diffusion simulations. This advanced technique combines a solution method called Rudolph's FIFD (fully-implicit finite difference method)[164] in order to find a significant improvement in efficiency and stability.

The (fully implicit) difference equations gives a high-level Richtmyer modification as

$$
\begin{aligned}
&\text{Two points: } \frac{\partial C_i^k}{\partial t} \approx \frac{C_i^k - C_i^{k-1}}{\Delta t} \\
&\text{Three points: } \frac{\partial C_i^k}{\partial t} \approx \frac{3C_i^k - 4C_i^{k-1} + C_i^{k-2}}{2\Delta t} \\
&\text{Four points: } \frac{\partial C_i^k}{\partial t} \approx \frac{11C_i^k - 18C_i^{k-1} + 9C_i^{k-2} - 2C_i^{k-3}}{6\Delta t} \\
&\text{Five points: } \frac{\partial C_i^k}{\partial t} \approx \frac{25C_i^k - 48C_i^{k-1} + 36C_i^{k-2} - 16C_i^{k-3} + 3C_i^{k-4}}{12\Delta t} \\
&\text{Six points: } \frac{\partial C_i^k}{\partial t} \approx \frac{137C_i^k - 120C_i^{k-1} + 120C_i^{k-2} - 200C_i^{k-3} + 75C_i^{k-4} - 12C_i^{k-5}}{60\Delta t} \\
&\text{Seven points: } \frac{\partial C_i^k}{\partial t} \approx \frac{147C_i^k - 360C_i^{k-1} + 450C_i^{k-2} - 400C_i^{k-3} + 225C_i^{k-4} - 72C_i^{k-5} + 10C_i^{k-6}}{60\Delta t}
\end{aligned}
\tag{2.26}
$$

2.3. Solution Methods

In the last section, the discretisation of space and time leads to system of equations for solving the equation for E mechanism at a planar electrode system. A useful form of the equation is arranged as

$$-\frac{D_{\mathrm{j}}\Delta t}{(\Delta x)^2}C_{i-1}^{k}+\left[1+\frac{2D_{\mathrm{j}}\Delta t}{(\Delta x)^2}\right]C_{i}^{k}-\frac{D_{\mathrm{j}}\Delta t}{(\Delta x)^2}C_{i+1}^{k}=C_{i}^{k-1} \tag{2.27}$$

To find a resolution for such a problem, we first fully expand Equation 2.27 to a whole set of equations

$$\begin{aligned}
&\vdots\\
&-\frac{D_{\mathrm{j}}\Delta t}{(\Delta x)^2}C_{i-2}^{k}+\left[1+\frac{2D_{\mathrm{j}}\Delta t}{(\Delta x)^2}\right]C_{i-1}^{k}-\frac{D_{\mathrm{j}}\Delta t}{(\Delta x)^2}C_{i}^{k}=C_{i-1}^{k-1}\\
&-\frac{D_{\mathrm{j}}\Delta t}{(\Delta x)^2}C_{i-1}^{k}+\left[1+\frac{2D_{\mathrm{j}}\Delta t}{(\Delta x)^2}\right]C_{i}^{k}-\frac{D_{\mathrm{j}}\Delta t}{(\Delta x)^2}C_{i+1}^{k}=C_{i}^{k-1}\\
&-\frac{D_{\mathrm{j}}\Delta t}{(\Delta x)^2}C_{i}^{k}+\left[1+\frac{2D_{\mathrm{j}}\Delta t}{(\Delta x)^2}\right]C_{i+1}^{k}-\frac{D_{\mathrm{j}}\Delta t}{(\Delta x)^2}C_{i+2}^{k}=C_{i+1}^{k-1}\\
&\vdots
\end{aligned} \tag{2.28}$$

with the boundary conditions.

For a fully reversible E mechanism with a fast electron transfer rate, the boundary conditions are obtained from the Nernst Equation, which gives

$$\begin{aligned}
C_{\mathrm{O}}(x=0)&=\frac{1}{1+e^{-\frac{F}{RT}(E-E^{0})}}\\
C_{\mathrm{R}}(x=0)&=\frac{1}{1+e^{\frac{F}{RT}(E-E^{0})}}
\end{aligned} \tag{2.29}$$

In a more general case, the empirical Butler-Volmer (BV) model has been the most widely used over many years in electrochemistry due to its simplicity and successful quantitative description of a vast number of electrochemical systems (in the absence of bonds being broken or formed). According to the BV model, the rate constants show a simple exponential dependence with the applied potential according to the following expressions:

$$k_{\mathrm{f}}=k_{0}e^{-\alpha\frac{F}{RT}(E-E^{0})} \tag{2.30}$$

$$k_{\mathrm{b}}=k_{0}e^{(1-\alpha)\frac{F}{RT}(E-E^{0})} \tag{2.31}$$

so that the electrode kinetics are parameterised as a function of the standard potential E^0, and the charge transfer coefficient α can take values in the range $0 \leq \alpha \leq 1$ (although typical values are in the range $0.3 < \alpha < 0.7$) and can be interpreted qualitatively as an indicator of the position of the transition state in the reaction coordinate. Thus, the configuration of the transition state in a reduction process is reactant-like when $\alpha > 0.5$ and product-like when $\alpha < 0.5$.

To deal with the implementation of the BV surface boundary condition in the simulation, the net reaction rate is given derived from Equations 1.8 and 1.14,

$$\frac{i}{FA} = -D\frac{\partial C_{\mathrm{O}}(x)}{\partial x} = k_0\left[C_{\mathrm{R}}(0,t)e^{(1-\alpha)\frac{F}{RT}(E-E^0)} - C_{\mathrm{O}}(0,t)e^{-\alpha\frac{F}{RT}(E-E^0)}\right] \qquad (2.32)$$

As mentioned before, when the diffusion coefficients of both electroactive species are the same, the total concentration of the species at any point of the solution and at any time is constant: $C_{\mathrm{O}}(x) + C_{\mathrm{R}}(x) = C_{\mathrm{O}}^* + C_{\mathrm{R}}^*$. After discretisation of the problem using a two-point approximation for the surface gradient we obtain,

$$D\frac{C_1^k - C_0^k}{\Delta x} = k_0 e^{-\alpha\frac{F}{RT}(E-E^0)}\left\{C_0^k - [C_{\mathrm{O}}^* + C_{\mathrm{R}}^* - C_0^k]e^{\frac{F}{RT}(E-E^0)}\right\} \qquad (2.33)$$

that can be arranged as

$$\begin{aligned} &C_0^k\left\{1 + \frac{\Delta x k_0}{D}e^{-\alpha\frac{F}{RT}(E-E^0)}\left[1 + e^{\frac{F}{RT}(E-E^0)}\right]\right\} - C_1^k \\ &= \frac{\Delta x k_0}{D}e^{-\alpha\frac{F}{RT}(E-E^0)}(C_{\mathrm{O}}^* + C_{\mathrm{R}}^*)e^{\frac{F}{RT}(E-E^0)} \end{aligned} \qquad (2.34)$$

Once the concentration profile of species O is calculated, that of species R can be obtained immediately by $C_{\mathrm{R}}(x) = C_{\mathrm{O}}^* + C_{\mathrm{R}}^* - C_{\mathrm{O}}(x)$. This surface boundary for electron transfer derived from BV model is employed throughout the thesis. The initial condition and the boundary condition at the bulk are defined by Equations 2.2 and 2.3, respectively. The problem now is fully interpreted into mathematic language, which is summarised in Scheme 2.1, and the expression of Equation 2.28 is now completed by the first and last parts obtained from boundary conditions.

E mechanism:

Governing equation:

$$\frac{\partial C_{\mathrm{O}}(x,t)}{\partial t} = D_{\mathrm{O}} \frac{\partial^2 C_{\mathrm{O}}(x,t)}{\partial x^2}$$

$$\frac{\partial C_{\mathrm{R}}(x,t)}{\partial t} = D_{\mathrm{R}} \frac{\partial^2 C_{\mathrm{R}}(x,t)}{\partial x^2}$$

Initial conditions:

$$C_{\mathrm{O}}(x,0) = C_{\mathrm{O}}^*,\ C_{\mathrm{R}}(x,0) = C_{\mathrm{R}}^*$$

Boundary conditions:

$$\lim_{x\to\infty} C_{\mathrm{O}}(x,t) = C_{\mathrm{O}}^*,\ \lim_{x\to\infty} C_{\mathrm{R}}(x,t) = C_{\mathrm{R}}^*$$

$$D_{\mathrm{O}} \frac{\partial C_{\mathrm{O}}(0,t)}{\partial x} = -k_0 \left[C_{\mathrm{R}}(0,t) e^{(1-\alpha)\frac{F}{RT}(E-E^0)} - C_{\mathrm{O}}(0,t) e^{-\alpha\frac{F}{RT}(E-E^0)} \right]$$

$$D_{\mathrm{R}} \frac{\partial C_{\mathrm{R}}(0,t)}{\partial x} = k_0 \left[C_{\mathrm{R}}(0,t) e^{(1-\alpha)\frac{F}{RT}(E-E^0)} - C_{\mathrm{O}}(0,t) e^{-\alpha\frac{F}{RT}(E-E^0)} \right]$$

Scheme 2.1: The kinetic-diffusion differential equation system for $\mathrm{O} + \mathrm{e}^- \rightleftharpoons \mathrm{R}$.

2.3.1. Linear Solver for Electrochemical Mechanism

The standard method of solving a set of simultaneous equations with a computer is to cast this set in a matrix notation, that holds the form

$$\mathbf{Ax} = \mathbf{b} \tag{2.35}$$

To find the set of solutions, **x**, we pre-multiply both sides of the equation by $\mathbf{A}^{-1}$, the inverse of **A**:

$$\mathbf{x} = \mathbf{A}^{-1}\mathbf{b} \tag{2.36}$$

Now combining Equation 2.28 and Nernst Equation boundary conditions, the equation set may be written as

$$\begin{pmatrix} 1 & 0 & 0 & 0 & 0 & 0 & 0 & 0 & 0 & 0 \dots \\ \alpha & \beta & \gamma & 0 & 0 & 0 & 0 & 0 & 0 & 0 \dots \\ 0 & \alpha & \beta & \gamma & 0 & 0 & 0 & 0 & 0 & 0 \dots \\ & & \ddots & \ddots & \ddots & & & & & \\ \dots 0 & 0 & \alpha & \beta & \gamma & 0 & 0 & 0 & 0 & \dots \\ \dots 0 & 0 & 0 & \alpha & \beta & \gamma & 0 & 0 & 0 & \dots \\ \dots 0 & 0 & 0 & 0 & \alpha & \beta & \gamma & 0 & 0 & \dots \\ & & & & & \ddots & \ddots & \ddots & & \\ \dots 0 & 0 & 0 & 0 & 0 & 0 & \alpha & \beta & \gamma & 0 \\ \dots 0 & 0 & 0 & 0 & 0 & 0 & 0 & \alpha & \beta & \gamma \\ \dots 0 & 0 & 0 & 0 & 0 & 0 & 0 & 0 & 0 & 1 \end{pmatrix} \begin{pmatrix} C_0^k \\ C_1^k \\ C_2^k \\ \vdots \\ C_{44}^k \\ C_{45}^k \\ C_{46}^k \\ \vdots \\ C_{n-3}^k \\ C_{n-2}^k \\ C_{n-1}^k \end{pmatrix} = \begin{pmatrix} 1/(1+e^{-\theta}) \\ C_1^{k-1} \\ C_2^{k-1} \\ \vdots \\ C_{44}^{k-1} \\ C_{45}^{k-1} \\ C_{46}^{k-1} \\ \vdots \\ C_{n-3}^{k-1} \\ C_{n-2}^{k-1} \\ 1 \end{pmatrix} \tag{2.37}$$

where $\alpha = -D_j\Delta t/(\Delta x)^2$, $\beta = 1 + 2D_j\Delta t/(\Delta x)^2$, $\gamma = -D_j\Delta t/(\Delta x)^2$, and $\theta = F/RT(E - E^0)$. The system of simultaneous equations may be solved by either direct methods such as Gaussian elimination (or by simply calculating the inverse of the coefficient matrix, **A**) or iterative methods such as Jacobi matrix. The details of these direct and indirect linear solvers employed for the solutions of the discretised form of the governing equations of the electrochemical system is given below.

2.3.1.1. Direct Methods

Gaussian elimination[165] is an automated way of solving a large set of simultaneous equations, by subtracting multiples of one equation from another (eliminating) until one equation can be solved, then back-substituting, to find all the other unknowns. If the coefficient matrix is not diagonally dominant, then pivoting (usually by selecting the largest element in a row as the coefficient to divide by, and sometimes by scaling the rows) can be used to improve the accuracy and avoid division by zero. The elimination process is equivalent to a **LU** decomposition since the reduced equations form the upper triangular (**U**) and the multipliers used in the elimination procedure form the unit lower triangular matrix (**L**).

$$\mathbf{Ax} = (\mathbf{LU})\mathbf{x} = \mathbf{L}(\mathbf{U})\mathbf{x} = \mathbf{b} \tag{2.38}$$

The time taken for the **LU** decomposition is proportional to the number or elements in **A,** the square of the number of equations. Definitely, **L** need not be stored, but if the same matrix needs to be operated on multiple right-hand-sides, once **L** and **U** have been computed/stored, only back substitution need be performed for each time.

For a tridiagonal matrix, Gaussian elimination simplifies to a procedure known as the Thomas Algorithm, which may solve the problem in a more efficient manner. Rather than directly calculating the product $\mathbf{A}^{-1}\mathbf{b}$, we use a process called **LU** factorisation, to factor **A** as the product of two other matrices: a lower and an upper triangular matrix, so that $\mathbf{A} = \mathbf{LU}$ shown in Equation 2.38. This process leaves us with the equation $(\mathbf{LU})\mathbf{x} = \mathbf{b}$. The algorithm then consists of two steps. First, we pre-multiply both sides of the equation by $\mathbf{L}^{-1}$,

$$\mathbf{Ux} = \mathbf{L}^{-1}\mathbf{b} \tag{2.39}$$

Then we calculate the product

$$\mathbf{d} = \mathbf{L}^{-1}\mathbf{b} \tag{2.40}$$

The vector d could be calculated by first evaluating the lower diagonal matrix, **L**, inversing it, then post-multiplying the result by **b**. In the second step of the algorithm, we pre-multiply both

sides of Equation 2.39 by $\mathbf{U}^{-1}$,

$$\mathbf{x} = \mathbf{U}^{-1}\mathbf{d} \tag{2.41}$$

Then we calculate the product $\mathbf{U}^{-1}$ to find the vector **x** of unknown C_i^k values.

Here we state some important mechanisms, for example, EC mechanism, EE mechanism and first-order EC' mechanism, corresponding to their governing partial differential equations and boundary conditions, similar to the one given in Scheme 2.1. The simultaneous equations generated from these problems can be solved by linear solvers in a direct way. The numerical resolution of the problem can refer to the E mechanism introduced before.

EC_{irre} mechanism:

Reaction scheme:

$$O + e^- \rightleftharpoons R$$

$$R \xrightarrow{k} Y$$

Governing equation:

$$\frac{\partial C_O(x,t)}{\partial t} = D_O \frac{\partial^2 C_O(x,t)}{\partial x^2}$$

$$\frac{\partial C_R(x,t)}{\partial t} = D_R \frac{\partial^2 C_R(x,t)}{\partial x^2} - kC_R(x,t)$$

$$\frac{\partial C_Y(x,t)}{\partial t} = D_Y \frac{\partial^2 C_Y(x,t)}{\partial x^2} + kC_R(x,t)$$

Initial conditions:

$$C_O(x,0) = C_O^*,\ C_R(x,0) = 0,\ C_Y(x,0) = 0$$

Boundary conditions:

$$\lim_{x\to\infty} C_O(x,t) = C_O^*,\ \lim_{x\to\infty} C_R(x,t) = 0,\ \lim_{x\to\infty} C_Y(x,t) = 0$$

$$D_O \frac{\partial C_O(0,t)}{\partial x} = -k_0 \left[C_R(0,t) e^{(1-\alpha)\frac{F}{RT}(E-E^0)} - C_O(0,t) e^{-\alpha\frac{F}{RT}(E-E^0)} \right]$$

$$D_R \frac{\partial C_R(0,t)}{\partial x} = k_0 \left[C_R(0,t) e^{(1-\alpha)\frac{F}{RT}(E-E^0)} - C_O(0,t) e^{-\alpha\frac{F}{RT}(E-E^0)} \right]$$

$$\frac{\partial C_Y(0,t)}{\partial x} = 0$$

Scheme 2.2: The kinetic-diffusion differential equation system for EC_{irre} mechanism.

EC_{rev} mechanism:

Reaction scheme:

$$O + e^- \rightleftharpoons R$$

$$R \underset{k_{-1}}{\overset{k_1}{\rightleftharpoons}} Y$$

Governing equation:

$$\frac{\partial C_O(x,t)}{\partial t} = D_O \frac{\partial^2 C_O(x,t)}{\partial x^2}$$

$$\frac{\partial C_R(x,t)}{\partial t} = D_R \frac{\partial^2 C_R(x,t)}{\partial x^2} - k_1 C_R(x,t) + k_{-1} C_Y(x,t)$$

$$\frac{\partial C_Y(x,t)}{\partial t} = D_Y \frac{\partial^2 C_Y(x,t)}{\partial x^2} + k_1 C_R(x,t) - k_{-1} C_Y(x,t)$$

Initial conditions:

$$C_O(x,0) = C_O^*,\ C_R(x,0) = 0,\ C_Y(x,0) = 0$$

Boundary conditions:

$$\lim_{x\to\infty} C_O(x,t) = C_O^*,\ \lim_{x\to\infty} C_R(x,t) = 0,\ \lim_{x\to\infty} C_Y(x,t) = 0$$

$$D_O \frac{\partial C_O(0,t)}{\partial x} = -k_0 \left[C_R(0,t) e^{(1-\alpha)\frac{F}{RT}(E-E^0)} - C_O(0,t) e^{-\alpha\frac{F}{RT}(E-E^0)} \right]$$

$$D_R \frac{\partial C_R(0,t)}{\partial x} = k_0 \left[C_R(0,t) e^{(1-\alpha)\frac{F}{RT}(E-E^0)} - C_O(0,t) e^{-\alpha\frac{F}{RT}(E-E^0)} \right]$$

$$\frac{\partial C_Y(0,t)}{\partial x} = 0$$

Scheme 2.3: The kinetic-diffusion differential equation system for EC mechanism.

EE mechanism:

Reaction scheme:

$$\mathrm{O} + \mathrm{e}^- \underset{E_1^0}{\overset{k_0^1}{\rightleftharpoons}} \mathrm{O}'$$

$$\mathrm{O}' + \mathrm{e}^- \underset{E_2^0}{\overset{k_0^2}{\rightleftharpoons}} \mathrm{R}$$

Governing equation:

$$\frac{\partial C_{\mathrm{O}}(x,t)}{\partial t} = D_{\mathrm{O}} \frac{\partial^2 C_{\mathrm{O}}(x,t)}{\partial x^2}$$

$$\frac{\partial C_{\mathrm{O}'}(x,t)}{\partial t} = D_{\mathrm{O}'} \frac{\partial^2 C_{\mathrm{O}'}(x,t)}{\partial x^2}$$

$$\frac{\partial C_{\mathrm{R}}(x,t)}{\partial t} = D_{\mathrm{R}} \frac{\partial^2 C_{\mathrm{R}}(x,t)}{\partial x^2}$$

Initial conditions:

$$C_{\mathrm{O}}(x,0) = C_{\mathrm{O}}^*,\ C_{\mathrm{O}'}(x,0) = 0,\ C_{\mathrm{R}}(x,0) = 0$$

Boundary conditions:

$$\lim_{x\to\infty} C_{\mathrm{O}}(x,t) = C_{\mathrm{O}}^*,\ \lim_{x\to\infty} C_{\mathrm{O}'}(x,t) = 0,\ \lim_{x\to\infty} C_{\mathrm{R}}(x,t) = 0$$

$$D_{\mathrm{O}} \frac{\partial C_{\mathrm{O}}(0,t)}{\partial x} = -k_0^1 \left[C_{\mathrm{O}'}(0,t) e^{(1-\alpha)\frac{F}{RT}\left(E-E_1^0\right)} - C_{\mathrm{O}}(0,t) e^{-\alpha\frac{F}{RT}\left(E-E_1^0\right)} \right]$$

$$D_{\mathrm{O}'} \frac{\partial C_{\mathrm{O}'}(0,t)}{\partial x} = k_0^1 \left[C_{\mathrm{O}'}(0,t) e^{(1-\alpha)\frac{F}{RT}\left(E-E_1^0\right)} - C_{\mathrm{O}}(0,t) e^{-\alpha\frac{F}{RT}\left(E-E_1^0\right)} \right] - k_0^2 \left[C_{\mathrm{R}}(0,t) e^{(1-\alpha)\frac{F}{RT}\left(E-E_2^0\right)} - C_{\mathrm{O}'}(0,t) e^{-\alpha\frac{F}{RT}\left(E-E_2^0\right)} \right]$$

$$D_{\mathrm{R}} \frac{\partial C_{\mathrm{R}}(0,t)}{\partial x} = k_0^2 \left[C_{\mathrm{R}}(0,t) e^{(1-\alpha)\frac{F}{RT}\left(E-E_2^0\right)} - C_{\mathrm{O}'}(0,t) e^{-\alpha\frac{F}{RT}\left(E-E_2^0\right)} \right]$$

Scheme 2.4: The kinetic-diffusion differential equation system for EE mechanism.

First-order EC' mechanism:

Reaction scheme:

$$\mathrm{O} + \mathrm{e}^- \rightleftharpoons \mathrm{R}$$

$$\mathrm{R} + \mathrm{Y} \underset{k_{-1}}{\overset{k_1}{\rightleftharpoons}} \mathrm{O} + \mathrm{Z}$$

Governing equation:

$$\frac{\partial C_\mathrm{O}(x,t)}{\partial t} = D_\mathrm{O}\frac{\partial^2 C_\mathrm{O}(x,t)}{\partial x^2} + k_1 C_\mathrm{R}(x,t) - k_{-1} C_\mathrm{O}(x,t)$$

$$\frac{\partial C_\mathrm{R}(x,t)}{\partial t} = D_\mathrm{R}\frac{\partial^2 C_\mathrm{R}(x,t)}{\partial x^2} - k_1 C_\mathrm{R}(x,t) + k_{-1} C_\mathrm{O}(x,t)$$

Initial conditions:

$$C_\mathrm{O}(x,0) = C_\mathrm{O}^*,\ C_\mathrm{R}(x,0) = 0$$

Boundary conditions:

$$\lim_{x\to\infty} C_\mathrm{O}(x,t) = C_\mathrm{O}^*,\ \lim_{x\to\infty} C_\mathrm{R}(x,t) = 0$$

$$D_\mathrm{O}\frac{\partial C_\mathrm{O}(0,t)}{\partial x} = -k_0\left[C_\mathrm{R}(0,t)e^{(1-\alpha)\frac{F}{RT}(E-E^0)} - C_\mathrm{O}(0,t)e^{-\alpha\frac{F}{RT}(E-E^0)}\right]$$

$$D_\mathrm{R}\frac{\partial C_\mathrm{R}(0,t)}{\partial x} = k_0\left[C_\mathrm{R}(0,t)e^{(1-\alpha)\frac{F}{RT}(E-E^0)} - C_\mathrm{O}(0,t)e^{-\alpha\frac{F}{RT}(E-E^0)}\right]$$

Other conditions:

$$C_\mathrm{X}^*, C_\mathrm{Y}^* \gg C_\mathrm{O}^*, C_\mathrm{R}^*$$

Scheme 2.5: The kinetic-diffusion differential equation system for first-order EC' mechanism.

Although the resolution of the above problem is more complex since (in general) we deal with coupled equation systems and the spatial and temporal grids may need to be refined when fast chemical processes occur, the mathematical problem nevertheless still consists of linear equations.

2.3.1.2. Indirect Methods

In this subsection, we consider cases where the chemical processes coupled to the electron transfer follow second-order chemical kinetics such that the linearity of the equation system is lost, and new mathematical procedures must be employed for the resolution of the corresponding kinetic-diffusion problem. First, the problem of a second-order electrocatalytic mechanism is described in Scheme 2.6,

Reaction scheme:

$$\mathrm{O} + \mathrm{e}^- \rightleftharpoons \mathrm{R}$$

$$\mathrm{R} + \mathrm{Y} \underset{k_{-1}}{\overset{k_1}{\rightleftharpoons}} \mathrm{O} + \mathrm{Z}$$

Governing equation:

$$\frac{\partial C_\mathrm{O}(x,t)}{\partial t} = D_\mathrm{O}\frac{\partial^2 C_\mathrm{O}(x,t)}{\partial x^2} + k_1 C_\mathrm{R}(x,t)C_\mathrm{Y}(x,t) - k_{-1}C_\mathrm{O}(x,t)C_\mathrm{Z}(x,t)$$

$$\frac{\partial C_\mathrm{R}(x,t)}{\partial t} = D_\mathrm{R}\frac{\partial^2 C_\mathrm{R}(x,t)}{\partial x^2} - k_1 C_\mathrm{R}(x,t)C_\mathrm{Y}(x,t) + k_{-1}C_\mathrm{O}(x,t)C_\mathrm{Z}(x,t)$$

$$\frac{\partial C_\mathrm{Y}(x,t)}{\partial t} = D_\mathrm{Y}\frac{\partial^2 C_\mathrm{Y}(x,t)}{\partial x^2} - k_1 C_\mathrm{R}(x,t)C_\mathrm{Y}(x,t) + k_{-1}C_\mathrm{O}(x,t)C_\mathrm{Z}(x,t)$$

$$\frac{\partial C_\mathrm{Z}(x,t)}{\partial t} = D_\mathrm{Z}\frac{\partial^2 C_\mathrm{Z}(x,t)}{\partial x^2} + k_1 C_\mathrm{R}(x,t)C_\mathrm{Y}(x,t) - k_{-1}C_\mathrm{O}(x,t)C_\mathrm{Z}(x,t)$$

Initial conditions:

$$C_\mathrm{O}(x,0) = C_\mathrm{O}^*,\ C_\mathrm{R}(x,0) = 0,\ C_\mathrm{Y}(x,0) = C_\mathrm{Y}^*,\ C_\mathrm{Z}(x,0) = 0$$

Boundary conditions:

$$\lim_{x\to\infty} C_\mathrm{O}(x,t) = C_\mathrm{O}^*,\ \lim_{x\to\infty} C_\mathrm{R}(x,t) = 0,\ \lim_{x\to\infty} C_\mathrm{Y}(x,t) = C_\mathrm{Y}^*,\ \lim_{x\to\infty} C_\mathrm{Z}(x,t) = 0$$

$$D_\mathrm{O}\frac{\partial C_\mathrm{O}(0,t)}{\partial x} = -k_0\left[C_\mathrm{R}(0,t)e^{(1-\alpha)\frac{F}{RT}(E-E^0)} - C_\mathrm{O}(0,t)e^{-\alpha\frac{F}{RT}(E-E^0)}\right]$$

$$D_\mathrm{R}\frac{\partial C_\mathrm{R}(0,t)}{\partial x} = k_0\left[C_\mathrm{R}(0,t)e^{(1-\alpha)\frac{F}{RT}(E-E^0)} - C_\mathrm{O}(0,t)e^{-\alpha\frac{F}{RT}(E-E^0)}\right]$$

$$\frac{\partial C_\mathrm{Y}(0,t)}{\partial x} = \frac{\partial C_z(0,t)}{\partial x} = 0$$

Scheme 2.6: The kinetic-diffusion differential equation system for second-order EC' mechanism.

where the chemical rate constants k_1 and k_{-1} are now second-order in unit, $\mathrm{cm^3\ s^{-1}\ mol^{-1}}$.

As anticipated, the governing equations of the Scheme 2.6 are nonlinear since they contain the product of two independent variables. A simple alternative is an iterative scheme in which the unknown concentration vector, **x**, can be solved from an initial guess. Given an approximation of **x**, the method generates an improved approximation **x**′. Iterations continue until the change between iterations, or norm of the residual is lower than a threshold value.

Jacobi perhaps is the most intuitive iterative scheme to rearrange each linear equation for $\mathbf{x}_i$ thus creating an expression for each element of the solution vector. For our 3-point implicit finite difference equation (in Equation 2.27) we would get:

$$\left[1+\frac{2D_{\mathrm{j}}\Delta t}{(\Delta x)^2}\right]C_i^k = C_i^{k-1} + \frac{D_{\mathrm{j}}\Delta t}{(\Delta x)^2}\left(C_{i-1}^k + C_{i+1}^k\right) \tag{2.42}$$

These equations can be used to generate the new value of each element from the old vector,

$$C'^k_i = \frac{C_i^{k-1} + \frac{D_{\mathrm{j}}\Delta t}{(\Delta x)^2}\left(C_{i-1}^k + C_{i+1}^k\right)}{\left[1+\frac{2D_{\mathrm{j}}\Delta t}{(\Delta x)^2}\right]} \tag{2.43}$$

When the norm of the residual is lower than a threshold value after starting the iteration scheme, C_i^k is treated as equivalent to C'^k_i.

Another way of thinking about iterative methods is to split the unwieldy system of PDEs into several simpler subproblems which holds physical representation of various underlying phenomena, like (diffusion, electrode reaction, coupled chemical reaction, etc.). The subproblems are discretised in time by the backward Euler method demonstrated in Figure 2.7 and treated respectively by specialised numerical algorithms.

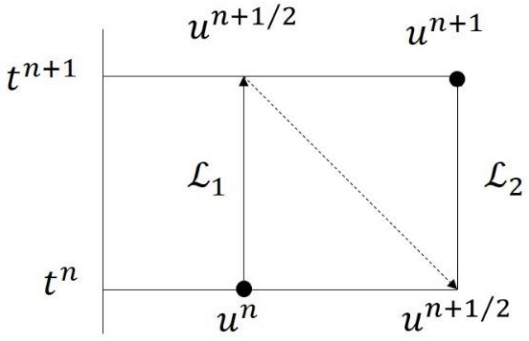

Figure 2.7: The schematic diagram of the backward Euler method.

2.3.2. Nonlinear Solver for Electrochemical Mechanism

When introducing kinetics, it is notable that second-order electrocatalytic reactions in Scheme 2.6 make the finite difference equation nonlinear and therefore the methods for the solution of the system of simultaneous linear equations outlined above cannot be applied directly. They can be employed after applying a global linearization method. This converts the nonlinear equations into an approximate linear form which may then be solved using a standard (linear) solver. This process is iterated until the 'true' nonlinear solution is reached.

A more general and rigorous approach is the determination of the concentrations by employing a multidimensional root-finding algorithm. Indeed, the unknown concentrations can be viewed as the roots of a set of nonlinear simultaneous equations to be zeroed, which are given by the discretised differential equations and boundary conditions. One of the simplest alternatives for multidimensional root finding is the Newton-Raphson method[166],

$$C_i^k = C_i^{k-1} - \frac{f\left(C_i^{k-1}\right)}{f'\left(C_i^{k-1}\right)} \tag{2.44}$$

where $f\left(C_i^{k-1}\right)$ is the set of finite difference equations with respect to the concentration of each species. Equation 2.44 then can be converted as a matrix form,

$$\boldsymbol{C}_i^k = \boldsymbol{C}_i^{k-1} - \frac{\boldsymbol{F}\left(C_i^{k-1}\right)}{\boldsymbol{J}\left(C_i^{k-1}\right)} \tag{2.45}$$

where $\boldsymbol{J}$ is the Jacobian $N \times N$ matrix of partial derivatives,

$$\boldsymbol{J} = \begin{pmatrix} \frac{\partial f(x_0)}{\partial x_0} & \cdots & \frac{\partial f(x_0)}{\partial x_{N-1}} \\ \vdots & \ddots & \vdots \\ \frac{\partial f(x_{N-1})}{\partial x_0} & \cdots & \frac{\partial f(x_{N-1})}{\partial x_{N-1}} \end{pmatrix} \tag{2.46}$$

The *Newton-Raphson* method is conveniently expressed as

$$\boldsymbol{J}\left(C_i^{k-1}\right)\boldsymbol{C}_i^k = \boldsymbol{J}\left(C_i^{k-1}\right)\boldsymbol{C}_i^{k-1} - \boldsymbol{F}\left(C_i^{k-1}\right) \tag{2.47}$$

and give a new linear system with the Jacobian as the coefficient matrix. This may be solved by one of the standard linear solvers described above.

Some other root-finding algorithms are briefly described here. The bisection method in mathematics is a simple and robust root-finding method that repeatedly bisects an interval and then selects a subinterval in which a root must lie for further processing. The method is sometimes called the interval halving method or the binary search method. However, it is relatively slow, which often leads to a rough approximation to a solution which is then used as a starting point for more rapidly converging methods. The Regula Falsi method[167] is one of the bracketing methods for finding roots of equations, which greatly increase the searching rate in the basis of bisection method. Regula Falsi assumes that a nonlinear equation f has two independent variables x and y, which guarantees the finding root z is located in the range from x to y. This definition promises a reversal sign between $f(x)$ and $f(y)$. The iteration starts from the calculation of z, that gives

$$z = \frac{xf(y) - yf(x)}{f(y) - f(x)} \tag{2.48}$$

If $f(x) \cdot f(z) > 0$, the root is located between z and y, and the new x is updated by the value of z; if $f(x) \cdot f(z) < 0$, the root is located between x and z, and the new y is updated by the value of z. The iteration won't stop until $f(x) \cdot f(z) \approx 0$ (a pre-designed threshold value), or the computational iteration approaching to the maximum iteration steps.

2.4. Performance and Convergence

A numerical method is said to be convergent if the numerical solution approaches the exact solution as the space and time intervals, Δx and Δt, approach zero. If the simulation is convergent, the accuracy will increase as these intervals shrink, but so too will the runtime and memory requirements. Conversely, if the size of the intervals is too large, the simulation may produce wildly inaccurate results. It is therefore the job of the researcher to determine values of Δx and Δt that give an acceptable compromise between accuracy and runtime. A convergence study can be found in literature[37].

It may often be the case that there is no known analytical solution that describes a property (such as peak height) of the simulated voltammetry. Nevertheless, it is still possible, and indeed sensible, to perform a convergence study. Note that without a known analytical solution, the correctness of a simulation cannot be tested through a convergence study; the researcher may have made a mistake and the simulation may be modelling something other than what was intended. The study simply verifies that the numerical model tends towards some exact solution as the size of the spatial and temporal increments tends to zero. It is usually simpler to test the effect of each variable in isolation, and without a known solution for comparison, we can still comment on whether or not the simulation is converged after checking the convergence.

A program's runtime may be analysed in terms of the size of its inputs. For a general example program, the preamble section (prior to the main simulation loop) contains a number of variable definitions, simple calculations, the initialisation of a stream for output, and a loop that calculates the values of the modified coefficients. The time taken to perform the variable definitions, calculations and stream initialisation is effectively constant for a given machine; it is dependent only on the specifics of the computer hardware and the compiler and is independent of the program's inputs. The loop will take a time proportional to the size of the spatial grid (which is the number of loop iterations), plus some small constant time to initialise the loop variable. The total runtime of the simulation is mainly decided by the simulation of a loop that iterates m times.

2.5. Conclusion and Outlook

This chapter described the basic numerical approach corresponding to the solution of diffusion equation coupled with the electrochemical Butler-Volmer kinetics. Important aspects of finite difference methods, such as unequally expanding spatial grads, explicit/implicit time derivatives, linear and nonlinear solvers were discussed. Different electrochemical systems considering only planar electrode are interpreted into mathematic languages, and the resolution strategies are applied to these problems. Finally, 2nd order homogeneous kinetics case is considered. Since the PDEs are highly nonlinear, the Newton-Raphson and other root-finding methods are described to solve the problem.

In Chapter 3, the cyclic voltammograms obtained from the numerical simulations will be discussed in detail to investigate the E, EC, EE, ECE and electrocatalytic mechanisms. A new numerical approach which solves the complex nonlinear nature of the electrochemical systems by splitting them into individual processes and performing sequential calculations will be illustrated. A comprehensive investigation begins from the construction of the scheme to the validation of the theoretical electrochemical reactions by employing an extended version of the Butler-Volmer formulation.

Chapter 3

3. A Novel High-Order, Operator-Splitting, Fully Implicit Finite Difference Methodology for Investigation of an Electrochemical Catalytic Mechanism

Numerical modelling of electrochemical experiments[168-170] is vital for the understanding of many critical technologies, such as fuel cells, electrochemical sensors and batteries. As noted in chapters 1 and 2 when investigating electrode reactions, we must not only consider the electron transfer characteristics but also several physical phenomena, for example, mass transport involving diffusion and convection, coupled chemical kinetics, etc. Some problems may be reduced to the basic mechanisms at the planar electrode, but most experimental cases show very complex mechanisms involving different geometries of electrodes.

A critical problem of the simulation work in this field is that the classic Butler-Volmer model (or sometimes Marcus-Hush model[171]) describes a nonlinear relationship between current response and applied potential. When the system involves various coupled processes like current flow in hydrodynamic electrodes, second-order homogeneous chemical kinetics, etc., the overall electrode reaction certainly leads to a stiff nonlinear problem. A traditional treatment to the nonlinear problem generated in electrochemical systems is to establish a set of discretised differential equations and boundary conditions, then solve them by either linearized simultaneous equation sets, or a root-finding algorithm such as Newton-Raphson method. The linearization requires a very small timestep to converge, and the Newton-Raphson method also has convergence problems when the initial guess is not good, that is, it is not near the root value.

In the past decade, there has been major advances in the development of numerical tools focused on the solutions of highly nonlinear problems in both science and industry[172-174]. One approach, called operator-splitting, is proved in several excellent examples including combustion[175,176] and

non-Newtonian fluid dynamics[177], where there are multi-physics phenomena occurring, thereby holding the system high nonlinear. The full mechanism is decomposed separately into simpler sub-problems, e.g., transport, chemical reaction and combustion. These locally accurate models, which are divided from a completely time-independent system, may require specialised numerical treatments, respectively. Recently, Schwer, Lu and co-workers have proposed a consistent-splitting scheme to emulating stiff steady-state reacting flow-fields with adaptive chemistry[178]. This literature implies that the operator-splitting scheme can solve a nonlinear problem in a diffusion-controlled system coupled with chemical reactions.

To the best of our knowledge, there is little open literature on operator-splitting methods employed in electrochemical systems which also possess several physical phenomena similar with those in combustion, fluid dynamics and even in the mentioned diffusion-controlled chemical reactions. This may offer a preferred choice to employ the operator-splitting method to deal with the numerical problems in electrochemistry. Therefore, having understood the applicability of operator-splitting methods in solving nonlinear multi-physics systems, we propose a novel numerical technique based on the concepts of operator-splitting method to solve stiff nonlinear electrochemical problems in this chapter.

The following work presents a theoretical case study in which we propose a new discretisation scheme for an arbitrary number of consecutive nonlinear operators. The following work is organised to describe the proposed operator-splitting method first. A validation will be given for non-catalytic electrochemical systems (EC, EE and ECE mechanisms) between a classic numerical technique (two-point temporal discretisation) and the developed high-order operator splitting method. The third section describes the cyclic voltammograms of more complex electrocatalytic mechanisms. We reformulate the electrocatalytic (EC') mechanism as a sequence of steady problems and discuss its accuracy, stability and convergence. A unique cyclic voltammetric response for hydrogenase is then examined and the discussion of implementation follows the measurement.

3.1. Operator-Splitting Scheme

We first recall the splitting method which was introduced in Subsection 2.3.1 as an iteration approach to the solution of a nonlinear problem raised by the second-order EC' mechanism. The strategy of splitting is to decompose unwieldy (systems of) PDEs into simpler sub-problems. To solve these separated problems, it is wise to employ specialised numerical algorithms individually. Once the sub-problems are all resolved, the overall problem is solved. We first consider a partial differential equation (PDE) with different operators $\mathcal{L}$ having the following form

$$\partial_t u = -\mathcal{L}u$$
$$\mathcal{L} = \sum_{s=1}^{S} \mathcal{L}_s \tag{3.1}$$

where $\mathcal{L}_s$ represents physical phenomena (diffusion, electrode reaction, chemical kinetics, etc.). A traditional first-order operator-splitting scheme is demonstrated in Figure 3.1, which discretises the problem in time by backward Euler method ($u^n \rightarrow u^{n+1/2} \rightarrow u^{n+1}$). The theory for constructing second- or higher-order accurate splitting algorithms can be founded in literature[179].

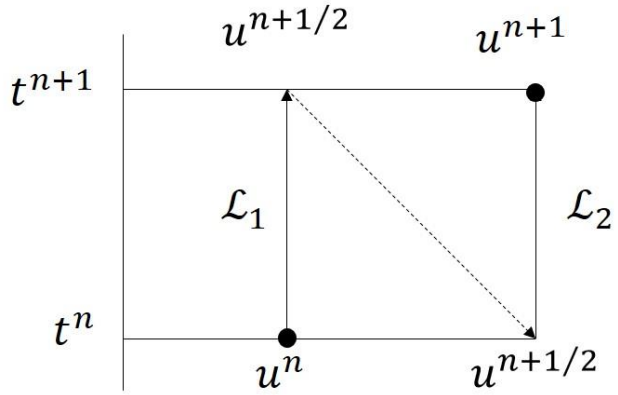

Figure 3.1: The scheme of first-order operator splitting method derived by backward Euler method.

For a steady state of diffusion-only electrode reaction at planar electrode, the Equation 3.1 can be treated as

$$0 = -\mathcal{L}_1(u) + \mathcal{L}_2(u) \tag{3.2}$$

Where the independent variable u might be considered as the concentration of species in solution. The proposed operator-splitting scheme reads

$$\begin{aligned} \frac{\phi^{n+1}}{\tau} &= -\mathcal{L}_1(u^n + \phi^{n+1} + \psi^n) \\ \frac{\psi^{n+1}}{\tau} &= -\mathcal{L}_2(u^n + \phi^{n+1} + \psi^{n+1}) \\ u^{n+1} &= u^n + \phi^{n+1} + \psi^{n+1} \end{aligned} \tag{3.3}$$

The fully-converged state can be easily verified, in which the splitting errors satisfy $\phi = -\psi$ and the summation of the first two equations in Equation 3.3 recovers Equation 3.2.

We now consider a diffusion-only electrode reaction coupled with homogeneous chemical kinetics model, in order to illustrate the convergence of this method. These two operators here are represented by diffusion phenomena and chemical reaction respectively

$$0 = D\frac{\partial^2 C}{\partial x^2} - bC \tag{3.4}$$

Substituting $C = u^k e^{-ikt}$ into Equation 3.4 and separating the diffusion and chemical step terms, one obtains Equation 3.3 for each wave number k, where $\mathcal{L}_1(k) = Dk^2$, $\mathcal{L}_2(k) = b$. Hereafter we omit the wave number for the sake of simplicity and Equation 3.3 can be re-written as:

$$\begin{aligned} \phi^{n+1} &= -\frac{\mathcal{L}_1\tau}{1+\mathcal{L}_1\tau}(u^n + \psi^n) \\ \psi^{n+1} &= -\frac{\mathcal{L}_2\tau}{(1+\mathcal{L}_1\tau)(1+\mathcal{L}_2\tau)}(u^n - \mathcal{L}_1\tau\psi^n) \\ (u^{n+1} - \psi^{n+1}) &= u^n - \frac{\mathcal{L}_1\tau}{1+\mathcal{L}_1\tau}(u^n - \psi^n) \end{aligned} \tag{3.5}$$

Introducing a new variable $\varphi = u - \psi$, the last two equations yield after some algebra,

$$\begin{aligned} \psi^{n+1} &= -\frac{\mathcal{L}_2\tau}{1+\mathcal{L}_2\tau}\left(\frac{1-\mathcal{L}_1\tau}{1+\mathcal{L}_1\tau}\psi^n + \frac{1}{1+\mathcal{L}_1\tau}\varphi^n\right) \\ \varphi^{n+1} &= \frac{1-\mathcal{L}_1\tau}{1+\mathcal{L}_1\tau}\psi^n + \frac{1}{1+\mathcal{L}_1\tau}\varphi^n \end{aligned} \tag{3.6}$$

Eigenvalues of the above system can be calculated

$$\lambda_1 = 0,\ \lambda_2 = \frac{1 + (\mathcal{L}_1\tau)(\mathcal{L}_2\tau)}{(1 + \mathcal{L}_1\tau)(1 + \mathcal{L}_2\tau)} \tag{3.7}$$

When $\lambda_2 < 1$, for any τ satisfying $0 < \tau < \infty$, it attains its minimum value at $\tau_* = (\mathcal{L}_1\mathcal{L}_2)^{-1/2}$, where

$$\lambda_{2,min} = \frac{2\sqrt{\mathcal{L}_1\mathcal{L}_2}}{\left(\sqrt{\mathcal{L}_1} + \sqrt{\mathcal{L}_2}\right)^2} \tag{3.8}$$

Equation 3.7 holds for any two operators with negative eigenvalues, that is, stability of the entire method follows from the stability of the sub-steps.

Recall that $\mathcal{L}_1(k)$ is a function of the wave number. Assume that at some scales k_0^2 diffusion is of the same order as reaction, for example, $k_0^2 D \approx b$. Therefor, $\tau_* = (k_0^2 D\mathcal{L}_2)^{-1/2} \approx b^{-1}$, what ensures that $\lambda_2(k_0) \approx 1/2$. For other wavenumbers, Equation 3.7 reads,

$$\lambda_2 \approx \frac{1 + b^{-1}k^2 D}{(1 + b^{-1}k^2 D)(1 + 1)} = \frac{1}{2} \tag{3.9}$$

That is, the optimum choice of τ for the main harmonics ensures the same convergence rate for other harmonics.

We now move our focus to the implementation of operator-splitting method on an electrochemical system. E mechanism is sampled to show how to build an operator-splitting model. The mathematic scheme for is recalled from last chapter,

Reaction scheme:

$$\mathrm{O} + \mathrm{e}^- \underset{k_\mathrm{b}}{\overset{k_\mathrm{f}}{\rightleftharpoons}} \mathrm{R}$$

Governing equation:

$$\frac{\partial C_\mathrm{O}(x,t)}{\partial t} = D_\mathrm{O}\frac{\partial^2 C_\mathrm{O}(x,t)}{\partial x^2}$$

$$\frac{\partial C_\mathrm{R}(x,t)}{\partial t} = D_\mathrm{R}\frac{\partial^2 C_\mathrm{R}(x,t)}{\partial x^2}$$

Initial conditions:

$$C_\mathrm{O}(x,0) = C_\mathrm{O}^*,\ C_\mathrm{R}(x,0) = C_\mathrm{R}^*$$

Boundary conditions:

$$\lim_{x\to\infty} C_{\mathrm{O}}(x,t) = C_{\mathrm{O}}^{*},\ \lim_{x\to\infty} C_{\mathrm{R}}(x,t) = C_{\mathrm{R}}^{*}$$

$$D_{\mathrm{O}}\frac{\partial C_{\mathrm{O}}(0,t)}{\partial x} = -k_0\left[C_{\mathrm{R}}(0,t)e^{(1-\alpha)\frac{F}{RT}(E-E^0)} - C_{\mathrm{O}}(0,t)e^{-\alpha\frac{F}{RT}(E-E^0)}\right]$$

$$D_{\mathrm{R}}\frac{\partial C_{\mathrm{R}}(0,t)}{\partial x} = k_0\left[C_{\mathrm{R}}(0,t)e^{(1-\alpha)\frac{F}{RT}(E-E^0)} - C_{\mathrm{O}}(0,t)e^{-\alpha\frac{F}{RT}(E-E^0)}\right]$$

Scheme 3.1: The kinetic-diffusion differential equation system for $\mathrm{O} + \mathrm{e}^{-} \rightleftharpoons \mathrm{R}$.

Here BV equations are revised by considering the uncompensated resistance R_{u} because of the measurement of nonlinearity for the operator-splitting model.

$$\begin{aligned} k_{\mathrm{f}} &= k_0 e^{-\alpha\frac{F}{RT}(E-E^0-iR_{\mathrm{u}})} \\ k_{\mathrm{b}} &= k_0 e^{(1-\alpha)\frac{F}{RT}(E-E^0-iR_{\mathrm{u}})} \end{aligned} \tag{3.10}$$

which leads to a production of capacitive current i_{c}, and the total current consists capacitive current and faradaic current

$$i = i_{\mathrm{c}} + i_{\mathrm{f}} \tag{3.11}$$

The capacitive current can be calculated by

$$i_{\mathrm{c}} = C_{\mathrm{dl}}\frac{\mathrm{d}E}{\mathrm{d}t} \tag{3.12}$$

and the faradic current is obtained from

$$i_{\mathrm{f}} = D_{\mathrm{O}}\frac{\partial C_{\mathrm{O}}(0,t)}{\partial x} \tag{3.13}$$

Equation 3.10 shows that the problem is stiff because of the high value of k_{f} and k_{b}, and highly nonlinear, because the derivative $\frac{\partial C_{\mathrm{O}}(0,t)}{\partial x}$ appears in the exponent.

It was proposed in Section 2.2 to approximate the time derivative in governing equations in Scheme 3.1 by using a backward multilevel finite difference scheme in Section 2.3, thus at k^{th} time level, the seven points scheme reads,

$$\begin{aligned} \frac{\partial C_i^k}{\partial t} &\approx \frac{a_0 C_i^k + a_1 C_i^{k-1} + a_2 C_i^{k-2} + a_3 C_i^{k-3} + a_4 C_i^{k-4} + a_5 C_i^{k-5} + a_6 C_i^{k-6}}{\Delta t} \\ &= \frac{147C_i^k - 360C_i^{k-1} + 450C_i^{k-2} - 400C_i^{k-3} + 225C_i^{k-4} - 72C_i^{k-5} + 10C_i^{k-6}}{60\Delta t} \end{aligned} \tag{3.14}$$

Substitution of Equation 3.14 into Fick's second law yields the following set of steady equations at the k^{th} time level for both species O and R,

$$\left(a_0 - D\frac{\partial^2}{\partial x^2}\right)C_i^k = -\sum_{m=1}^{6} a_k C_i^{k-m} \tag{3.15}$$

Equation 3.15 are linear, while the reactive boundary conditions (Equation 3.10) are not; it is natural to split the problem into the transport and electron transfer reaction. The operator-splitting method allowing for solution of Equations 3.15 and 3.10 is described below.

Repeating the argument from Equation 3.3, the transport part for species O and R are given as,

$$\frac{\delta_{0/i}}{\tau}\phi_i^{n+1} = -\left(a_0 - D\frac{\partial^2}{\partial x^2}\right)\left(C_i^k + \phi_i^{n+1} + \psi_i^n\right) - \sum_{m=1}^{6} a_k C_i^{k-m} \tag{3.16}$$

Equation 3.16 can be rearranged as

$$\left(\frac{\delta_{0/i}}{\tau} + a_0 - D\frac{\partial^2}{\partial x^2}\right)\phi_i^{n+1} = -\left(a_0 - D\frac{\partial^2}{\partial x^2}\right)\left(C_i^k + \psi_i^n\right) - \sum_{m=1}^{6} a_k C_i^{k-m} \tag{3.17}$$

The set of equations ϕ_i^{n+1} for O and R in Equation 3.15 is straightforwardly solved by a finite-volumes method on a uniform spatial grid ($\Delta x = x_{i+1} - x_i$) under diffusion layer. The sub-model is now a linear tridiagonal problem that can be easily solved by the Thomas algorithm. The nodes are positioned in the centres of the control volumes that hold Δx as the size of each volume, except the 0^{th} one at the electrode surface, only half-size volume with $\frac{1}{2}\Delta x$ (because the first node is located in electrode). The Kronecker's delta $\delta_{0/i}$ here employed is to suggest the pseudo-time derivative term is active only in the 0^{th} cell resulted from following electron transfer only in the electrode surface. Now, the diffusion sub-problem is over.

The next stage is electron-transfer step, but only the alteration in 0^{th} volume has to be solved. The operator now built for species O is given

$$\frac{\Delta x}{2\tau}\psi_{[\mathrm{O}],i}^{n+1} = -k_{\mathrm{f}}\left(C_{[\mathrm{O}],i}^k + \phi_{[\mathrm{O}],i}^{n+1} + \psi_{[\mathrm{O}],i}^{n+1}\right) + k_{\mathrm{b}}\left(C_{[\mathrm{R}],i}^k + \phi_{[\mathrm{R}],i}^{n+1} + \psi_{[\mathrm{R}],i}^{n+1}\right) \tag{3.18}$$

and for species R

$$\frac{\Delta x}{2\tau}\psi_{[\mathrm{R}],i}^{n+1} = k_{\mathrm{f}}\left(C_{[\mathrm{O}],i}^{k} + \phi_{[\mathrm{O}],i}^{n+1} + \psi_{[\mathrm{O}],i}^{n+1}\right) - k_{\mathrm{b}}\left(C_{[\mathrm{R}],i}^{k} + \phi_{[\mathrm{R}],i}^{n+1} + \psi_{[\mathrm{R}],i}^{n+1}\right) \tag{3.19}$$

and Equations 3.18 and 3.19 can be rearranged

$$\psi_{[\mathrm{O}],i}^{n+1} = -\psi_{[\mathrm{R}],i}^{n+1} = -\frac{k_{\mathrm{f}}\left(C_{[\mathrm{O}],i}^{k} + \phi_{[\mathrm{O}],i}^{n+1}\right) - k_{\mathrm{b}}\left(C_{[\mathrm{R}],i}^{k} + \phi_{[\mathrm{R}],i}^{n+1}\right)}{\frac{\Delta x}{2\tau} + k_{\mathrm{f}} + k_{\mathrm{b}}} \tag{3.20}$$

where k_{f} and k_{b} are the forward and backward electron transfer rate, respectively, which can be obtained from BV equations

$$\begin{aligned} k_{\mathrm{f}} &= k_0 e^{-\alpha\frac{F}{RT}\left(E - E^0 - iR_{\mathrm{u}}\right)} \\ k_{\mathrm{b}} &= k_0 e^{(1-\alpha)\frac{F}{RT}\left(E - E^0 - iR_{\mathrm{u}}\right)} \end{aligned} \tag{3.21}$$

Now the current response now can be calculated as

$$\begin{aligned} \frac{i}{FA} &= \frac{\Delta x}{2\tau}\psi_{[\mathrm{O}],i}^{n+1} = -\frac{\Delta x}{2\tau}\psi_{[\mathrm{R}],i}^{n+1} \\ &= -k_{\mathrm{f}}\left(C_{[\mathrm{O}],i}^{k} + \phi_{[\mathrm{O}],i}^{n+1} + \psi_{[\mathrm{O}],i}^{n+1}\right) + k_{\mathrm{b}}\left(C_{[\mathrm{R}],i}^{k} + \phi_{[\mathrm{R}],i}^{n+1} + \psi_{[\mathrm{R}],i}^{n+1}\right) \end{aligned} \tag{3.22}$$

Substitution of Equation 3.21 into the Equation 3.22, the current behaviour equation rewrites

$$\begin{aligned} \frac{i}{FA} &= -k_0 e^{-\alpha\frac{F}{RT}\left(E - E^0 - iR_{\mathrm{u}}\right)}\left(C_{[\mathrm{O}],i}^{k} + \phi_{[\mathrm{O}],i}^{n+1} + \psi_{[\mathrm{O}],i}^{n+1}\right) \\ &+ k_0 e^{(1-\alpha)\frac{F}{RT}\left(E - E^0 - iR_{\mathrm{u}}\right)}\left(C_{[\mathrm{R}],i}^{k} + \phi_{[\mathrm{R}],i}^{n+1} + \psi_{[\mathrm{R}],i}^{n+1}\right) \end{aligned} \tag{3.23}$$

Equation 3.23 is a stiff nonlinear equation when R_{u} is not zero. But Equation 3.22 implies that the problem can be reduced to a univariate nonlinear equation due to $i_{[\mathrm{O}]} = -i_{[\mathrm{R}]}$ all the time at the 0^{th} volume. The current (or current density) can be bracketed by

$$\frac{\Delta x}{2\tau}\psi_{[\mathrm{O}],i}^{n+1} \leq \frac{i}{FA} \leq \frac{\Delta x}{2\tau}\psi_{[\mathrm{R}],i}^{n+1} \tag{3.24}$$

Equation 3.24 is suggested to be solved by a Bisection method, but better by Regula Falsi method, both introduced in Chapter 2. Once the converged value of current is obtained, it is used to update the concentration field at level k and the new time point is advanced.

As the practical electrochemical system always involves a few preceding steps or is following other reactions, for example, EE, ECE or electrocatalytic mechanism, the approach is not limited

to a two-operator splitting. In the following sections, a series of validations for different mechanism is presented from non-catalytic system to very complex hydrogenase model. The results are obtained by the revised model for each specific mechanism on the basis of split E mechanism detailed in this section.

3.2. Non-Catalytic Electrochemical Systems

Non-catalytic electrochemical systems generally hold examples including but not limited to E, EE, EC, ECE mechanism. One feature of these systems is that the governing partial differential equations can be transformed into a linear set of simultaneous equations and can easily find a solution by linear solvers. Although, very limited analytical solutions can be obtained in these cases, the widely used numerical techniques based on a two-point (lower-order) temporal discretisation fully implicit finite difference method has been proven to be rigorous and stable. Therefore, it is necessary to compare any new techniques developed for electrochemical system to the classic approach, and to validate the cyclic voltammogram as a basic but very reliable reference.

3.2.1. Single Electron Transfer

The first test case is the simulation of simple but classical voltammetry, holding single electron transfer under fully reversible electrochemical kinetics (very large k_0).

$$\mathrm{O} + \mathrm{e}^- \underset{E^0}{\overset{k_0}{\rightleftharpoons}} \mathrm{R}$$

This scheme gives the governing equation and Figure 3.2 shows the cyclic voltammograms for $\alpha = 0.5$, $E^0 = 0$ V and $D_\mathrm{O} = D_\mathrm{R} = 1 \times 10^{-5}$ cm^2 s^{-1}. For convenience, the output potential and current are reduced to a set of dimensionless parameters as summarised in Nomenclature, which are employed throughout the rest of this chapter.

It is clear that the experiential validated model shows a very good agreement to the analytical values. Furthermore, since the current is normalised, the result also confirms that the dimensional peak current is proportional to the square root of the scan rate[24].

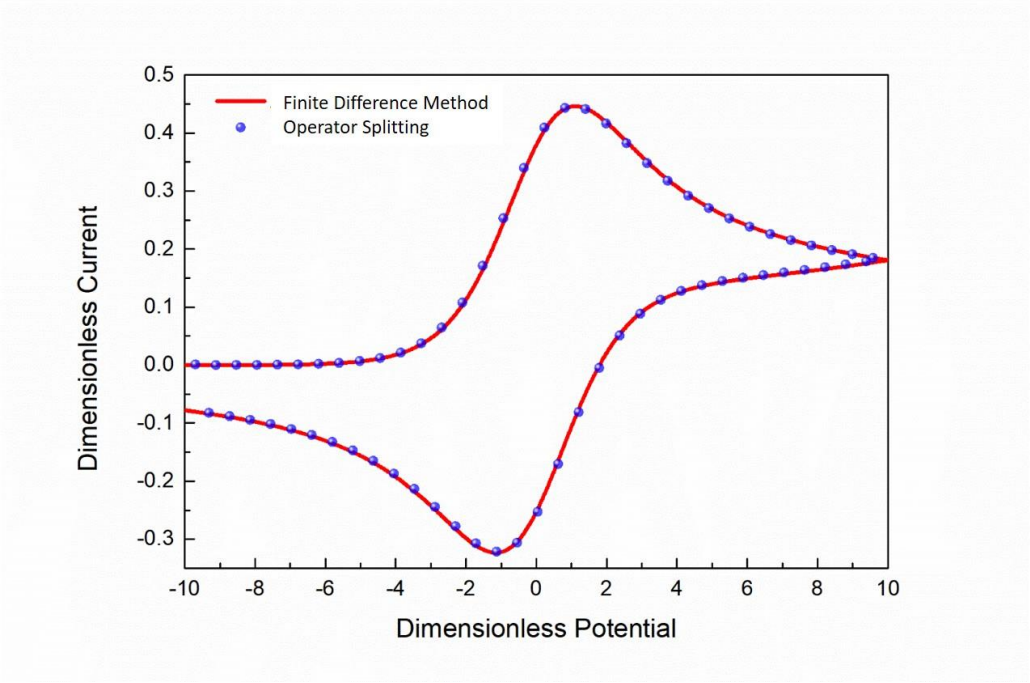

Figure 3.2: Validation of the simulated cyclic voltammogram by operator-splitting method for one-electron transfer step at $k_0 = 1$ cm s^{-1}. The red solid lines (−) represent the simulation results that are generated by typical finite difference method and the blue balls (o) represents the model predictions by operator-splitting method.

3.2.2. EC Reaction

We next consider a little complex EC mechanism, in which an irreversible homogeneous chemical reaction follows the electron transfer given in Scheme 3.2. The kinetic constant for electrode reaction is still swift (very large k_0) in order to show the influence of C step.

$$\mathrm{O} + \mathrm{e}^- \underset{E^0}{\overset{k_0}{\rightleftharpoons}} \mathrm{R}$$ $$\mathrm{R} \xrightarrow{k} \mathrm{Y}$$
Scheme 3.2: EC mechanism including an electrode reaction followed by an irreversible chemical step.

As it follows from the description of the algorithm, it is not limited to a two-operator splitting, nor to boundary reactions. In the EC mechanism, an electrogenerated species R (the "mediator") produces some other solution species Y (the "product"). The general governing equations for the reacting species

$$\begin{aligned} \frac{\partial C_{\mathrm{O}}(x,t)}{\partial t} &= D_{\mathrm{O}} \frac{\partial^2 C_{\mathrm{O}}(x,t)}{\partial x^2} \\ \frac{\partial C_{\mathrm{R}}(x,t)}{\partial t} &= D_{\mathrm{R}} \frac{\partial^2 C_{\mathrm{R}}(x,t)}{\partial x^2} - kC_{\mathrm{R}}(x,t) \\ \frac{\partial C_{\mathrm{Y}}(x,t)}{\partial t} &= D_{\mathrm{Y}} \frac{\partial^2 C_{\mathrm{Y}}(x,t)}{\partial x^2} + kC_{\mathrm{Y}}(x,t) \end{aligned} \tag{3.25}$$

with additional initial and boundary conditions for Y,

$$C_{\mathrm{Y}}(x,0) = 0,\ \lim_{x\to\infty} C_{\mathrm{Y}}(x,t) = 0,\ \frac{\partial C_{\mathrm{Y}}(0,t)}{\partial x} = 0 \tag{3.26}$$

In this case, there is an extra operator corresponding to the chemical kinetics. The splitting error equations for each species O, R and Y under this operator are respectively,

$$\begin{aligned} \varphi_{[\mathrm{O}],i}^{n+1} &= 0 \\ \frac{\varphi_{[\mathrm{R}],i}^{n+1}}{\tau} &= -k\left(C_{[\mathrm{R}],i}^{k} + \varphi_{[\mathrm{R}],i}^{n+1}\right) \\ \frac{\varphi_{[\mathrm{Y}],i}^{n+1}}{\tau} &= k\left(C_{[\mathrm{R}],i}^{k} + \varphi_{[\mathrm{R}],i}^{n+1}\right) \end{aligned} \tag{3.27}$$

The second and third equations for R and Y in Equation 3.27 are still linear, which can be given a simple expression,

$$\varphi_{[\mathrm{R}],i}^{n+1} = -\varphi_{[\mathrm{Y}],i}^{n+1} = \frac{-k\tau C_{[\mathrm{R}],i}^{k}}{1+k\tau} \tag{3.28}$$

Thus, under presence of chemical reaction, there are three operators to be considered: the pure diffusion process (Equation 3.15), the electron transfer (Equations 3.18 and 3.19) and the coupled homogeneous chemical kinetics (Equation 3.27). The splitting order can start from mass transport to homogenous reaction, and finally reach to electrode reaction. Once convergence is achieved, the order of splitting won't affect the result.

For EC mechanism, there is no access to the analytical solution. An alternative approximation of dimensionless i-E curve developed by two-point time evolution derivative method is taken as a reference result with the same set of parameters.

The effect of the chemical reaction on the cyclic voltammograms of EC mechanism at a planar electrode is demonstrated in Figure 3.3. Both two-point time evolution derivative approximation and operator splitting method illustrate that the backward peak current gradually decreases and fully disappears from a slow chemical reaction in 3.3(A), (B) and (C) to a fast chemical conversion in 3.3(D), (E) and (F). The agreement between two different numerical techniques is good over a range of chemical rate constant.

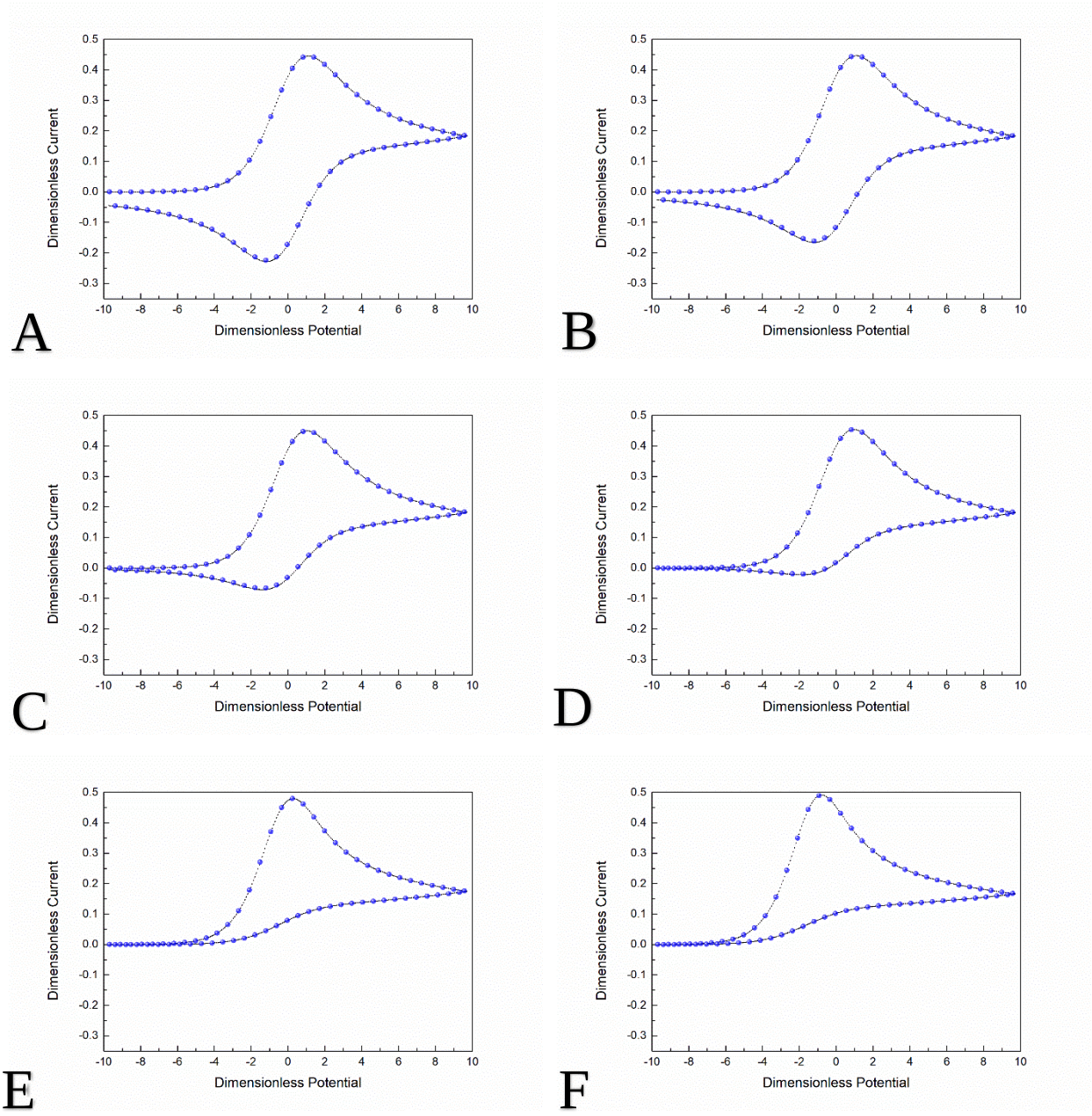

Figure 3.3: Validation of the model predictions of EC mechanism for different k. Validation of various numerical techniques of the current behaviour for $k = 0.01\ \mathrm{s}^{-1}$ (A), $k = 0.02\ \mathrm{s}^{-1}$ (B), $k = 0.05\ \mathrm{s}^{-1}$ (C), $k = 0.10\ \mathrm{s}^{-1}$ (D), $k = 1.0\ \mathrm{s}^{-1}$ (E), $k = 10.0\ \mathrm{s}^{-1}$ (F). The solid lines $(-)$ represent the dimensionless current approximated by two-point time evolution derivative method and the blue balls (**o**) represents the model predictions by operator splitting method.

3.2.3. EE Reaction

It is also frequently observed that the electroactive species exchange more than one electron in successive transfer steps, which arise to multi-E mechanisms. We now consider a simple case in which there are two reversible heterogeneous electron-transfer reaction given in Scheme 3.3. The appearance of the voltammogram relies on the location of the standard potentials, E_1^0 and E_2^0, and the spacing $\Delta E^0 = E_2^0 - E_1^0$ is an important variable to observe the shape changing feature for EE mechanism.

$$\mathrm{O} + e^- \underset{E_1^0}{\overset{k_0^1}{\rightleftharpoons}} \mathrm{O}'$$

$$\mathrm{O}' + e^- \underset{E_2^0}{\overset{k_0^2}{\rightleftharpoons}} \mathrm{R}$$

Scheme 3.3: EE mechanism including two reversible heterogeneous electron-transfer processes.

In the calculation, the extra electroactive species O' is added into mass transfer operator and electrode reaction operator as intermediate, and the diffusion equation for O, O' and R is updated in Equation 3.29, respectively.

$$\begin{aligned} \frac{\partial C_{\mathrm{O}}(x,t)}{\partial t} &= D_{\mathrm{O}} \frac{\partial^2 C_{\mathrm{O}}(x,t)}{\partial x^2} \\ \frac{\partial C_{\mathrm{O}\prime}(x,t)}{\partial t} &= D_{\mathrm{O}\prime} \frac{\partial^2 C_{\mathrm{O}\prime}(x,t)}{\partial x^2} \\ \frac{\partial C_{\mathrm{R}}(x,t)}{\partial t} &= D_{\mathrm{R}} \frac{\partial^2 C_{\mathrm{R}}(x,t)}{\partial x^2} \end{aligned} \tag{3.29}$$

and electron transfer process for O, O' and R is updated in Equation 3.30

$$\begin{aligned} \frac{\Delta x}{2\tau}\psi_{[\mathrm{O}],i}^{n+1} &= -k_{\mathrm{f}}^1\left(C_{[\mathrm{O}],i}^k + \phi_{[\mathrm{O}],i}^{n+1} + \psi_{[\mathrm{O}],i}^{n+1}\right) + k_{\mathrm{b}}^1\left(C_{[\mathrm{O}\prime],i}^k + \phi_{[\mathrm{O}\prime],i}^{n+1} + \psi_{[\mathrm{O}\prime],i}^{n+1}\right) \\ \frac{\Delta x}{2\tau}\psi_{[\mathrm{O}\prime],i}^{n+1} &= k_{\mathrm{f}}^1\left(C_{[\mathrm{O}],i}^k + \phi_{[\mathrm{O}],i}^{n+1} + \psi_{[\mathrm{O}],i}^{n+1}\right) - k_{\mathrm{b}}^1\left(C_{[\mathrm{O}']_,i}^k + \phi_{[\mathrm{O}']_,i}^{n+1} + \psi_{[\mathrm{O}']_,i}^{n+1}\right) \\ &\quad - k_{\mathrm{f}}^2\left(C_{[\mathrm{O}']_,i}^k + \phi_{[\mathrm{O}']_,i}^{n+1} + \psi_{[\mathrm{O}']_,i}^{n+1}\right) + k_{\mathrm{b}}^2\left(C_{[\mathrm{R}],i}^k + \phi_{[\mathrm{R}],i}^{n+1} + \psi_{[\mathrm{R}],i}^{n+1}\right) \\ \frac{\Delta x}{2\tau}\psi_{[\mathrm{R}],i}^{n+1} &= k_{\mathrm{f}}^2\left(C_{[\mathrm{O}\prime],i}^k + \phi_{[\mathrm{O}\prime],i}^{n+1} + \psi_{[\mathrm{O}\prime],i}^{n+1}\right) - k_{\mathrm{b}}^2\left(C_{[\mathrm{R}],i}^k + \phi_{[\mathrm{R}],i}^{n+1} + \psi_{[\mathrm{R}],i}^{n+1}\right) \end{aligned} \tag{3.30}$$

Since Equation 3.30 holds $\psi_{[\mathrm{O}],i}^{n+1} + \psi_{[\mathrm{O}\prime],i}^{n+1} + \psi_{[\mathrm{R}],i}^{n+1} = 0$, two E steps could be considered in the same operator, and the total current is calculated as

$$\begin{aligned}\frac{i}{FA} = &-k_0^1 e^{-\alpha\frac{F}{RT}\left(E-E_1^0-iR_\mathrm{u}\right)}\left(C_{[\mathrm{O}],i}^k + \phi_{[\mathrm{O}],i}^{n+1} + \psi_{[\mathrm{O}],i}^{n+1}\right)\\ &+ k_0^1 e^{(1-\alpha)\frac{F}{RT}\left(E-E_1^0-iR_\mathrm{u}\right)}\left(C_{[\mathrm{O}\prime],i}^k + \phi_{[\mathrm{O}\prime],i}^{n+1} + \psi_{[\mathrm{O}\prime],i}^{n+1}\right)\\ &- k_0^2 e^{-\alpha\frac{F}{RT}\left(E-E_2^0-iR_\mathrm{u}\right)}\left(C_{[\mathrm{O}\prime],i}^k + \phi_{[\mathrm{O}\prime],i}^{n+1} + \psi_{[\mathrm{O}\prime],i}^{n+1}\right)\\ &+ k_0^2 e^{(1-\alpha)\frac{F}{RT}\left(E-E_2^0-iR_\mathrm{u}\right)}\left(C_{[\mathrm{R}],i}^k + \phi_{[\mathrm{R}],i}^{n+1} + \psi_{[\mathrm{R}],i}^{n+1}\right)\end{aligned} \tag{3.31}$$

An alternative way to solve the EE mechanism is to separate two electron-transfer steps and to solve them individually. However, this path needs iteration twice to find a root from the nonlinear electrode reaction which is solved by the Regula Falsi method.

Typical cyclic voltammograms for the variation of the peak current of the anodic and cathodic waves are shown in Figure 3.4 using two different numerical approximation techniques. When $\Delta E^0 < 100$ mV, one observes a single wave with characteristics indistinguishable from a single, Nernstian, two-electron transfer process. As ΔE^0 increases, two waves can be seen which are fully resolvable at $\Delta E^0 = 150$ mV. The agreement between operator splitting method and two-point temporal discretisation derivative approximation is better than that in EC mechanism, which suggests fewer splitting errors with fewer splitting operators (two in EE mechanism and three in EC mechanism).

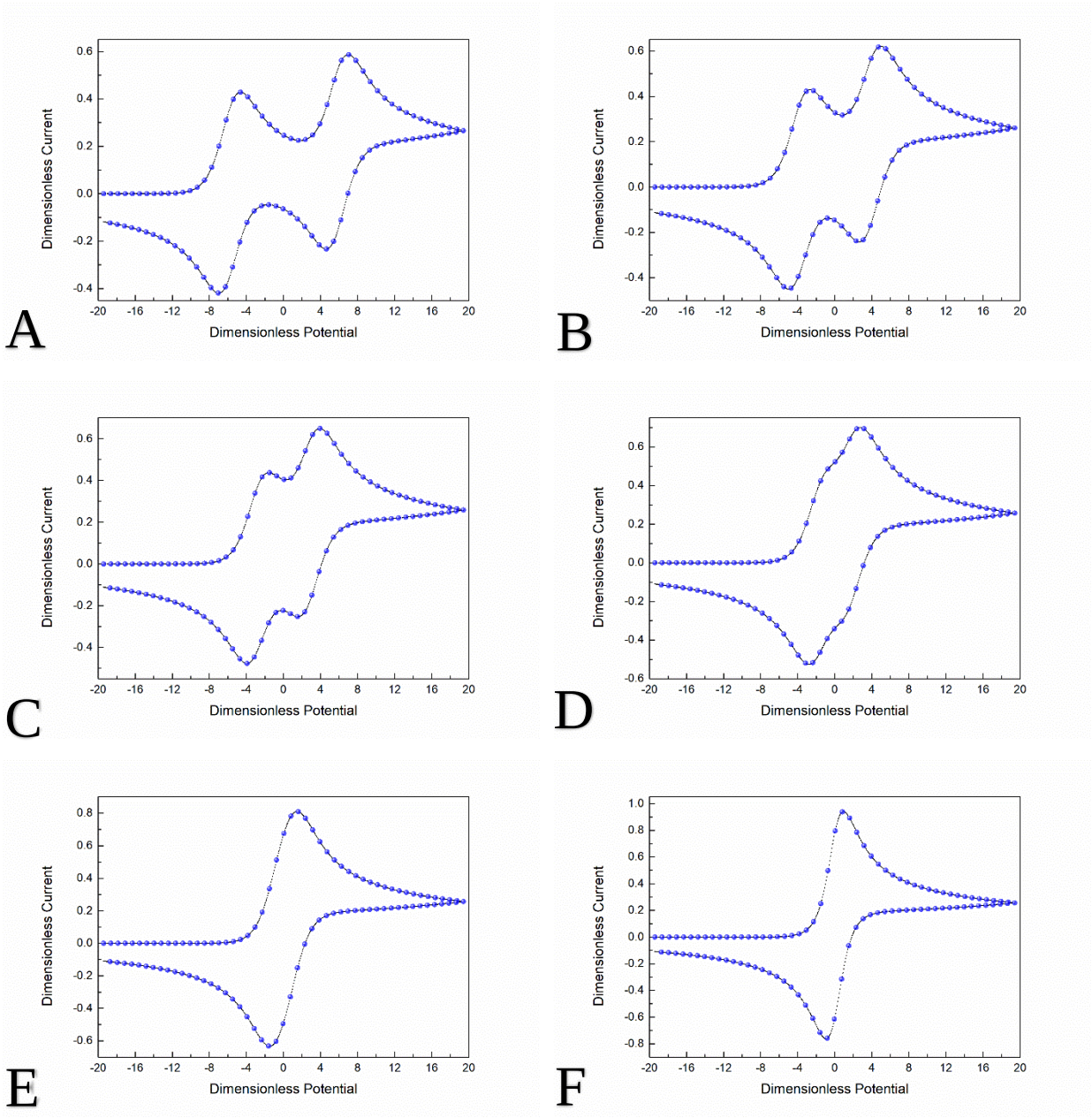

Figure 3.4: Validation of the model predictions of EE mechanism for different ΔE^0. Validation of different numerical techniques of the current behaviour with $k_0^1 = k_0^2 = 1$ cm s^{-1} for $\Delta E^0 = 300$ mV (A), $\Delta E^0 = 200$ mV (B), $\Delta E^0 = 150$ mV (C), $\Delta E^0 = 100$ mV (D), $\Delta E^0 = 50$ mV (E), $\Delta E^0 = 10$ mV (F). The solid lines $(-)$ represent the dimensionless current approximated by two-point temporal discretisation derivative method and the blue balls (**o**) represents the model predictions generated by operator splitting method.

3.2.4. ECE Reaction

A more complex and comprehensive mechanism involving both EC and EE features is termed as ECE reaction and the mechanism has been summarised in Scheme 3.4. Typically, E_1^0 and E_2^0 are given the value -0.15 V and -0.45 V, respectively. Thus, we have $\Delta E^0 = E_2^0 - E_1^0 < -200$ mV which leads to sequential stepwise addition of electrons results in two voltammetric waves when the chemical step occurs near the positive potential[24]. Under presence of C and E steps, total four operators need to be considered: the pure mass transport, the electrode reaction, the chemical kinetics and again the electrode reaction. The procedures can follow the derivatives of EC and EE mechanisms.

$$\mathrm{O} + \mathrm{e}^- \underset{E_1^0}{\overset{k_0^1}{\rightleftharpoons}} \mathrm{X}$$

$$\mathrm{X} \overset{k}{\rightarrow} \mathrm{Y}$$

$$\mathrm{Y} + \mathrm{e}^- \underset{E_2^0}{\overset{k_0^2}{\rightleftharpoons}} \mathrm{R}$$

Scheme 3.4: ECE mechanism involving a fast electrode reaction followed by irreversible chemical step and another electrochemical reaction.

For the ECE case under consideration here, only a single peak (wave I in Figure 3.5(A)) can be observed on the forward scan. This peak is close to E_1^0, because species Y formed at this potential is immediately reduced to R. On the backward scan, a reversal wave (wave II in Figure 3.5(A)) is recorded for oxidation of X if k is small enough. As the reverse scan continues, a second reversal peak (wave III in Figure 3.5(B)) might be observed because of repeating oxidation of R to Y. If we scan from the very negative potential again, a corresponding cathodic peak (wave IV in Figure 3.5(B)) appears as a result of the reduction of Y to R. The relative sizes of waves II, III and IV are decided by the magnitudes of the chemical kinetics. A meaningful dimensionless parameter of interest, λ, is given by the expression $(k/v)(RT/F)$ to define the current responses in ECE reaction. More general treatments of ECE system and λ can be found in these excellent literatures with the applications of zone diagrams[24]. Both numerical techniques show the same trends of the model predictions, however, the agreement between two approaches is not as good as EC or EE mechanism. This might be caused by the increasing number of the splitting operators.

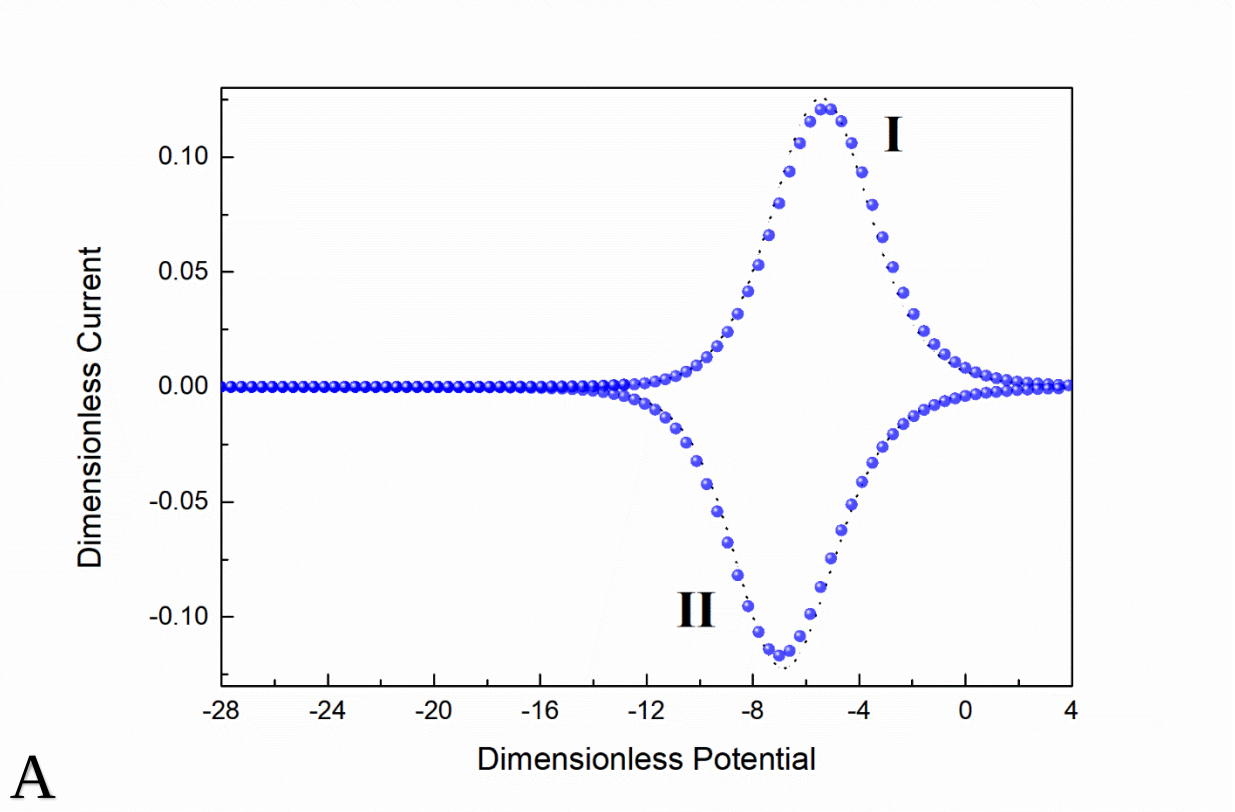
Dimensionless Current
0.10
0.05
0.00
-0.05
-0.10
I
II
-28
-24
-20
-16
-12
-8
-4
0
4
Dimensionless Potential

A

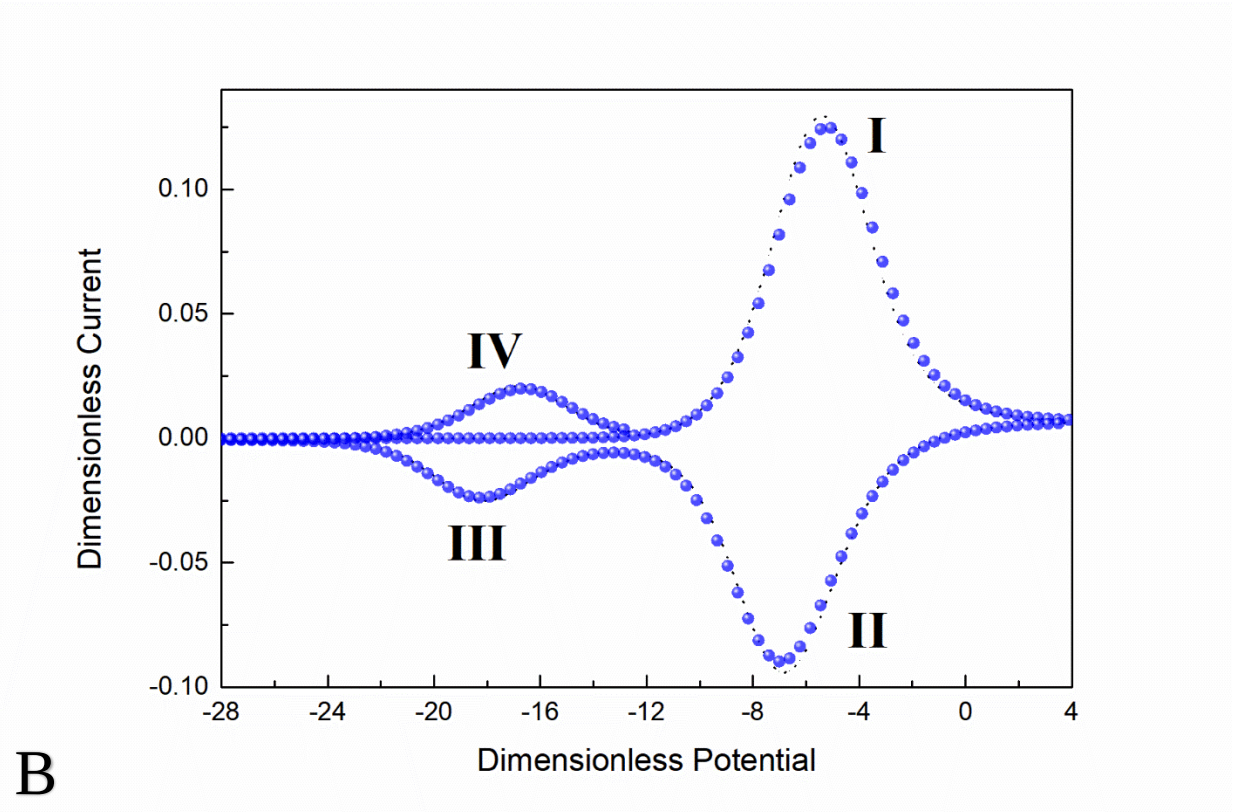
Dimensionless Current
0.10
0.05
0.00
-0.05
-0.10
I
IV
III
II
-28
-24
-20
-16
-12
-8
-4
0
4
Dimensionless Potential

B

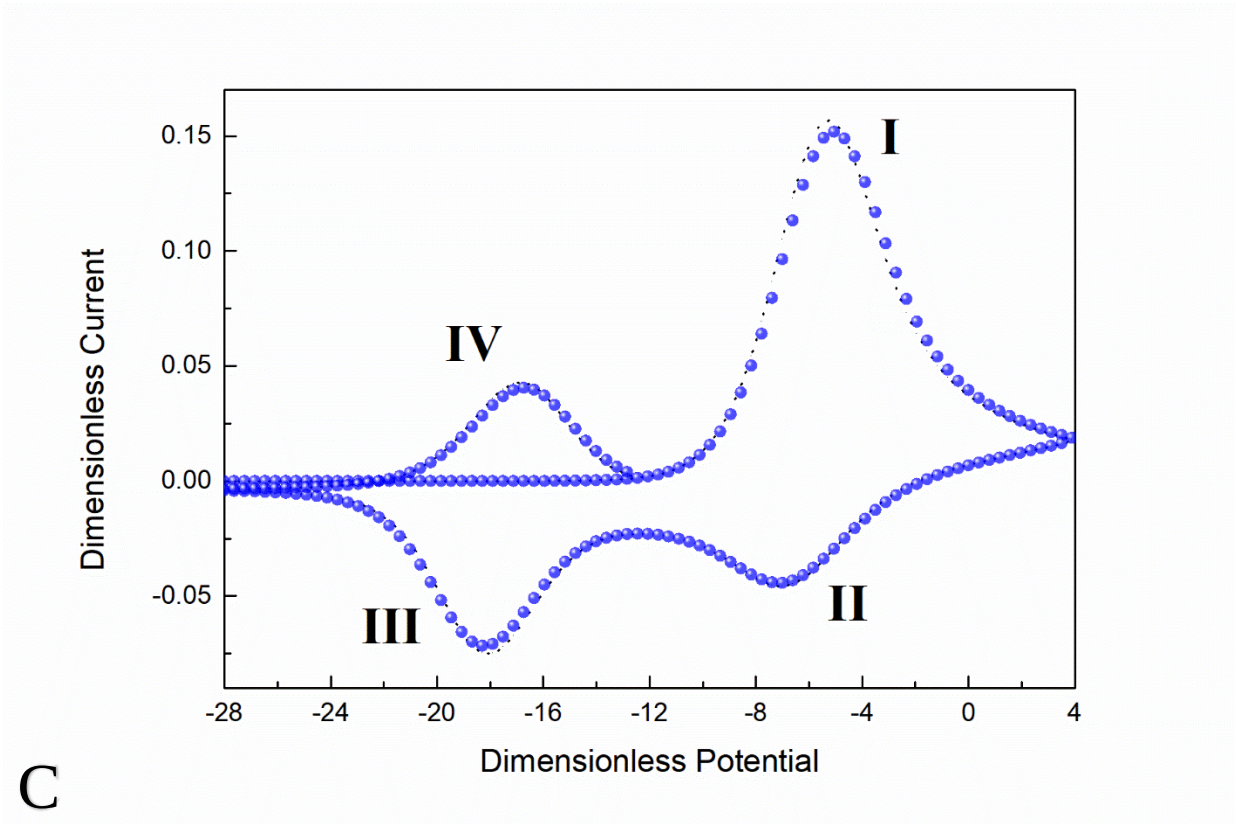

Figure 3.5: Cyclic voltammograms for the ECE mechanism predicted by two numerical techniques for different values of $\lambda = (k/v)(RT/F)$. Validation of numerical techniques of the current behaviour with $k_0^1 = k_0^2 = 1$ cm s^{-1} for $\lambda = 0$ (A), $\lambda = 0.02$ (B), $\lambda = 0.2$ (C). The solid lines $(-)$ represent the dimensionless current approximated by two-point time evolution derivative method and the blue balls (**o**) represents the model predictions generated by operator splitting method.

3.3. Electrocatalytic Systems

We now move our focus to some more complex mechanism, the electrocatalytic scheme, in which second- or sometimes high-order reactions are considered. The investigation starts from the basic electrocatalytic system, EC' mechanism, which holds only two reaction steps, but is very different to the non-catalytic electrochemical systems that we introduced in the last Section 3.2.

$$O + e^- \rightleftharpoons R$$ $$R + Y \xrightarrow{k} O$$
Scheme 3.5: EC' mechanism including a reversible electron-transfer reaction followed by an irreversible second-order catalytic process.

The governing equations can be first written as Equation 3.32 for EC' mechanism

$$\begin{aligned}
\frac{\partial C_O(x,t)}{\partial t} &= D_O \frac{\partial^2 C_O(x,t)}{\partial x^2} + kC_R(x,t)C_Y(x,t) \\
\frac{\partial C_R(x,t)}{\partial t} &= D_R \frac{\partial^2 C_R(x,t)}{\partial x^2} - kC_R(x,t)C_Y(x,t) \\
\frac{\partial C_Y(x,t)}{\partial t} &= D_Y \frac{\partial^2 C_Y(x,t)}{\partial x^2} - kC_R(x,t)C_Y(x,t)
\end{aligned} \tag{3.32}$$

In the electrocatalytic mechanism, an electroactive species R reacts with some other solution species Y (called "substrate") and regenerates the original electroactive material O which can thus undergo further electron transfer at the electrode. The initial and boundary conditions here for Y obey

$$C_Y(x,0) = C_Y^*, \lim_{x\to\infty} C_Y(x,t) = C_Y^*, \frac{\partial C_Y(0,t)}{\partial x} = 0 \tag{3.33}$$

One primary difference between second-order EC' mechanism and first-order EC mechanism is that the coupled homogeneous chemical reaction now is dependent on two independent variables of concentrations. The reaction kinetics k is also updated to a second-order rate constant. When $C_Y^* \gg C_R^*$, the second-order problem can be reduced to first-order treatment with $k' \approx kC_Y^*$.

In this case, the splitting error equations for each species O, R and Y under chemical step operator are respectively,

$$\begin{aligned}
\frac{\varphi_{[\mathrm{O}],i}^{n+1}}{\tau} &= k\left(C_{[\mathrm{R}],i}^{k}+\varphi_{[\mathrm{R}],i}^{n+1}\right)\left(C_{[\mathrm{Y}],i}^{k}+\varphi_{[\mathrm{Y}],i}^{n+1}\right)\\
\frac{\varphi_{[\mathrm{R}],i}^{n+1}}{\tau} &= -k\left(C_{[\mathrm{R}],i}^{k}+\varphi_{[\mathrm{R}],i}^{n+1}\right)\left(C_{[\mathrm{Y}],i}^{k}+\varphi_{[\mathrm{Y}],i}^{n+1}\right)\\
\frac{\varphi_{[\mathrm{Y}],i}^{n+1}}{\tau} &= -k\left(C_{[\mathrm{R}],i}^{k}+\varphi_{[\mathrm{R}],i}^{n+1}\right)\left(C_{[\mathrm{Y}],i}^{k}+\varphi_{[\mathrm{Y}],i}^{n+1}\right)
\end{aligned} \tag{3.34}$$

The second and third equations leading to a quadratic equation because of $\varphi_{[\mathrm{R}],i}^{n+1}=\varphi_{[\mathrm{Y}],i}^{n+1}$,

$$\frac{\varphi_{[\mathrm{R}],i}^{n+1}}{\tau} = -k\left(C_{[\mathrm{R}],i}^{k}+\varphi_{[\mathrm{R}],i}^{n+1}\right)\left(C_{[\mathrm{Y}],i}^{k}+\varphi_{[\mathrm{R}],i}^{n+1}\right) \tag{3.35}$$

Thus, one can solve for the variables, $\varphi_{[\mathrm{R}],i}^{n+1}$, $\varphi_{[\mathrm{Y}],i}^{n+1}$ and $\varphi_{[\mathrm{O}],i}^{n+1}$ in sequence. The species concentration fields are then updated accordingly using these variables.

This approach also leads to the solution of second-order non-catalytic electrochemical reactions, in contrast, if the EC' mechanism has a first-order catalytic step, the problem can be solved referring to the resolution of EC mechanism.

In the following work, the simulations of cyclic voltammetry under electrocatalytic mechanism is measured. For such a complex system, the convergence and computational performance are presented by different timestep, Δt. Due to the 7-point level time discretisation approximation in time, one can run the calculations with rather high timestep ($\Delta t = 0.01$), while for the two-point level implicit methods much lower (($\Delta t = 10^{-6}$) timesteps are needed. Numerical experiments then show that for a wide range of parameters nearly optimum convergence rate is achieved with $\tau = 0.1\Delta t$. From 10 to 30 iterations are needed to achieve the stopping criteria,

$$\varepsilon = \frac{|\phi+\psi|}{|\phi|+|\psi|} \leq 10^{-9} \tag{3.36}$$

3.3.1. EC' Reaction

The first test case is the simulation of cyclic voltammogram to investigate the features of EC' mechanism detailed in Scheme 3.5. Figure 3.6 shows the cyclic voltammogram for $\alpha = 0.5$, $E^0 = 0\,\mathrm{V}$, $C_{\mathrm{dl}} = 0\,\mathrm{F}$ and $D_{\mathrm{O}} = D_{\mathrm{R}} = 1 \times 10^{-5}\,\mathrm{cm^2\,s^{-1}}$. The traces show that as the substrate concentration increases, both the pre-wave and main peak currents increase, which is matched with the property of EC' mechanism reported in open literature.

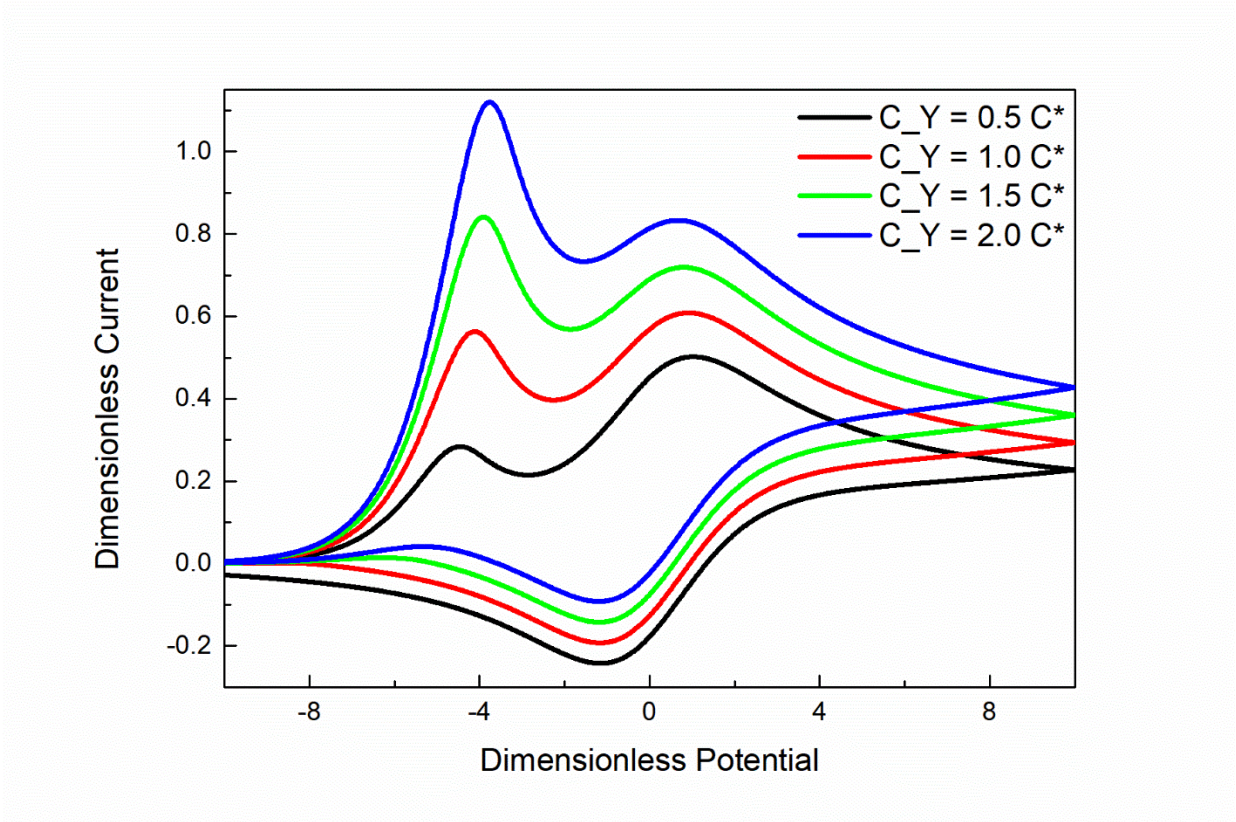

Figure 3.6: Cyclic voltammograms for the EC' case obtained by operator splitting method with different initial values of substrate Y's concentrations: $C_{\mathrm{Y}}^{*} = 0.5\ C^{*}$ (−), $C_{\mathrm{Y}}^{*} = 1.0\ C^{*}$ (−), $C_{\mathrm{Y}}^{*} = 1.5\ C^{*}$ (−), $C_{\mathrm{Y}}^{*} = 2.0\ C^{*}$ (−).

In order to illustrate the efficiency, stability and accuracy of this novel method, we performed a series of calculations for the EC' mechanism using the current method with 7-point time evolution derivative in comparison to the standard first-order operator splitting method and classic 2-point temporal discretisation implicit difference finite method. Results of the calculations are presented

from Figures 3.7 to 3.9 and Table 3.1. Since no analytical solution is available in this case we refer to the 2-point OS solution with $\Delta t = 10^{-6}$ as a benchmark solution and calculate the relative error.

The code in this part is implemented in C++ programming language, using the open source software Code::Block version 13.12. All the programs are run on laptop equipped with Intel Core i7, 2.4 GHz and 4GB of RAM. The running time for the simulation varies under 10 minutes. In general, longer running time is required for a smaller convergence criterion and smaller timesteps. This fact is especially important for EC' mechanism in which high k often requires both stringent convergence and small timestep.

Table 3.1: The comparison of the computational performance of EC' mechanism simulation between standard 2-point OS method and 7-point OS method.

Δt	CPU time (s)	Relative error (%)
2-point OS method		
10^{-4}	41	6.27
10^{-5}	202	2.08
10^{-6}	2298	0.211
5×10^{-7}	4207	0.101
7-point OS method		
10^{-2}	47	0.022
5×10^{-2}	61	0.011
10^{-3}	167	-

In Figure 3.7, the standard 2-point OS method with $\Delta t = 10^{-4}$ and comparable CPU time provides absolutely inadequate results; in order to approach the "truth" using the standard 2-point OS method one has decrease the time step by two orders of magnitude with corresponding increase of the computational time.

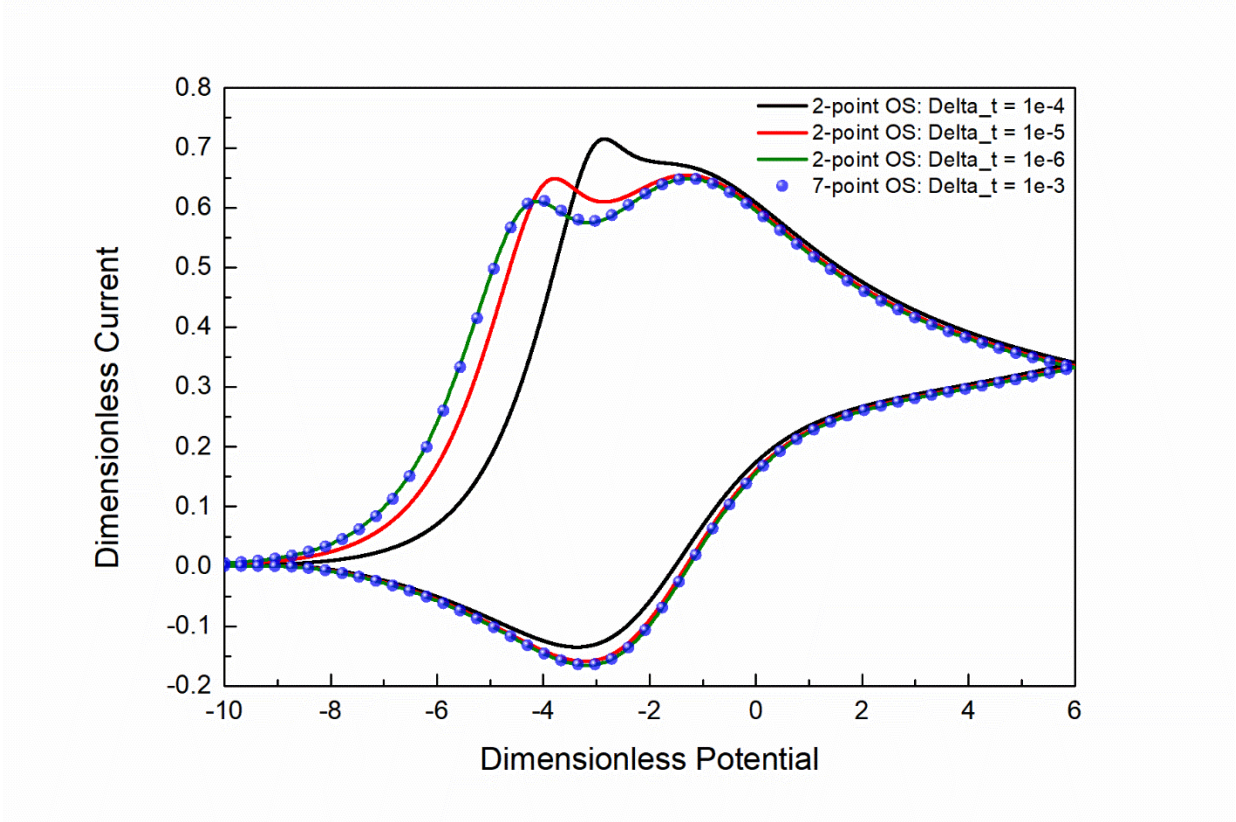

Figure 3.7: EC' cyclic voltammogram for standard 2-point OS method with different values of timestep, $\Delta t = 10^{-4}$, $\Delta t = 10^{-5}$, and $\Delta t = 10^{-6}$ in comparison to 7-point OS method using a relatively large timestep, $\Delta t = 10^{-3}$.

In Figure 3.8, the 7-point method with $\Delta t = 10^{-2}$ provides results similar to the benchmark solution, and the convergence is still promised when Δt increases to 5×10^{0}. The computational running time and relative error are summarised in Table 3.1 between two numerical techniques, of which our new developed method is efficient and stable.

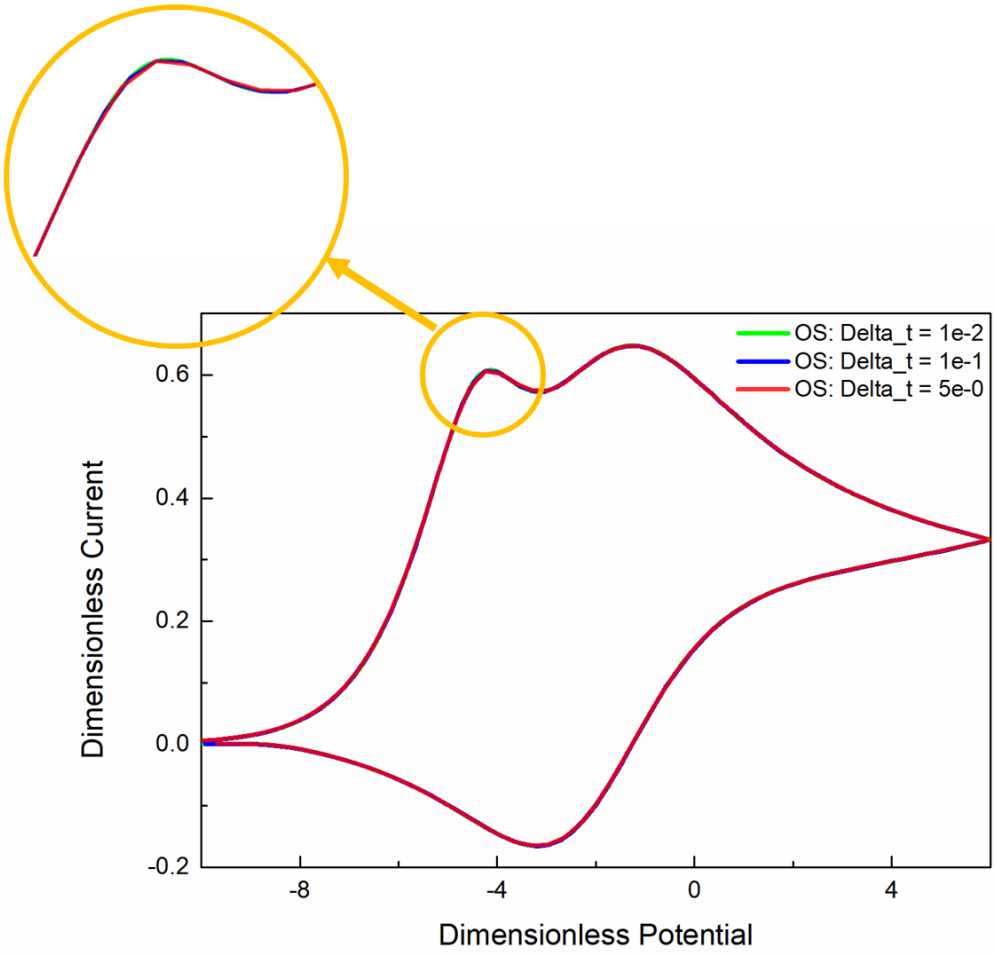

Figure 3.8: EC' cyclic voltammogram for 7-point operator splitting method with large timestep, $\Delta t = 10^{-2}$, $\Delta t = 10^{-1}$, and $\Delta t = 5 \times 10^{0}$. Inset: The green smooth curve (~) implies more data points generated in the simulation, which is obtained with a smaller timestep (10^{-2}). In contrast, the red straight line (–) implies fewer data points generated in the simulation, which is obtained with a bigger timestep (5×10^{0}). The overlap here promises the convergence when given a large timestep.

Conventional 2-point temporal discretisation FDMs is introduced to compare the results generated from operator-splitting methods. This approach is classic and widely used in the simulations of electrochemistry. Some inputs are given to these methods, only by varying the size of timestep. In Figure 3.9, a more accurate result is observed by high-order OS when given the same Δt to 7-point OS and 2-point FDM. The running time is close if both of high-order OS and 2-point FDM employ the uniform spatial grids of diffusion layer.

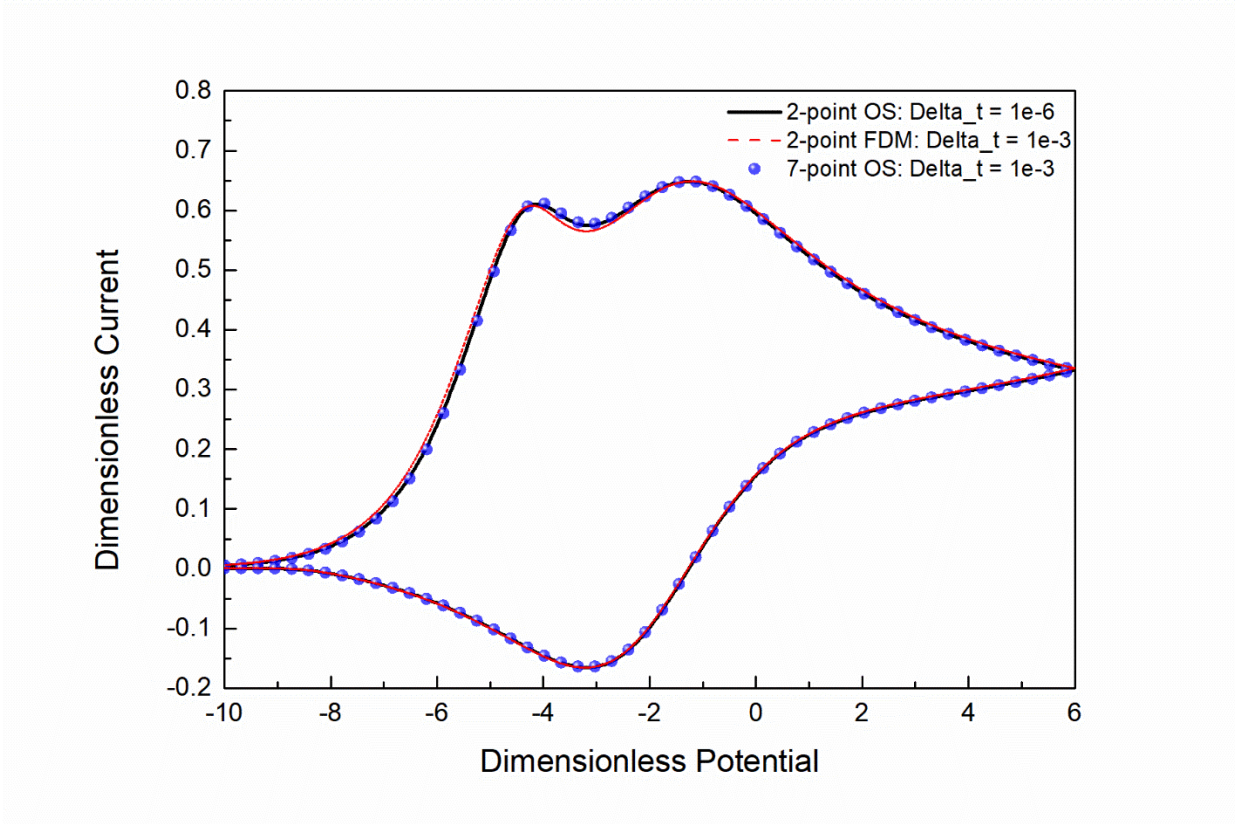

Figure 3.9: EC' cyclic voltammogram: the comparation of the validation of model prediction among standard 2-point OS method with small timestep $\Delta t = 10^{-6}$ $(-)$, 2-point FDM with moderate timestep $\Delta t = 10^{-3}$ (--) and the high-order OS method holding the same size of timestep, $\Delta t = 10^{-3}$ (o).

3.3.2. Hydrogenase Mechanism

One significant contemporary challenge for the widespread adoption of energy conversion systems is the need for efficient, stable, and cost-effective catalysts against efficient but expensive and scarce noble metal catalysts[180-182]. A very promising perspective in this regard is to tailor an efficient catalyst using molecular synthetic engineering[183,184]. This can be achieved by understanding and translating the biological catalytic principles to design "model" synthetic mimics. Delving deep into reaction mechanisms and kinetics and thermodynamic parameters that occur during the catalytic reaction is central to this effort[65,185-188]. In this regard, Nature has offered extremely efficient enzymes called hydrogenases.

3.3.2.1. Introduction

Hydrogenases, remarkable active catalysts for oxidative transformation due to the specific reactive sites of their metal centres, are highly used in this context[189-192]. This enzyme catalyses the reversible interconversions between H_2 and H^+ at high turnover rates, but is inactivated by O_2 converting the active site into different inactive forms. This inactivation affects dramatically the shape of the electrocatalytic response, at the forward scan, the catalytic current due to hydrogen oxidation increases and significantly drops as the potential becomes more positive (i.e., inactivation occurs). However, this behaviour is reversed on the subsequent sweep back to a more negative potential (i.e., reactivation occurs).

Although the exact mechanism of this inactivation-activation process (IAP) causing this odd shape remains to be elucidated, previous research has provided insights and hypotheses. Limoges and Savéant suggested that the immobilised enzymes such as hydrogenase on the electrode surface represent a twisted reverse trace behaviour[193]. The latter is "unusual" in comparison to the "classical" regenerative mechanisms of electrocatalysis[194,195]. The authors derive a complex electrocatalytic framework involving a five-step reaction scheme to depict the interconversion within the IAP of surface-confined enzymes. This scheme links the hysteresis between forward and backward catalytic responses to the inhibition process. In the mathematical models, the occurrence of twisted reverse oxidation peaks is obtained from a delicate combination of thermodynamic and kinetic parameters of the different reactions involved in the mechanism[193]. This peculiar behaviour is better observed when a large rate constant exists for the reactivation of the electrocatalytically active enzyme.

Investigations by Armstrong and his co-workers, however, highlighted the experimental mechanistic relationship between these biocatalysts and hydrogen oxidation[187,196,197]. They reported a similar behaviour to depict the anaerobic interconversion between the inactivation and reactivation of [NiFe] hydrogenase from different microorganisms. A parameter, E_{switch} derived from the cyclic voltammetry, was defined as the position of the first inflection on the reduction sweep towards lower potential, gives a qualitative diagnosis to compare the ease with which various hydrogenases can be reactivated after oxidative inactivation[196]. In mechanistic investigations, this parameter was used to infer the acidity constants via $\mathrm{pE/pH}$ diagrams, and to calculate the entropies and enthalpies by analysing the dependence on temperature. Nevertheless, Léger *et al.* suggested that the reduction potential for the so-called [NiB] state which is electrocatalytically inactive, cannot be estimated directly by the voltammetric data[198]. E_{switch} changes in proportion to the logarithm of scan rate, and for this reason, it was quantified as a kinetic characteristic rather than a thermodynamic parameter[198]. It was also supported theoretically, by the fact that the normalised governing variables involve the dependence between the IAP's rate constants and scan rate[193].

3.3.2.2. Voltammetric Analysis

We now move into a practical case, *Aquifex aeolicus* [NiFe] hydrogenase, to examine the performance of our new approach. A unique current behaviour of hydrogenase is reprinted from Léger's work[198]. The cyclic voltammogram of an enzymatic process shows a totally inverted backward peak occurring on the reversal scan reprinted in Figure 3.10(A). The reaction is estimated by the authors to hold a very complex electrocatalytic mechanism reprinted in Figure 3.10(B).

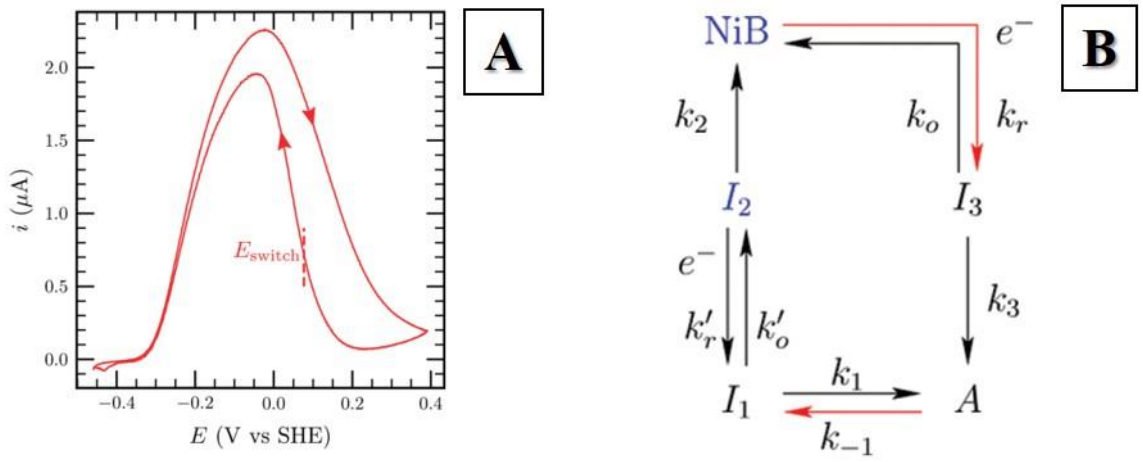

Figure 3.10: Cyclic voltammogram (A) of *Aquifex aeolicus* [NiFe] hydrogenase adsorbed onto a rotating disk electrode. Mechanistic scheme (B) proposed for the activation of the [NiB] State of standard [NiFe] Hydrogenases. Reprinted from Fourmond *et al.*'s work[198].

This case offers a total five-step mechanism with the phenomena including material balance, electron transfer and adsorption, which is treated as a highly nonlinear problem. Such a case is a great challenge for both conventional FDM and operator-splitting. We employed a direct approach based on Limoges and Savéant's work[193]: using an empirical Butler-Volmer model and deriving the current-potential relationship from a kinetic scheme. With only the schematic diagram shown in Figure 3.10(B) corresponding to the estimated kinetics and thermodynamics from Fourmond *et al.*'s work[198], both FDM and operator-splitting lead to outrageous current behaviours that are difficult to employ in a mechanistic analysis. This scenario may be caused by the reaction processes carrying too many unknown parameters which cannot be directly obtained from the experiment fitting results. The rate constants of electrochemical reactions, k_{o}, k_{r}, k'_{o} and k'_{r} are

approximated by the overall inactivation and activation rate k_{A} and k_{I} instead of measuring from an electron-transfer process. Although some work has been extensively studied for hydrogenases, their catalytic mechanism cannot be fully understood yet due to the intricacy of inner necessary electrical wiring, desorption and complex biochemical environment.

These uncertainties, which lead to gaps in the theoretical understanding of the mechanism, significantly constrain the construction of a model-based computational simulation, which also implies an insufficient understanding of hydrogenase. In order to provide a fair competition between the efficiency and accuracy of two different approaches employed in this chapter, it is suggested that well-defined mathematical model describing the electrochemical system in its complete complexity exits.

3.4. Conclusion and Outlook

A novel high-order operator-splitting (OS) scheme, with fully implicit finite difference (FIFD) method is proposed and for the first time applied to electrochemical problems in Chapter 3. The stability and convergence of this pseudo-time approach are analysed by using a model scalar equation. The method consists of a number of steps of an implicit Euler method, which promises a large size timestep.

The separated sub-problems are completely independent to each operator, in which individual sub-step can be resolved by a most suitable numerical method. In some typical mechanisms, the method has been shown for a homogenous reaction can be straightforwardly included into the algorithm, which greatly widens the range of its application. A better competition result of accuracy, stability and efficiency is also obtained from novel seven-point operator-splitting method for the simulation of EC' mechanism in comparison to that from the traditional two-point finite difference method. However, we have observed the limitations of this scheme when working on very complex hydrogenase mechanism with unknown parameters or processes, which are not captured by conventional methods as well. This drawback may arise due to incomplete definition of the mathematical model describing these systems. The implementation of this work needs to tested on a well-defined system.

Chapter 4

4. Model-Based Computational Study into Hydrogenase-Like Electrocatalytic Activation and Inactivation Mechanism

In this chapter, the comparison between operator-splitting scheme and traditional finite difference method continues. The challenge we met at the end of last chapter implies that an efficient and accurate path to solution using model-based computational design highly depends on the understanding of the problem, and subsequent formulation of the governing mathematical model.

Fortunately, a similar behaviour was observed for a bio-derived porphyrin complex modified with rhodium as the catalytic active site. This complex presents an electrocatalytic behaviour, which can be consistent with hydrogenase's electrocatalytic response[199]. However, the kinetics and the intricate molecular mechanisms of these interconversions are not fully understood. The extension of this biomimetic capability is subjected to a more detailed thermodynamic and kinetic scrutiny. Mechanistic studies were employed to elucidate the electrocatalytic behaviour, providing models that feature catalyst inactivation and activation process (IAP). Advantageously, this catalyst presents an excellent and stable electron transfer enabling a straightforward estimation of the thermodynamic and kinetic parameters from its non-catalytic signal.

Nonetheless, the hydrogenase IAP analysis is more challenging because of desorption, electrical wiring, complex chemical environment and instability. For these reasons, very few mechanistic studies investigating hydrogenase IAP were attempted due to the fact that it would require the determination and evaluation of too many unknown parameters. Therefore, we believe this work could eventually be inspirational to explicate the complexity of hydrogenase pathways. Experimental work developed in collaboration with Dr Kamal Elouarzaki have been applied to quantitatively analyse electrocatalytic activation and inactivation mechanism. Density function theory (DFT) calculation for electron transfer kinetics is contributed by Haoxiang Xu.

Here, we used a 3D binder-free deuteroporphyrin dimethylester rhodium(III) ((DPDE)Rh^{III}) confined on an interconnected multi-walled carbon nanotube (MWCNT) network to obtain deep insight into the twisted reverse voltammetric responses (Figure 4.1) with glucose as a substrate. The study begins with the characterisation and mechanistic determination of the non-catalytic reaction scheme (ECE) of the catalyst. Then, the twisted traces were investigated with the introduction of glucose into the system. Based on the experimentally elucidated ECE scheme, we determined another complex electrocatalytic (EC'CE) scheme that is fully consistent with the electrocatalytic data. The mathematical models based on EC'CE enabled the approximation of the reaction kinetics at an elementary level. For better understanding of the key parameters causing this twisted shape, we established the dependence of inactivation and activation reaction rates on potential from experimentally validated EC'CE and generated the 3D surface concentration profiles. We further confirmed the robustness and validity the EC'CE model with respect to different kinetic conditions (scan rate and concentration). The overall mechanism explaining the IAP was constructed based on our experimentally validated models and compared to hydrogenase IAP. The above procedures are all simulated by a tradition two-point time evolution finite difference scheme. Finally, this fully understood EC'CE model is tested by the operator-splitting method to verify its convergence.

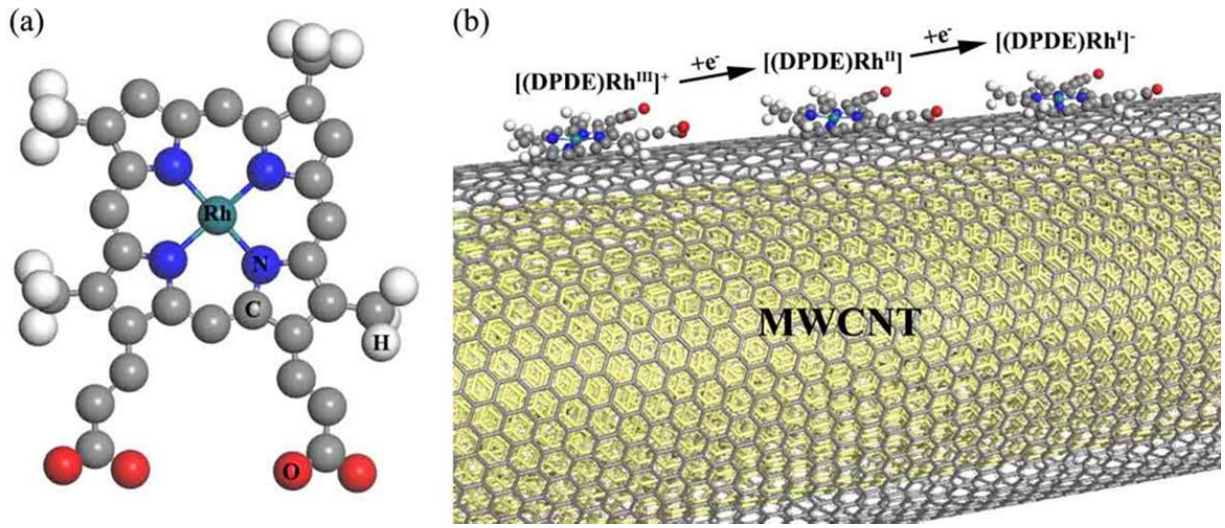

Figure 4.1: 3D binder-free hybrid (DPDE)Rh^{III} hydrogenase-like electrode (a) Configuration of (DPDE)Rh^{III} molecule (b) Schematic structure of two-electron transfer process from (DPDE)Rh^{I} into (DPDE)Rh^{II} supported on MWCNT.

4.1. General Non-Catalytic Electrochemical Properties of Surface Confined (DPDE)Rh^{III}

Commercially available analytical grade reagents, α-D-Glucose, $Rh_2Cl_2(CO)_4$, 1-methyl-2-pyrrolidinone (NMP), Deuteroporphine IX dimethyl ester, and potassium hydroxide (KOH) were purchased from Sigma-Aldrich. Commercial grade thin Multi-Walled Carbon Nanotubes (MWCNT) ($9.5\,nm$ diameter, purity >98%), obtained from Nanocyl were used as received without any purification step. Deuteroporphyrine IX dimethyl ester Rhodium(III) ((DPDE)Rh^{III}) was synthetized and characterized by NMR according to literature, electrospray ionization mass spectrometry (ESI-MS), UV-visible spectroscopy[199].

The (DPDE)Rh^{III} was immobilised onto MWCNT by mixing (DPDE)Rh^{III} and MWCNTs in tetrahydrofuran (THF) under magnetic stirring. After 12 hours, the mixture was filtered under vacuum over a polytetrafluoroethylene (PTFE) membrane. The binder-free (DPDE)Rh^{III}/MWCNT matrix was rinsed with THF and deionized water to remove any unbound components. The resulting dried powder was peeled off from the surface of the filter and re-dispersed in THF. The morphological changes and the nanoscale mixture proprieties of (DPDE)Rh^{III}/MWCNT matrix were characterised both by scanning electron microscopy (SEM) and transmission electron microscopy (TEM). To carry out TEM, drops of dilute (DPDE)Rh^{III}/MWCNTs matrix in THF were deposited onto electron microscopy grids and allowed to dry. TEM revealed that the immobilized porphyrins are distinguished at the sidewalls of the MWCNTs compared to the MWCNTs in the absence of porphyrins Figure 4.2(B(b), B(c)). It clearly appears that the layer formation uniformly increases the diameter of the nanotubes from an average diameter value of $8-10\,nm$ to $12-16\,nm$. Finally, the 3D binder-free (DPDE)Rh^{III}/MWCNT electrode was prepared by dispersing (DPDE)Rh^{III}/MWCNT in N-Methyl-2-pyrrolidone (NMP). The resulting homogenous dispersion was placed on top of the glassy carbon (GC) and evaporated leaving a stable film. Based on this transfer process, a reproducible $15-20\,\mu m$ thick film was obtained on the electrodes. SEM images Figure 4.2(B(a)) confirmed that the MWCNT film exhibits a 3D porous high-branched interconnected MWCNT network nanostructure, indicative of the high electroactive area of the electrodes. Additional details including the fabrication of the electrode, SEM and TEM microscopy, DFT for electron transfer kinetics and electrochemical measurements in the experiments are available on the Appendix.

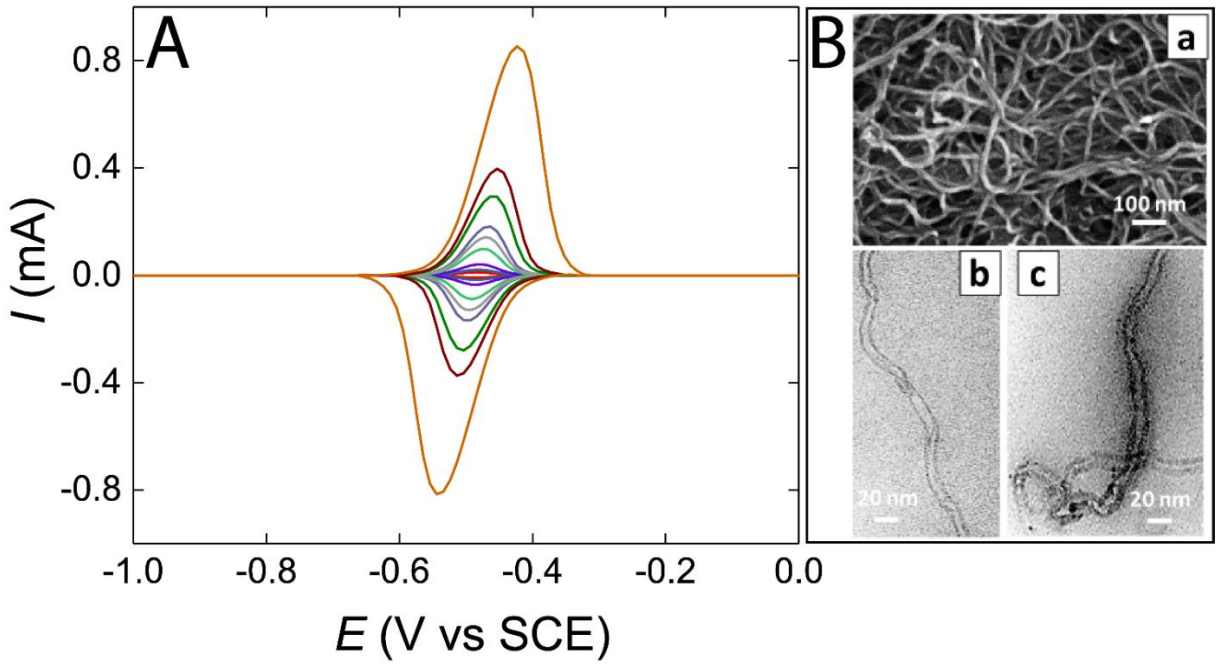

Figure 4.2: Characterisation of the electrode material. Experimental deconvoluted cyclic voltammograms for the non-catalytic (DPDE)Rh^{III} at different scan rates $\nu = 5, 10, 20, 50, 75, 100, 150, 200, 500\ \mathrm{mV/s}$ (A). SEM image of the carbon nanotubes modified with (DPDE)Rh (B(a)), TEM image of the carbon nanotube before modification (B(b)) and TEM image of the carbon nanotube modified with (DPDE)Rh (B(c)).

The hybrid (DPDE)Rh^{III} film onto GC was directly used as electrodes, in which no polymer binder or additives were added. A series of successive deconvoluted[200] cyclic voltammograms (CVs) observed when the potential is scanned between 0 and -1.2 V at pH 14 are presented in Figure 4.2(A). The CVs display well-defined reversible peak at -485 V vs. SCE assigned to the Rh redox couple of the complex (DPDE)Rh^{III}. As the scan rate is systematically varied from 0.005 to $0.5\ \mathrm{V/s}$, the analysis of the electrochemical characteristics, including $E - \nu$ plot of the peak positions in relation to the scan rate where ν is the scan rate, indicates two electrons surface-confined process shown in Figure 4.3. Furthermore, upon repetitive sweeping over periods up to 5 h, the peak heights change by less than 3%, indicating that these electrodes are remarkably stable over time in alkaline condition.

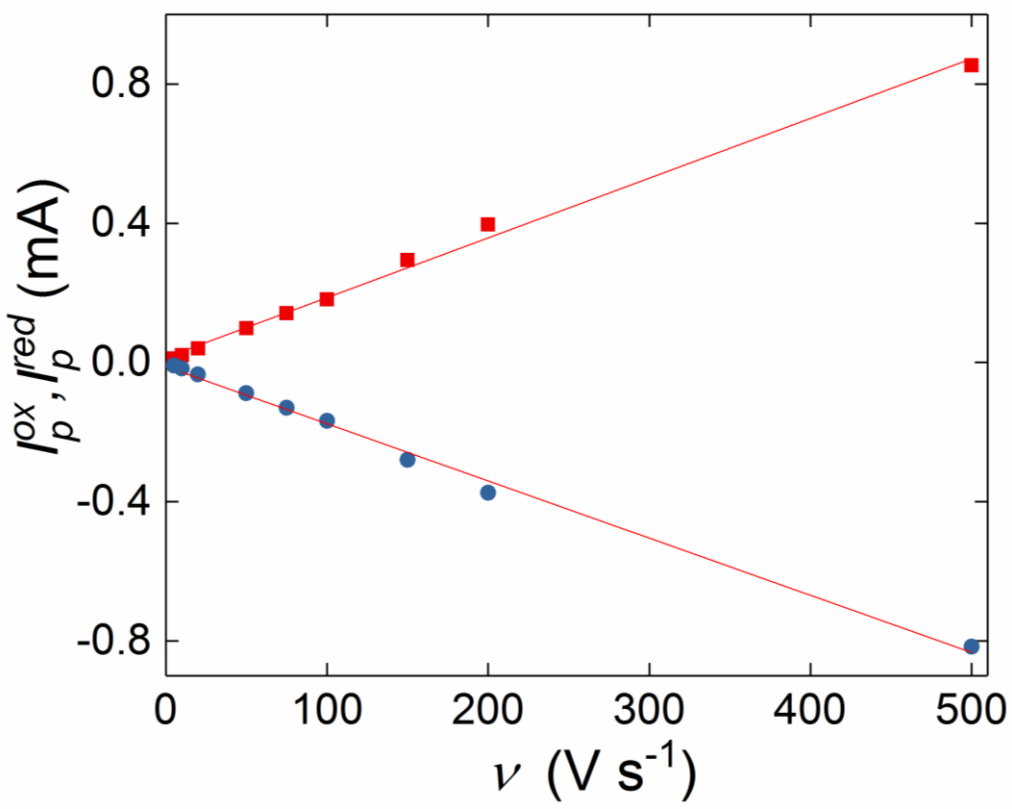

Figure 4.3: Linear dependence of the peak currents with scan rate. A linear dependence of the anodic (red solid squares) and a cathodic (blue solid circles) peak currents with the scan rate ν. The red lines show the linear fit of the points. The linear dependence confirms the electrochemical system to be a surface confined one.

4.2. Non-Catalytic Electrochemical Characteristics of Immobilised (DPDE)Rh^{III}

To delve deep into the overall mechanism, digital simulations of the recorded CVs were used. To achieve this, the $E^0_{1,2,3}$ values, the standard heterogeneous rate constants ($k_0^{1,2,3}$), the chemical rate constants (k_f/k_b), and α must be estimated. These values will then be used in a semi-empirical Butler-Volmer[24] (BV) formalism including the effect of the rate constant to obtain the model predictions, as

$$\frac{i}{FA} = \sum_{j=1}^{3} \frac{i^j}{FA} = -k^j_{\mathrm{red}}\Gamma_{\mathrm{ox}} + k^j_{\mathrm{ox}}\Gamma_{\mathrm{red}} \tag{4.1}$$

where the rate constants of BV model, k^j_{red} and k^j_{ox}, have an exponential dependence with the applied potential which can be written as,

$$\begin{aligned} k^j_{\mathrm{red}} &= k^j_0 e^{-\alpha\frac{F}{RT}\left(E-E^0_j\right)} \\ k^j_{\mathrm{ox}} &= k^j_0 e^{(1-\alpha)\frac{F}{RT}\left(E-E^0_j\right)} \end{aligned} \tag{4.2}$$

The apparent heterogeneous rate constant k_0 and α were estimated from Laviron's formalism[201]. The slopes of the anodic and cathodic peak potentials from Figure 4.4 were 61 mV and -63 mV respectively. From these values, α was estimated to be 0.48 ± 0.01. Thus, we consider $\alpha = 0.5$ for all our simulations and to calculate the heterogeneous rate constant k_0 at a scan rate of $50\ \mathrm{mV/s}$ with $\Delta E = 121\ \mathrm{mV}$. The heterogeneous rate constant for these conditions was calculated as $2.5 \pm 1.5\ \mathrm{s^{-1}}$.

The validity of Laviron's formalism is confirmed by the half-way peak width of 60 mV which is close to the theoretical value of $(62.5/\alpha n)$ mV [201]. This calculated k_0 is relatively slow that it provokes a peak splitting at higher scan rates[202]. An increased ΔE at these scan rates is most likely observed when the time constant of interfacial kinetic is close to the imposed time scale of the voltammetric sweep, RT/Fv. To consolidate this experimental value, we also carried out density function theory (DFT) calculations of the rhodium active site (Appendix) to compute the energy difference between the (DPDE)Rh^{I} and (DPDE)Rh^{III} coordinated to hydroxide via two one-

electron transfer. The estimated interfacial transfer rate constant of $k_0 = 2.16\ s^{-1}$ agrees well with the experimental value.

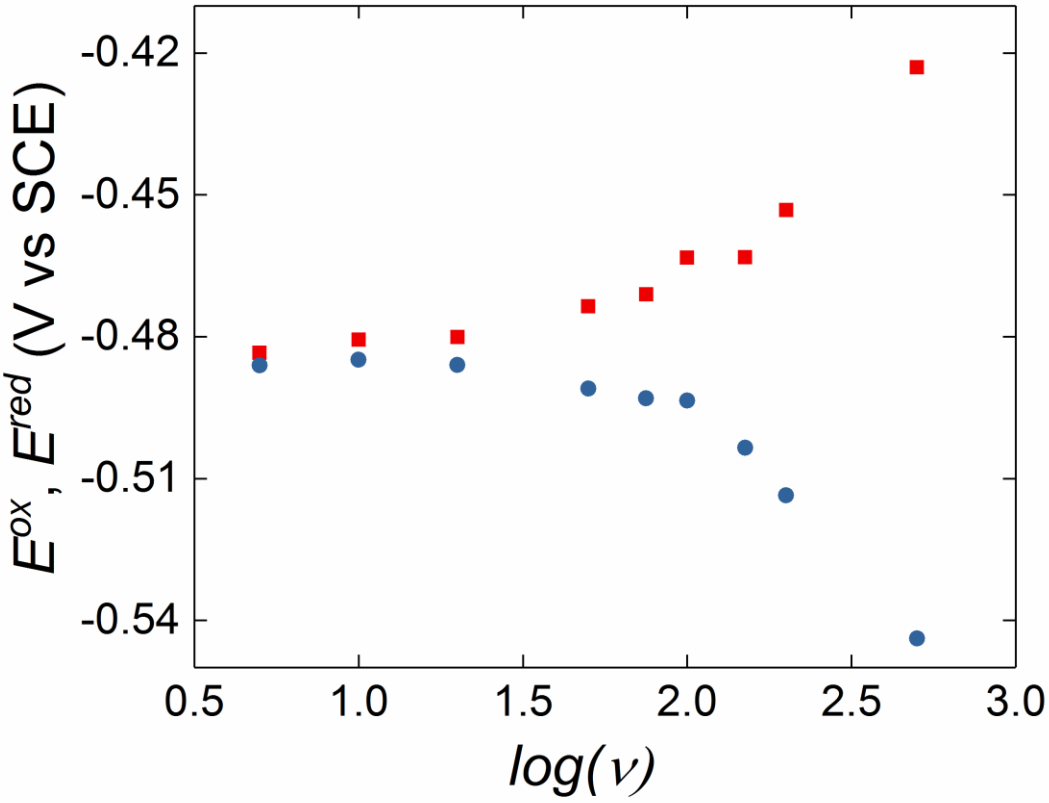

Figure 4.4: Logarithm of the scan rates vs peak potentials. The anodic (red solid squares) and cathodic (blue solid circles) are presented as a function of the logarithm of the scan rates to apply Laviron's theory to evaluate α and k_0.

In addition, at pH 14, the E^0 values for the electrochemical redox couple of the Rh complex was estimated from the experimental CVs and the relation between the chemical coordination rate constant is obtained from the pKa of the equilibrium between $Rh^{III}(OH)$ and Rh^{III} [199].

Numerical analyses of the CV were used to investigate the mechanism model. At higher pH, the characteristics of the voltammogram from Figure 4.2 suggests that the redox of the rhodium complex is a two-electron transfer process at the electrode surface[199,203]. Figure 4.3 presents a typical surface confined behaviour.

The redox complexes (DPDE)Rh^{I} and (DPDE)Rh^{III}, the intermediate (DPDE)Rh^{II}, and inactive (DPDE)Rh^{III}(OH) are represented as Rh^{I}, Rh^{III}, Rh^{II} and Rh^{III}(OH) respectively, and the mechanism is defined by Equation 4.3

$$\begin{gathered} Rh^{III} + e^- \underset{E_1^0}{\overset{k_0^1}{\rightleftharpoons}} Rh^{II} + e^- \underset{E_2^0}{\overset{k_0^2}{\rightleftharpoons}} Rh^{I} \\ Rh^{III} \underset{k_b}{\overset{k_f}{\rightleftharpoons}} Rh^{III}(OH) \\ Rh^{III}(OH) + e^- \underset{E_3^0}{\overset{k_0^3}{\rightleftharpoons}} Rh^{II} + e^- \underset{E_2^0}{\overset{k_0^2}{\rightleftharpoons}} Rh^{I} \end{gathered} \tag{4.3}$$

To describe the model used in this study we start with the mechanism given by Equation 4.3 and define the governing Equation 4.4 where mass transfer is not taken into account.

$$\begin{gathered} \frac{\partial \Gamma_{Rh^{III}}}{dt} = \frac{i^1}{FA} - k_f \Gamma_{Rh^{III}} + k_b \Gamma_{Rh^{III}(OH)} \\ \frac{\partial \Gamma_{Rh^{III}(OH)}}{\partial t} = \frac{i^3}{FA} + k_f \Gamma_{Rh^{III}} - k_b \Gamma_{Rh^{III}(OH)} \\ \frac{\partial \Gamma_{Rh^{II}}}{\partial t} = -\frac{i^1}{FA} - \frac{i^3}{FA} + \frac{i^2_{Rh^{III}/Rh^{I}}}{FA} + \frac{i^2_{Rh^{III}(OH)/Rh^{I}}}{FA} \\ \frac{\partial \Gamma_{Rh^{I}}}{\partial t} = -\frac{i^2_{Rh^{III}/Rh^{I}}}{FA} - \frac{i^2_{Rh^{III}(OH)/Rh^{I}}}{FA} \end{gathered} \tag{4.4}$$

And the total surface concentrations with time are linked to the flowing current:

$$\frac{i}{FA} = \frac{i^1}{FA} + \frac{i^2_{Rh^{III}/Rh^{I}}}{FA} + \frac{i^2_{Rh^{III}(OH)/Rh^{I}}}{FA} + \frac{i^3}{FA} = -\left(\frac{2\partial \Gamma_{Rh^{I}}}{\partial t} + \frac{\partial \Gamma_{Rh^{II}}}{\partial t}\right) \tag{4.5}$$

According to Equation 4.4, the sum of the oxidised and reduced concentrations is a constant number on the electrode surface,

$$\Gamma_{Rh^{I}} + \Gamma_{Rh^{II}} + \Gamma_{Rh^{III}} + \Gamma_{Rh^{III}(OH))} = \Gamma^* \tag{4.6}$$

The applied potential varies with time during the forward and backward sweep of the cyclic voltammetry (CV) as,

$$\begin{gathered} E = E_i + vt \ (dE/dt = v) \\ E = E_v - v(t - t_R) \ (dE/dt = -v) \end{gathered} \tag{4.7}$$

For the model described above, the initial conditions at $t = 0$ are given as

$$\Gamma_{\mathrm{Rh^{III}}} = \Gamma^{*}, \Gamma_{\mathrm{Rh^{III}(OH)}} = 0, \Gamma_{\mathrm{Rh^{II}}} = 0, \Gamma_{\mathrm{Rh^{I}}} = 0 \tag{4.8}$$

And the following boundary conditions result at surface ($x = 0$) as

$$\begin{gathered} \frac{i^1}{FA} = -k^1_{\mathrm{red}}\Gamma_{\mathrm{Rh^{III}}} + k^1_{\mathrm{ox}}\Gamma_{\mathrm{Rh^{II}}} \\ \frac{i^2}{FA} = \frac{i^2_{\mathrm{Rh^{III}/Rh^{I}}}}{FA} + \frac{i^2_{\mathrm{Rh^{III}(OH)/Rh^{I}}}}{FA} = -k^2_{\mathrm{red}}\Gamma_{\mathrm{Rh^{III}}} + k^2_{\mathrm{ox}}\Gamma_{\mathrm{Rh^{II}}} \\ \frac{i^3}{FA} = -k^3_{\mathrm{red}}\Gamma_{\mathrm{Rh^{III}(OH)}} + k^3_{\mathrm{ox}}\Gamma_{\mathrm{Rh^{II}}} \end{gathered} \tag{4.9}$$

The rate constants of BV model, k^j_{red} and k^j_{ox}show an exponential dependence with the applied potential as

$$\begin{gathered} k^j_{\mathrm{red}} = k^j_0 e^{-\alpha\frac{F}{RT}\left(E - E^0_j\right)} \\ k^j_{\mathrm{ox}} = k^j_0 e^{(1-\alpha)\frac{F}{RT}\left(E - E^0_j\right)} \end{gathered} \tag{4.10}$$

The mathematical model of the surface confined system along with its initial and boundary conditions presented above are treated numerically using a Crank-Nicolson method solved by Thomas algorithm. Numerical evaluation of such a complex model uses a mixed compressing-expanding mesh schemes to ensure convergence as well as to reduce the computation runtime[37]. The temporal discretisation employs a classic two-level derivative with sufficiently small timestep $\Delta t = 2 \times 10^{-4}$. Simulations were calibrated against the experimental data following the mentioned conditions and parameters.

Table 4.1: Parameters for calibration of the non-catalytic CVs.

k^2_0/s^{-1}	$K_A = k_{\mathrm{f}}/k_{\mathrm{b}}$	α
3.5	10^7	0.5

Figure 4.5(A) shows the calibration of the simulated CV with use of the values listed in Table 4.1. These values show a good correspondence between the simulated and experimental CV.

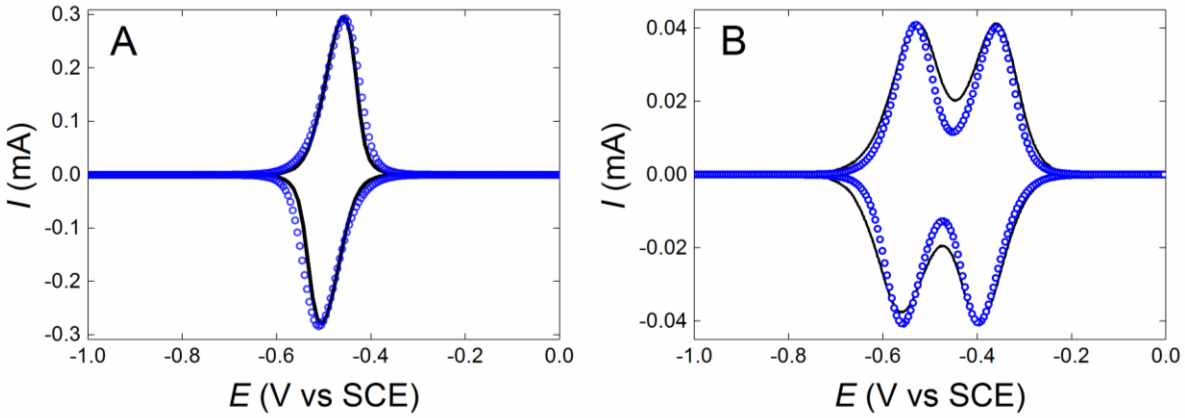

Figure 4.5: Validation of the model predictions for the non-catalytic (DPDE)Rh^{III}. Experimental validation of the simulated CV curve at $\nu = 150$ mV/s and pH 14 (A) and at $\nu = 50$ mV/s and pH 12 (B), assuming Butler-Volmer kinetics and Laviron's model. The solid lines (−) represent experiments and the blue circles (**o**) represent the model predictions.

Moreover, the experimental validation of the model for different scan rates is also presented in Figure 4.6. The simulations were able to accurately describe the trend of the experimental CVs produced at pH 14 with different scan rates. The agreement with experiments suggests that the mechanism of electron transfer follows ECE-type mechanism where a chemical reaction coupled with two electron-transfer reactions, given schematically as

$(\mathrm{DPDE})\mathrm{Rh}^{\mathrm{III}} + \mathrm{e}^- \underset{E_1^0}{\overset{k_0^1}{\rightleftharpoons}} (\mathrm{DPDE})\mathrm{Rh}^{\mathrm{II}} + \mathrm{e}^- \underset{E_2^0}{\overset{k_0^2}{\rightleftharpoons}} (\mathrm{DPDE})\mathrm{Rh}^{\mathrm{I}}$
$(\mathrm{DPDE})\mathrm{Rh}^{\mathrm{III}} + \mathrm{OH}^- \underset{k_\mathrm{b}}{\overset{k_\mathrm{f}}{\rightleftharpoons}} (\mathrm{DPDE})\mathrm{Rh}^{\mathrm{III}}(\mathrm{OH})$
$(\mathrm{DPDE})\mathrm{Rh}^{\mathrm{III}}(\mathrm{OH}) + \mathrm{e}^- \underset{E_3^0}{\overset{k_0^3}{\rightleftharpoons}} (\mathrm{DPDE})\mathrm{Rh}^{\mathrm{II}} + \mathrm{OH}^- + \mathrm{e}^- \underset{E_2^0}{\overset{k_0^2}{\rightleftharpoons}} (\mathrm{DPDE})\mathrm{Rh}^{\mathrm{I}} + \mathrm{OH}^-$
Scheme 4.1: ECE mechanism followed by (DPDE)Rh in the absence of a substrate.

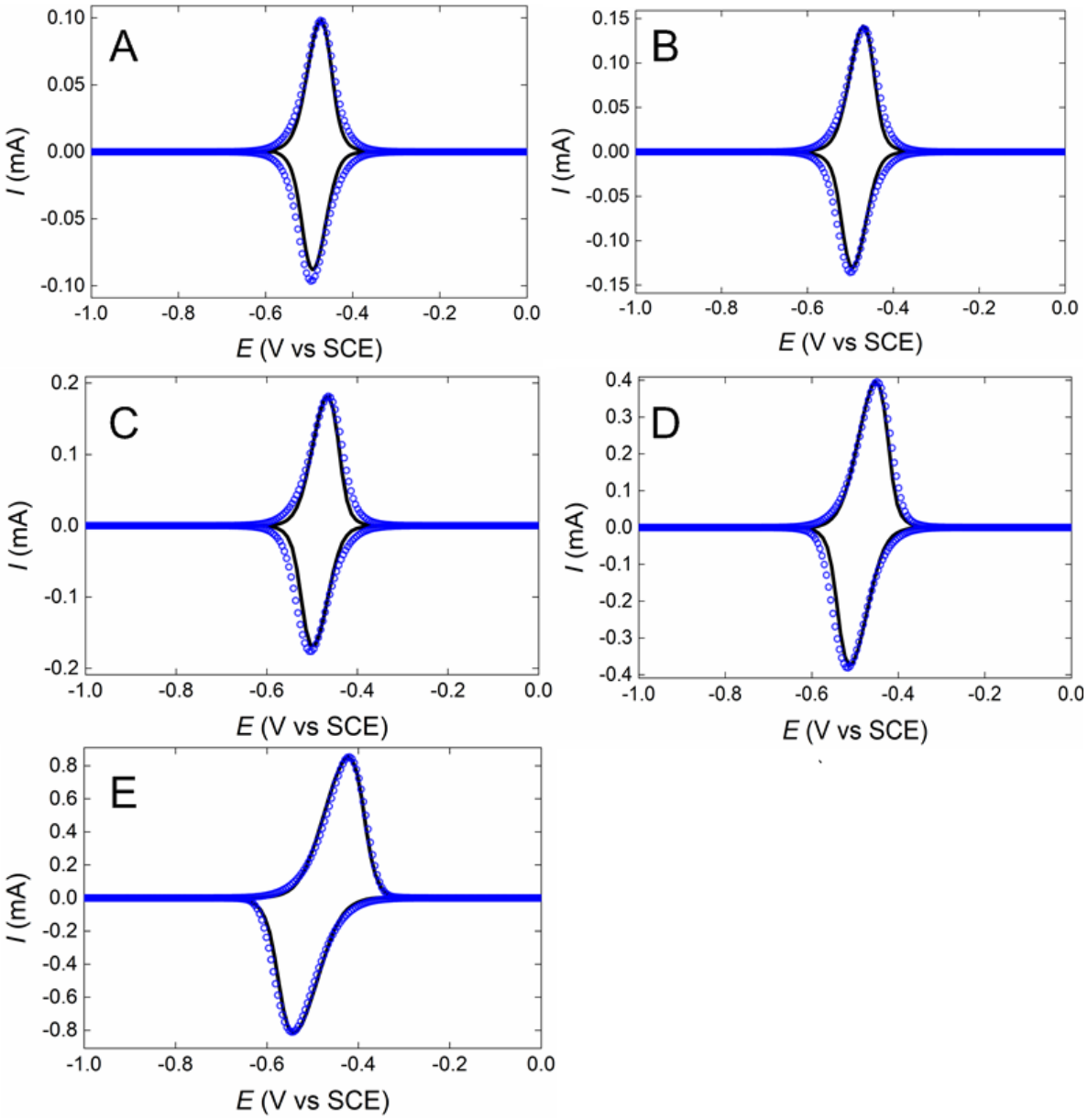

Figure 4.6: Validation of the model predictions for non-catalytic system at different scan rates. The black solid line (−) represent the experiments and the blue circles (o) represent the model predictions at scan rates of 50 mV/s (A), 75 mV/s (B), 100 mV/s (C), 200 mV/s (D) and 500 mV/s (E). These validations are for the experimental data obtained at pH 14. The proposed model according to the Scheme 4.1 successfully captures the voltammetric traces at different scan rates.

According to this mechanism, the reduction wave observed on the forward scan involves two one-electron reductions separated by a chemical step. The chemical step is a hydroxide coordination step producing $Rh^{III}(OH)$ from Rh^{III} [199,204]. The reverse scan shows one wave corresponding to two one-electron oxidations where the reduction of $Rh^{III}(OH)$ to Rh^{I} is thermodynamically more favourable than that of Rh^{III} at pH 14 ($k_f \gg k_b$ and $pKa_{Rh^{III}(OH)|Rh^{III}} = 6.4$)[199,203]. In addition, the ECE scheme presented above, the Rh^{II} intermediate formed is the rate limiting step ($k_0^2 < k_0^1 = k_0^3$) [199] indicating that the lifetime of the Rh^{II} is extremely short to be captured at this pH. Therefore, $k_0 \simeq k_0^2$ which is the rate constant of the formation of the Rh^{II} intermediate.

To ensure further validity of this reaction path, the system was interrogated at a different thermodynamic condition by decreasing the pH value (pH 12). Under this condition, the CV shows that the two one-electron transfer process becomes distinguishable compared to pH 14. Figure 4.5(B) shows the experimental validation of this difference in the responses at pH 14 and pH 12 captured by the mathematical model, which confirms the steps presented in Scheme 4.1.

All the numerical analyses were performed using a traditional finite difference method on the commercial platform MATLAB[205] and the rest parameters used in the mathematical models are listed in Table 4.2.

Table 4.2: Summary of the parameters estimated from experiments employed for the numerical analyses of the non-catalytic behaviour of (DPDE)Rh^{III}.

Parameter	Value	Unit
A (fixed)	1.0 ± 0.2	cm^2
E_i (fixed)	-1.2	V
E_1^0	-0.485 at pH $= 14$ -0.375 at pH $= 12$	V
E_2^0	-0.485 at pH $= 14$ -0.525 at pH $= 12$	V
E_3^0	-0.485 at pH $= 14$ -0.375 at pH $= 12$	V
E_v (fixed)	0.2	V
k_0^1	6.0 at pH $= 14$ 1.8 at pH $= 12$	s^{-1}
k_0^2	3.5 at pH $= 14$ 1.8 at pH $= 12$	s^{-1}
k_0^3	6.0 at pH $= 14$ 1.8 at pH $= 12$	s^{-1}
K_A	10^7	–
α	0.5	–
Γ^* (fixed)	$(6 \pm 1) \times 10^{-10}$	mol cm^{-2}

4.3. Identification of Electrocatalytic Inactivation and Activation Processes (IAPs)

After investigating the characteristics of MWCNT/(DPDE)Rh^{III} electrodes, glucose was introduced as a substrate into the system. Experimental response at $10\ mV/s$ can be observed in Figure 4.7(A). Upon addition of glucose, the current due to glucose oxidation increases, and begins to level off as the potential becomes more positive to reach a maximum value close to $E_{1/2}$ (ca. $-0.485\ V$). As the potential is raised above $E_{1/2}$, the current drops dramatically due to the inactivation mechanism. However, this inactivation is reversed by a reactivation on the subsequent sweep back to a more negative potential. Similar trends of CVs were obtained in hydrogenase/MWCNT/GC with an [NiFe] active site Figure 4.7(A(inset)) as previously reported for an enzymatic IAP[189-192,196,198].

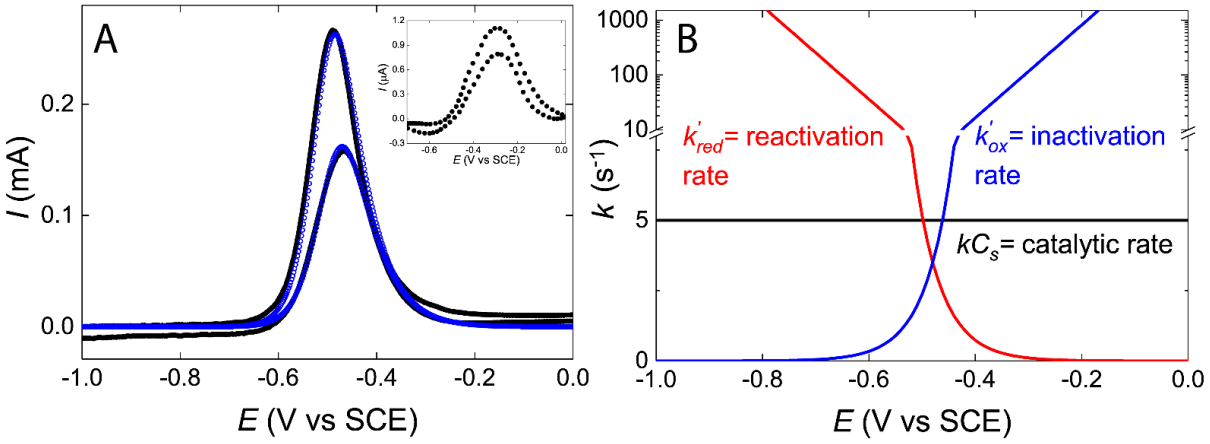

Figure 4.7: Validation of the model predictions for the electrocatalysis of (DPDE)Rh^{III} and the kinetic parameters as a function of the applied potential. Inset: Voltammogram of hydrogenase. Experimental validation of the model predictions showing the electrochemical reactivation of (DPDE)Rh^{III} catalyst in the presence of 50 mM glucose at pH 14 and at $\nu = 10\ mV\ s^{-1}$ (A). Voltammogram of hydrogenase with an [NiFe] active site at 45°C in pH 7.4 under H_2 and at $\nu = 5\ mV\ s^{-1}$ is presented in the inset (A). Kinetic parameters k'_{ox} = inactivation rate (blue line), k'_{red} = reactivation rate (red line) and $k[S]$ = catalytic rate at a substrate concentration of 50 mM, as a function of the applied potential (E) (B).

To analyse the mechanisms for the occurrence of IAP, we adopt a new scheme derived from the combination of the aforementioned ECE scheme 1 and Limoges and Savéant's enzymatic catalytic scheme[193].

The mechanism is interpreted using an EC'CE scheme which connects the active and inactive forms according to electrochemical terminology[24]. At pH 14, the electrochemical steps are simplified to involve simultaneous two electron transfer processes during the catalytic cycle. The form of this EC'CE reaction is summarised in Scheme 4.2,

$$(\mathrm{DPDE})\mathrm{Rh^{III}} + 2\mathrm{e^-} \underset{k_{\mathrm{ox}}}{\overset{k_{\mathrm{red}}}{\rightleftharpoons}} (\mathrm{DPDE})\mathrm{Rh^{I}}$$

$$(\mathrm{DPDE})\mathrm{Rh^{I}} + [\mathrm{S}] \xrightarrow{k} (\mathrm{DPDE})\mathrm{Rh^{III}} + [\mathrm{P}]$$

$$(\mathrm{DPDE})\mathrm{Rh^{III}} + \mathrm{OH^-} \underset{k_{\mathrm{b}}}{\overset{k_{\mathrm{f}}}{\rightleftharpoons}} (\mathrm{DPDE})\mathrm{Rh^{III}}(\mathrm{OH})$$

$$(\mathrm{DPDE})\mathrm{Rh^{III}}(\mathrm{OH}) + 2\mathrm{e^-} \underset{k'_{\mathrm{ox}}}{\overset{k'_{\mathrm{red}}}{\rightleftharpoons}} (\mathrm{DPDE})\mathrm{Rh^{I}} + \mathrm{OH^-}$$

Scheme 4.2: EC'CE reaction mechanism of the IAP at pH 14.

k_{red}, k_{ox}, k'_{red}, and k'_{ox} are the rate constants of the electrochemical reactions and k, k_{f} and k_{b} are the rate constants of the chemical reactions. The surface reaction is suggested to follow the empirical BV formalism for electron transfer and the diffusion of glucose obeys Fick's law in the solution.

The robustness and validity of Scheme 4.2 was evaluated by mathematical models. The equations for the model used in the EC'CE simulations are derived as follows:

The governing equations for the surface concentrations of the rhodium species are

$$\begin{aligned}\frac{\partial \Gamma_{\mathrm{Rh^{I}}}}{\partial t} &= -\frac{i_{\mathrm{Rh^{III}/Rh^{I}}}}{nFA} + k[\mathrm{S}]\Gamma_{\mathrm{Rh^{III}}} - \frac{i_{\mathrm{Rh^{III}(OH)/Rh^{I}}}}{nFA} \\ \frac{\partial \Gamma_{\mathrm{Rh^{III}}}}{dt} &= \frac{i_{\mathrm{Rh^{III}/Rh^{I}}}}{nFA} - k[\mathrm{S}]\Gamma_{\mathrm{Rh^{III}}} - k_{\mathrm{f}}\Gamma_{\mathrm{Rh^{III}}} + k_{\mathrm{b}}\Gamma_{\mathrm{Rh^{III}(OH)}} \\ \frac{\partial \Gamma_{\mathrm{Rh^{III}(OH)}}}{\partial t} &= k_{\mathrm{f}}\Gamma_{\mathrm{Rh^{III}}} - k_{\mathrm{b}}\Gamma_{\mathrm{Rh^{III}(OH)}} + \frac{i_{\mathrm{Rh^{III}(OH)/Rh^{I}}}}{nFA}\end{aligned} \tag{4.11}$$

The total surface concentration is constant and can be given as

$$\Gamma_{\mathrm{Rh^{I}}} + \Gamma_{\mathrm{Rh^{III}}} + \Gamma_{\mathrm{Rh^{III}(OH)}} = \Gamma^{*} \tag{4.12}$$

Substrate transport to the electrode is given by the linear diffusion equation as

$$\frac{\partial [\mathrm{S}]}{\partial t} = D_{\mathrm{s}}\frac{\partial^{2}[\mathrm{S}]}{\partial x^{2}} - k[\mathrm{S}]\Gamma_{\mathrm{Rh^{III}}} \tag{4.13}$$

The contributions to the measured current are given as $i_{\mathrm{Rh^{III}/Rh^{I}}}$ and $i_{\mathrm{Rh^{III}(OH)/Rh^{I}}}$ corresponding to the oxidation of (DPDE)$\mathrm{Rh^{I}}$ to (DPDE)$\mathrm{Rh^{III}}$ and the reduction of (DPDE)$\mathrm{Rh^{III}}$(OH) to (DPDE)$\mathrm{Rh^{I}}$, respectively. The total current for an applied potential is given as,

$$\begin{aligned} i &= i_{\mathrm{Rh^{III}/Rh^{I}}} + i_{\mathrm{Rh^{III}(OH)/Rh^{I}}} \\ &= [-k_{\mathrm{red}}\Gamma_{\mathrm{Rh^{III}}} + k_{\mathrm{ox}}\Gamma_{\mathrm{Rh^{I}}}] + \left[-k'_{\mathrm{red}}\Gamma_{\mathrm{Rh^{III}(OH)}} + k'_{\mathrm{ox}}\Gamma_{\mathrm{Rh^{I}}}\right] \end{aligned} \tag{4.14}$$

The contributions to the measured current are given as $i_{\mathrm{Rh^{III}/Rh^{I}}}$ and $i_{\mathrm{Rh^{III}(OH)/Rh^{I}}}$ corresponding to the oxidation of (DPDE)$\mathrm{Rh^{I}}$ to the catalytically active (DPDE)$\mathrm{Rh^{III}}$ and the reduction of the inactive form (DPDE)$\mathrm{Rh^{III}}$(OH) to (DPDE)$\mathrm{Rh^{I}}$, respectively. The initial conditions in the system are

$$\Gamma_{\mathrm{Rh^{I}}} = \Gamma^{*}, \Gamma_{\mathrm{Rh^{III}}} = \Gamma_{\mathrm{Rh^{III}(OH)}} = 0, [\mathrm{S}] = [\mathrm{S}]^{*} \tag{4.15}$$

Assuming that semi-infinite linear diffusion conditions hold, the boundary conditions can be defined as

$$\frac{i_{\mathrm{Rh^{III}/Rh^{I}}}}{nFA} = k_{\mathrm{ox}}\Gamma_{\mathrm{Rh^{I}}} - k_{\mathrm{red}}\Gamma_{\mathrm{Rh^{III}}}$$
$$\frac{i_{\mathrm{Rh^{III}(OH)/Rh^{I}}}}{nFA} = -k'_{\mathrm{red}}\Gamma_{\mathrm{Rh^{III}(OH)}} + k'_{\mathrm{ox}}\Gamma_{\mathrm{Rh^{I}}} \quad (4.16)$$

$$x \to \infty, [\mathrm{S}] = [\mathrm{S}]^{*} \quad (4.17)$$

From the electron transfer rate constant k_0 obtained in the previous section, the rate constants for the reactivation step can be given following the BV model as

$$k'_{\mathrm{red}} = k'_0 e^{-\alpha\frac{F}{RT}\left(E - E^0_{\mathrm{Rh^{III}(OH)/Rh^{I}}}\right)}$$
$$k'_{\mathrm{ox}} = k'_0 e^{(1-\alpha)\frac{F}{RT}\left(E - E^0_{\mathrm{Rh^{III}(OH)/Rh^{I}}}\right)} \quad (4.18)$$

with the electron transfer rate constant for the last equation in Scheme 4.2, k'_0 is assumed to be proportional to k_0, as both are electron transfer limited reactions, according to the relation

$$k_0 = \Phi k'_0 \quad (4.19)$$

The standard potentials of both the electrochemical reactions in Scheme 4.2 are assumed to be equal according to the Pourbaix diagram of the system at pH 14,

$$E^0_{\mathrm{Rh^{III}(OH)/Rh^{I}}} = E^0_{\mathrm{Rh^{III}/Rh^{I}}} \quad (4.20)$$

Hence, the relationship between the total current versus the applied potential is given by Equation 4.21

$$i = i_{\mathrm{Rh^{III}/Rh^{I}}} + i_{\mathrm{Rh^{III}(OH)/Rh^{I}}}$$
$$= nFAk_0[e^{(1-\alpha)\frac{F}{RT}\left(E - E^0_{\mathrm{Rh^{III}/Rh^{I}}}\right)}(1+\Phi)\Gamma_{\mathrm{Rh^{I}}}$$
$$- e^{-\alpha\frac{F}{RT}\left(E - E^0_{\mathrm{Rh^{III}/Rh^{I}}}\right)}\left(\Gamma_{\mathrm{Rh^{III}(OH)}} - \Phi\Gamma_{\mathrm{Rh^{III}}}\right)] \quad (4.21)$$

Parameter estimation was carried out using the experimental data for different values of Φ to obtain k_0, k, k_{f}, k_{b}, and k'_0 found in Table 4.3.

To the best of our knowledge, obtaining a closed form analytical solution for the system of partial differential equations presented here is not straight forward. Therefore, a numerical integration

procedure is adopted and is implemented using the same finite difference solver mentioned in ECE mechanism to obtain the model predictions[24,37,206,207].

Table 4.3: Summary of the parameters estimated from experiments for the numerical analyses of IAP.

Parameter	Value	Unit
A (fixed)	1.0 ± 0.2	cm^2
$E^0_{\mathrm{Rh^{III}/Rh^{I}}}$	-0.45 ± 0.03	V
$E^0_{\mathrm{Rh^{III}(OH)/Rh^{I}}}$	-0.45 ± 0.03	V
E_i (fixed)	-1.2	V
E_v (fixed)	0.2	V
F (fixed)	96485	$\mathrm{C\ mol^{-1}}$
k	$(1 \pm 0.1) \times 10^5$	$\mathrm{cm^3\ s^{-1}\ mol^{-1}}$
k_0	3.5	$\mathrm{s^{-1}}$
K_A	10^7	–
n (fixed)	2	–
R (fixed)	8.3145	$\mathrm{J\ mol^{-1}\ K^{-1}}$
T (fixed)	293.15	K
α	0.5	–
Γ^* (fixed)	$(11 \pm 1) \times 10^{-10}$	$\mathrm{mol\ cm^{-2}}$
Φ	1 ± 0.1	–

The validation of the model for 150 mM at 10 mV/s is presented and for other set of experiments performed at different scan rates in Figure 4.7(A) and Figure 4.8 and 4.9, respectively. The agreement between the calculated and experimental CVs is good over a range of scan rates.

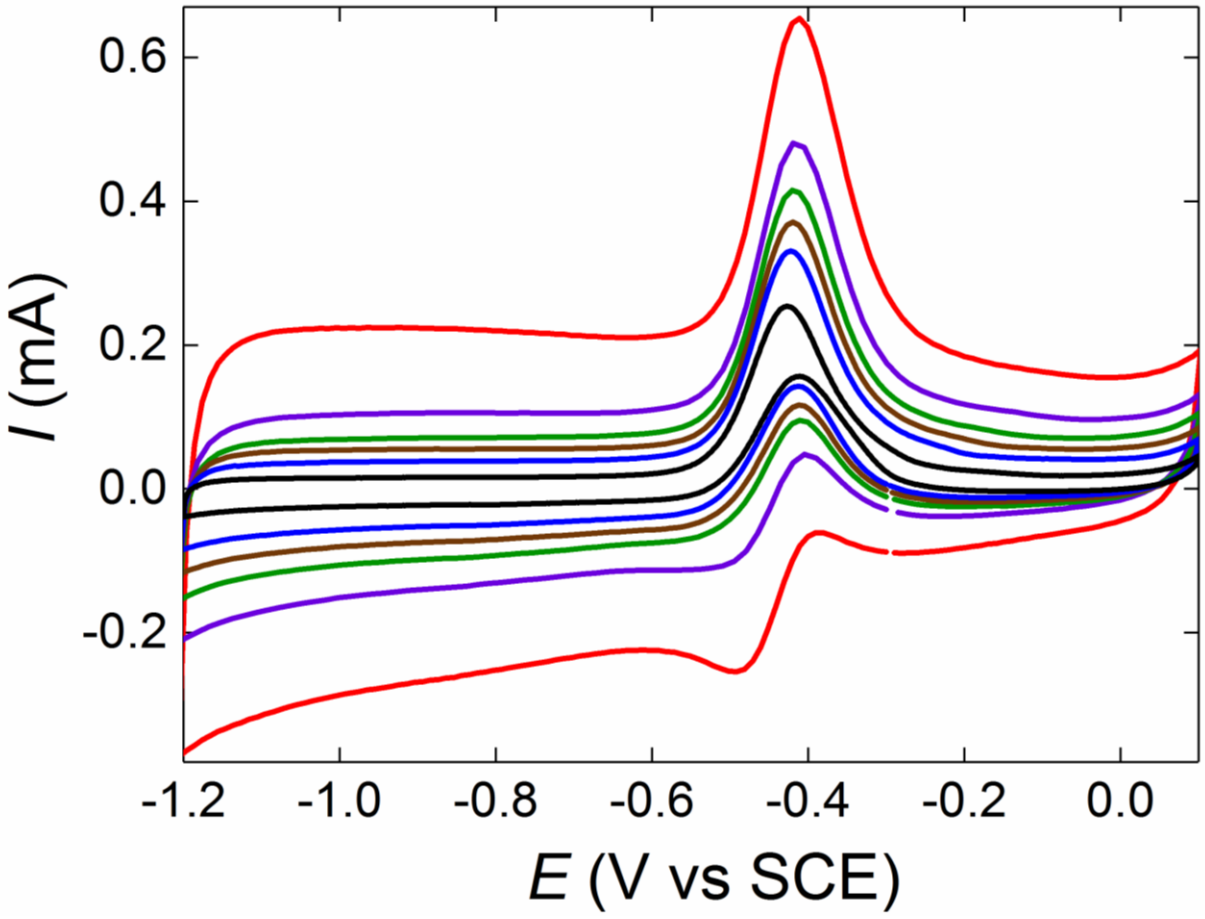

Figure 4.8: Experimental cyclic voltammograms for the catalytic system at different scan rates. Experimental voltammogram obtained for the catalytic behaviour of (DPDE)Rh^{III} in the presence of 150 mM glucose at $\nu = 20$ mV/s (black line), 50 mV/s (blue line), 75 mV/s (brown line), 100 mV/s (green line), 150 mV/s (purple line) and 200 mV/s (red line).

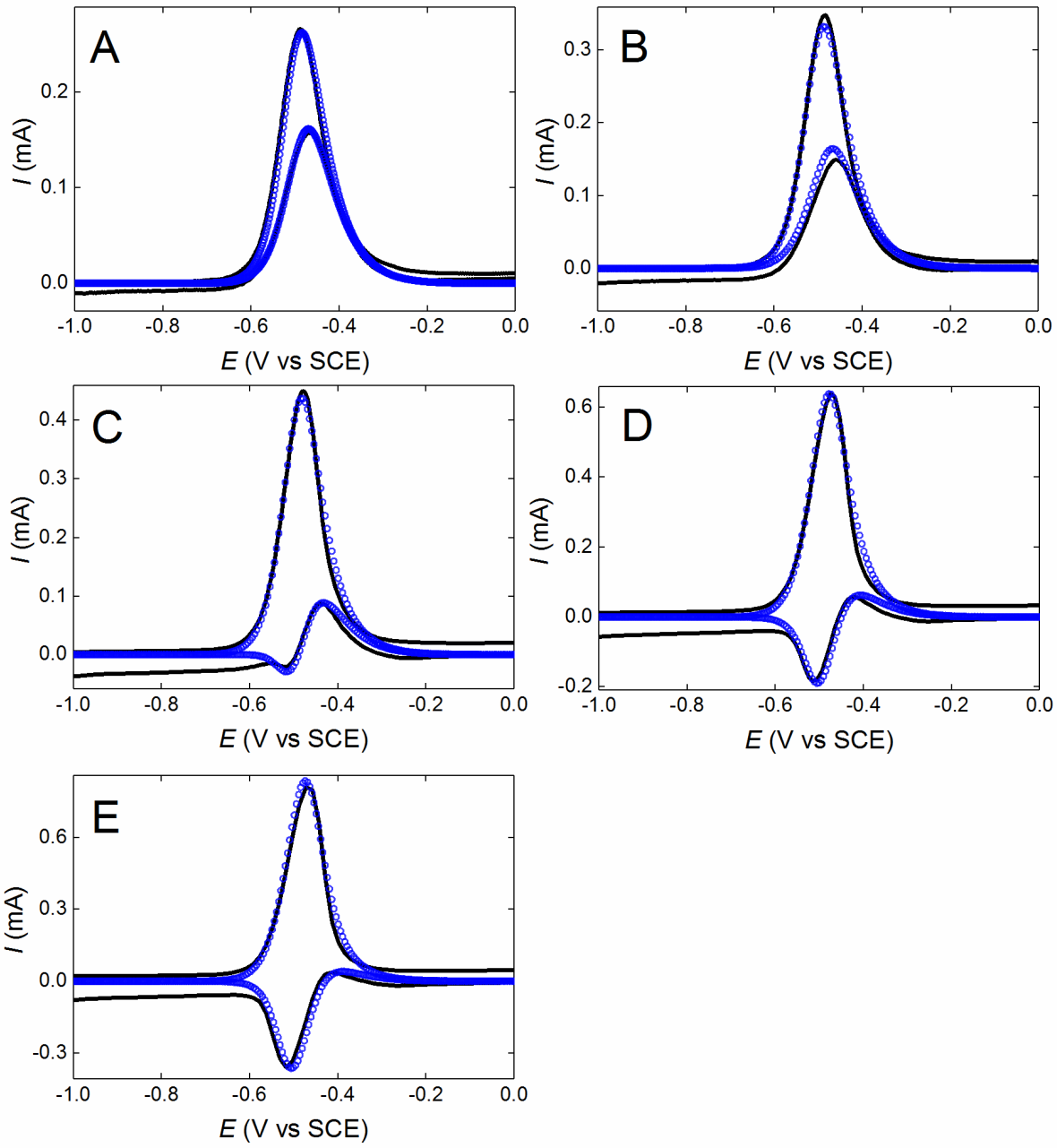

Figure 4.9: Validation of the model predictions for the catalytic system at different scan rates. The black solid line (−) represent the experiments and the blue circles (o) represent the model predictions at scan rates of 10 mV/s (A), 20 mV/s (B), 50 mV/s (C), 100 mV/s (D) and 150 mV/s (E) for a substrate concentration [S] of 50 mM. These validations are for the experimental data obtained at pH 14. The proposed model according to the Scheme 4.2 successfully captures the voltammetric traces at different scan rates.

Before discussing the mechanistic implications of scan rates and concentrations, we first explain how a subtle combination of thermodynamics and kinetics of the reactions results in the twisted reverse CV. This can be obtained by analysing the dependence of k'_{red} (reactivation rate) and k'_{ox} (inactivation rate) on potential. For this reason, we have applied the validated EC'CE model to generate the profiles of k'_{red} and k'_{ox} as well as the 3D surface concentration profiles of all the electroactive species at a given potential range which is important to indicate the limiting process and predict the pathway that the system follows. The generated curves are presented in Figure 4.7(B) and 4.10. From Figure 4.7(B), the rate of activation and inactivation are symmetrical, and both are dependent on the potential unlike the rate constants of a few enzymatic systems reported earlier[198]. This attributes to the reductive oxidation peak being quasi-symmetrical to the oxidation peak in Figure 4.7(A).

During the forward scan, k'_{ox} (inactivation rate) increases exponentially when the potential increases and dominates the process under very oxidising conditions Figure 4.7(B) in sharp contrast with the result collected for hydrogenase where the rate of inactivation is independent of potential [198]. This difference in terms of rate of inactivation engenders a sharper decreasing slope on the forward scan for the present catalyst molecular catalyst. Mechanistically, by increasing the potential, the catalytically active form (DPDE)Rh^{I} is oxidised to (DPDE)Rh^{III} in Figure 4.10(A) and 4.10(B). The chemical inactivation reaction can be considered as quasi-irreversible because the rate of the chemical coordination step, k_{f} has a value 10^{7} times higher than k_{b} (Table 4.3). This suggests that the coordination of the generated $(\mathrm{DPDE})\mathrm{Rh}^{\mathrm{III}}$ and formation of chemically inactive (DPDE)Rh^{III}(OH) is the dominating process at high potential yielding a high surface concentration of $(\mathrm{DPDE})\mathrm{Rh}^{\mathrm{III}}(\mathrm{OH})$ after attaining $0.2\mathrm{V}$ as seen in in the Nernst plot in Figure 4.10(C) compared to Figure 4.10(A) and 4.10(B). The catalytic current dramatically dropping to almost 0 A is a consequence of this non-regeneration of (DPDE)Rh^{III}. The fact that the rate of activation tends to zero at high potential confirms that the reactivation process is only driven by an electron transfer from the electrode.

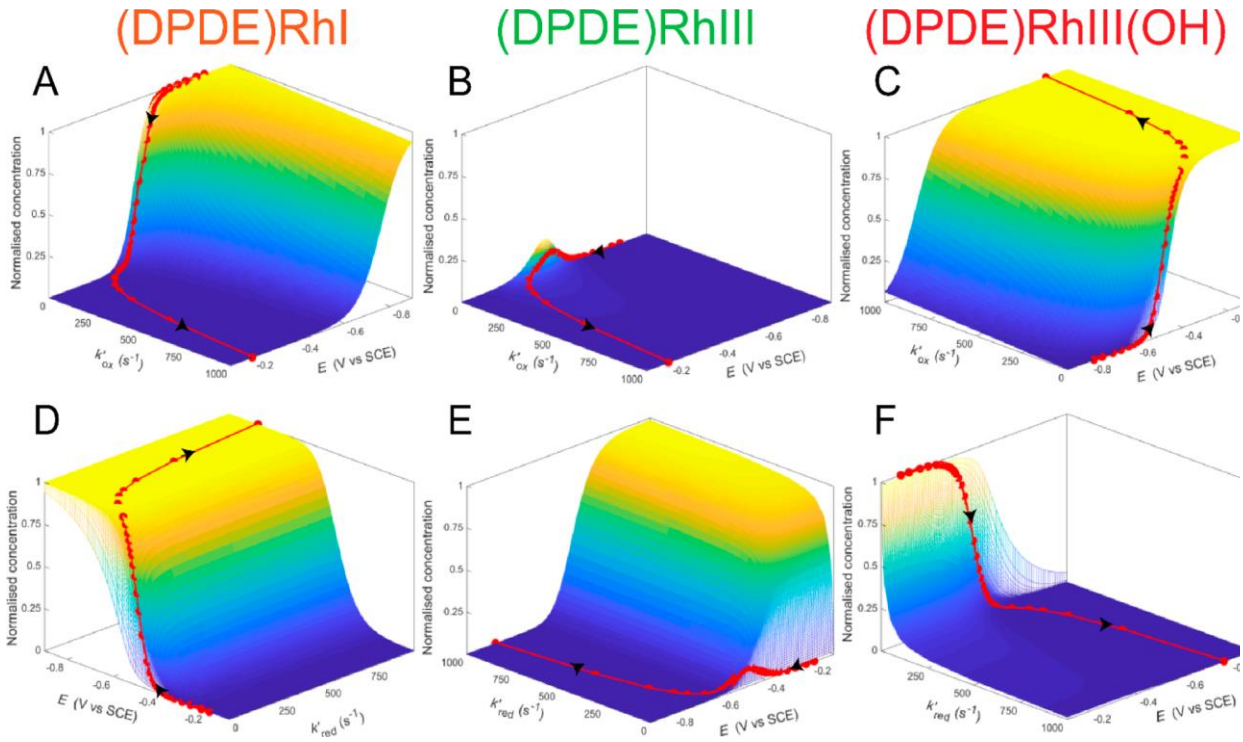

Figure 4.10: Nernst plot relating the normalised concentration of (DPDE)Rh^{I} with the inactivation rate constant k'_{ox} (A) and reactivation rate constant k'_{red} (D) and the applied potential; Nernst plot relating the normalised concentration of (DPDE)Rh^{III} with the inactivation rate constant k'_{ox} (B) and reactivation rate constant k'_{red} (E) and the applied potential; and Nernst plot relating the normalised concentration of (DPDE)Rh^{III}(OH) with the inactivation rate constant k'_{ox} (C) and reactivation rate constant k'_{red} (F) and the applied potential.

In contrast, k'_{red} (activation rate) increases exponentially when the potential decreases and governs the process at very negative potential. Similar dependence has been observed for hydrogenase[198]. As the backward scan commences, the large generated surface concentration of (DPDE)Rh^{III}(OH) in Figure 4.10(F) gets electrochemically reduced into (DPDE)Rh^{I} intermediate (ready) when the potential approaches $E_{1/2}$. (DPDE)Rh^{I} is referred to as an intermediate here, as it gets oxidised spontaneously to form (DPDE)Rh^{III} owing to the high rate constant k'_{ox} at the operating potential ($E \geq E_{1/2} = -0.485$ V) in Figure 4.7. During this oxidation process, there exists a competition between the coordination of glucose and the coordination of hydroxide. However, the surface concentration of $(\mathrm{DPDE})\mathrm{Rh}^{\mathrm{III}}(\mathrm{OH}) \gg (\mathrm{DPDE})\mathrm{Rh}^{\mathrm{III}}(\mathrm{glucose})$ (Figure 4.10(E) and 4.10(F)) in this potential range and thus, the formation of (DPDE)Rh^{III}(glucose) is not thermodynamically favoured till the potential approaches $E_{1/2}$. An increase in the concentration of (DPDE)Rh^{III} in Figure 4.10(E), explains the appearance of the reductive reactivation catalytic peak due the catalytic oxidation of glucose, as seen in Figure 4.5.

Moreover, from Figure 4.7, the rate of activation and inactivation are symmetrical, and both are dependent on the potential unlike the rate constants of a few enzymatic systems reported earlier[198].

4.4. Mechanistic Analysis of Kinetics of the Reactions

After investigating and expounding the mechanism leading to the odd shape in the previous section, we now examine the EC'CE model whether it is able to reproduce the available kinetic data at different operating conditions. From Figure 4.8, it can be observed that the shape of the CVs is very sensitive to scan rates. Thus, the contribution of each reaction varies according to its kinetic parameters. To include depth to the analysis, the effect of scan rate was taken into account for the model predictions and the validation is provided in Figure 4.9.

One immediate inference is that, as the scan rate decreases, the reactivation (twisted peak) becomes more apparent. In contrast, at high scan rate a reductive peak appears. With further increase in scan rate, the reduction peak becomes more dominant. Two factors could lead to such behaviour: First, the rate of the catalytic chemical reaction which is a second order reaction. For a better use of this factor, this reaction should be converted to a first order reaction by multiplication with the concentration (reaction turnover) and its reciprocal equates the time constant of the catalytic reaction as $t_c = 1/k[S]$. The second factor is the natural time scale of voltammetry given as $t_v = RT/Fv$. By comparison of these two factors which measure the interference of the inactivation reaction against the time-scale of the experiment governed by the scan rate, the change of the CV shapes can be explained based on the validated EC'CE mechanism.

The t_c is 0.2 s for a glucose concentration of 50 mM (Figure 4.9). For $v = 10$ mV/s, $t_v \gg t_c$ and this condition yields a twisted peak in the reductive scan and no reduction peak corresponding to the reduction of (DPDE)Rh^{III}(OH) can be obtained (Figure 4.9(A) and 4.9(B)). In this case, the catalytic reaction is fast relative to the time scale of the experiment. As t_c approaches t_v, a distinguishable reduction peak is obtained in addition to the twisted peak (at $v = 100$ mV/s) (Figure 4.9(C) and 4.9(D)). Here, the chemical reaction is in the same range with respect to the time scale of the experiment. However, at $v \geq 200$ mV/s, $t_v \ll t_c$ and the electroreduction (DPDE)Rh^{III}(OH) to (DPDE)Rh^{I} is dominating the process and theoretically, as $v \to \infty$, the reduction peak becomes purely reversible. This condition explains that the electrocatalysis does not proceed under fast scan rate because of the slow catalytic turnover and the rapid electroreduction by two-electron transfer of any formed (DPDE)Rh^{III}(OH) quenches the catalytic reaction and thus the whole cycle. In other words, the reactivation period is shortened at relatively fast scan rate or even absent at very fast scan rate. Therefore, the twisted peak corresponds to the

entire catalytic cycle and the reduction peak corresponds to the electrochemical regeneration of (DPDE)Rh^{I} from (DPDE)Rh^{III}(OH) by the electrode. This behaviour is in consensus with the effect of the kinetic parameter, $\lambda = k[S]/v$ discussed by Savéant *et al.*[193].

It is expected that the above reasoning should not fail when t_c changes by changing substrate concentrations [S] at a fixed experiment time scale. To check this, we performed experiments at different [S]. Figure 4.11 presents the resulting CVs as well as their validations for different values of t_c. At small t_c values ([S] large, high turnover), the contribution of the catalytic rate constant engenders the twisted peak behaviour in Figure 4.11(C) and 4.11(D). In contrast, for a large t_c value ([S] small, low turnover), the electroreduction peak is obtained. In addition, it should be noted that, when t_c for Figure 4.11(B) was decreased through forced convection by a rotating disk electrode (RDE) at 2500 rpm ([S] and v unchanged), the reduction peak disappears. Compared to the stagnant medium, the convective flux at the RDE increases the catalytic turnover which in turn decreases the t_c. These arguments further bolster the above reasoning.

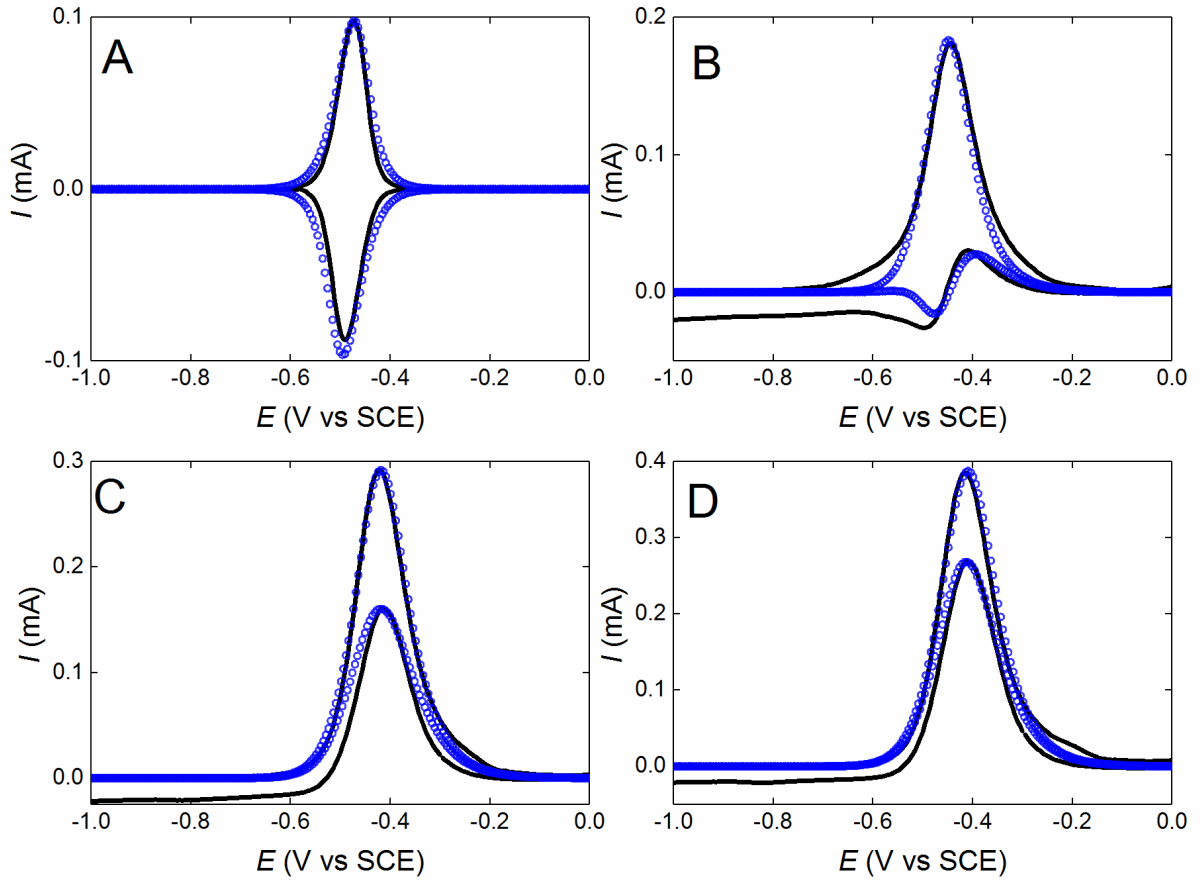

Figure 4.11: Validation of the model predictions of (DPDE)Rh^{III} for different λ. Experimental validation of the model predictions of the catalytic behaviour of (DPDE)Rh^{III} at $v = 50$ mV/s for $\lambda = k[S]/v$ at the substrate concentration $[S] = 0$ mM (A), 50 mM (B), 150 mM (C) and 225 mM (D). The solid lines (−) represent experiments and the blue circles (**o**) represent the model predictions.

4.5. Mechanistic Analysis of Kinetics via Using Hydrogenase Parameter E_{switch}

Considering that E_{switch} is extensively used in enzymatic research to characterize hydrogenases, the analysis of the molecular IAP with respect to E_{switch} was studied in a similar way to that of hydrogenase IAPs. E_{switch} was introduced by Armstrong *et al.* and is a potential value at which the enzyme undergoes reductive reactivation with a switch on potential[196]. The switch potential can be calculated from the first derivative $\mathrm{d}i/\mathrm{d}E$ of the CV, where the minimum corresponds to the E_{switch} potential.

As noted before, the experiments recorded successively with the same (DPDE)Rh^{III} electrode at 6 different scan rates (Figure 4.8), shows that the shape of the derivative $\mathrm{d}i/\mathrm{d}E$ curves is strongly dependent on scan rate (Figure 4.11). An E_{switch} at -0.367 V can be observed corresponding to the reductive interconversion between the inactive and active form. The profile of the $\mathrm{d}i/\mathrm{d}E$ curve showing E_{switch} is strikingly similar to the $\mathrm{d}i/\mathrm{d}E$ curve of hydrogenase with an [NiFe] active site at 45℃ in pH 7.4 under H_2 (Figure 4.11(inset)). It is noteworthy that the E'_{switch} at -0.525 V appears at $\nu \geq 100$ mV/s and gets more pronounced and dominating as scan rate increases, while the E_{switch} at -0.367 V significantly decreases and disappears at 200 mV/s. Additionally, at $\nu = 10$ mV/s, $t_{\text{v}} \gg t_{\text{c}}$ yields only one E_{switch}. E_{switch} is actually the potential, at which the catalytic turnover is inferior to the reciprocal of the natural time constant of the experiment. As $t_{\text{c}} \rightarrow t_{\text{v}}$, both the E_{switch} and E'_{switch} coexist (at $\nu = 100$ mV/s). During this transition state, the value of E_{switch} is slightly shifting from the fact that another E_{switch} is appearing. This may be key to explain the dependence of E_{switch} value on scan rate and the effect of the electrical wiring of hydrogenase[20]. At $t_{\text{v}} \ll t_{\text{c}}$, the catalytic reaction cannot be captured and only E'_{switch} corresponding to the regeneration of (DPDE)Rh^{I} can be obtained. E'_{switch} is the potential at which the catalytic turnover is greater than the reciprocal of the natural time constant of the CV. Therefore, E_{switch} corresponds to the entire catalytic cycle and E'_{switch} corresponds to the electrochemical regeneration of (DPDE)Rh^{I} from (DPDE)Rh^{III}(OH).

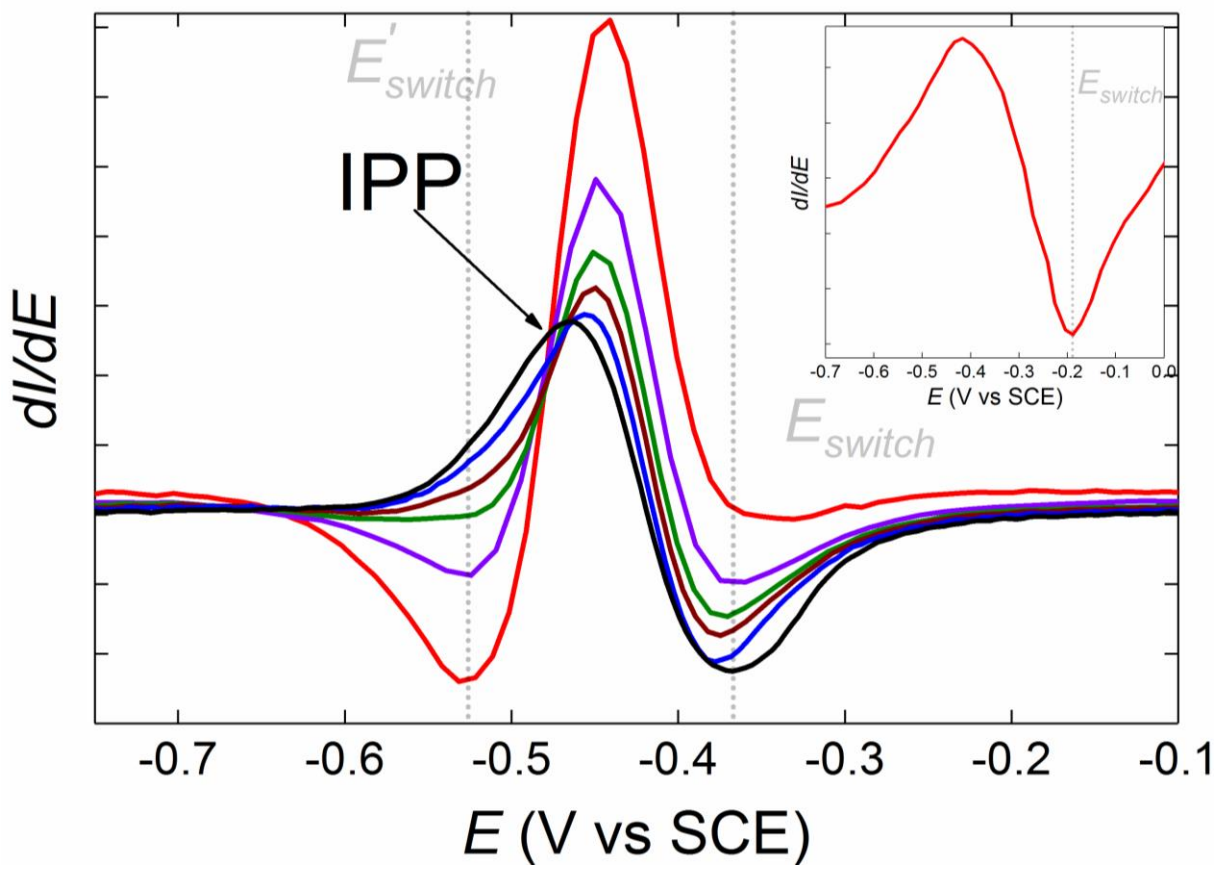

Figure 4.12: E_{switch} Inset: E_{switch} for hydrogenase catalysis. Derivative of the current/potential profile during the reductive scan of the voltammogram obtained for the catalytic behaviour of (DPDE)Rh^{III} in the presence of 150 mM glucose at $\upsilon = 20$ mV/s (black line), 50 mV/s (blue line), 75 mV/s (brown line), 100 mV/s (green line), 150 mV/s (purple line) and 200 mV/s (red line). The inset presents the derivative of the current/potential profile during the reductive scan of the voltammogram obtained for the catalytic behaviour of hydrogenase with an [NiFe] active site in pH 7.4 at 45℃ under H_2 at $\upsilon = 5$ mV/s.

Another proof supporting the switch mechanism is the occurrence of an isopotential point[208,209] (IPP) at -0.477 V in Figure 4.12. An IPP, the electrochemical equivalent to an isosbestic point in spectroscopy, arises in voltammetry when one electroactive species undergoes a transformation to another. The existence of an IPP implies that the transformation is quantitative, and the sum of the reactants and products remain constant. If there are any side reactions involving either set of species, an IPP will not be ensued. Therefore, the IPP in Figure 4.12 is attributed to the transition between E_{switch} and E'_{switch}. IPP is observed for this molecular catalyst, but, to the best of our knowledge never for a system where hydrogenase is immobilized. This is consistent with the fact that electronic connection of the hydrogenase active site to the electrode is very tricky compared to the present molecular catalyst.

Our results conclude that E_{switch} is not the reduction potential of the inactive or active form at different operating potentials but it strongly depends on the reduction potential of the inactive form and/or reaction(s) responsible for the reactivation process. Experimentally, this dependence is related to the quality of the electrical connection of the inactive and active site to the electrode, the profile of the rate constant of reactivation and the imposed time scale of the CV. Following these results, the catalytic mechanism for the overall IAP is presented in Figure 4.13 in a way similar to that of a hydrogenase catalytic cycle (Figure 4.13(inset)).

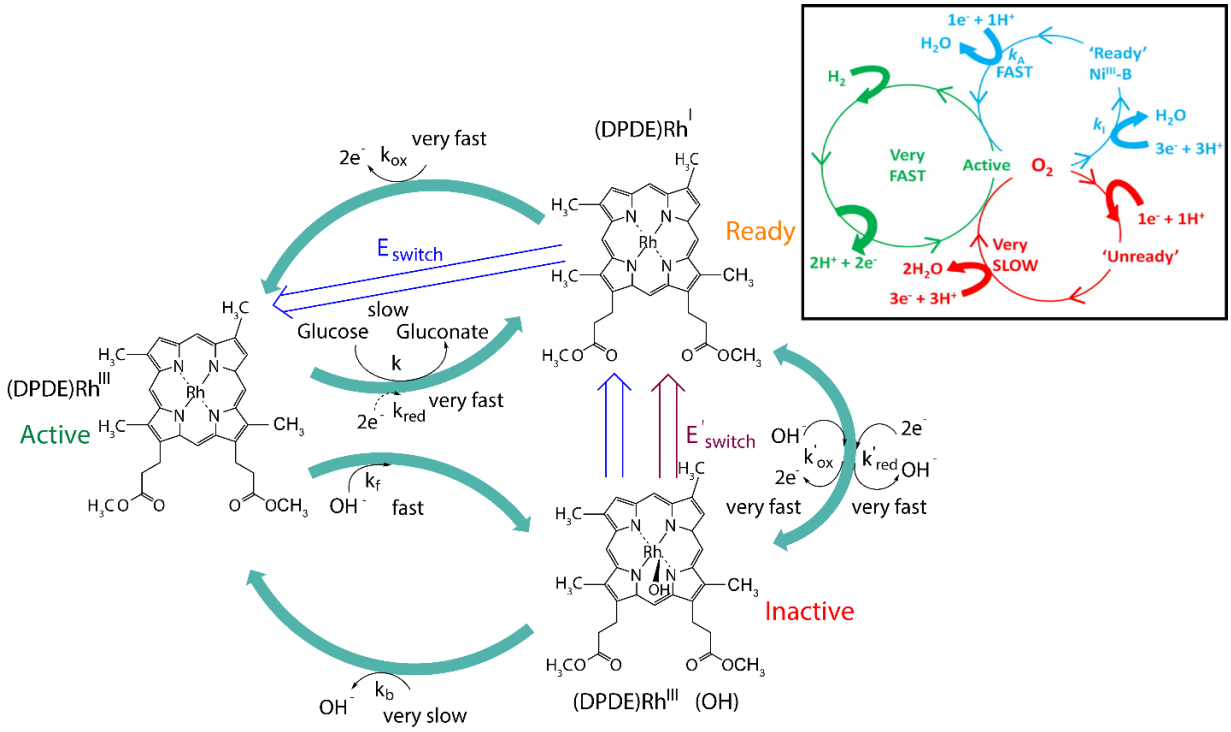

Figure 4.13: Overall catalytic cycle. Inset: Overall catalytic cycle of hydrogenase with an Ni active site[210].

4.6. Voltammetric Analysis by Operator-Splitting Scheme

Figure 4.13 gives a distinct map describing that the overall catalytic mechanism for the IAP are deeply investigated. The numerical simulations conducted in this Chapter are completely based on the traditional two-point time evolution finite difference method. The validation of the experimental data and model-based design presented in Figures 4.5, 4.6, 4.7(A), 4.9 and 4.11, successfully proves the rigorousness and robustness of the classic numerical technique that is most frequently used in electrochemistry.

A well-defined hydrogenase-like system holding a clear EC'CE mechanism in Scheme 4.2 with all detected parameters, now can be employed to conduct a voltammetric verification by operator-splitting method. The operator-splitting model construction obeys the rules defined in Chapter 3, totally five operators considered in sequent: mass transport for only substrate → electron transfer for (DPDE)Rh^{I} and (DPDE)Rh^{III} → second-order catalytic chemical reaction → first-order chemical reaction → electron transfer for (DPDE)Rh^{I} and (DPDE)Rh^{I}(OH). There is also a shortcut optimised for the above map, in which the procedures can be reduced only two operators including chemical reaction → electron transfer. Two electron-transfer steps are suggested to be combined into one like the treatment for EE mechanism described in Chapter 3. The second-order catalytic step might be reduced to first-order reaction if assuming large amounts of substrate concentration ($k'_{\mathrm{cat}} \approx k_{\mathrm{cat}}[\mathrm{S}]$), and the updated catalytic step integrates the first-order chemical reaction.

However, the result generated by OS is not quite satisfactory. The model with a sufficient small timestep does not approach to the convergence through either a full journey or taking a shortcut. For a full journey pathway, five separated operators involving two electron-transfer steps lead to two-times long iteration process in a single timestep. As a result, the root-finding Regula Falsi method often provides a local minimum value. If overly combining the operators into small number, solution searching for one species in single operator will be much more difficult since high-order (> 2) polynomial function may rise. The problem triggers an embedded root-searching iteration, which easily approaches to a local minimum.

4.7. Conclusion and Outlook

To compare two different numerical techniques, a well-defined system is required with clear reaction processes including fewer unknown parameters. The present study elucidates the mechanism of molecular IAP (summarised in Figure 4.13) and shows how the kinetic and thermodynamic parameters of the surface-confined rhodium-porphyrinic catalyst causes odd voltammetric traces. The combination of experimental results and the mathematical models confirmed that the role of the hydroxide ions as an inhibitor in the catalytic cycle is comparable to the inactivation process of hydrogenase during the hydrogen oxidation.

The voltammetric verification is a preferred choice of operator-splitting method. The classic finite difference method guarantees an accurate and stable validation in this hydrogenase-like system, in contrast, the operator splitting scheme got limitations in solving the same problem due to more than one-time iteration in a single timestep. While it has limitations in solving certain complex mechanisms, when integrated with multi-current-searching steps, the operator-splitting method has a potential to solve complex systems. In this chapter, to the best of our knowledge, for the first time we have developed a numerical methodology by integrating operator-splitting technique in solving electrochemical systems. Subsequently we have demonstrated the feasibility and applicability of this novel numerical strategy.

Chapter 5

5. A Deep Insight into Surface Deuteroporphyrin Dimethylester Rhodium(III) ((DPDE)Rh^{III}) with Model-Based Computational Design

In this Chapter, the exploration of the hydrogenase-like inactivation and activation processes (IAPs) continues. A "two-step" chronoamperometric method is recently proposed to study the anaerobic inactivation of [NiFe] hydrogenase[198]. The technique allows measuring both activation and inactivation rate constants direct from the experimental data. This knowledge offers an alternative pathway to estimate the important kinetic parameters. The chronoamperometric verification is employed to the experimental data generated from the same EC'CE mechanism.

5.1. Chronoamperometric Analysis for Studying Inactivation and Activation Kinetics

In the mechanistic analysis, we use both Laviron's formalism and density function theory to probe the apparent heterogeneous rate constant k_0 for electron transfer. This parameter plays a critical role towards the whole work because the estimation value not only describes the property of the electrode interface but also decides the kinetics of the whole catalytic processes. In hydrogenase, the electron-transfer rate constant is generally difficult to estimate because of the complex inner structure of enzyme, which greatly limits the quantitative analysis. Our molecular-based catalyst holds a great advantage that k_0 is relatively large in comparison to the one in hydrogenase, and the value might be evaluated if the system is well-defined. The past efforts provide us a reliable result.

Recently, Léger *et al*. reported a two-step chronoamperometric method that can obtain the kinetic information straightforward from experiments in hydrogenase[198]. In this method, the potential is either stepped up to inactivate the enzyme or stepped down to activate the enzyme to record the relaxation of the current. Through such an approach the intricacy of time and potential that is inherent to voltammetric experiments can be circumvented. In chronoamperometry, the current is proportional to the instant concentration of active enzyme and the transient states are interpreted into a simple scheme in which only active and inactive form of enzyme,

$$\text{active} \underset{k_{\mathrm{A}}(E)}{\overset{k_{\mathrm{I}}(E)}{\rightleftharpoons}} \text{inactive} \tag{5.1}$$

where $k_{\mathrm{I}}(E)$ and $k_{\mathrm{A}}(E)$ are the rate constant of inactivation and activation processes, respectively. The information about the mechanism can be obtained by analysing the dependence of $k_{\mathrm{I}}(E)$ and $k_{\mathrm{A}}(E)$ on potential, temperature, pH value, H_2 concentration[198]. This "two-step" chronoamperometric methods deal in a better way with a reversible IAPs mechanism since single potential step only yields the sum of $k_{\mathrm{I}}(E) + k_{\mathrm{A}}(E)$ rather than a separate value.

This robust multi-step chronoamperometric approach inspired us to monitor the current responses under a switch between inactivation potential and re-activation potential for the validation of the rate constants. Here, we propose a similar approach to the theoretical calculation used for determining the activation and inactivation rate constants.

One simple schematic model involving only active and inactive reactant forms obtained from the mechanistic analysis in last chapter, is given in Equation 5.2 that defines the relationship between Rh^{III} and $Rh^{III}(OH)$. $k_I(E)$ and $k_A(E)$ represent potential-dependent inactivation and activation rate constants, respectively, which are different from the previous set of rate constants k_0, k, k_f and k_b in EC'CE mechanism. Another important reactant Rh^{I} discussed in the same numerical model is regarded as an intermediate here.

$$Rh^{III} \underset{k_A}{\overset{k_I}{\rightleftharpoons}} Rh^{III}(OH) \tag{5.2}$$

The expression for the fraction of the conversion of Rh^{III} is described in Equation 5.3. The function is expressed by the fraction of only active rhodium form (Rh^{III}) when applying a constant potential,

$$\frac{d\Phi_{Rh^{III}}}{dt} = -k_I \Phi_{Rh^{III}} + k_A(1 - \Phi_{Rh^{III}}) \tag{5.3}$$

The Equation 5.4 is obtained with the initial condition and boundary conditions,

$$\Phi_{Rh^{III}} = \left(\Phi^*_{Rh^{III}} - \frac{k_A}{k_I + k_A}\right) e^{-(k_I + k_A)t} + \frac{k_A}{k_I + k_A} \tag{5.4}$$

where $\Phi^*_{Rh^{III}} = \Phi_{Rh^{III}}$ at $t = 0$ is the starting fraction of the rhodium in active form. Meaningful parameters are introduced, in which $\Phi^{\infty}_{Rh^{III}}$ is the asymptotic value and $1/k_{tot}$ is the time constant of the exponential relaxation toward steady-state

$$\begin{aligned} \Phi^{\infty}_{Rh^{III}} &= \frac{k_A}{k_I + k_A} \\ \frac{1}{k_{tot}} &= \frac{1}{k_I + k_A} \end{aligned} \tag{5.5}$$

In the transient-state kinetics, this is a typical treatment of relaxation experiments[211,212]. The total catalytic current equals the time-dependent fraction times the steady-state current behaviour of the active rhodium, $i^{lim}_{Rh^{III}}$, at a certain high driving force.

$$i = \Phi_{Rh^{III}}\, i^{lim}_{Rh^{III}} \tag{5.6}$$

The limiting current is given

$$i^{lim}_{Rh^{III}} = 2FA\Gamma^* k_{cat} \tag{5.7}$$

where A is the electrode surface area, Γ^* is the total surface total surface excess, and k_{cat} is the potential-dependent turnover rate of the completely active reactant. The total current is represented in Equation 5.8 by summation of Equations 5.3 to 5.7.

$$i = i_{\text{Rh}^{\text{III}}}^{\lim}\left[\left(\Phi_{\text{Rh}^{\text{III}}}^{*} - \Phi_{\text{Rh}^{\text{III}}}^{\infty}\right)e^{-k_{\text{tot}}t} + \Phi_{\text{Rh}^{\text{III}}}^{\infty}\right] \tag{5.8}$$

We define $i_0 = i_{\text{Rh}^{\text{III}}}^{\lim}\Phi_{\text{Rh}^{\text{III}}}^{*}$ and $i_\infty = i_{\text{Rh}^{\text{III}}}^{\lim}\Phi_{\text{Rh}^{\text{III}}}^{\infty}$, and Equation 5.8 can be reorganised

$$i = (i_0 - i_\infty)e^{-k_{\text{tot}}t} + i_\infty \tag{5.9}$$

Equation 5.9 implies that fitting an exponential relaxation to the chronoamperometric data provides the currents and k_{tot}, which can deduce the kinetics by combining the initial value of $\Phi_{\text{Rh}^{\text{III}}}$ and $\Phi_{\text{Rh}^{\text{III}}}^{*}$. k_I and k_A obeys,

$$\begin{aligned} k_A &= \Phi_{\text{Rh}^{\text{III}}}^{*}\frac{i_\infty}{i_0}k_{\text{tot}} \\ k_I &= k_{\text{tot}} - k_A \end{aligned} \tag{5.10}$$

Here, we recall the quantitative description of chronoamperometry introduced in Chapter 1

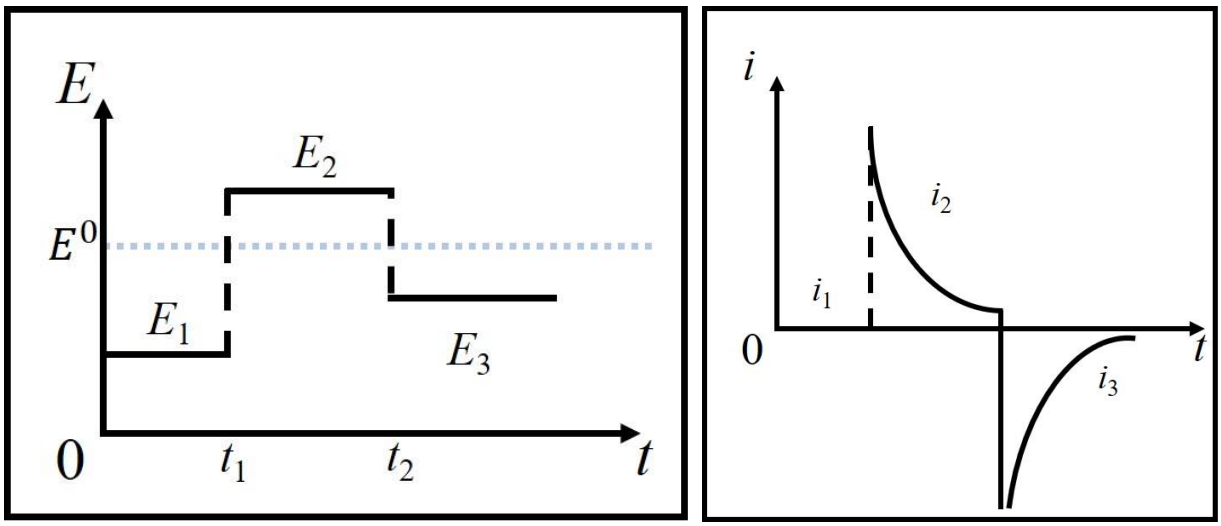

Figure 5.1: Waveform for a chronoamperometric reversal techniques (Left), and the current response with time (Right).

Electrolysis will not occur if the applied potential fully activates the electrocatalysis, like the out of working potential E_1 in Figure 5.1. When abruptly switching the potential to E_2, the inactivation process promises a current response, and then stepping down the potential to E_3 to induce the activation process again.

The governing equations of current value are shown below after giving a certain time,

$$i(t_1 < t < t_2) = i^{\lim}_{\mathrm{Rh^{III}}}(E_1)\left\{\left[1 - \Phi^{\infty}_{\mathrm{Rh^{III}}}(E_1)\right]e^{-k_{\mathrm{tot}}(t-t_1)} + \Phi^{\infty}_{\mathrm{Rh^{III}}}(E_1)\right\} \quad (5.11)$$

$$i(t_2 < t < t_3) = i^{\lim}_{\mathrm{Rh^{III}}}(E_2)\left\{\left[\Phi'_{\mathrm{Rh^{III}}} - \Phi^{\infty}_{\mathrm{Rh^{III}}}(E_2)\right]e^{-k_{\mathrm{tot}}(t-t_2)} + \Phi^{\infty}_{\mathrm{Rh^{III}}}(E_2)\right\} \quad (5.12)$$

$$i(t > t_3) = i^{\lim}_{\mathrm{Rh^{III}}}(E_3)\left\{\left[\Phi''_{\mathrm{Rh^{III}}} - \Phi^{\infty}_{\mathrm{Rh^{III}}}(E_3)\right]e^{-k_{\mathrm{tot}}(t-t_3)} + \Phi^{\infty}_{\mathrm{Rh^{III}}}(E_3)\right\} \quad (5.13)$$

in Equation 5.11, the starting fraction as initial boundary assumes as unity because of giving enough time to be active. From Equations 5.12 and 5.13, the starting fractions when stepping down the applied potential are given as the results at the sweeping-potential time, and the value can be calculated as following,

$$\Phi'_{\mathrm{Rh^{III}}} = \left[1 - \Phi^{\infty}_{\mathrm{Rh^{III}}}(E_1)\right]e^{-k_{\mathrm{tot}}(t_2-t_1)} + \Phi^{\infty}_{\mathrm{Rh^{III}}}(E_1) \quad (5.14)$$

$$\Phi''_{\mathrm{Rh^{III}}} = \left[\Phi'_{\mathrm{Rh^{III}}} - \Phi^{\infty}_{\mathrm{Rh^{III}}}(E_1)\right]e^{-k_{\mathrm{tot}}(t_3-t_2)} + \Phi^{\infty}_{\mathrm{Rh^{III}}}(E_2) \quad (5.15)$$

The chronoamperometric experiment shown in Figure 5.2 is operated under forced convection by a rotating disk electrode (RDE) at 2500 rpm in order to reduce the influence of substrate concentration caused by material balance. The experiment starts at $E_1 = -0.7$ V that guarantees fully activation for rhodium over a range of time $t_1 = 200$ s. The potential is then shifted into E_2 and a distinct negative exponential trace can be observed, which agrees with the theoretical derivation according to Equation 5.11. Over 1800 s running time is given to the inactivation process, which is suggested to compromise the re-activation trace observed. When stepping down the potential to $E_3 = -0.6$ V, the current behaviour still shows very little positive exponential curve and then approach to the steady-state is very fast. We then lower the potential further to check the re-activation process. At $E_4 = -0.7$ V, and the current also reflects the re-activation step in Figure 5.2. However, one problem rises here that the magnitude of re-activation curves is too small to capture enough data points. The range of time in reality for the re-activation current to approach its steady-state is significantly smaller rather than the results published for A. aeolicus hydrogenase in Léger's work[198] (2 s $vs.$ 100 s).

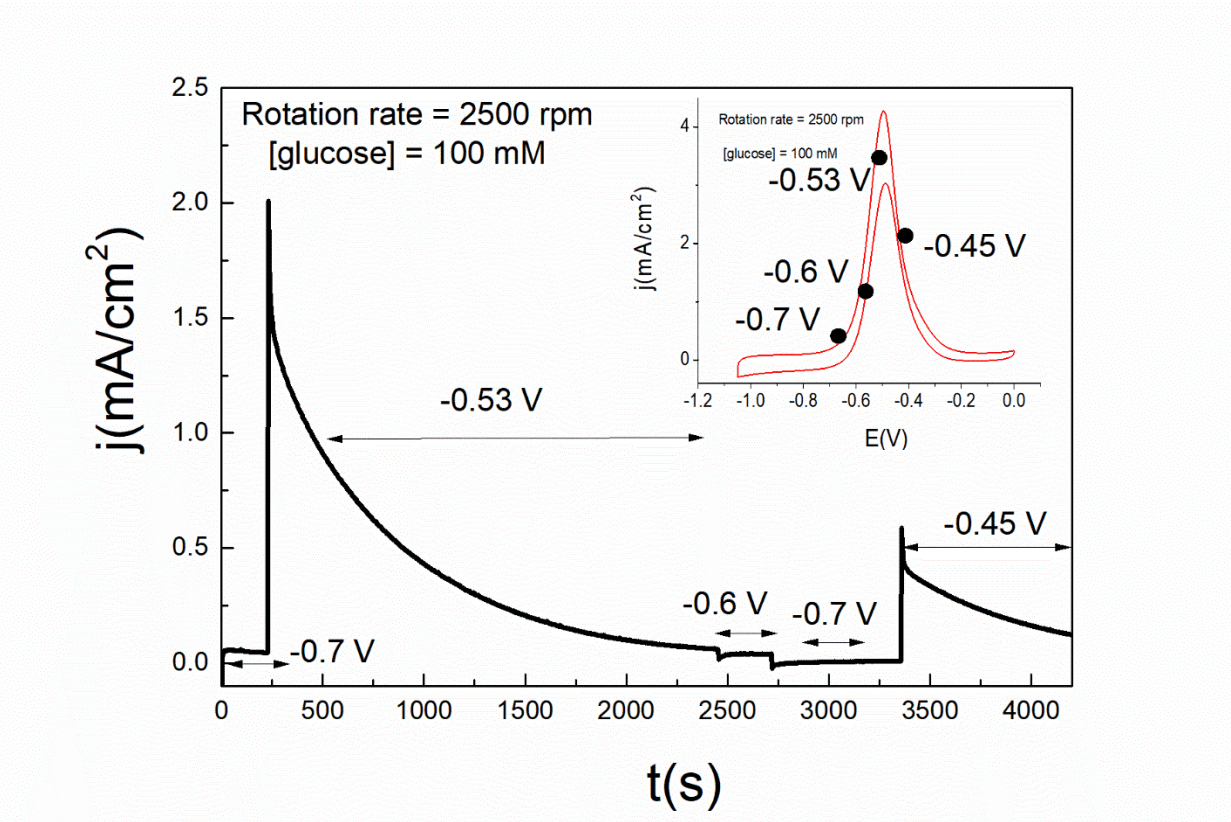

Figure 5.2: Typical chronoamperogram illustrating the application of multi-step method to electrocatalysis of (DPDE)Rh^{III}. Experimental conditions: electrochemical reactivation of (DPDE)Rh^{III} catalyst in the presence of 100 mM glucose in pH 14 through forced convection by a rotating disk electrode (RDE) at 2500 rpm. Inset: Voltammogram of electrocatalysis of (DPDE)Rh^{III}.

This problem might be solved by increasing the potential gap between inactivation and re-activation, and another set of chronoamperometric measurement is performed and the experimental result is given below. However, the current reaches the steady-state much faster than the result from Figure 5.3, and even fewer data points are recorded in the second experiment. To explain this phenomenon during the transient, we need to recall the analysed kinetics problem from last chapter. Figure 4.7(B) is reprinted in the Figure 5.3(Inset). At $E_3 = -0.72$ V, the re-activation rate constant is far greater than the inactivation rate constants (including both k'_{ox} and $k[S]$), which leads to a larger slope making the current faster towards equilibrium. When $E_3 = -0.6$ V, it is very

close to an isopotential point (IPP) where the re-activation is hard to observe, although the slope trends to a flatter profile.

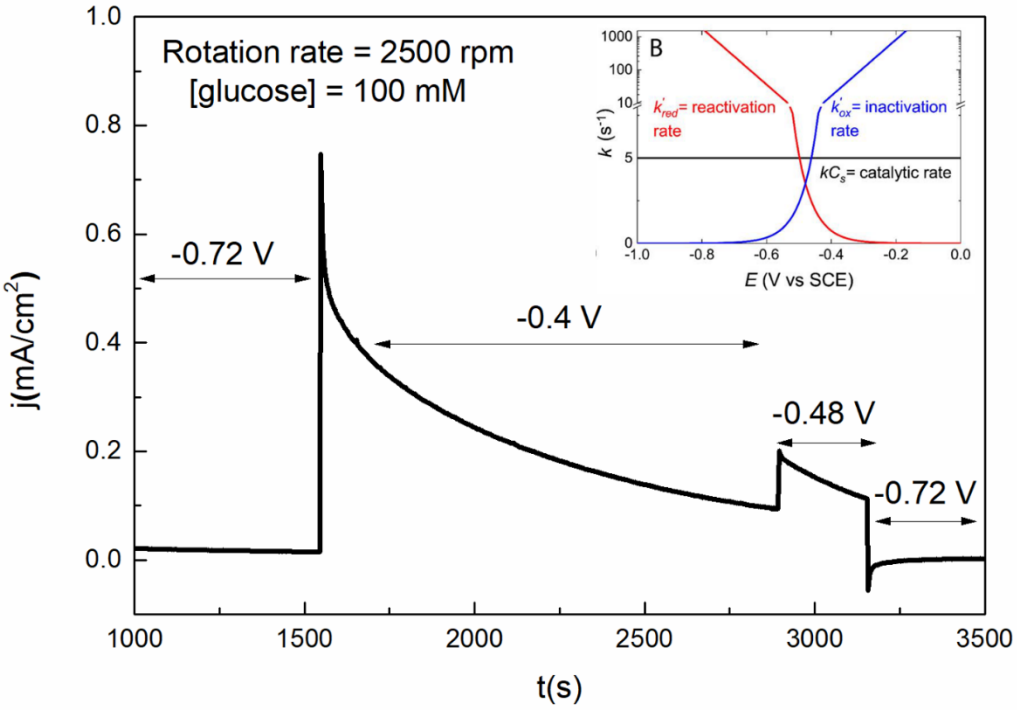

Figure 5.3: Typical chronoamperogram illustrating the application of multi-step method to electrocatalysis of (DPDE)Rh^{III}. Experimental conditions: electrochemical reactivation of (DPDE)Rh^{III} catalyst in the presence of 100 mM glucose in pH 14 through forced convection by a rotating disk electrode (RDE) at 2500 rpm. Inset: Kinetic parameters k'_{ox} = inactivation rate (blue line), k'_{red} = reactivation rate (red line) and $k[S]$ = catalytic rate at a substrate concentration of 50 mM, as a function of the applied potential (E) (Recalling from Figure 4.7).

The multi-step chronoamperometric traces match the literature in Léger's work[198], but the failure of direct estimation leads to a different result. The information from the current response is hard to capture because the rate constant of electron transfer for molecular-based catalyst is much higher than that for enzymatic catalyst. The electron-transfer reaction in our case is estimated extremely fast holding a magnitude $\sim 10^0\ s^{-1}$, which provokes the whole system reach the steady state in seconds and the natural time parameter $1/k_{tot}$ is not big enough for us to record a clear exponential

curve to fit the experimental data, especially for the reactivation process. In contrast, k_I and k_A in enzymatic hydrogenase case give a fitting result in $\sim 10^{-3}$ s^{-1} order.

Thus, an indirect approach is proposed to validate our kinetics in chronoamperometry. The analysed EC'CE mechanism model is given a theoretical simulation by the step potentials instead of cyclic voltammetry, to compare the experimental data directly. The diffusion of substrate in the EC'CE model is treated as a constant when a large concentration of substrate is employed. The chronoamperometric result is shown in Figure 5.4, and the agreement between the experimental and simulated chronoamperometry is good. The result implies a good estimation of the kinetics.

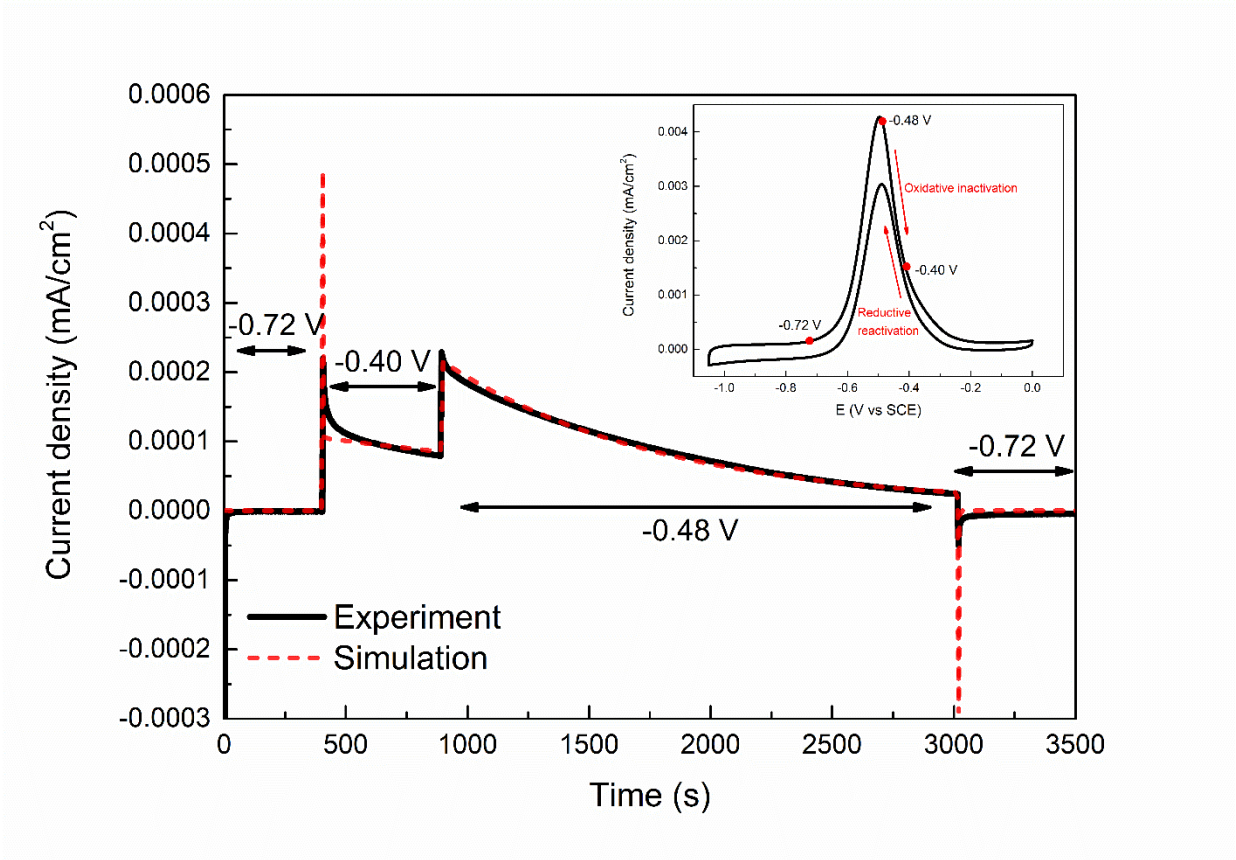

Figure 5.4: Typical chronoamperogram illustrating the application of multi-step method to electrocatalysis of (DPDE)Rh^{III}. Experimental conditions: electrochemical reactivation of (DPDE)Rh^{III} catalyst in the presence of 100 mM glucose in pH 14. The kinetics used in numerical simulation: $k = (1 \pm 0.1) \times 10^5$ cm^3 s^{-1} mol^{-1}, and $k_0 = 3.5$ s^{-1}.

5.2. Identification of Formation of a Dimeric (DPDE)Rh^{II} Species

In the last section, a multi-step chronoamperometric method is described to help quantify the kinetics of the electrocatalytic IAPs. Although a direct estimation is difficult to realise because of the large magnitude of the rate constants in molecular catalysts, one set of experimental data from cyclic voltammograms attracts our attention when we tried to increase the scanning potential range to capture more kinetic information. The result is given in Figure 5.5, where an interesting result is observed at a relative low scan rate. The anodic peak current increases with an extension of the scan range, but the cathodic peak current remains stable. In a well-defined system, the difference between these two peaks will not change unless some critical points are missing.

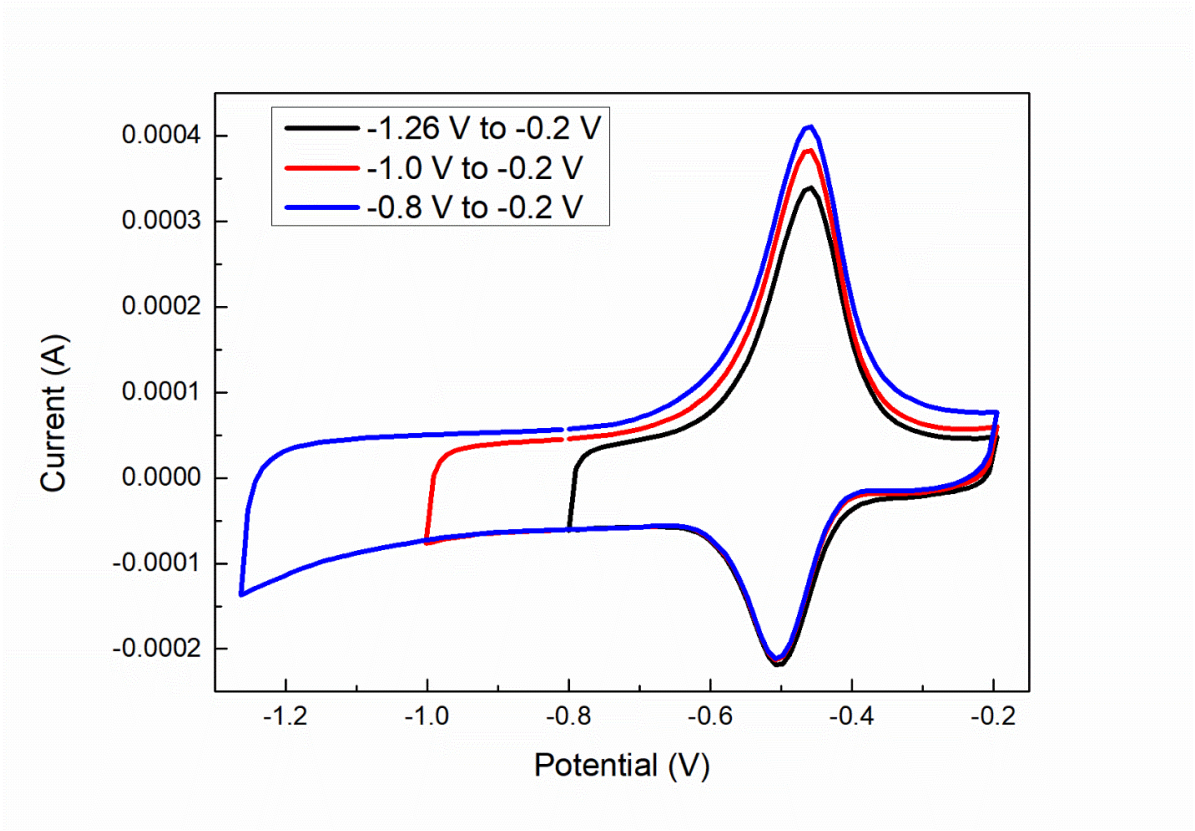

Figure 5.5: Experimental cyclic voltammograms for the non-catalytic mechanism at $v = 10\ \mathrm{mV/s}$ when given to different scanning ranges

Recalling the non-catalytic validation results from Figure 4.6, one can observe a gap between experimental data and simulation results in the highlighted part in Figure 5.5(A). When the scan

rate increases to 500 mV/s, the agreement between experiment and simulation is far more excellent.

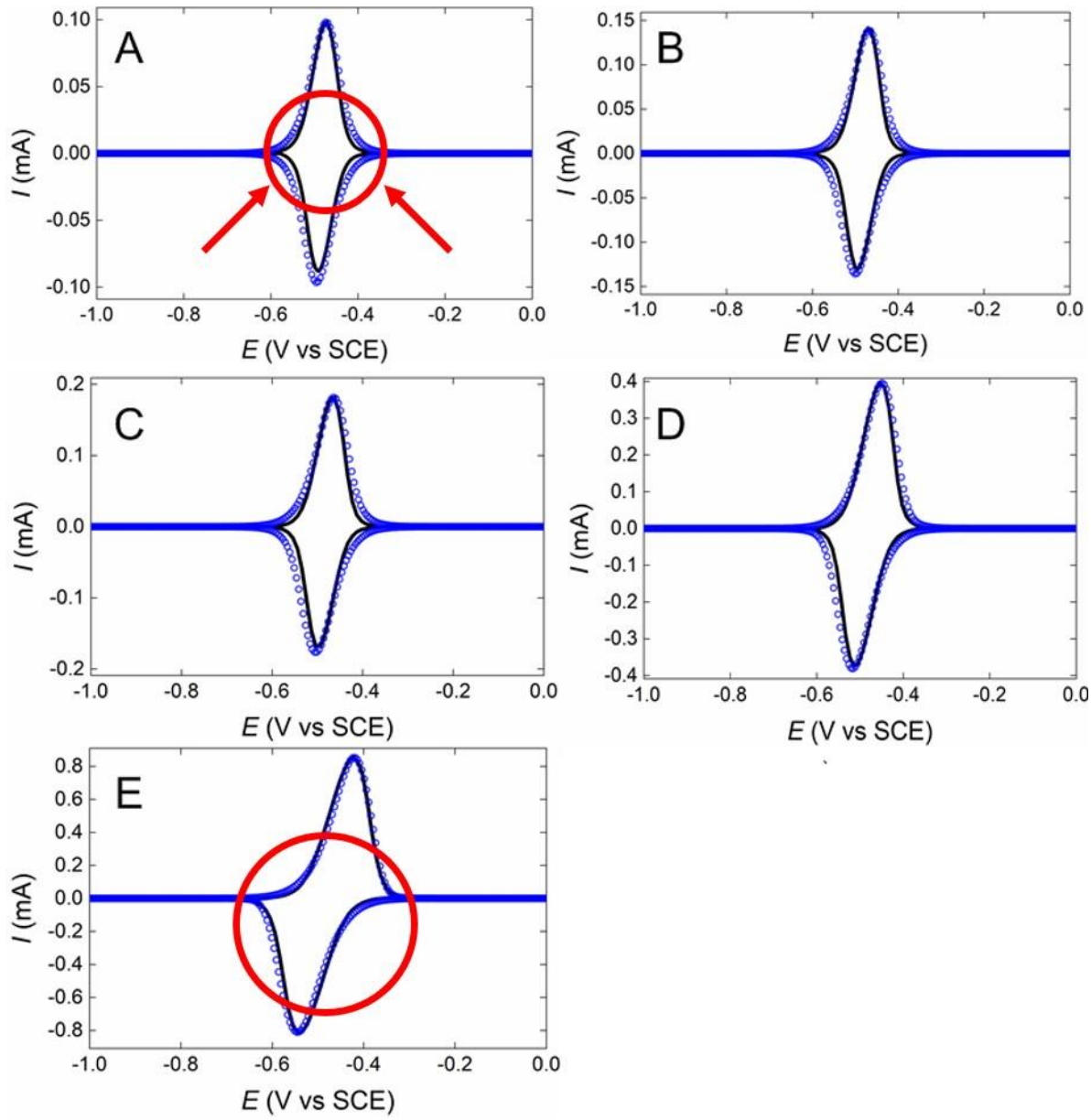

Figure 5.6: Validation of the model predictions for non-catalytic system at different scan rates. The black solid line (−) represent the experiments and the blue circles (o) represent the model predictions at scan rates of 50 mV/s (A), 75 mV/s (B), 100 mV/s (C), 200 mV/s (D) and 500 mV/s (E). These validations are for the experimental data obtained at pH 14. The proposed model according to the Scheme 4.1 successfully captures the voltammetric traces at different scan rates (Recalling from Figure 4.6).

At a low scan rate ($v = 5$ mV/s), the relative error between i_{pa} and i_{pc} reaches 22% calculated from experimental data. The comparison is given in Figure 5.7. The relative error between i_{pa} and i_{pc} at different scan rate is summarised in Table 5.1.

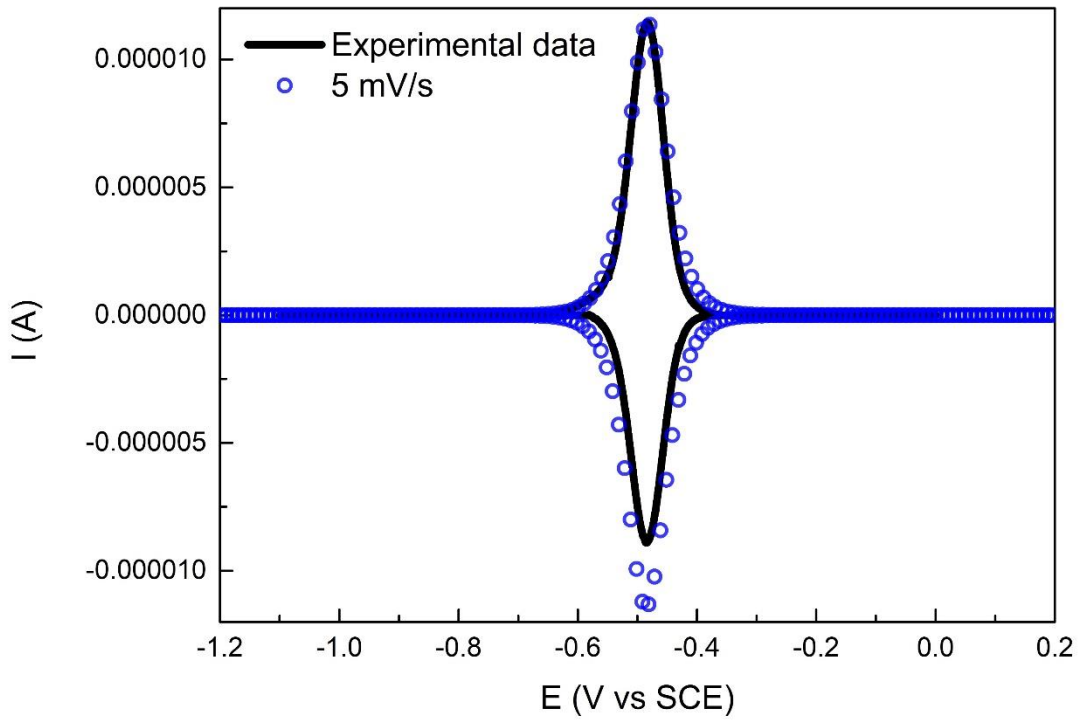

Figure 5.7: Comparison of the model predictions for non-catalytic system. The black solid line (−) represent the experiments and the blue circles (o) represent the model predictions at scan rates of 5 mV/s.

Table 5.1: Relative error calculated from experimental data at different scan rate.			
Scan rate ($\mathrm{mV/s}$)	i_{pa} (A)	i_{pc} (A)	Relative error
5	0.1145	-0.089	22%
20	0.40744	-0.3485	14%
50	0.98156	-0.8785	10%
75	1.4159	-1.301	8%
100	1.8147	-1.681	7%
150	2.9401	-2.796	5%
200	3.9634	-3.745	6%
500	8.5304	-8.159	4%

A case has been noted in the literature where a similar observation of the anodic charge for peak current is always slightly bigger than the cathodic charge from a redox electrocatalysis in the surface of chloro(phthalocyaninato)rhodium(III) species[203]. This phenomenon is resulted from some loss of a dimeric species every time the electrode is polarised positive of the anodic component. In addition, the anodic peak increases with the reduction of scan rate. In another word, lower scan rate leads to a bigger difference between i_{pa} and i_{pc}. From Figure 3(A) in this reference, an extra reduction peak occurs at a very negative potential $E = -0.11\ \mathrm{V}$. The occurrence of a rhodium dimer confirms our initial hypothesis on the intermediate reactant $\mathrm{Rh^{II}}$, further, this explanation is greatly helpful to understand the hydrogenase-like mechanism.

5.3. Voltammetric Analysis of Kinetics of Rhodium Dimer Formation

To understand the dimer formation on the mechanism, model-based experimental simulations were employed using cyclic voltammogram established from our previous work. A comprehensive scheme is derived from the combination of the aforementioned EC'CE scheme and catalytic scheme.

The mechanistic scheme is interpreted using an EC'CECE scheme which combined the IAPs and formation of a dimeric species according to electrochemical terminology. According to this scheme, the electrochemical steps strictly follow two one-electron transfer process during the catalytic cycle. The overall mechanism is summarised by Equations 5.16 to 5.21,

$$(\mathrm{DPDE})\mathrm{Rh^{III}} + \mathrm{e^-} \underset{k_{\mathrm{ox}}^1}{\overset{k_{\mathrm{red}}^1}{\rightleftharpoons}} (\mathrm{DPDE})\mathrm{Rh^{II}} + \mathrm{e^-} \underset{k_{\mathrm{ox}}^2}{\overset{k_{\mathrm{red}}^2}{\rightleftharpoons}} (\mathrm{DPDE})\mathrm{Rh^{I}} \tag{5.16}$$

$$(\mathrm{DPDE})\mathrm{Rh^{III}} + [\mathrm{S}] \overset{k}{\rightarrow} (\mathrm{DPDE})\mathrm{Rh^{I}} + [\mathrm{P}] \tag{5.17}$$

$$(\mathrm{DPDE})\mathrm{Rh^{III}} + \mathrm{OH^-} \underset{k_{1\mathrm{b}}}{\overset{k_{1\mathrm{f}}}{\rightleftharpoons}} (\mathrm{DPDE})\mathrm{Rh^{III}}(\mathrm{OH}) \tag{5.18}$$

$$(\mathrm{DPDE})\mathrm{Rh^{III}}(\mathrm{OH}) + \mathrm{e^-} \underset{k_{\mathrm{ox}}^3}{\overset{k_{\mathrm{red}}^3}{\rightleftharpoons}} (\mathrm{DPDE})\mathrm{Rh^{II}} + \mathrm{OH^-} + \mathrm{e^-} \underset{k_{\mathrm{ox}}^2}{\overset{k_{\mathrm{red}}^2}{\rightleftharpoons}} (\mathrm{DPDE})\mathrm{Rh^{I}} + \mathrm{OH^-} \tag{5.19}$$

$$2(\mathrm{DPDE})\mathrm{Rh^{II}} \underset{k_{2\mathrm{b}}}{\overset{k_{2\mathrm{f}}}{\rightleftharpoons}} \left[(\mathrm{DPDE})\mathrm{Rh^{II}}\right]_2 \tag{5.20}$$

$$\left[(\mathrm{DPDE})\mathrm{Rh^{II}}\right]_2 + 2\mathrm{e^-} \underset{k_{\mathrm{ox}}^4}{\overset{k_{\mathrm{red}}^4}{\rightleftharpoons}} 2(\mathrm{DPDE})\mathrm{Rh^{I}} \tag{5.21}$$

$k_{\mathrm{red}}^{\mathrm{j}}$ and $k_{\mathrm{ox}}^{\mathrm{j}}$ are the rate constants for *j*th step of electrochemical reactions, and k, $k_{1\mathrm{f}}$, $k_{1\mathrm{b}}$, $k_{2\mathrm{f}}$ and $k_{2\mathrm{b}}$ are the rate constants of the chemical reactions. The surface reaction is suggested to follow a semi-empirical Butler-Volmer (BV) equation for electron transfer and the diffusion of glucose obeys Fick's law in the solution. The validity of the scheme was evaluated by mathematical models. The equations for the model used in the EC'CECE simulations are derived as follows:

The governing equations for the surface concentrations of the rhodium species are:

$$\frac{\partial \Gamma_{\mathrm{Rh^{I}}}}{\partial t} = -\frac{i_{\mathrm{Rh^{II}/Rh^{I}}}}{FA} + k[\mathrm{S}]\Gamma_{\mathrm{Rh^{III}}} - \frac{1}{2}\frac{i_{[\mathrm{Rh^{II}}]_2/\mathrm{Rh^{I}}}}{FA} \tag{5.22}$$

$$\frac{\partial \Gamma_{\mathrm{Rh^{II}}}}{\partial t} = -\frac{i_{\mathrm{Rh^{III}/Rh^{II}}}}{FA} - \frac{i_{\mathrm{Rh^{III}(OH)/Rh^{II}}}}{FA} + \frac{i_{\mathrm{Rh^{II}/Rh^{I}}}}{FA} + \frac{1}{2}k_{2\mathrm{b}}\Gamma_{[\mathrm{Rh^{II}}]_2} - \frac{1}{2}k_{2\mathrm{f}}\Gamma_{\mathrm{Rh^{II}}}^2 \tag{5.23}$$

$$\frac{\partial \Gamma_{\mathrm{Rh^{III}}}}{dt} = \frac{i_{\mathrm{Rh^{III}/Rh^{II}}}}{FA} - k[\mathrm{S}]\Gamma_{\mathrm{Rh^{III}}} - k_{\mathrm{f}}\Gamma_{\mathrm{Rh^{III}}} + k_{\mathrm{b}}\Gamma_{\mathrm{Rh^{III}(OH)}} \tag{5.24}$$

$$\frac{\partial \Gamma_{\mathrm{Rh^{III}(OH)}}}{\partial t} = k_{\mathrm{f}}\Gamma_{\mathrm{Rh^{III}}} - k_{\mathrm{b}}\Gamma_{\mathrm{Rh^{III}(OH)}} + \frac{i_{\mathrm{Rh^{III}(OH)/Rh^{II}}}}{FA} \tag{5.25}$$

$$\frac{\partial \Gamma_{[\mathrm{Rh^{II}}]_2}}{\partial t} = \frac{i_{[\mathrm{Rh^{II}}]_2/\mathrm{Rh^{I}}}}{FA} + k_{2\mathrm{f}}\Gamma_{\mathrm{Rh^{II}}}^2 - k_{2\mathrm{b}}\Gamma_{[\mathrm{Rh^{II}}]_2} \tag{5.26}$$

The overall surface concentration is a constant value and can be written as

$$\Gamma_{\mathrm{Rh^{I}}} + \Gamma_{\mathrm{Rh^{II}}} + \Gamma_{\mathrm{Rh^{III}}} + \Gamma_{\mathrm{Rh^{III}(OH)}} + \Gamma_{[\mathrm{Rh^{II}}]_2} = \Gamma^{*} \tag{5.27}$$

Substrate transport to the electrode surface is treated as a linear diffusion, and the equation is given

$$\frac{\partial [\mathrm{S}]}{\partial t} = D_{\mathrm{s}}\frac{\partial^2 [\mathrm{S}]}{\partial x^2} - k[\mathrm{S}]\Gamma_{\mathrm{Rh^{III}}} \tag{5.28}$$

The contributions to the measured current are given from $i_{\mathrm{Rh^{II}/Rh^{I}}}$, $i_{\mathrm{Rh^{III}/Rh^{II}}}$, $i_{\mathrm{Rh^{III}(OH)/Rh^{II}}}$ and $i_{[\mathrm{Rh^{II}}]_2/\mathrm{Rh^{I}}}$ related to the reduction of (DPDE)$\mathrm{Rh^{II}}$ to (DPDE)$\mathrm{Rh^{II}}$, (DPDE)$\mathrm{Rh^{III}}$ to (DPDE)$\mathrm{Rh^{II}}$, (DPDE)$\mathrm{Rh^{III}}$(OH) to (DPDE)$\mathrm{Rh^{II}}$ and [(DPDE)$\mathrm{Rh^{II}}$]$_2$ to (DPDE)$\mathrm{Rh^{I}}$, respectively. The resulting current follows BV equation involving the influence of rate constant taken to predict experiments,

$$\begin{aligned} i &= i_{\mathrm{Rh^{III}/Rh^{II}}} + i_{\mathrm{Rh^{II}/Rh^{I}}} + i_{\mathrm{Rh^{III}(OH)/Rh^{II}}} + i_{[\mathrm{Rh^{II}}]_2/\mathrm{Rh^{I}}} \\ &= \left[-k_{\mathrm{red}}^{1}\Gamma_{\mathrm{Rh^{III}}} + k_{\mathrm{ox}}^{1}\Gamma_{\mathrm{Rh^{II}}}\right] + \left[-k_{\mathrm{red}}^{2}\Gamma_{\mathrm{Rh^{II}}} + k_{\mathrm{ox}}^{2}\Gamma_{\mathrm{Rh^{I}}}\right] \\ &+ \left[-k_{\mathrm{red}}^{3}\Gamma_{\mathrm{Rh^{III}(OH)}} + k_{\mathrm{ox}}^{3}\Gamma_{\mathrm{Rh^{II}}}\right] + \left[-k_{\mathrm{red}}^{4}\Gamma_{[\mathrm{Rh^{II}}]_2} + k_{\mathrm{ox}}^{4}\Gamma_{\mathrm{Rh^{I}}}\right] \end{aligned} \tag{5.29}$$

where the rate constants of BV model, $k_{\mathrm{red}}^{\mathrm{j}}$ and $k_{\mathrm{ox}}^{\mathrm{j}}$, got have an exponential dependence with the applied potential which can be described as

$$\begin{aligned} k_{\mathrm{red}}^{\mathrm{j}} &= k_0^{\mathrm{j}} e^{-\alpha\frac{F}{RT}\left(E - E_{\mathrm{j}}^{0}\right)} \\ k_{\mathrm{ox}}^{\mathrm{j}} &= k_0^{\mathrm{j}} e^{(1-\alpha)\frac{F}{RT}\left(E - E_{\mathrm{j}}^{0}\right)} \end{aligned} \tag{5.30}$$

Except for the standard potential ($E^0_{1,2,3}$), the standard heterogeneous rate constants ($k_0^{1,2,3}$) and other parameters estimated to describe the IAPs before, addition variables including the rate of formation of dimeric rhodium(II) species (k_{2f}/k_{2b}) and electro-degradation parameters k_0^4 and E_4^0 are introduced to depict the occurrence of rhodium dimer.

The estimation values of the parameters derived from IAPs are also shown in Table 5.2. To the best of our knowledge, it is not straight forward to achieve a closed form analytical solution for the system of partial differential Equations 5.22 to 5.26 and 5.28. Therefore, a model-based experimental simulation is adopted and implemented by using a finite difference solver to predict the model.

The validation of the model without substrate(non-catalytic) at 5 mV/s is presented in Figure 5.8. The agreement between the calculated and experimental CVs is good over a range of scan rates and the estimated physical parameters, k_{2f}, k_{2b}, k_0^4 and E_4^0 obtained from this model are given in Table 5.3.

During the forward scan, the concentration percentage of (DPDE)Rh^{I} trends to unity at the very negative potential. When the potential increases and dominates the process under very oxidising conditions in the vicinity of E_4^0, no anodic current can be observed which implies an irreversible electron transfer step in Equation 5.21 ($k_{ox}^4 \approx 0$). Keeping raising the potential gives the same mechanistic explanation of IAPs, which can be found in our previous studies.

Table 5.3: Parameters estimated from the voltammograms showing the rhodium dimer formation.

$k_{2f}/\text{cm}^3\ \text{s}^{-1}\ \text{mol}^{-1}$	k_{2b}/s^{-1}	$k_0^4\ (k_{ox}^4)/\text{s}^{-1}$	E_4^0/V
10^8	≤ 1.0	10.0 (0.0)	-1.36

The main difference appears from the backward sweep, in which the cathodic current peak (**x**) is 20% smaller in comparison to the one (**o**) generated from old EC'CE scheme at low scan rate. However, the ratio of i_{pc}/i_{pa} continuously decreases with the increases of scan rate, and the value trends to unity at $\nu = 500$ mV/s. When the potential keeps reducing, a small reduction peak can be observed near -1.2 V at only $\nu = 5$ mV/s.

Table 5.2: Summary of the parameters estimated from experiments employed for the numerical analyses of dimeric rhodium formation.

Parameter	Value	Unit
A (fixed)	1.0 ± 0.2	cm^2
E_i (fixed)	-1.5	V
E_1^0	-0.475 ± 0.01	V
E_2^0	-0.475 ± 0.01	V
E_3^0	-0.475 ± 0.01	V
E_4^0	-1.36	V
E_v (fixed)	0.2	V
F (fixed)	96485	$\mathrm{C\ mol^{-1}}$
k	$(1 \pm 0.1) \times 10^5$	$\mathrm{cm^3\ s^{-1}\ mol^{-1}}$
$k_{2\mathrm{f}}$	10^8	$\mathrm{cm^3\ s^{-1}\ mol^{-1}}$
$k_{2\mathrm{b}}$	≤ 1.0	$\mathrm{s^{-1}}$
k_0^1	6.0	$\mathrm{s^{-1}}$
k_0^2	3.5	$\mathrm{s^{-1}}$
k_0^3	6.0	$\mathrm{s^{-1}}$
k_0^4	10.0	$\mathrm{s^{-1}}$
K_A	10^7	–
R (fixed)	8.3145	$\mathrm{J\ mol^{-1}\ K^{-1}}$
T (fixed)	293.15	K
α	0.5	–
Γ^* (fixed)	$(6 \pm 1) \times 10^{-10}$	$\mathrm{mol\ cm^{-2}}$

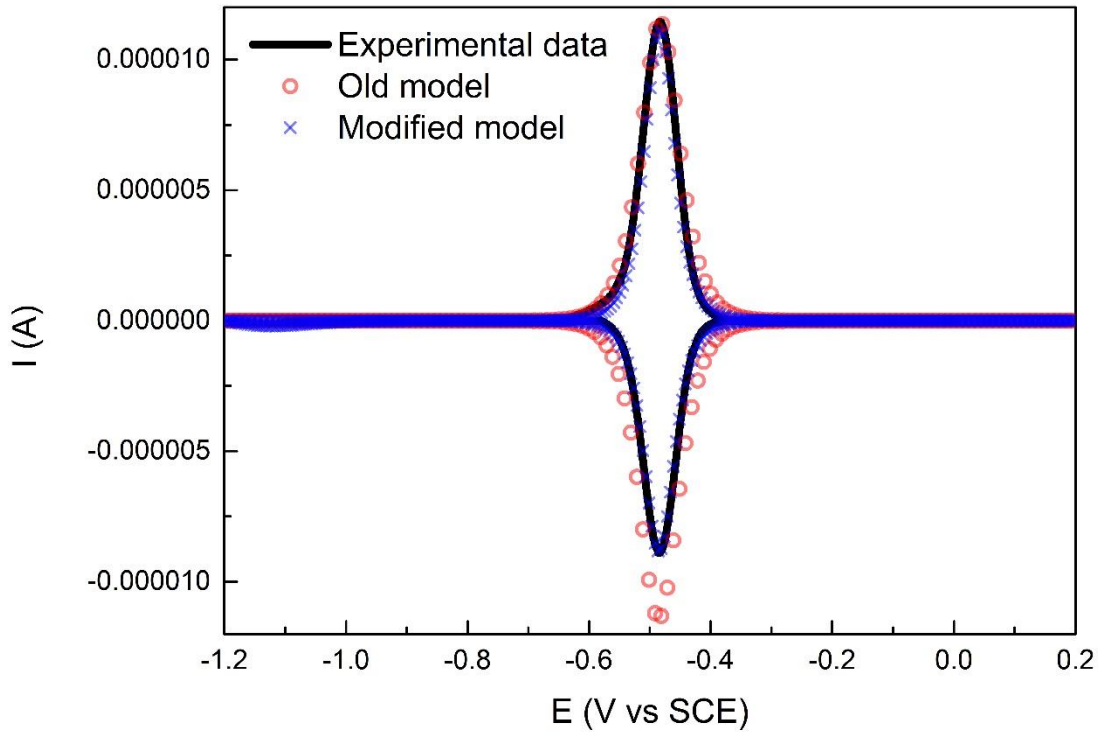

Figure 5.8: Comparison of the two model predictions for non-catalytic system to the experimental data. The black solid line (−) represent the experiments, the red circles (**o**) represent the EC'CE model predictions and the blue crosses (**x**) represent the EC'CECE model predictions at scan rates of 5 mV/s.

5.4. Mechanistic Analysis of Kinetics

After exploring the appearance of the signal of rhodium dimer formation at slow scan rate in the previous section, we next investigate the EC'CECE model and its current characteristics at different operating conditions. It is already confirmed that the shape of the CVs is very sensitive to scan rate and the contribution of each reaction varies according to its kinetic parameters.

One immediate deduction is that, as the scan rate decreases, the formation (negative potential reduction peak) becomes more apparent. In contrast, at high scan rate, the reduction peak cannot be observed and the ratio of $i_{\mathrm{pc}}/i_{\mathrm{pa}}$ turns to unity. These three factors could explain the formation of dimeric rhodium:

First, the rate of chemical degradation of [(DPDE)$\mathrm{Rh^{II}}$]$_2$, which is a first order chemical reaction and can be described as $t_{\mathrm{cd}} = 1/k_{2\mathrm{b}}$. Secondly the rate of electrochemical decomposition of [(DPDE)$\mathrm{Rh^{II}}$]$_2$, is also a first order rate constant and its reciprocal equates the time constant of the dimer decomposition reaction as $t_{\mathrm{ed}} = 1/k_{\mathrm{red}}^{4}$. Third factor is the natural time scale of voltammetry given as $t_{\mathrm{v}} = RT/Fv$. By comparing these three factors which measure the interference of the dimer formation reaction against the time-scale of the experiment governed by the scan rate, the change of the CV shapes can be explained based on the validated EC'CECE mechanism.

For $v = 5\ \mathrm{mV/s}$, $t_{\mathrm{v}} \gg (t_{\mathrm{cd}} + t_{\mathrm{ed}})$ promises time for (DPDE)$\mathrm{Rh^{II}}$ tardily accumulating at the electrode surface, which guarantees the production of [(DPDE)$\mathrm{Rh^{II}}$]$_2$. When the overpotential ($\eta_4 = E^{\mathrm{app}} - E_4^0$) for Equation 5.21 is bigger than zero, there is no routine to consume the concentration of [(DPDE)$\mathrm{Rh^{II}}$]$_2$ at the electrode surface. When the applied potential sweep into a more negative value, the reduction of [(DPDE)$\mathrm{Rh^{II}}$]$_2$ is activated and a cathodic peak appears near E_4^0. For $v = 200\ \mathrm{mV/s}$, $t_{\mathrm{v}} \ll (t_{\mathrm{cd}} + t_{\mathrm{ed}})$ lets that the system yields very low concentration of [(DPDE)$\mathrm{Rh^{II}}$]$_2$. The accumulation may not lead to an obvious current peak, thus the curve looks plate at high scan rate.

5.5. Conclusion and Outlook

A multi-step chronoamperometric method is employed to directly detect the reaction kinetics in the hydrogenase-like system. The information from the current response is hard to capture because the rate constant of electron transfer for molecular-based catalyst is much higher than that for enzymatic catalyst. A good agreement is achieved by an indirect approach where the EC'CE mechanism analysed from Chapter 4 is applied a step potential function to validate the chronoamperometric voltammogram.

An unexpected difference between oxidation and reduction peak current is observed when the sweeping range is changed from a few experiments under cyclic voltammetry, which implies extra electron-transfer step (coupled chemical kinetics). This "accident" leads to a discovery of dimeric rhodium intermediate. A more comprehensive mechanism of the surface-confined rhodium-porphyrinic catalyst is summarised in Figure 5.9.

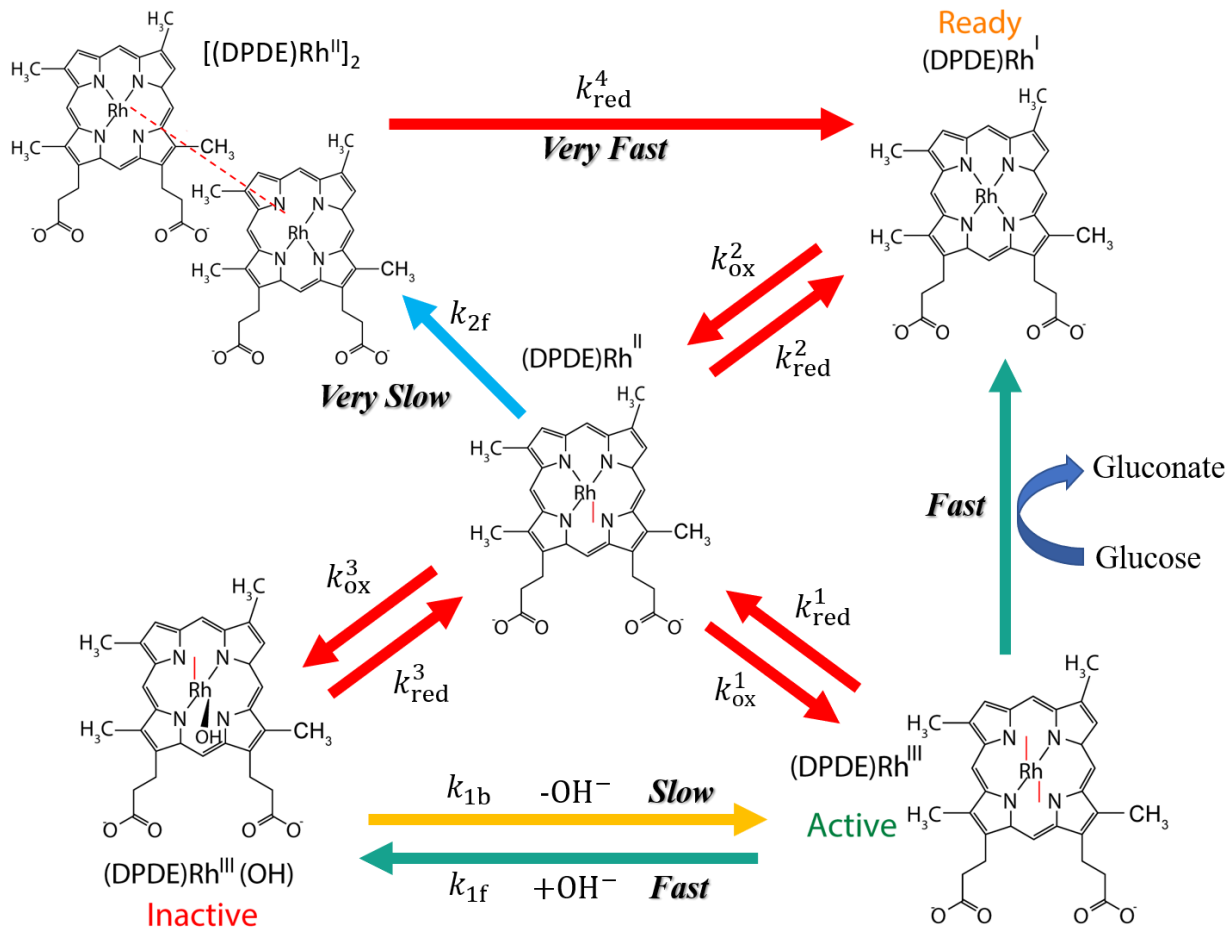

Figure 5.9: Overall catalytic cycle including rhodium dimer formation. The red arrows represent the very fast electron transfer step. The rest arrows in different colour represent different chemical steps, which are defined from Equations 5.16 to 5.21.

6. Conclusions

The thesis has detailed model-based experimental frameworks working in mechanistic analysis and validating the experiments of some highly complex electrochemical systems. The conventional Butler-Volmer model is applied to describe the fundamental electrochemical reaction. Cyclic and chronoamperometric voltammetry is employed to quantitatively study a hydrogenase-like electrocatalytic inactivation and activation process.

Chapter 3 proposes a novel high-order operator-splitting (OS) fully implicit finite difference (FIFD) method for the first time tested to solve nonlinear diffusion-controlled electrode reaction problem. This new approach shows excellent agreements with typical mechanisms where a homogenous reaction can be straightforwardly included into the algorithm. The method has been tested and validated for various electrocatalytic reaction mechanisms and has been found to be more efficient and stable numerical techniques when compared to the result obtained from conventional finite difference method. However, this work also highlights some limitations of this scheme when working on some complex and incompletely defined system such as hydrogenase mechanism.

Chapter 4 describes a mechanistic study of hydrogenase-like electrocatalytic activation and inactivation mechanism in order to compare the operator-splitting scheme to classic finite difference method. The investigation of electrocatalytic inactivation and activation processes (IAPs) is fully model-based design corresponding to an EC'CE mechanism analysed in the basis on a unique current behaviour obtained from cyclic voltammogram of non-enzymatic catalyst by preparing rhodium-porphyrin catalyst on a multi-walled carbon nanotube matrix. The present study elucidates the mechanism of molecular IAP (summarised in Figure 4.13) and shows how the kinetic and thermodynamic parameters of the surface-confined rhodium-porphyrinic catalyst causes odd voltammetric traces in both the experimental results and the mathematical models. The verification of operator-splitting method in this well-defined system shows some constraints in solving certain complex mechanisms because two inner iterations for root finding which often leads to the local minima of the current value. But the method is still believed having a replace to solve complex systems when given the feasibility and applicability of this novel numerical strategy.

Chapter 5 keeps exploring the electrocatalysis of rhodium-porphyrin catalyst. The very critical rate constants of electron transfer are suggested to verify by a multi-step chronoamperometric method

which is proven successfully employed in [NiFe] hydrogenase. Although the high electron transfer rate constant of molecular-catalyst cannot help to directly fit the experimental data to the model, we applied a step potential function to the explored EC'CE mechanism and a good agreement can be obtained indirectly between experiments and simulations. An additional rhodium dimer formation step is accidently detected originated from an unexpected difference between oxidation and reduction peak current. the cyclic voltammogram over a larger potential range helps to find out this underlying mechanism at very low scan rate, and the overall electrocatalytic mechanism of rhodium-porphyrin catalyst maps an EC'CECE scheme summarised in Figure 5.9.

The combination of experimental results and mathematical models confirms that the role of the hydroxide ions as an inhibitor in the catalytic cycle is comparable to the inactivation process of [NiFe] hydrogenase during the hydrogen oxidation. However, hydroxide ions play a significant role in the glucose deprotonation to facilitate the catalytic reaction at the metal centre. Such a deprotonation step can be replaced by the introduction of Brønsted bases avoiding chemically inactive and unfavourable intermediates that arise from the hydroxide coordination. Thus, Brønsted bases may be employed to test the similarities of the inactivation of the porphyrins at pH 7 and to compare it with hydrogenase at this pH, which could lead to important breakthroughs in electrocatalysis. In addition, two-electron oxidation steps are intrinsic to electrochemical reactions involving H_2, CO_2, and numerous other molecules. These results and observations might have important impacts and implications for the development of efficient molecular electrocatalysts composed of very low loading of precious metals, with applications extending beyond alcohol or sugar oxidation.

Appendix

Materials

Commercially available analytical grade reagents, α-D-Glucose, $Rh_2Cl_2(CO)_4$, 1-methyl-2-pyrrolidinone (NMP), Deuteroporphine IX dimethyl ester, and potassium hydroxide (KOH) were purchased from Sigma-Aldrich. Commercial grade thin Multi-Walled Carbon Nanotubes (MWCNT) (9.5 nm diameter, purity >98%), obtained from Nanocyl were used as received without any purification step. Deuteroporphyrine IX dimethyl ester Rhodium(III) ((DPDE)Rh^{III}) was synthetized and characterized by NMR according to literature, electrospray ionization mass spectrometry (ESI-MS), UV-visible spectroscopy[199].

Electrochemical Measurements

Cyclic voltammetry (CV) was performed in a conventional three-electrode cell equipped with a glassy carbon (GC) electrode (geometric area $= 0.071$ cm^2), a platinum wire counter-electrode and a saturated calomel electrode (SCE) as reference electrode. The surface of GC electrodes was polished with a 2 µm diamond paste, washed with water using ultrasound, and rinsed with acetone and ethanol.

CVs were recorded after three successive reproducible scans. Electrochemical experiments were performed in aqueous KOH solutions in the pH 14, 0.1 M. Britton-Robinson buffer solutions were used for the preparation of pH 12. pH measurements were conducted during all experiments. All $E_{1/2}$ values reported in this work were determined from CV as an average of the oxidative and reductive peak potentials $\left(E^{\mathrm{ox}} + E^{\mathrm{red}}\right)/2$. The solutions were deoxygenated by purging and keeping argon prior to each experiment over the solution and during the whole experiment.

SEM and TEM microscopy

The morphology of the modified electrodes was investigated by SEM using an ULTRA 55 FESEM based on the GEMENI FESEM column with beam booster (Nanotechnology Systems Division, Carl Zeiss NTS GmbH, Germany) and a tungsten gun and TEM (JEOL, JEM-2010, 200 kV).

Fabrication of MWCNT/(DPDE)Rh^{III} electrode

MWCNT/(DPDE)Rh^{III} were prepared with the aim to produce electrodes via π stacking interactions. This MWCNT/(DPDE)Rh^{III} matrix was prepared via a simple filtration of MWCNTs dispersion in presence of (DPDE)Rh^{III}. Experimentally, commercial MWCNTs (5 mg) were dispersed in 10 ml of THF and subjected to sonication for 1 h in order to form homogeneous suspension. Then, 5 mg of (DPDE)Rh^{III} was added to the MWCNTs dispersion under magnetic stirring. After 12 hours , the mixture was then filtered under vacuum over a PTFE membrane filter with a pore size of 0.45 μm. The formed MWCNT/(DPDE)Rh^{III} matrix was rinsed with THF and deionized water to remove any unbound components. The formed powder on a PTFE membrane was then dried in a vacuum oven at 80℃ for 60 mins and carefully peeled off from the surface of the filter. MWCNT/(DPDE)Rh^{III} electrode was fabricated using the following procedure: MWCNT/(DPDE)Rh^{III} powder was added to 1 ml of NMP solvent. The suspension was homogenized by magnetic stirring for 60 mins. The resulting supernatant was used as catalyst ink. For electrochemical investigations, a portion (20 μL) of this suspension was dropped onto a freshly polished GC disk electrode (3 mm diameter) and the solvent was removed under reduced pressure.

Fabrication of MWCNT/Hydrogenase electrode

Aquifex aeolicus [NiFe] hydrogenase was purified and prepared as described[213]. The deposition MWCNT was performed by drop-coating of 20 µL of MWCNT dispersion in NMP on GC electrodes followed by evaporation of the solvent under vacuum. The modified electrodes were then washed with phosphate buffer solution (PBS) several times. Finally, the electrodes were incubated in 20 µL of [NiFe] hydrogenase (5 µM in PBS pH 7.4) for 4 hours at 4°C. The resulting electrodes were then washed with phosphate buffer solution.

DFT calculation

Geometry optimisations, total energy calculations were performed by using first-principle calculations within the framework of density functional theory (DFT), as implemented in the plane wave set Vienna ab initio Simulation Package (VASP) code[214,215]. The Perdew-Burke-Ernzerhof (PBE) functional[216] within the generalized gradient approximation (GGA) was used to model exchange correlation energy. The projector augmented wave (PAW) pseudo-potentials[217,218] were used to describe the interaction between valence electron and ionic cores. A cut-off kinetic energy for plane-wave basis set was fixed to 500 eV. A Gaussian smearing with $\sigma = 0.05$ eV to the orbital occupation is applied to broaden the Fermi level for electronic convergence during structure relaxation. We calculate thermodynamic corrections derived from solvent effect (G_{solv}) by using VASPsol.[219] The energy barrier for the two-electron transfer process from (DPDE)Rh^{III} into (DPDE)Rh^{I} approximates to the Gibbs free reaction energy (ΔG) for the electron transfer process from (DPDE)Rh^{III} into (DPDE)Rh^{II}, since we regard (DPDE)Rh^{II} as the saddle Point for the two-electron transfer process. ΔG is calculated through the following expression:

$$\Delta G = \Delta E + \Delta E_{\mathrm{ZPE}} - T\Delta S$$

where ΔE is reaction energy derived from DFT calculation, ΔE_{ZPE} is the zero-point energy difference for the two-electron transfer process obtained from vibrational frequency calculation. ΔS is the entropy difference due to the reaction. The corresponding results are shown in the Appendix Table.

Appendix Table: Parameters obtained for DFT calculations			
ΔG (eV)	ΔE (eV)	ΔE_{ZPE} (eV)	$T\Delta S$ (eV) (T = 298.15K)
0.42	0.382	0.038	0.000416

References

1 Maheshwari, V., Rangaiah, G. P. & Samavedham, L. Multiobjective framework for model-based design of experiments to improve parameter precision and minimize parameter correlation. *Industrial & Engineering Chemistry Research* **52**, 8289-8304 (2013).

2 Borders, W. A., Akima, H., Fukami, S., Moriya, S., Kurihara, S., Horio, Y., Sato, S. & Ohno, H. Analogue spin–orbit torque device for artificial-neural-network-based associative memory operation. *Applied Physics Express* **10**, 013007 (2016).

3 Fu, T., Peng, X., Zhao, Y., Feng, C., Huang, C., Li, Q. & Wang, Z. MD simulation of effect of crystal orientations and substrate temperature on growth of Cu/Ni bilayer films. *Applied Physics A* **122**, 67 (2016).

4 Wang, Y., Dolde, F., Biamonte, J., Babbush, R., Bergholm, V., Yang, S., Jakobi, I., Neumann, P., Aspuru-Guzik, A., Whitfield, J. D. & Wrachtrup, J. Quantum simulation of helium hydride cation in a solid-state spin register. *ACS nano* **9**, 7769-7774 (2015).

5 Abou-Taouk, A., Farcy, B., Domingo, P., Vervisch, L., Sadasivuni, S., & Eriksson, L. E. Optimized reduced chemistry and molecular transport for large eddy simulation of partially premixed combustion in a gas turbine. *Combustion Science and Technology* **188**, 21-39 (2016).

6 Zhou, L., Lu, Z., Ren, Z., Lu, T. & Luo, K. Large eddy simulation of an n-heptane spray flame with dynamic adaptive chemistry under different oxygen concentrations. *SAE International Journal of Engines* **8**, 447-454 (2015).

7 Stănescu, D. G., Ardeleanu, M. E. & Stan, A. C. Designing, simulation and testing of low current passive filters used in the didactic activity. In *Modern Power Systems (MPS), 2017 International Conference*, 1-4 (2017).

8 Zhang, H., Yu, K., Wang, C., Su, Z., Wang, C., Sun, D., Cai, H., Chen, Z. & Zhou, B. pH and ligand dependent assembly of Well–Dawson arsenomolybdate capped architectures. *Inorganic chemistry* **53**, 12337-12347 (2014).

9 Kubas, A., Orain, C., De Sancho, D., Saujet, L., Sensi, M., Gauquelin, C., Meynial-Salles, I., Soucaille, P., Bottin, H., Baffert, C. & Fourmond, V. Mechanism of O_2 diffusion and reduction in FeFe hydrogenases. *Nature chemistry* **9**, 88 (2017).

10 Roncaroli, F., Bill, E., Friedrich, B., Lenz, O., Lubitz, W., & Pandelia, M. E. Cofactor composition and function of a H_2-sensing regulatory hydrogenase as revealed by Mössbauer and EPR spectroscopy. *Chemical science* **6**, 4495-4507 (2015).

11 Ozkop, E. & Altas, I. H. Control, power and electrical components in wave energy conversion systems: A review of the technologies. *Renewable and Sustainable Energy Reviews* **67**, 106-115 (2017).

12 Yaramasu, V. & Wu, B. Predictive control of a three-level boost converter and an NPC inverter for high-power PMSG-based medium voltage wind energy conversion systems. *IEEE Trans. Power Electron* **29**, 5308-5322 (2014).

13 Ma, T., Yang, H. & Lu, L. Development of hybrid battery–supercapacitor energy storage for remote area renewable energy systems. *Applied Energy* **153**, 56-62 (2015).

14 Raihan, M., Smith, K., Almoraya, A. & Khan, F. Interior permanent magnet synchronous machine (IPMSM) design for environment friendly hybrid electric vehicle (HEV) applications. In *Humanitarian Technology Conference (R10-HTC), 2017 IEEE Region 10.* 375-378 (2017).

15 Ruan, J., Zheng, J., Dong, L. & Qiu, R. Environment-friendly technology of recovering full resources of waste capacitors. *ACS Sustainable Chemistry & Engineering* **5**, 287-293 (2016).

16 Hossain, J., Hossain, E., Sakib, N. & Bayindir, R. Modelling and Simulation of Permanent Magnet Synchronous Generator Wind Turbine: A Step to Microgrid Technology. *International Journal of Renewable Energy Research (IJRER)* **7**, 443-450 (2017).

17 Tashtoush, B. & Younes, M. B. Comparative Thermodynamic Study of Refrigerants to Select the Best Environment-Friendly Refrigerant for Use in a Solar Ejector Cooling System. *Arabian Journal for Science and Engineering*, 1-20 (2018).

18 Mathew, S., Yella, A., Gao, P., Humphry-Baker, R., Curchod, B. F., Ashari-Astani, N., Tavernelli, I., Rothlisberger, U., Nazeeruddin, M. K. & Grätzel, M. Dye-sensitized solar cells with 13% efficiency achieved through the molecular engineering of porphyrin sensitizers. *Nature chemistry* **6**, 242 (2014).

19 Wassenaar, T. A., Ingólfsson, H. I., Böckmann, R. A., Tieleman, D. P. & Marrink, S. J. Computational lipidomics with insane: a versatile tool for generating custom membranes for molecular simulations. *Journal of chemical theory and computation* **11**, 2144-2155 (2015).

20 Chen, H.-Y., Lin, M.-H., Wang, C.-Y., Chang, Y.-M. & Gwo, S. Large-scale hot spot engineering for quantitative SERS at the single-molecule scale. *Journal of the American Chemical Society* **137**, 13698-13705 (2015).

21 Mancilla, E., Palacios-Morales, C. A., Córdova-Aguilar, M. S., Trujillo-Roldán, M. A., Ascanio, G., & Zenit, R. A hydrodynamic description of the flow behavior in shaken flasks. *Biochemical engineering journal* **99**, 61-66 (2015).

22 Acebes, S., Fernandez-Fueyo, E., Monza, E., Lucas, M. F., Almendral, D., Ruiz-Dueñas, F. J., Lund, H., Martinez, A. T. & Guallar, V. Rational enzyme engineering through biophysical and biochemical modeling. *ACS Catalysis* **6**, 1624-1629 (2016).

23 Zhuang, K. H. & Herrgård, M. J. Multi-scale exploration of the technical, economic, and environmental dimensions of bio-based chemical production. *Metabolic engineering* **31**, 1-12 (2015).

24 Bard, A. J. & Faulkner, L. R. *Fundamentals and applications* Vol. 2 (2001).

25 Zhu, C., Du, D., Eychmüller, A. & Lin, Y. Engineering ordered and nonordered porous noble metal nanostructures: synthesis, assembly, and their applications in electrochemistry. *Chemical reviews* **115**, 8896-8943 (2015).

26 Jiang, Y., Xu, K. & Zeng, C. Use of electrochemistry in the synthesis of heterocyclic structures. *Chemical reviews* **118**, 4485-4540 (2017).

27 He, L., Weniger, F., Neumann, H. & Beller, M. Synthesis, characterization, and application of metal nanoparticles supported on nitrogen-doped carbon: catalysis beyond electrochemistry. *Angewandte Chemie International Edition* **55**, 12582-12594 (2016).

28 An, S., Jo, H. S., Kim, D. Y., Lee, H. J., Ju, B. K., Al-Deyab, S. S., Ahn, J. H., Qin, Y., Swihart, M. T., Yarin, A. L. & Yoon, S. S. Self-Junctioned Copper Nanofiber Transparent Flexible Conducting Film via Electrospinning and Electroplating. *Advanced Materials* **28**, 7149-7154 (2016).

29 Zhao, K., Yu, H., Zhang, H. & Zhong, X. Electroplating cuprous sulfide counter electrode for high-efficiency long-term stability quantum dot sensitized solar cells. *The Journal of Physical Chemistry C* **118**, 5683-5690 (2014).

30 Tocci, M., Pola, A., La Vecchia, G. & Modigell, M. Characterization of a new aluminium alloy for the production of wheels by Hybrid Aluminium Forging. *Procedia Engineering* **109**, 303-311 (2015).

31 Ageeva, E., Ageev, E., Horyakova, N. & Malukhov, V. Production of copper electroerosion nanopowders from wastes in kerosene medium. *Журнал нано-та електронної фізики*, 6, № 3, 03011-1 (2014).

32 Zhang, M., Liao, C., Mak, C. H., You, P., Mak, C.L. & Yan, F. Highly sensitive glucose sensors based on enzyme-modified whole-graphene solution-gated transistors. *Scientific reports* **5**, 8311 (2015).

33 Niu, X., Li, X., Pan, J., He, Y., Qiu, F., & Yan, Y. Recent advances in non-enzymatic electrochemical glucose sensors based on non-precious transition metal materials: opportunities and challenges. *RSC Advances* **6**, 84893-84905 (2016).

34 Yan, D., Hu, M., Li, S., Liang, J., Wu, Y., & Ma, S. Electrochemical deposition of ZnO nanostructures onto porous silicon and their enhanced gas sensing to NO_2 at room temperature. *Electrochimica Acta* **115**, 297-305 (2014).

35 Li, Z., Li, P., Xu, Q. & Li, H. Europium (III)–β-diketonate complex-containing nanohybrid luminescent pH detector. *Chemical Communications* **51**, 10644-10647 (2015).

36 Hou, M., Chen, L., Guo, Z., Dong, X., Wang, Y., & Xia, Y. A clean and membrane-free chlor-alkali process with decoupled Cl_2 and H_2/NaOH production. *Nature communications* **9**, 438 (2018).

37 Compton, R. G. & Banks, C. E. *Understanding voltammetry* (Imperial College Press, 2011).

38 Butler, J. A. V. The thermodynamics of the surfaces of solutions. *Proceedings of the Royal Society of London. Series A* **135**, 348-375 (1932).

39 Erdey-Gruz, T. & Volmer, M. The theory of hydrogen overvoltage. *Zeitschrift für Physikalische Chemie* **150**, 203-213 (1930).

40 Laidler, K. J. The development of the Arrhenius equation. *Journal of Chemical Education* **61**, 494 (1984).

41 Lasaga, A. C. Transition state theory. *Reviews in Mineralogy and Geochemistry* **8** (1981).

42 Gilbert, R. G. & Smith, S. C. Theory of unimolecular and recombination reactions (1990).

43 Hele, T. J. & Althorpe, S. C. Derivation of a true (t→ 0+) quantum transition-state theory. I. Uniqueness and equivalence to ring-polymer molecular dynamics transition-state-theory. *The Journal of chemical physics* **138**, 084108 (2013).

44 Ebert, M., Lyu, S., Rise, M. & Wolf, M. *Biomaterials for Artificial Organs* 81-112 (2011).

45 Aoki, K. Theory of ultramicroelectrodes. *Electroanalysis* **5**, 627-639 (1993).

46 Bard, A. J. & Mirkin, M. V. *Scanning electrochemical microscopy* (2012).

47 Robinson, P. J., Noronha, J., DeGeorge, J. J., Freed, L. M., Nariai, T., & Rapoport, S. I. A quantitative method for measuring regional in vivo fatty-acid incorporation into and turnover within brain phospholipids: review and critical analysis. *Brain research reviews* **17**, 187-214 (1992).

48 Pishko, M. V., Michael, A. C. & Heller, A. Amperometric glucose microelectrodes prepared through immobilization of glucose oxidase in redox hydrogels. *Analytical Chemistry* **63**, 2268-2272 (1991).

49 Li, R. Z., Peng, R., Kihm, K. D., Bai, S., Bridges, D., Tumuluri, U., Wu, Z., Zhang, T., Compagnini, G., Feng, Z. & Hu, A. High-rate in-plane micro-supercapacitors scribed onto photo paper using in situ femtolaser-reduced graphene oxide/Au nanoparticle microelectrodes. *Energy & Environmental Science* **9**, 1458-1467 (2016).

50 Vitale, F., Summerson, S. R., Aazhang, B., Kemere, C. & Pasquali, M. Neural stimulation and recording with bidirectional, soft carbon nanotube fiber microelectrodes. *ACS nano* **9**, 4465-4474 (2015).

51 Fisher, A. C. *Electrode Dynamics* (Oxford University Press, 1996).

52 Kaufmann, R. S. *Geochemistry* 245-246 (Springer Netherlands, 1998).

53 Bird, R. B., Stewart, W. E. & Lightfoot. *Transport phenomena* (John Wiley & Sons, 2007).

54 Higuchi, E., Uchida, H. & Watanabe, M. Effect of loading level in platinum-dispersed carbon black electrocatalysts on oxygen reduction activity evaluated by rotating disk electrode. *Journal of Electroanalytical Chemistry* **583**, 69-76 (2005).

55 Arino, C., Serrano, N., Díaz-Cruz, J. M. & Esteban, M. Voltammetric determination of metal ions beyond mercury electrodes. A review. *Analytica chimica acta* **990**, 11-53 (2017).

56 Gajdar, J., Horakova, E., Barek, J., Fischer, J. & Vyskocil, V. Recent applications of mercury electrodes for monitoring of pesticides: A critical review. *Electroanalysis* **28**, 2659-2671 (2016).

57 Im, H., Kim, T., Song, H., Choi, J., Park, J. S., Ovalle-Robles, R., Yang, H. D., Kihm, K. D., Baughman, R. H., Lee, H. H. & Kang, T. J. High-efficiency electrochemical thermal energy harvester using carbon nanotube aerogel sheet electrodes. *Nature communications* **7**, 10600 (2016).

58 Amatore, C. & Fosset, B. Equivalence between microelectrodes of different shapes: Between myth and reality. *Analytical Chemistry* **68**, 4377-4388 (1996).

59 Cochran, W. *Mathematical Proceedings of the Cambridge Philosophical Society* 365-375 (Cambridge University Press, 1934).

60 Wolfbauer, G., Bond, A. M., Eklund, J. C. & MacFarlane, D. R. A channel flow cell system specifically designed to test the efficiency of redox shuttles in dye sensitized solar cells. *Solar energy materials and solar cells* **70**, 85-101 (2001).

61 Fuhrmann, J., Zhao, H., Holzbecher, E., Langmach, H., Chojak, M., Halseid, R., Jusys, Z. & Behm, J. Experimental and numerical model study of the limiting current in a channel flow cell with a circular electrode. *Physical Chemistry Chemical Physics* **10**, 3784-3795 (2008).

62 Arias, A. C., Ready, S. E., Lujan, R., Wong, W. S., Paul, K. E., Salleo, A., Chabinyc, M. L., Apte, R., Street, R. A., Wu, Y. & Liu, P. All jet-printed polymer thin-film transistor active-matrix backplanes. *Applied Physics Letters* **85**, 3304-3306 (2004).

63 Noguchi, Y., Sekitani, T., Yokota, T. & Someya, T. Direct inkjet printing of silver electrodes on organic semiconductors for thin-film transistors with top contact geometry. *Applied Physics Letters* **93**, 273 (2008).

64 Cummings, C. Y., Zoppi, G., Forbes, I., Colombara, D., Peter, L. M. & Marken, F. Rocking disc electro-deposition of CuIn alloys, selenisation, and pinhole effect minimisation in CISe solar absorber layers. *Electrochimica Acta* **79**, 141-147 (2012).

65 Ahn, S. D., Fisher, A. C., Buchard, A., Bull, S. D., Bond, A. M. & Marken, F. Hydrodynamic Rocking Disc Electrode Study of the TEMPO-mediated Catalytic Oxidation of Primary Alcohols. *Electroanalysis* **28**, 2093-2103 (2016).

66 Lindsay, S. *Introduction to Nanoscience* (Oxford university press, 2009).

67 Kirby, B. J. *Micro-and nanoscale fluid mechanics: transport in microfluidic devices*. (Cambridge university press, 2010).

68 Probstein, R. *Physicochemical Hydrodynamics* (Wiley, 1994).

69 Cottrell, F. Application of the Cottrell equation to chronoamperometry. *Z Physik Chem* **42**, 385 (1902).

70 Kambara, T. Polarographic diffusion current observed with square wave voltage. I. Effect produced by the sudden change of electrode potential. *Bulletin of the Chemical Society of Japan* **27**, 523-526 (1954).

71 Reinmuth, W. Three-dimensional representation of voltammetric processes. *Analytical Chemistry* **32**, 1509-1512 (1960).

72 Ngamchuea, K., Eloul, S., Tschulik, K. & Compton, R. G. Planar diffusion to macro disc electrodes—what electrode size is required for the Cottrell and Randles-Sevcik equations to apply quantitatively? *Journal of Solid State Electrochemistry* **18**, 3251-3257 (2014).

73 Barker, G. C. & Jenkins, I. L. Square-wave polarography. *Analyst* **77**, 685-696 (1952).

74 Trnková, L., Kizek, R. & Vacek, J. Square wave and elimination voltammetric analysis of azidothymidine in the presence of oligonucleotides and chromosomal DNA. *Bioelectrochemistry* **63**, 31-36 (2004).

75 Osteryoung, J. G. & Osteryoung, R. A. Square wave voltammetry. *Analytical Chemistry* **57**, 101-110 (1985).

76 Osteryoung, J. & Odea, J. Square-wave voltammetry. *Electroanalytical chemistry* **14**, 209-308 (1986).

77 Ramaley, L. & Krause, M. S. Theory of square wave voltammetry. *Analytical Chemistry* **41**, 1362-1365 (1969).

78 Gavaghan, D. & Bond, A. A complete numerical simulation of the techniques of alternating current linear sweep and cyclic voltammetry: analysis of a reversible process by conventional and fast Fourier transform methods. *Journal of Electroanalytical Chemistry* **480**, 133-149 (2000).

79 Song, P., Fisher, A. C., Wadhawan, J. D., Cooper, J. J., Ward, H. J. & Lawrence, N. S. A mechanistic study of the EC' mechanism–the split wave in cyclic voltammetry and square wave voltammetry. *RSC Advances* **6**, 70237-70242 (2016).

80 Song, P., Ma, H., Meng, L., Wang, Y., Nguyen, H. V., Lawrence, N. S. & Fisher, A. C. Fourier transform large amplitude alternating current voltammetry investigations of the split wave phenomenon in electrocatalytic mechanisms. *Physical Chemistry Chemical Physics* **19**, 24304-24315 (2017).

81 Horn, E. J., Rosen, B. R. & Baran, P. S. Synthetic organic electrochemistry: an enabling and innately sustainable method. *ACS central science* **2**, 302-308 (2016).

82 Mitsudo, K., Kurimoto, Y., Yoshioka, K. & Suga, S. Miniaturization and Combinatorial Approach in Organic Electrochemistry. *Chemical reviews* (2018).

83 Little, R. D. & Moeller, K. D. Introduction: Electrochemistry: Technology, synthesis, energy, and materials. *ACS Publications* (2018).

84 Najafpour, M. M., Moghaddam, N. J., Hosseini, S. M., Madadkhani, S., Hołyńska, M., Mehrabani, S., Bagheri, R. & Song, Z. Nanolayered manganese oxides: insights from inorganic electrochemistry. *Catalysis Science & Technology* **7**, 3499-3510 (2017).

85 Meng, X., Quenneville, F., Venne, F., Di Mauro, E., Işık, D., Barbosa, M., Drolet, Y., Natile, M. M., Rochefort, D., Soavi, F. & Santato, C. Correction to "Electrolyte-Gated WO3 Transistors: Electrochemistry, Structure, and Device Performance". *The Journal of Physical Chemistry C* **119**, 23292-23292 (2015).

86 de Biani, F. F. & Zanello, P. The competition between chemistry and biology in assembling iron-sulfur derivatives. Molecular structures and electrochemistry. Part IV. {[Fe_3S_4](SγCys)$_3$} proteins. *Inorganica Chimica Acta* **455**, 319-328 (2017).

87 Song, X. Z., Song, S. Y., Zhao, S. N., Hao, Z. M., Zhu, M., Meng, X., Wu, L. L. & Zhang, H. J. Single-Crystal-to-Single-Crystal Transformation of a Europium (III) Metal–Organic Framework Producing a Multi-responsive Luminescent Sensor. *Advanced Functional Materials* **24**, 4034-4041 (2014).

88 Zhong, Y., Trinh, M. T., Chen, R., Purdum, G. E., Khlyabich, P. P., Sezen, M., Oh, S., Zhu, H., Fowler, B., Zhang, B. & Wang, W. Molecular helices as electron acceptors in high-performance bulk heterojunction solar cells. *Nature communications* **6**, 8242 (2015).

89 Lukatskaya, M. R., Dunn, B. & Gogotsi, Y. Multidimensional materials and device architectures for future hybrid energy storage. *Nature communications* **7**, 12647 (2016).

90 Hammarström, L. Accumulative charge separation for solar fuels production: coupling light-induced single electron transfer to multielectron catalysis. *Accounts of chemical research* **48**, 840-850 (2015).

91 Blumberger, J. Recent advances in the theory and molecular simulation of biological electron transfer reactions. *Chemical reviews* **115**, 11191-11238 (2015).

92 Wang, C., Zhang, X. & Liu, Y. Promotion of multi-electron transfer for enhanced photocatalysis: a review focused on oxygen reduction reaction. *Applied Surface Science* **358**, 28-45 (2015).

93 Sumliner, J. M., Lv, H., Fielden, J., Geletii, Y. V. & Hill, C. L. Polyoxometalate Multi-Electron-Transfer Catalytic Systems for Water Splitting. *European Journal of Inorganic Chemistry* **2014**, 635-644 (2014).

94 Ding, J., Zhou, Y., Li, Y., Guo, S. & Huang, X. MoS_2 nanosheet assembling superstructure with a three-dimensional ion accessible site: a new class of bifunctional materials for batteries and electrocatalysis. *Chemistry of Materials* **28**, 2074-2080 (2016).

95 Gong, M. & Dai, H. A mini review of NiFe-based materials as highly active oxygen evolution reaction electrocatalysts. *Nano Research* **8**, 23-39 (2015).

96 Chen, X. A., Chen, X., Xu, X., Yang, Z., Liu, Z., Zhang, L., Xu, X., Chen, Y. & Huang, S. Sulfur-doped porous reduced graphene oxide hollow nanosphere frameworks as metal-free electrocatalysts for oxygen reduction reaction and as supercapacitor electrode materials. *Nanoscale* **6**, 13740-13747 (2014).

97 Wood, M. & Zhang, B. Bipolar electrochemical method for dynamic in situ control of single metal nanowire growth. *ACS nano* **9**, 2454-2464 (2015).

98 Görlin, M., Chernev, P., Ferreira de Araújo, J., Reier, T., Dresp, S., Paul, B., Krähnert, R., Dau, H. & Strasser, P. Oxygen evolution reaction dynamics, faradaic charge efficiency, and the active metal redox states of Ni–Fe oxide water splitting electrocatalysts. *Journal of the American Chemical Society* **138**, 5603-5614 (2016).

99 Fabbri, E., Nachtegaal, M., Binninger, T., Cheng, X., Kim, B. J., Durst, J., Bozza, F., Graule, T., Schäublin, R., Wiles, L. & Pertoso, M. Dynamic surface self-reconstruction is the key of highly active perovskite nano-electrocatalysts for water splitting. *Nature materials* **16**, 925 (2017).

100 Liu, X., Shi, L. & Gu, J.-D. Microbial electrocatalysis: Redox mediators responsible for extracellular electron transfer. *Biotechnology advances* (2018).

101 Roy-Mayhew, J. D., Pope, M. A., Punckt, C. & Aksay, I. A. Intrinsic Catalytic Activity of Graphene Defects for the CoII/III (bpy) 3 Dye-Sensitized Solar Cell Redox Mediator. *ACS applied materials & interfaces* **8**, 9134-9141 (2016).

102 McCloskey, B. D. & Addison, D. A viewpoint on heterogeneous electrocatalysis and redox mediation in nonaqueous Li-O2 batteries. *ACS Publications* (2016).

103 Noh, H., Kung, C. W., Otake, K.I., Peters, A. W., Li, Z., Liao, Y., Gong, X., Farha, O. K. & Hupp, J. T. Redox Mediator-Assisted Electrocatalytic Hydrogen Evolution from Water by a Molybdenum Sulfide-Functionalized Metal–Organic Framework. *ACS Catalysis* (2018).

104 Qi, J., Zhang, W., Xiang, R., Liu, K., Wang, H. Y., Chen, M., Han, Y. & Cao, R. Porous nickel–iron oxide as a highly efficient electrocatalyst for oxygen evolution reaction. *Advanced Science* **2**, 1500199 (2015).

105 Chen, Z., Ma, Z., Song, J., Wang, L. & Shao, G. A novel approach for the preparation of Ni–CeO 2 composite cathodes with enhanced electrocatalytic activity. *RSC Advances* **6**, 60806-60814 (2016).

106 She, X., Yang, D., Jing, D., Yuan, F., Yang, W., Guo, L. & Che, Y. Nitrogen-doped one-dimensional (1D) macroporous carbonaceous nanotube arrays and their application in electrocatalytic oxygen reduction reactions. *Nanoscale* **6**, 11057-11061 (2014).

107 Lobaccaro, P., Singh, M. R., Clark, E. L., Kwon, Y., Bell, A. T. & Ager, J. W. Effects of temperature and gas–liquid mass transfer on the operation of small electrochemical cells for the quantitative evaluation of CO_2 reduction electrocatalysts. *Physical Chemistry Chemical Physics* **18**, 26777-26785 (2016).

108 Feng, L. L., Yu, G., Wu, Y., Li, G. D., Li, H., Sun, Y., Asefa, T., Chen, W. & Zou, X. High-index faceted Ni_3S_2 nanosheet arrays as highly active and ultrastable electrocatalysts for water splitting. *Journal of the American Chemical Society* **137**, 14023-14026 (2015).

109 Yoon, D., Seo, B., Lee, J., Nam, K. S., Kim, B., Park, S., Baik, H., Joo, S. H. & Lee, K. Facet-controlled hollow Rh_2S_3 hexagonal nanoprisms as highly active and structurally robust catalysts toward hydrogen evolution reaction. *Energy & Environmental Science* **9**, 850-856 (2016).

110 Ahn, S. H. & Manthiram, A. Direct growth of ternary Ni–Fe–P porous nanorods onto nickel foam as a highly active, robust bi-functional electrocatalyst for overall water splitting. *Journal of Materials Chemistry A* **5**, 2496-2503 (2017).

111 Liu, X., Cui, S., Sun, Z. & Du, P. Robust and highly active copper-based electrocatalyst for hydrogen production at low overpotential in neutral water. *Chemical Communications* **51**, 12954-12957 (2015).

112 Del Barrio, M., Sensi, M., Orain, C., Baffert, C., Dementin, S., Fourmond, V. & Léger, C. Electrochemical investigations of hydrogenases and other enzymes that produce and use solar fuels. *Accounts of chemical research* **51**, 769-777 (2018).

113 Zhang, L., Beaton, S. E., Carr, S. B. & Armstrong, F. A. Direct visible light activation of a surface cysteine-engineered [NiFe]-hydrogenase by silver nanoclusters. *Energy & Environmental Science* **11**, 3342-3348 (2018).

114 Vignais, P. M., Billoud, B. & Meyer, J. Classification and phylogeny of hydrogenases. *FEMS microbiology reviews* **25**, 455-501 (2001).

115 Vignais, P. M. & Billoud, B. Occurrence, classification, and biological function of hydrogenases: an overview. *Chemical reviews* **107**, 4206-4272 (2007).

116 Cammack, R., Frey, M. & Robson, R. *Hydrogen as a fuel: learning from nature*. (CRC Press, 2015).

117 Tamagnini, P., Axelsson, R., Lindberg, P., Oxelfelt, F., Wünschiers, R. & Lindblad, P. Hydrogenases and hydrogen metabolism of cyanobacteria. *Microbiology and Molecular Biology Reviews* **66**, 1-20 (2002).

118 Tamagnini, P., Leitão, E., Oliveira, P., Ferreira, D., Pinto, F., Harris, D. J., Heidorn, T. & Lindblad, P. Cyanobacterial hydrogenases: diversity, regulation and applications. *FEMS microbiology reviews* **31**, 692-720 (2007).

119 Thauer, R. K., Kaster, A. K., Goenrich, M., Schick, M., Hiromoto, T. & Shima, S. Hydrogenases from methanogenic archaea, nickel, a novel cofactor, and H_2 storage. *Annual review of biochemistry* **79**, 507-536 (2010).

120 Fontecilla-Camps, J. C., Amara, P., Cavazza, C., Nicolet, Y. & Volbeda, A. Structure–function relationships of anaerobic gas-processing metalloenzymes. *Nature* **460**, 814 (2009).

121 Fontecilla-Camps, J. C., Volbeda, A., Cavazza, C. & Nicolet, Y. Structure/function relationships of [NiFe]-and [FeFe]-hydrogenases. *Chemical reviews* **107**, 4273-4303 (2007).

122 Volbeda, A., Garcin, E., Piras, C., de Lacey, A. L., Fernandez, V. M., Hatchikian, E. C., Frey, M. & Fontecilla-Camps, J. C. Structure of the [NiFe] hydrogenase active site: evidence for biologically uncommon Fe ligands. *Journal of the American Chemical Society* **118**, 12989-12996 (1996).

123 Happe, R. P., Roseboom, W., Pierik, A. J., Albracht, S. P. & Bagley, K. A. Biological activition of hydrogen. *Nature* **385**, 126 (1997).

124 Teixeira, M., Moura, I., Fauque, G., Czechowski, M., Berlier, Y., Lespinat, P. A., Le Gall, J., Xavier, A. V. & Moura, J. J. G. Redox properties and activity studies on a nickel-containing hydrogenase isolated from a halophilic sulfate reducer Desulfovibrio salexigens. *Biochimie* **68**, 75-84 (1986).

125 Rieder, R., Cammack, R. & Hall, D. O. Purification and properties of the soluble hydrogenase from *Desulfovibrio desulfuricans* (strain Norway 4). *European journal of biochemistry* **145**, 637-645 (1984).

126 Garcin, E., Vernede, X., Hatchikian, E. C., Volbeda, A., Frey, M. & Fontecilla-Camps, J. C. The crystal structure of a reduced [NiFeSe] hydrogenase provides an image of the activated catalytic center. *Structure* **7**, 557-566 (1999).

127 Shima, S., Lyon, E. J., Thauer, R. K., Mienert, B. & Bill, E. Mössbauer studies of the iron−sulfur cluster-free hydrogenase: the electronic state of the mononuclear Fe active site. *Journal of the American Chemical Society* **127**, 10430-10435 (2005).

128 Shima, S., Lyon, E. J., Sordel‐Klippert, M., Kauß, M., Kahnt, J., Thauer, R. K., Steinbach, K., Xie, X., Verdier, L. & Griesinger, C. The Cofactor of the Iron–Sulfur Cluster Free Hydrogenase Hmd: Structure of the Light-Inactivation Product. *Angewandte Chemie* **116**, 2601-2605 (2004).

129 Schwörer, B., Fernandez, V. M., Zirngibl, C. & Thauer, R. K. H_2-forming N^5, N^{10}-methylenetetrahydromethanopterin dehydrogenase from methanobacterium thermoautotrophicum: Studies of the catalytic mechanism of H_2 formation using hydrogen isotopes. *European journal of biochemistry* **212**, 255-261 (1993).

130 Ogata, H., Hirota, S., Nakahara, A., Komori, H., Shibata, N., Kato, T., Kano, K. & Higuchi, Y. Activation process of [NiFe] hydrogenase elucidated by high-resolution X-ray analyses: conversion of the ready to the unready state. *Structure* **13**, 1635-1642 (2005).

131 Nicolet, Y., Piras, C., Legrand, P., Hatchikian, C. E. & Fontecilla-Camps, J. C. Desulfovibrio desulfuricans iron hydrogenase: the structure shows unusual coordination to an active site Fe binuclear center. *Structure* **7**, 13-23 (1999).

132 Lubitz, W., Ogata, H., Rüdiger, O. & Reijerse, E. Hydrogenases. *Chemical reviews* **114**, 4081-4148 (2014).

133 Wu, L.-F. & Mandrand, M. Microbial hydrogenases: primary structure, classification, signatures and phylogeny. *FEMS microbiology reviews* **10**, 243-269 (1993).

134 Cammack, R. Bioinorganic chemistry: hydrogenase sophistication. *Nature* **397**, 214 (1999).

135 Hatchikian, E. C., Forget, N., Fernandez, V. M., Williams, R. & Cammack, R. Further characterization of the [Fe]-hydrogenase from *Desulfovibrio desulfuricans* ATCC 7757. *European journal of biochemistry* **209**, 357-365 (1992).

136 Sherigara, B. S., Kutner, W. & D'Souza, F. Electrocatalytic properties and sensor applications of fullerenes and carbon nanotubes. *Electroanalysis: An International Journal Devoted to Fundamental and Practical Aspects of Electroanalysis* **15**, 753-772 (2003).

137 Shao, Y., Wang, J., Wu, H., Liu, J., Aksay, I. A. & Lin, Y. Graphene based electrochemical sensors and biosensors: a review. *Electroanalysis: An International Journal Devoted to Fundamental and Practical Aspects of Electroanalysis* **22**, 1027-1036 (2010).

138 Toghill, K. E. & Compton, R. G. Electrochemical non-enzymatic glucose sensors: a perspective and an evaluation. *Int. J. Electrochem. Sci* **5**, 1246-1301 (2010).

139 Sun, Y., Buck, H. & Mallouk, T. E. Combinatorial discovery of alloy electrocatalysts for amperometric glucose sensors. *Analytical chemistry* **73**, 1599-1604 (2001).

140 Wang, J. Glucose biosensors: 40 years of advances and challenges. *Electroanalysis: An International Journal Devoted to Fundamental and Practical Aspects of Electroanalysis* **13**, 983-988 (2001).

141 Patel, H., Li, X. & Karan, H. Amperometric glucose sensors based on ferrocene containing polymeric electron transfer systems—a preliminary report. *Biosensors and Bioelectronics* **18**, 1073-1076 (2003).

142 Tsujimura, S., Kojima, S., Kano, K., Ikeda, T., Sato, M., Sanada, H. & Omura, H. Novel FAD-dependent glucose dehydrogenase for a dioxygen-insensitive glucose biosensor. *Bioscience, biotechnology, and biochemistry* **70**, 654-659 (2006).

143 Ferri, S., Kojima, K. & Sode, K. Review of glucose oxidases and glucose dehydrogenases: a bird's eye view of glucose sensing enzymes. *SAGE Publications* (2011).

144 Palmisano, F., Zambonin, P. G., Centonze, D. & Quinto, M. A Disposable, Reagentless, Third-Generation Glucose Biosensor Based on Overoxidized Poly (pyrrole)/Tetrathiafulvalene− Tetracyanoquinodimethane Composite. *Analytical chemistry* **74**, 5913-5918 (2002).

145 Tang, H., Cai, D., Ren, T., Xiong, P., Liu, Y., Gu, H. & Shi, G. Fabrication of a low background signal glucose biosensor with 3D network materials as the electrocatalyst. *Analytical biochemistry* **567**, 63-71 (2019).

146 Lawrence, N. S., Davis, J. & Compton, R. G. Analytical strategies for the detection of sulfide: a review. *Talanta* **52**, 771-784 (2000).

147 Lawrence, N. S., Tustin, G. J., Faulkner, M. & Jones, T. G. Ferrocene sulfonates as electrocatalysts for sulfide detection. *Electrochimica Acta* **52**, 499-503 (2006).

148 Banks, C. E., Yashina, A. S., Tustin, G. J., Lafitte, V. G., Jones, T. G. & Lawrence, N. S. Exploring alkylated ferrocene sulfonates as electrocatalysts for sulfide detection.

Electroanalysis: An International Journal Devoted to Fundamental and Practical Aspects of Electroanalysis **19**, 2518-2522 (2007).

149 Lawrence, N.S., Thompson, M., Prado, C., Jiang, L., Jones, T. G. & Compton, R. G. Amperometric detection of sulfide at a boron doped diamond electrode: The electrocatalytic reaction of sulfide with ferricyanide in aqueous solution. *Electroanalysis: An International Journal Devoted to Fundamental and Practical Aspects of Electroanalysis* **14**, 499-504 (2002).

150 Dutta, S., Shimpalee, S. & Van Zee, J. Three-dimensional numerical simulation of straight channel PEM fuel cells. *Journal of Applied Electrochemistry* **30**, 135-146 (2000).

151 Zhang, X., Shyy, W. & Sastry, A. M. Numerical simulation of intercalation-induced stress in Li-ion battery electrode particles. *Journal of the Electrochemical Society* **154**, A910-A916 (2007).

152 Patankar, N. A. & Hu, H. H. Numerical simulation of electroosmotic flow. *Analytical Chemistry* **70**, 1870-1881 (1998).

153 Sklyar, O., Kueng, A., Kranz, C., Mizaikoff, B., Lugstein, A., Bertagnolli, E. & Wittstock, G. Numerical Simulation of Scanning Electrochemical Microscopy Experiments with Frame-Shaped Integrated Atomic Force Microscopy−SECM Probes Using the Boundary Element Method. *Analytical chemistry* **77**, 764-771 (2005).

154 Forsythe, G. & Wasow, W. R. *Finite-Difference Methods for Partial Differential Equations, Applied Mathematical Series* (Wiley, New York, 1960).

155 Tavella, D. & Randall, C. *Pricing Financial Instruments: The Finite Difference Method (Wiley Series in Financial Engineering)* (Wiley New York, 2000).

156 Narasimhan, T. & Witherspoon, P. An integrated finite difference method for analyzing fluid flow in porous media. *Water Resources Research* **12**, 57-64 (1976).

157 Kunz, K. S. & Luebbers, R. J. *The finite difference time domain method for electromagnetics* (CRC press, 1993).

158 Ferrigno, R., Brevet, P. & Girault, H. Finite element simulation of the chronoamperometric response of recessed and protruding microdisc electrodes. *Electrochimica acta* **42**, 1895-1903 (1997).

159 Li, R., Chen, Z. & Wu, W. *Generalized difference methods for differential equations: numerical analysis of finite volume methods*. (CRC Press, 2000).

160 Eichstädt, J., Green, M., Turner, M., Peiró, J. & Moxey, D. Accelerating high-order mesh optimisation with an architecture-independent programming model. *Computer Physics Communications* **229**, 36-53 (2018).

161 Foy, W. H. Position-location solutions by Taylor-series estimation. *IEEE Transactions on Aerospace and Electronic Systems*, 187-194 (1976).

162 Britz, D. & Strutwolf, J. Higher-order spatial discretisations in electrochemical digital simulations. Part 4. Discretisation on an arbitrarily spaced grid. *Computational biology and chemistry* **27**, 327-337 (2003).

163 Feldberg, S. W. & Goldstein, C. I. Examination of the behavior of the fully implicit finite-difference algorithm with the Richtmyer modification: behavior with an exponentially expanding time grid. *Journal of Electroanalytical Chemistry* **397**, 1-10 (1995).

164 Rudolph, M. A fast implicit finite difference algorithm for the digital simulation of electrochemical processes. *Journal of electroanalytical chemistry and interfacial electrochemistry* **314**, 13-22 (1991).

165 Strassen, V. Gaussian elimination is not optimal. *Numerische mathematik* **13**, 354-356 (1969).

166 Ypma, T. J. Historical development of the Newton–Raphson method. *SIAM review* **37**, 531-551 (1995).

167 Dowell, M. & Jarratt, P. A modified regula falsi method for computing the root of an equation. *BIT Numerical Mathematics* **11**, 168-174 (1971).

168 Kumar, A., Ciucci, F., Morozovska, A. N., Kalinin, S. V. & Jesse, S. Measuring oxygen reduction/evolution reactions on the nanoscale. *Nature chemistry* **3**, 707 (2011).

169 Um, S., Wang, C. Y. & Chen, K. Computational fluid dynamics modeling of proton exchange membrane fuel cells. *Journal of the Electrochemical society* **147**, 4485-4493 (2000).

170 Krawiec, H., Vignal, V. & Akid, R. Numerical modelling of the electrochemical behaviour of 316L stainless steel based upon static and dynamic experimental microcapillary-based techniques. *Electrochimica Acta* **53**, 5252-5259 (2008).

171 Henstridge, M. C., Laborda, E., Rees, N. V. & Compton, R. G. Marcus–Hush–Chidsey theory of electron transfer applied to voltammetry: A review. *Electrochimica Acta* **84**, 12-20 (2012).

172 LeVeque, R. J. *Numerical Methods for Conservation Laws* 122-135 (Springer, 1990).

173 Liao, S. On the homotopy analysis method for nonlinear problems. *Applied Mathematics and Computation* **147**, 499-513 (2004).

174 Hock, W. & Schittkowski, K. Test examples for nonlinear programming codes. *Journal of Optimization Theory and Applications* **30**, 127-129 (1980).

175 Singer, M., Pope, S. & Najm, H. Operator-splitting with ISAT to model reacting flow with detailed chemistry. *Combustion Theory and Modelling* **10**, 199-217 (2006).

176 Sportisse, B. An analysis of operator splitting techniques in the stiff case. *Journal of Computational Physics* **161**, 140-168 (2000).

177 Siauw, W., Ng, E. & Mazumdar, J. Unsteady stenosis flow prediction: a comparative study of non-Newtonian models with operator splitting scheme. *Medical engineering & physics* **22**, 265-277 (2000).

178 Schwer, D. A., Lu, P., Green, W. H. & Semiao, V. A consistent-splitting approach to computing stiff steady-state reacting flows with adaptive chemistry. *Combustion Theory and Modelling* **7**, 383-399 (2003).

179 Glowinski, R. & Le Tallec, P. *Augmented Lagrangian and operator-splitting methods in nonlinear mechanics*. Vol. 9 (SIAM, 1989).

180 Yan, Y., Xia, B.Y., Ge, X., Liu, Z., Fisher, A. & Wang, X. A flexible electrode based on iron phosphide nanotubes for overall water splitting. *Chemistry-A European Journal* **21**, 18062-18067 (2015).

181 Zhang, J., Zhao, Z., Xia, Z. & Dai, L. A metal-free bifunctional electrocatalyst for oxygen reduction and oxygen evolution reactions. *Nature nanotechnology* **10**, 444-452 (2015).

182 Zeng, Z., Chang, K.-C., Kubal, J., Markovic, N. M. & Greeley, J. Stabilization of ultrathin (hydroxy) oxide films on transition metal substrates for electrochemical energy conversion. *Nature Energy* **2**, 17070 (2017).

183 Elouarzaki, K., Mandoc, L.R.P., Gorgy, K., Holzinger, M., Amarandei, C.A., Ungureanu, E.M. & Cosnier, S. Synthesis and electrochemical characterization of original "TEMPO" functionalized multiwall carbon nanotube materials: application to iron (II) detection. *Electrochemistry Communications* **60**, 131-134 (2015).

184 Altamura, L., Horvath, C., Rengaraj, S., Rongier, A., Elouarzaki, K., Gondran, C., Maçon, A.L., Vendrely, C., Bouchiat, V., Fontecave, M. & Mariolle, D. A synthetic redox biofilm made from metalloprotein–prion domain chimera nanowires. *Nature chemistry* **9**, 157 (2017).

185 Nekrassova, O., Allen, G.D., Lawrence, N.S., Jiang, L., Jones, T.G. & Compton, R.G. The oxidation of cysteine by aqueous ferricyanide: a kinetic study using boron doped diamond electrode voltammetry. *Electroanalysis* **14**, 1464-1469 (2002).

186 Deshpande, A.G., Gu, Y., Matthews, S.M., Yunus, K., Slater, N.K., Brennan, C.M. & Fisher, A.C. Hydrodynamic focusing studies in microreactors using voltammetric analysis: Theory and experiment. *Chemical Engineering Journal* **149**, 428-434 (2009).

187 Hexter, S. V., Chung, M.-W., Vincent, K. A. & Armstrong, F. A. Unusual reaction of [NiFe]-hydrogenases with cyanide. *Journal of the American Chemical Society* **136**, 10470-10477 (2014).

188 Elouarzaki, K., Fisher, A. C. & Lee, J.-M. Molecular porphyrinic freestanding buckypaper electrodes from carbon nanotubes for glucose fuel cells. *Journal of Materials Chemistry A* **5**, 8927-8932 (2017).

189 Vincent, K. A., Parkin, A., Lenz, O., Albracht, S.P., Fontecilla-Camps, J.C., Cammack, R., Friedrich, B. & Armstrong, F.A. Electrochemical definitions of O_2 sensitivity and oxidative inactivation in hydrogenases. *Journal of the American Chemical Society* **127**, 18179-18189 (2005).

190 Ceccaldi, P., Marques, M. C., Fourmond, V., Pereira, I. C. & Léger, C. Oxidative inactivation of NiFeSe hydrogenase. *Chemical Communications* **51**, 14223-14226 (2015).

191 Orain, C., Saujet, L., Gauquelin, C., Soucaille, P., Meynial-Salles, I., Baffert, C., Fourmond, V., Bottin, H. & Léger, C. Electrochemical measurements of the kinetics of inhibition of two FeFe hydrogenases by O_2 demonstrate that the reaction is partly reversible. *Journal of the American Chemical Society* **137**, 12580-12587 (2015).

192 Megarity, C. F., Esselborn, J., Hexter, S. V., Wittkamp, F., Apfel, U. P., Happe, T. & Armstrong, F. A. Electrochemical Investigations of the Mechanism of Assembly of the Active-site H-Cluster of [FeFe]-hydrogenases. *Journal of the American Chemical Society* **138**, 15227-15233 (2016).

193 Limoges, B. t. & Savéant, J.-M. Catalysis by immobilized redox enzymes. Diagnosis of inactivation and reactivation effects through odd cyclic voltammetric responses. *Journal of Electroanalytical Chemistry* **562**, 43-52 (2004).

194 Savéant, J. & Su, K. Homogeneous redox catalysis of electrochemical reaction: Part VI. Zone diagram representation of the kinetic regimes. *Journal of electroanalytical chemistry and interfacial electrochemistry* **171**, 341-349 (1984).

195 Artero, V. & Saveant, J. -M. Toward the rational benchmarking of homogeneous H_2-evolving catalysts. *Energy & environmental science* **7**, 3808-3814 (2014).

196 Jones, A. K., Lamle, S. E., Pershad, H. R., Vincent, K. A., Albracht, S.P. & Armstrong, F. A. Enzyme electrokinetics: electrochemical studies of the anaerobic interconversions between active and inactive states of Allochromatium vinosum [NiFe]-hydrogenase. *Journal of the American Chemical Society* **125**, 8505-8514 (2003).

197 Lukey, M. J., Parkin, A., Roessler, M. M., Murphy, B. J., Harmer, J., Palmer, T., Sargent, F. & Armstrong, F. A. How Escherichia coli is equipped to oxidize hydrogen under different redox conditions. *Journal of Biological Chemistry* **285**, 3928-3938 (2010).

198 Fourmond, V., Infossi, P., Giudici-Orticoni, M.-T. r. s., Bertrand, P. & Léger, C. "Two-step" chronoamperometric method for studying the anaerobic inactivation of an oxygen tolerant NiFe hydrogenase. *Journal of the American Chemical Society* **132**, 4848-4857 (2010).

199 Elouarzaki, K., Le Goff, A., Holzinger, M., Thery, J. & Cosnier, S. Electrocatalytic oxidation of glucose by rhodium porphyrin-functionalized MWCNT electrodes: application to a fully molecular catalyst-based glucose/O_2 fuel cell. *Journal of the American Chemical Society* **134**, 14078-14085 (2012).

200 Costentin, C., Porter, T. R. & Savéant, J.-M. How Do Pseudocapacitors Store Energy? Theoretical Analysis and Experimental Illustration. *ACS Applied Materials & Interfaces* **9**, 8649-8658 (2017).

201 Laviron, E. General expression of the linear potential sweep voltammogram in the case of diffusionless electrochemical systems. *Journal of Electroanalytical Chemistry and Interfacial Electrochemistry* **101**, 19-28 (1979).

202 Stevenson, G. P., Lee, C. Y., Kennedy, G. F., Parkin, A., Baker, R. E., Gillow, K., Armstrong, F. A., Gavaghan, D. J. & Bond, A. M. Theoretical analysis of the two-electron transfer reaction and experimental studies with surface-confined cytochrome c peroxidase using large-amplitude Fourier transformed AC voltammetry. *Langmuir* **28**, 9864-9877 (2012).

203 Tse, Y. H., Seymour, P., Kobayashi, N., Lam, H., Leznoff, C. C. & Lever, A. B. P. Surface electrochemistry of chloro (phthalocyaninato) rhodium (III) species and oxygen reduction electrocatalysis. Formation of a dimeric species. *Inorganic Chemistry* **30**, 4453-4459 (1991).

204 Crank, J. & Nicolson, P. *Mathematical Proceedings of the Cambridge Philosophical Society*. 50-67 (Cambridge University Press, 2008).

205 Thompson, C. M. & Shure, L. *Image processing toolbox: User's guide*. (The MartWorks, 1995).

206 Mocak, J. & Feldberg, S. W. The Richtmyer modification of the fully implicit finite difference algorithm for simulations of electrochemical problems. *Journal of Electroanalytical Chemistry* **378**, 31-37 (1994).

207 Crank, J. & Nicolson, P. A practical method for numerical evaluation of solutions of partial differential equations of the heat-conduction type. *Advances in Computational Mathematics* **6**, 207-226 (1996).

208 Untereker, D. & Bruckenstein, S. Interpretation of isopotential points. Common intersection in families of current-potential curves. *Analytical Chemistry* **44**, 1009-1020 (1972).

209 Gaudiello, J. G., Wright, T. C., Jones, R. A. & Bard, A. J. Electrochemical reduction and reoxidation accompanied by reversible geometric isomerization. Electrochemistry of bis (dicarbonyl-. mu.-di-tert-butylphosphidorhodium). Isolation and x-ray crystal structure of bis (tetra-n-butylammonium) bis (dicarbonyl-. mu.-di-tert-butylphosphidorhodate). *Journal of the American Chemical Society* **107**, 888-897 (1985).

210 Armstrong, F. A., Evans, R. M., Hexter, S. V., Murphy, B. J., Roessler, M.M. & Wulff, P. Guiding principles of hydrogenase catalysis instigated and clarified by protein film electrochemistry. *Accounts of chemical research* **49**, 884-892 (2016).

211 Limoges, B. ı. & Savéant, J.-M. Catalysis by immobilized redox enzymes. Diagnosis of inactivation and reactivation effects through odd cyclic voltammetric responses. *Journal of Electroanalytical Chemistry* **562**, 43-52 (2004).

212 Pandelia, M. E., Fourmond, V., Tron-Infossi, P., Lojou, E., Bertrand, P., Léger, C., Giudici-Orticoni, M. T. & Lubitz, W. Membrane-bound hydrogenase I from the hyperthermophilic bacterium *Aquifex aeolicus*: enzyme activation, redox intermediates and oxygen tolerance. *Journal of the American Chemical Society* **132**, 6991-7004 (2010).

213 Luo, X., Brugna, M., Tron-Infossi, P., Giudici-Orticoni, M. T. & Lojou, E. Immobilization of the hyperthermophilic hydrogenase from Aquifex aeolicus bacterium onto gold and carbon nanotube electrodes for efficient H_2 oxidation. *JBIC Journal of Biological Inorganic Chemistry* **14**, 1275-1288 (2009).

214 Kresse, G. & Furthmüller, J. Efficiency of ab-initio total energy calculations for metals and semiconductors using a plane-wave basis set. *Comput. Mater. Sci.* **6**, 15-50 (1996).

215 Kresse, G. & Furthmüller, J. Efficient iterative schemes for *ab initio* total-energy calculations using a plane-wave basis set. *Phys. Rev. B* **54**, 11169-11186 (1996).

216 Perdew, J. P., Burke, K. & Ernzerhof, M. Generalized gradient approximation made simple. *Phys. Rev. Lett.* **77**, 3865-3868 (1996).

217 PE, B. Projector augmented-wave method. *Phys. Rev. B* **50**, 17953-17979 (1994).

218 Kresse, G. & Joubert, D. From ultrasoft pseudopotentials to the projector augmented-wave method. *Phys. Rev. B* **59**, 1758-1775 (1999).

219 Mathew, K., Sundararaman, R., Letchworthweaver, K., Arias, T. A. & Hennig, R. G. Implicit solvation model for density-functional study of nanocrystal surfaces and reaction pathways. *J Chem Phys* **140**, 084106 (2014).